eman ta zabal zazu

Universidad del País Vasco
Euskal Herriko Unibertsitatea

MULTI-CRYSTALLINE POLYMER SYSTEMS:

BIODEGRADABLE TRIBLOCK TERPOLYMERS

AND

NANOSTRUCTURED BLENDS

MORPHOLOGY, CRYSTALLIZATION AND PROPERTIES

JORDANA KARIN PALACIOS GUTIÉRREZ

PhD Thesis

Polymer Science and Technology Department,

Faculty of Chemistry.

Donostia-San Sebastián, 2017

eman ta zabal zazu

Universidad del País Vasco
Euskal Herriko Unibertsitatea

Multi-Crystalline Polymer Systems: Biodegradable Triblock Terpolymers and Nanostructured Blends. Morphology, Crystallization and Properties

by

Jordana Karin Palacios Gutérrez

Advisor

Prof. Alejandro Jesús Müller Sánchez

Polymer Science and Technology Department,

Faculty of Chemistry.

Donostia-San Sebastián, 2017

ABSTRACT

In this PhD thesis, the morphology, crystallization behavior and properties of two multi-crystalline polymer systems with at least two crystallizable phases were addressed. The two systems chosen were: triple crystalline biodegradable PEO-*b*-PCL-*b*-PLLA triblock terpolymers and double crystalline PP/PA6 nanostructured blends with nanosilica and compatibilizer agents. The PEO-*b*-PCL-*b*-PLLA triblock terpolymers, with increasing PLLA content, exhibited a triple crystalline nature. The three blocks are able to crystallize separately and sequentially upon cooling from a homogeneous melt, as it was proven by SAXS, WAXS and DSC analysis. The crystallization sequence is as follows: first the PLLA block, then the PCL block, and finally the PEO block. PLOM demonstrated that the PLLA block templates the spherulitic morphology of the terpolymer. The subsequent crystallization of PCL and PEO blocks occurs inside the interlamellar spaces of the previously formed PLLA spherulites. Thus, three different lamellae of PLLA, PCL and PEO coexist together within the same spherulite. The nanoscale morphology evaluated by SAXS and AFM consists of lamellae of each block alternated with a mixed amorphous phase in between. The theoretical analysis of the SAXS curves suggests that only one lamella of PCL or one lamella of PEO is inserted randomly between two adjacent PLLA lamellae. Complex competitive effects such as plasticizing, nucleation, anti-plasticizing and confinement occurred during the isothermal crystallization of the terpolymers. The second system, 80:20 PP/PA6 blends with a fixed amount of PPgMA and decreasing nanosilica content, was prepared by melt mixing. After optimization by varying components and composition, a PP/PA6 blend, stabilized with 1.6 % hydrophobic nanosilica and compatibilized with high grafting level PPgMA, exhibited a droplet size reduced morphology with enhanced ductility and barrier properties. The droplet size reduction is a result of the preferential location of the nanosilice at the interface avoiding drop coalescence. Owing to the reduced droplet size, the PA6 dispersed phase crystallizes in a fractioned fashion, and self-nucleation experiments elucidated the nature of the phenomenon. Nanosilica particles act as outstanding stabilizers but do not promote interfacial adhesion between the phases. Therefore, the use of an optimal content of nanosilica along with a compatibilizer yields a synergistic effect on the PP/PA6 blend.

TABLE OF CONTENTS

CHAPTER I.

CHAPTER II.

CHAPTER III.

CHAPTER IV.

CHAPTER V.

CHAPTER VI.

LIST OF TABLES

LIST OF FIGURES

CHAPTER I

GENERAL INTRODUCTION AND OBJECTIVES

1.1 INTRODUCTION

Nowadays, the complexity in polymeric materials increases as the demand for new products and specific applications. The growing strategies to design tuned-property materials are almost infinite. Some of them include new synthetic routes and architectures, polymer blending, copolymerization, functionalization, grafting, and polymers mixed with fillers. Among them, block copolymers [1-3] and polymer blending with nanofillers [4-6] are of the most importance.

Both of them involve the coexistence of two or more phases. Block copolymerization potentially joins the features of different homopolymers in a synergistic manner at the nanoscale level. And polymer blending is one of the most straightforward strategies to combine the best individual features of at least two polymers, providing a proper interaction between the phases.

Many of the novel applications of these multiphasic materials make use of polymers of semicrystalline nature. The crystallinity properties of pure polymers, such as crystal structure, morphology, crystallization kinetics and thermal transitions, are different from those exhibited when they are part of a polymer blend or copolymerized with other monomers. And the crystalline features and structure ultimately influence the physical performance of the final material.

Therefore, the potential use of multi-crystalline polymeric systems requires a deep comprehension of how the involved phases interact at the microscale, as in a polymer blend, and at the nanoscale, as in a block copolymer. The aim of this PhD thesis is to study the morphology and properties of multiphasic polymeric materials with two or more crystalline phases. Compared to amorphous polymers, semicrystalline phases make more complex the understanding of the structure-properties relationship, since the amorphous phase also plays a role in the final behavior. To that purpose, two multiphasic polymeric systems were chosen: triple crystalline biodegradable poly(ethylene oxide)-*b*-poly(ε-caprolactone)-*b*-poly(L-lactide) (PEO-*b*-PCL-*b*-PLLA) triblock terpolymers and double crystalline Polypropylene/Polyamide 6 (PP/PA6) nanostructured blends with nanosilica and compatibilizer agents. The morphology and properties of each system will be assessed, with additional emphasis in the crystallization behavior. The relevance of the current research in these subjects will be presented henceforth, starting with block copolymerization.

Block copolymers have been in the focus of researchers in the field of polymer physics during the past two decades [1-3]. The recent advances in novel block copolymerization routes have allowed obtaining very interesting materials of different molecular architectures, such as linear and cyclic diblock and triblock copolymers and terpolymers, as well as more complicated configurations like stars and combs [2, 7].

Morphology and crystallization of block copolymers are in direct relationship with their physical properties and final performance in several fields. To name a few, block copolymers have been used in biomedical applications, cell adhesion coatings, drug delivery, nanotechnology, stimuli-responsive nanostructured materials, nanoparticles, lithography, patterning and templating in optoelectronics devices, and hydrogels [8-11]. Therefore, understanding the morphology and overall crystallinity is of major interest from scientific and technological points of view [1, 8, 12-15]. Both, structure and crystallization are influenced by the chemical nature, microstructure, molecular weight, composition and segregation strength between blocks. The crystallization conditions also play an important role in the final structure and physical properties of the material. [8, 13-24].

In block copolymers, segments of different chemical nature and chain length are joined together [7]. Because of the chemical differences between segments, the polymer chains can self-assemble into a wide range of ordered superstructures depending on the transition temperatures (order-disorder, crystallization and glass transition) and the miscibility of the blocks. The final morphology is a consequence of the microphase separation driven by either the crystallization event or by the immiscibility between the blocks. Nanostructures of different geometries are exhibited by strongly segregated systems, while miscible block copolymers form mixed spherulitic-type structures with a distinctive birefringence alteration. Well-defined Maltese cross spherulites, concentric spherulites, banded spherulites, axialities and 2D aggregates have been observed [8, 15].

Different crystallization phenomena, such as retarded or first order crystallization kinetics, confined and fractionated crystallization, reduced crystallinity, and plasticizing and nucleating effects have been extensively investigated in miscible diblock and triblock copolymers and terpolymers with one or two crystallizable blocks [8, 14, 19-22, 25]. Particularly, miscible diblock copolymers composed of biodegradable and biocompatible blocks such as PEO, PCL and PLLA exhibit two main behaviors: a plasticizing effect over the PLLA block crystallization, and both nucleating effect and retarded crystallization kinetics of the crystallization of the PCL and PEO blocks [9, 20]. PCL-*b*-PLLA and PEO-*b*-PLLA diblock copolymers attract high interest, because the biodegradation features, physical properties and mechanical performance are directly related to the nano and micro crystalline morphology [8, 20, 21].

The addition of a third crystallizable block raises the complexity of the crystallization behavior of these materials, and only two works have been published in this subject [26, 27]. Sun et al. [26] detected the triple crystalline nature of triblock and pentablock terpolymers of PLLA, PCL and PEO employing DSC and WAXS analysis. Chiang et al.[27] reported single crystals of PEO-*b*-PCL-*b*-PLLA triblock terpolymers obtained from solution in thin films. Therefore, one the aims of this PhD research is a comprehensive understanding of the morphology and crystallization behavior of this new generation of **triple crystalline ABC triblock terpolymers** composed of PEO, PCL and PLLA (PEO-*b*-PCL-*b*-PLLA) [28]. The remarkable tricrystalline structure and the complex crystallization behavior of these materials have been studied by wide angle X-ray scattering (WAXS), small angle X-ray scattering (SAXS), differential scanning calorimetry (DSC), atomic force (AFM), and polarized light optical microscopy (PLOM), and the outcome of the research will be presented in the Chapter 2 of this manuscript. Additional studies performed by fast scanning calorimetry (FSC) will be presented in Chaper 3.

The second aim of this PhD project is to analyze the structure-properties relationship, including the crystallization behavior, of an optimized **double crystalline PP/PA6 blend mixed with compatibilizing agents and silica nanoparticles**.

Immiscible polymers blends with asymmetric compositions (e.g., 90/10, 80/20 or 70/30) typically exhibit sea-island morphologies with large droplet sizes and a lack of adhesion between the components, as a result of the high interfacial tension between the two immiscible phases. As a consequence, these blends generally exhibit poor mechanical performance, since the final properties are a function of blend morphology and interfacial interactions.

To overcome the aforementioned issues, several compatibilization strategies that include adding block copolymers, compatibilizing agents and nanoparticles have been developed in the last few decades [4, 29-34]. The role of a compatibilizer includes: 1) reducing the interfacial tension that leads to an enhancement of the interfacial adhesion and a reduction of the droplet size of the dispersed phase; 2) stabilizing the dispersed phase by suppressing coalescence; and 3) promoting an effective stress transfer between the phases, leading to an improvement of blend performance.

Extensive research has been focused on the potential use of nanoparticles, such as nanosilica (NS) [35-41], not as reinforcement agents but as compatibilizers or stabilizers in immicible polymer blends [33, 34, 42, 43]. The nanoparticles can be located within the polymer matrix, inside the dispersed phase, or at the interface (or at several locations at the same time). When the preferential location is at the interface, nanoparticles can act as solid emulsifiers that stabilize the droplets of the dispersed phase [33, 43]. The interfacial location is due to thermodynamic and kinetic factors: particles surface chemistry, polarity of the polymer phases and shear induced dispersion and collisions mechanism. As a consequence, the blends exhibit a fine-tuned morphology with a significant reduced droplet size and droplet size distribution [33, 34, 42, 43]. The reduction of the droplet size is attributed to several factors: 1) a reduced interfacial tension, 2) a reduced coalescence due to the physical barrier created by the nanoparticles around the droplets [34, 43], 3) a change of the viscosity of the phase (or phases) due to the nanoparticles presence, and 4) strong polymer chain–filler interactions [34, 43].

NS nanoparticles are effective to stabilize 80/20 PP/PA6 blends regardless of the processing conditions employed to prepare or to post-process the blend. The droplet size reduction was a result of the preferential location of NS at the interface. However, the mechanical performance is not been largely improved even though the droplet size reduces [35, 44]. The same behavior occurs in PP/PS [45], PA6/SEBS [46], PP/PET [47] and PS/ABS [48] blends mixed with NS or organoclay nanoparticles. It seems that rigid nanoparticles located at the interface act as stress concentrators without any improvement in interfacial adhesion.

In view of the poor mechanical performance of immiscible blends containing NS with refined morphologies, the proposed strategy is to use compatibilizing agents in addition to NS, in order to obtain stabilized PP/PA6 blends with well-balanced properties. Two PPgMA compatibilizing agents and two NS nanoparticles of different chemical nature, one hydrophilic and other hydrophobic, were employed. A comprehensive study of the morphology, crystallization behavior, mechanical performance and barrier properties is presented in Chapter 4. The morphology of the blends was evaluated by scanning (SEM) and transmission electron microscopy (TEM) and analyzed in terms of interfacial tension estimates. Special interest was placed in the study of the crystallization behavior of the minority PA6 phase and self-nucleation experiments were conducted. Tensile, impact resistance and permeability analysis demonstrated that by carefully choosing the type of compatibilizer agent and the NS content, a compatibilized PP/PA6/NS blend with a good balance between morphology and properties can be obtained.

Closing the manuscript, Chapter 5 summarizes the global remarks and perspectives of the PhD research in these multiphasic polymer systems. Understanding the structure-properties relationship of polymeric materials with multiple crystalline phases is of major importance to tackle novel developments and potential applications.

1.2 OBJECTIVES

1.2.1 General

The main purpose is to study the morphology, crystallization behavior and properties of multiphasic polymeric materials with at least two crystallizable phases. In order to fulfill this objective, two main systems were selected: triple crystalline biodegradable PEO-*b*-PCL-*b*-PLLA triblock terpolymers and double crystalline PP/PA6 nanostructured blends with nanosilica and compatibilizer agents.

1.2.2 Specifics

Triple crystalline biodegradable PEO-b-PCL-b-PLLA triblock terpolymers

- Analysis of the miscibility of the PEO-*b*-PCL-*b*-PLLA triblock terpolymers by SAXS.
- Study of the non isothermal sequential crystallization behavior of the PEO-*b*-PCL-*b*-PLLA triblock terpolymers by DSC and WAXS.
- Analysis of the microscale morphology of the PEO-*b*-PCL-*b*-PLLA triblock terpolymers by PLOM.
- Analysis of the nanoscale morphology of a PEO-*b*-PCL-*b*-PLLA triblock terpolymer and the corresponding PCL-*b*-PLLA diblock copolymer by AFM and SAXS.
- Evaluation of the overall isothermal crystallization kinetics of the PLLA block in the PEO-*b*-PCL-*b*-PLLA triblock terpolymers and PCL-*b*-PLLA diblock copolymers by DSC.
- Evaluation of the overall isothermal crystallization kinetics of the PCL block in the PEO-*b*-PCL-*b*-PLLA triblock terpolymers and PCL-*b*-PLLA diblock copolymers by DSC.
- Evaluation of the overall isothermal crystallization kinetics of the PEO block in a PEO-*b*-PCL-*b*-PLLA triblock terpolymer by DSC.
- Study of the fast scanning calorimetry (FSC) technique and its application in the crystallization analysis of selected homopolymers, PCL-*b*-PLLA diblock copolymers and PEO-*b*-PCL-*b*-PLLA triblock terpolymers.

Double crystalline PP/PA6 nanostructured blends with nanosilica and compatibilizer agents.

- Analysis of the effect of two compatibilizing agents of different grafting level in the morphology of PP/PA6 blends.
- Analysis of the combined effect of both compatibilizing agents and NS nanoparticles in the morphology of PP/PA6 blends.
- Study of the effect of NS chemical nature in the morphology of PP/PA6 blends.
- Optimization of the blend morphology and properties by changing the NS content.
- Evaluation of the interfacial tension by means of contact angle measurements.
- Analysis of the non isothermal crystallization behavior of the PP and PA6 phases in the blends by DSC.
- Further analysis of the crystallization behavior of the PA6 minority phase by means of self-nucleation experiments.
- Evaluation of the tensile properties and impact resistance as a function of the compatibilizing agent, the type of nanosilica and its composition.
- Evaluation of the barrier properties of the optimum blends.

1.3 REFERENCES

[1] C. M. Bates and F. S. Bates, "50th Anniversary Perspective: Block Polymers—Pure Potential," *Macromolecules,* vol. 50, no. 1, pp. 3-22, 2017/01/10 2017.

[2] I. W. Hamley, "Block Copolymers," in *Encyclopedia of Polymer Science and Technology,* vol. 1: John Wiley & Sons, Inc., 2002, pp. 457-482.

[3] I. W. Hamley, *The Physics of Block Copolymers*. Oxford: Oxford University Press, 1998.

[4] C. Koning, M. V. Duin, C. Pagnoulle, and R. Jerome, "Strategies for compatibilization of polymer blends," *Progress in Polymer Science,* vol. 23, pp. 707-757, 1998.

[5] C. C. Sarath, R. A. Shanks, and S. Thomas, "Chapter 1 - Polymer Blends," in *Nanostructured Polymer Blends*Oxford: William Andrew Publishing, 2014, pp. 1-14.

[6] E. R. Sadiku and E. S. Ogunniran, "Chapter 4 - Compatibilization as a Tool for Nanostructure Formation," in *Nanostructured Polymer Blends*Oxford: William Andrew Publishing, 2014, pp. 101-131.

[7] N. Hadjichristidis, M. Pitsikalis, and H. Iatrou, "Synthesis of block copolymers," *Advances in Polymer Science,* vol. 189, pp. 1-124, 2005.

[8] S. Huang and S. Jiang, "Structures and morphologies of biocompatible and biodegradable block copolymers," *RSC Advances,* vol. 4, no. 47, pp. 24566-24583, 2014.

[9] M. J. Barthel, F. H. Schacher, and U. S. Schubert, "Poly(ethylene oxide) (PEO)-based ABC triblock terpolymers-synthetic complexity vs. application benefits," *Polymer Chemistry,* vol. 5, no. 8, pp. 2647-2662, 2014.

[10] X. Guo, L. Wang, X. Wei, and S. Zhou, "Polymer-based drug delivery systems for cancer treatment," *Journal of Polymer Science, Part A: Polymer Chemistry,* Review vol. 54, no. 22, pp. 3525-3550, 2016.

[11] H. Danafar, "Applications of copolymeric nanoparticles in drug delivery systems," *Drug Research,* Review vol. 66, no. 10, pp. 506-519, 2016.

[12] L. Zha and W. Hu, "Molecular simulations of confined crystallization in the microdomains of diblock copolymers," *Progress in Polymer Science,* Review vol. 54-55, pp. 232-258, 2016.

[13] S. Nakagawa, H. Marubayashi, and S. Nojima, "Crystallization of polymer chains confined in nanodomains," *European Polymer Journal,* Review vol. 70, pp. 262-275, 2015.

[14] W. N. He and J. T. Xu, "Crystallization assisted self-assembly of semicrystalline block copolymers," *Progress in Polymer Science,* vol. 37, no. 10, pp. 1350-1400, 2012.

[15] C. Yu, Q. Xie, Y. Bao, G. Shan, and P. Pan, " Crystalline and Spherulitic Morphology of Polymers Crystallized in Confined Systems," *Crystals* vol. 7, p. 147, 2017.

[16] R. M. Michell and A. J. Müller, "Confined Crystallization of Polymeric Materials," *Progress in Polymer Science,* vol. 54-55, pp. 183-216, 2016.

[17] A. J. Müller, M. L. Arnal, and A. T. Lorenzo, "Crystallization in Nano-Confined Polymeric Systems," in *Handbook of Polymer Crystallization*, E. Piorkowska and G. C. Rutledge, Eds. Hoboken, New Jersey: John Wiley and Sons, 2013, pp. 347-372.

[18] H. Takeshita, T. Shiomi, K. Takenaka, and F. Arai, "Crystallization and higher-order structure of multicomponent polymeric systems," *Polymer,* vol. 54, no. 18, pp. 4776-4789, 2013.

[19] S. Li and R. A. Register, "Crystallization in Copolymers " in *Handbook of Polymer Crystallization*, E. Piorkowska and G. C. Rutledge, Eds. Hoboken, New Jersey: John Wiley and Sons, 2013, pp. 327-346.

[20] R. V. Castillo and A. J. Müller, "Crystallization and morphology of biodegradable or biostable single and double crystalline block copolymers," *Progress in Polymer Science,* vol. 34, no. 6, pp. 516-560, 2009.

[21] A. J. Müller, M. L. Arnal, and V. Balsamo, "Crystallization in block copolymers with more than one crystallizable block," *Lecture Notes in Physics,* vol. 714, pp. 229-259, 2007.

[22] A. J. Müller, V. Balsamo, and M. L. Arnal, "Nucleation and crystallization in diblock and triblock copolymers," *Advances in Polymer Science,* vol. 190, pp. 1-63, 2005.

[23] V. Abetz and P. F. W. Simon, "Phase behaviour and morphologies of block copolymers," *Advances in Polymer Science,* vol. 189, pp. 125-212, 2005.

[24] I. Hamley, "Crystallization in Block Copolymers," *Advances in Polymer Science,* vol. 148, pp. 113-137, 1999.

[25] Y. L. Loo, R. A. Register, and A. J. Ryan, "Modes of crystallization in block copolymer microdomains: Breakout, templated, and confined," *Macromolecules,* Article vol. 35, no. 6, pp. 2365-2374, 2002.

[26] L. Sun, L. J. Shen, M. Q. Zhu, C. M. Dong, and Y. Wei, "Synthesis, self-assembly, drug-release behavior, and cytotoxicity of triblock and pentablock copolymers composed of poly(ε-caprolactone), poly(L -lactide), and poly(ethylene glycol)," *Journal of Polymer Science Part A: Polymer Chemistry,* vol. 48, no. 20, pp. 4583-4593, 2010.

[27] Y.-W. Chiang, Y.-Y. Hu, J.-N. Li, S.-H. Huang, and S.-W. Kuo, "Trilayered Single Crystals with Epitaxial Growth in Poly(ethylene oxide)-block-poly(ε-caprolactone)-block-poly(l-lactide) Thin Films," *Macromolecules,* vol. 48, no. 23, pp. 8526-8533, 2015/12/08 2015.

[28] J. Zhao, D. Pahovnik, Y. Gnanou, and N. Hadjichristidis, "Sequential polymerization of ethylene oxide, ε-caprolactone and l-lactide: A one-pot metal-free route to tri- and pentablock terpolymers," *Polymer Chemistry,* vol. 5, no. 12, pp. 3750-3753, 2014.

[29] C. Bucknall and D. R. Paul, *Polymer blends, formulation and performance* New York John Wiley and Sons, 2000.

[30] L. M. Robeson, *Polymer Blends, a comprehensive review*. Cincinnati: Carl Hanser Publisher, 2007.

[31] A. Isayev, *Encyclopedia of polymer blends. Fundamentals*. Weinheim: Wiley-VCH, 2011.

[32] A. Ajji, "Interphase and Compatibilization by Addition of a Compatibilizer," in *Polymer Blends Handbook,* L. A. Utracki and C. A. Wilkie, Eds. 2nd ed. Dordrecht: Springer, 2014, pp. 447-516.

[33] A. Taguet, P. Cassagnau, and J.-M. Lopez-Cuesta, "Structuration, selective dispersion and compatibilizing effectof (nano)fillers in polymer blends," *Progress in Polymer Science,* vol. 39, pp. 1526-1563, 2014.

[34] S. C. Agwuncha *et al.*, "Immiscible Polymer Blends Stabilized with Nanophase," in *Design and Applications of Nanostructured Polymer Blends and Nanocomposite Systems,* R. Shanks and S. Chandrasekharakurup, Eds. Boston: William Andrew Publishing, 2016, pp. 215-237.

[35] F. Laoutid, E. Estrada, R. M. Michell, L. Bonnaud, A. J. Müller, and P. Dubois, "The influence of nanosilica on the nucleation, crystallization and tensile properties of PP-PC and PP-PA blends," *Polymer*, vol. 54, pp. 3982-3993, 2013.

[36] F. Laoutid, D. Francois, Y. Paint, L. Bonnaud, and P. Dubois, "Using nanosilica to fine-tune morphology and properties of polyamide 6/poly(propylene) blends," *Macromolecular Materials and Engineering*, vol. 298, pp. 328-338, 2013.

[37] F. Laoutid, D. Francois, Y. Paint, L. Bonnaud, and P. Dubois, "Morphology and properties of polyamide 6 / poly(propylene) blends fine-tuned with nanosilica," *Macromolecular Symposia*, vol. 321-322, pp. 90-84, 2012.

[38] L. Elias, F. Fenouillot, J.-C. Majeste, G. Martin, and P. Cassagnau, "Migration of nanosilica particles in polymer blends," *Journal of Polymer Science Part B: Polymer Physics*, vol. 46, pp. 1976-1983, 2008.

[39] L. Elias, F. Fenouillot, J. C. Majesté, P. Alcouffe, and P. Cassagnau, "Immiscible polymer blends stabilized with nano-silica particles: Rheology and effective interfacial tension," *Polymer*, vol. 49, no. 20, pp. 4378-4385, 2008.

[40] L. Elias, F. Fenouillot, J.-C. Majesté, and P. Cassagnau, "Morphology and rheology of immiscible polymer blends filled with silica nanoparticles," *Polymer*, vol. 48, pp. 6029-6040, 2007.

[41] J. Vermant, G. Cioccolo, K. Golapan Nair, and P. Moldenaers, "Coalescence suppression in model immiscible polymer blends by nano-sized colloidal particles," *Rheologica Acta*, vol. 43, no. 5, pp. 529-538, 2004.

[42] M. Salzano de Luna and G. Filippone, "Effects of nanoparticles on the morphology of immiscible polymer blends – Challenges and opportunities," *European Polymer Journal*, vol. 79, pp. 198-218, 2016.

[43] R. Scaffaro and L. Botta, "Nanofilled Thermoplastic-Thermoplastic Polymer Blends " in *Nanostructured Polymer Blends*, S. Thomas, R. Shanks, and S. Chandrasekharakurup, Eds. United Kingdom: Elsevier, 2014, pp. 133-160.

[44] L. Sangroniz *et al.*, "The outstanding ability of nanosilica to stabilize dispersions of Nylon 6 droplets in a polypropylene matrix," *Journal of Polymer Science Part B: Polymer Physics*, vol. 53, no. 22, pp. 1567-1579, 2015.

[45] Q. Zhang, H. Yang, and Q. Fu, "Kinetics-controlled compatibilization of immiscible polypropylene/ polystyrene blends using nano-SiO2 particles," *Polymer*, vol. 45, no. 6, pp. 1913-1922, 2004.

[46] B. Zhang, J. S.-P. Wong, D. Shi, R. C.-M. Yam, and R. K.-Y. Li, "Investigation on the mechanical performances of ternary nylon 6/SEBS elastomer/nano-SiO2 hybrid composites with controlled morphology," *Journal of Applied Polymer Science*, vol. 115, no. 1, pp. 469-479, 2010.

[47] M. Entezam, H. A. Khonakdar, A. A. Yousefi, S. H. Jafari, U. Wagenknecht, and G. Heinrich, "On nanoclay localization in polypropylene/poly(ethylene terephthalate) blends: Correlation with thermal and mechanical properties," *Materials & Design*, vol. 45, pp. 110-117, 2013.

[48] B. Chen and J. R. G. Evans, "Mechanical properties of polymer-blend nanocomposites with organoclays: Polystyrene/ABS and high impact polystyrene/ABS," *Journal of Polymer Science Part B: Polymer Physics*, vol. 49, no. 6, pp. 443-454, 2011.

CHAPTER II

CRYSTALLIZATION AND MORPHOLOGY OF TRIPLE CRYSTALLINE BIODEGRADABLE PEO-*b*-PCL-*b*-PLLA TRIBLOCK TERPOLYMERS

Many works have been dedicated to study the crystallization behavior of miscible or weakly segregated block copolymer systems [1-10]. However, special interest has been put on three particular block copolymers over the past decades. Poly(ethylene oxide)-*b*-poly(ε-caprolactone) (PEO-*b*-PCL) [11-29], poly(ethylene oxide)-*b*-poly(L-lactide) (PEO-b-PLLA) [30-43] and poly(ε-caprolactone)-*b*-poly(lactide)s (PCL-*b*-PLA) [4, 6, 8, 44-51]. AB diblock copolymers and ABA terpolymers have attracted the attention of the scientific community due to their biodegradable and biocompatible features that make them suitable for potential applications in the biomedical field [52-56]. Those features can be tailored by modifying the composition and molecular weight of the copolymers, but also by adjusting the crystallization conditions in order to alter the crystallinity of the final material.

2.1 GENERAL CONCEPTS AND STATE OF ART

Since the main focus of Chapter 2 is the morphology and crystallization behavior of block copolymers and terpolymers, basic concepts on crystallization, the basic polymer crystallization theory, and particularly the Avrami solution, will be first summarized briefly. Then, some features of the three polymer blocks: poly (Lactide), poly (ε-caprolactone) and poly (ethylene oxide) will be described. Finally, it is presented an up-to-date and comprehensive state of art of the last 8 years about the crystallization of AB diblock copolymers and ABA and ABC terpolymers of PEO, PCL and PLLA.

2.1.1 Crystallization of polymers

Crystallization of polymers is a first-order phase transformation of a supercooled liquid [57]. Unlike low molecular weight molecules that crystallize immediately after reaching the equilibrium melting point, polymers only start to crystallize at considerable high supercooling. First, slowly, then more rapidly, and finally slowly again as the crystallization temperature is further decreased [57]. This behavior is the result of two superimposed effects. Polymer crystallization takes place at temperatures between the melting temperature (T_m) and the glass transition temperature (T_g). As the temperature decreases, the crystallization rate increases due to the thermodynamic forces that drive the phase transformation. But further increasing the supercooling leads to a decrease of the molecular segments mobility that reduces the crystallization rate. This effect becomes more significant as the temperature approach the glass transition. Hence, the crystallization rate of polymers follows a bell shape trend with a maximum crystallization rate. The high-temperature limit is controlled by the thermodynamic forces and the low-temperature limit is related to the loss of mobility of molecular segments [58].

Polymer crystallization involves primary crystallization, secondary crystallization and crystal reorganization or crystal perfection. During primary crystallization two mechanisms take place: nucleation and secondary nucleation or crystal growth.

Nucleation

The crystal formation in a polymer melt starts with a nucleation step. It involves the formation of a nucleus of supercritical size. This step is controlled by the free enthalpy change due to the phase transformation. At a nucleus critical size, the enthalpy barrier required to allow the nucleus growth is surpassed [58]. The formation of the nuclei may occur in the bulk phase (homogeneous nucleation) or on preexisting surfaces or heterogeneities (heterogeneous nucleation).

If the nucleation goes through a homogeneous mechanism, particles with an enhanced inner order (or embryos) are formed in the melt due to thermal fluctuations. For very small particles the decrease in free energy due to phase transition is exceeded by the increase in interfacial free energy. There is a critical size separating those particles whose free energy of formation increases during growth from those whose energy decreases. If the size of an embryo surpasses this critical value, it turns into the nucleus of a growing crystal. Otherwise, it disappears again. The nucleation step is an active process associated with a free energy barrier to be overcome [59, 60].

The free energy barrier for primary homogeneous nucleation is higher whereas it is lower heterogeneous nucleation. That is because homogeneous nucleation involves the formation of six new surfaces, while heterogeneous nucleations involve fewer surfaces. For that reason, a true primary homogeneous nucleation hardly ever occurs since it requires 50-100 degrees of supercooling. Instead, in the practice, nucleation mostly initiates on the surface of foreign heterogeneities [61]. For this reason, heterogeneous nucleation often is thermodynamically favored, in particular at low supercooling of the melt.

The mechanism of nucleation may changes as a function of temperature. As the supercooooling increases, the thermodynamic driving force for the phase transformation also increases, and as a result, the critical size of the nucleus and the free-enthalpy barrier decrease [57], and an increase in the nucleation rate is observed. But a further increase in the supercooling leads to maximum in the nucleation rate, after which it starts to decrease.

Crystal growth

After nucleation, crystal growth occurs by secondary and tertiary nucleation. The initial step is the formation of a secondary nucleus, which is followed by a series of tertiary nucleation events [61]. Many lamellar crystallites develop simultaneously and the growing crystal can show a quasi-spherical symmetry from the very beginning [59]. The formation of spherulites is the typical semicrystalline morphology observed in many polymers. The size of the spherulites is in the range of micrometers.

The spherulitic growth rate (G) trend with temperature is similar to that of the primary nucleation. It involves two factors: the transport (diffusion) term and the secondary nucleation term. Because both terms have an opposite temperature dependence behavior, the growth rate exhibits a maximum and follows a bell shape curve as function of the crystallization temperature (or the supercooling). At high supercooling (left side of the bell shape curve), the molecular transport is the dominant term. The diffusion of the macromolecules to the growing front becomes very difficult as the temperature reaches the glass transition and the growth rate decreases to zero. At high crystallization temperatures (right side of the bell shape curve), the growth rate is driven by thermodynamic forces of the secondary nucleation (see Figure 2.1) [62]. The growing lamella keeps a constant thickness. Crystal growth takes place in the lateral direction only, i.e., it is two-dimensional. There is no growth in chain direction perpendicular to the layer surface [59].

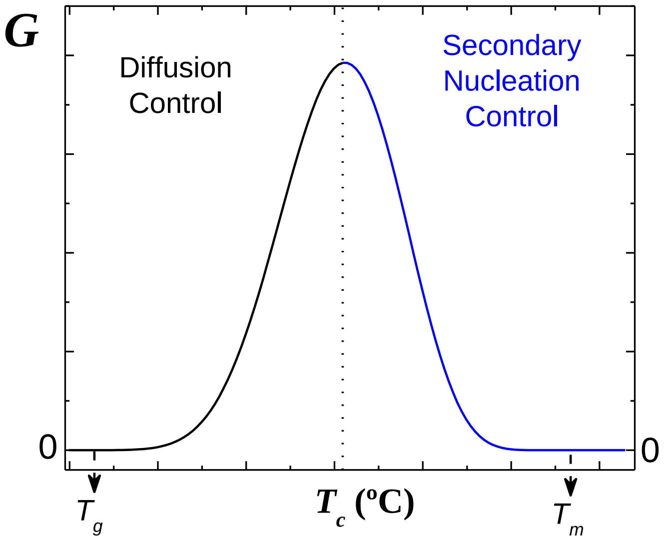

Figure 2.1 Crystal growth rate (*G*) as a function of the isothermal crystallization temperature.

Further crystallization events

After the crystal growth is completed and the sperulites are impingement, a secondary crystallization process may take place inside the interspherulitic regions. Additionally, crystal reorganization and perfection of crystals can be induced under particular conditions such as, long crystallization times, annealing at specific temperatures prior melting, among others. Thermodynamically more stable crystals can be obtained by internal rearrangements, crystalline phase transitions, lamellar thickening, or removal of lattice defects. Crystal reorganization prior melting occurs at local scale. It involves melting of unstable crystals; recrystallization into more stables ones, and subsequent remelting [57].

2.1.2 Polymer crystallization theory

In polymers is not possible to attain high levels of crystallinity, not even for homopolymers of regular structure. High levels of crystallinity can only be achieved at crystallization temperatures closer to the melting temperature but that requires infinite times [63]. Since the crystalline phase only develops, at reasonable rates, at temperatures well below the equilibrium melting temperature, the final state is a non-equilibrium one that is a result of a competition between the thermodynamic and kinetic factors involved in the transformation [63].

Crystallization involves both nucleation and diffusion of the crystallizable units to the crystal front. Short-range diffusion occurs more rapidly at higher temperatures. All diffusive movements are completely 'frozen in' at temperatures below the glass transition temperature. When the diffusing molecule reaches the crystal boundary, it has to form a stable nucleus. The conditions for stability are described by nucleation theory as follows [61]. The increase in free energy is due to the positive contribution from the surface energies ($\sigma_i A_i$, where σ_i is the specific surface energy of surface *i)* and the negative contribution from the crystallization free energy ($\Delta g V_{\text{crystal}}$, where Δg is the specific change in free energy and V_{crystal} is the volume of the nucleus) [60, 61].

Considering a spherical crystal:

$$\Delta G = \frac{4\pi r^3}{3}.\Delta g + 4\pi r^2 \sigma \qquad \text{Eq. 2-1}$$

The critical radius of the sphere (r^*) associated with the free energy barrier is obtained by setting the derivative of ΔG with respect to r and equal to zero:

$$r^* = -\frac{2\sigma T_m^0}{\Delta h^0 \Delta T} \qquad \text{Eq. 2-2}$$

It means that the radius of the critical nucleus increases with decreasing degree of supercooling. By inserting Eq. 2-2, the free energy barrier (AG^*) can be derived:

$$\Delta G^* = \frac{4\pi\sigma^3 (T_m^0)^2}{(\Delta h^0)^2 \Delta T^2}\left[-\frac{8}{3} + 4\right] = \frac{16\pi\sigma^3 (T_m^0)^2}{3(\Delta h^0)^2 \Delta T^2} \qquad \text{Eq. 2-3}$$

From aforementioned equations, nucleation occurs more readily at lower crystallization temperatures because of the lower critical nucleus size and the lower free energy barrier associated with the process [61]. Besides the supercooling, the primary nucleation might be affected by the density of heterogeneities or the presence of nucleating agents [62].

Polymer crystallization theories can take into consideration the overall crystallization kinetics, which includes both primary nucleation and crystal growth contributions [60], or the secondary nucleation (crystal growth) exclusively. The underlying theoretical basis comes from the adaptation of crystallization theories developed for low molecular substances (metals, monomers) [62, 63]. Among the theories that follow the crystallization in polymers, it can be distinguished the Lauritzen and Hoffman (LH) model [59, 61, 63, 64], the Sadler and Gilmer theory [61, 65], the Strobl mesomorphic precursors thesis [59], and the "free growth" theory formulated by Göler and Sachs [63, 66, 67]. The last is one of the first theories developed to study this phenomenon and the Avrami equation is one of its possible solutions. The LH model was developed to provide analytical expressions to quantify the energy barrier associated to the crystal growth.

The "free growth" theory establishes that once a given nuclei is created, it grows unrestricted without the influence of others that may have also been nucleated and could be growing within the same time [62, 63, 68]. Assuming that the polymer structure can be described by a two phase model and *N'* as the steady-state nucleation rate per unit of untransformed mass, then:

$$1 - \lambda(t) = \frac{\rho_c}{\rho_l} \int_o^t v(t,\tau)\,.\,N(\tau).\lambda(\tau).\,dt \qquad \text{Eq. 2-4}$$

where $N(\tau)$ is the nucleation frequency per untransformed volume, $v(t,\tau)$ is the volume of a given center at time t, that was started at time $\tau\,(\tau \le t)$, $\lambda(t)$ is the relative untransformed fraction at time t, and ρ_c and ρ_l are the crystalline and liquid densities, respectively. The parameter $\lambda(t)$ ranges from 1 to 0 indicating that the relative untransformed fraction varies from 0 (fully amorphous) to 1, or to complete conversion to the semi-crystalline state [62]. To solve the expression, a constant nucleation rate and a linear growth in 1 to 3 dimensions is considered. A solution to the expression is the Avrami equation.

2.1.3 The Avrami equation

The Avrami equation was originally obtained by statistical geometrical considerations dealing with the problem of how a sample volume gets covered by growing objects of a certain shape [59]. It was developed by Evans, Kolmogoroff, Johnson and Mehl, and Avrami during the 1930s and 1940s. The fundamentals of the model assumed that crystallization starts randomly at different locations and propagates outwards from the nucleation sites [61]. Certain limitations and special considerations regarding the Avrami analysis for polymers are [61]:

1. The solidified polymer is always only semicrystalline.
2. The volume of the system changes during crystallization.
3. The nucleation is seldom either simple athermal or simple thermal. A mixture of the two is common.
4. Crystallization always follows two stages: (a) primary crystallization, characterized by radial growth of spherulites or axialites; (b) secondary crystallization, i.e. the slow crystallization behind the crystal front caused by crystal thickening, the formation of subsidiary crystal lamellae and crystal perfection. Secondary crystallization is slow and the initial rapid crystallization is usually dominated by primary crystallization.

The simplest form of the Avrami equation, considering a constant nucleation rate and constant linear growth, can be expressed as [60, 62]:

$$1 - v_c = exp(-Kt^n) \qquad \text{Eq. 2-5}$$

where V_c is the relative volumetric transformed fraction, n is the Avrami index and k the overall crystallization rate constant that includes contributions from both nucleation and growth.

The Avrami index (n) is an integer whose value depends on the mechanism of nucleation and on the form of crystal growth. It is composed of two terms:

$$n = n_d + n_n \qquad \text{Eq. 2-6}$$

where n_n represents the time dependence of the nucleation and n_d represents the dimensionality of the growing crystals. The nucleation can be purely instantaneous ($n_n = 0$) or purely sporadic ($n_n = 1$). The dimensionality term n_d can be 1, 2 or 3. In polymers, the possible dimensions of the growing crystal are 2 or 3. They represent axialites (two dimensional lamellar aggregates) and spherulites (superstructural three dimensional aggregates), respectively. Because the nucleation may not be completely sporadic or completely instantaneous, non-integer contributions to the Avrami index are obtained. For instance, when the growth of spherulites is not linear with time, the crystallization process may be governed by diffusion and n_n can have a value of 0.5, which indicates the Fickian dependence of growth with the square root of time [62, 68, 69]. The theoretically expected Avrami index is presented in Table 2.1 [60, 62, 63].

Table 2.1 Avrami Index *n* for various types of nucleation and crystal dimensionality.

Dimension	Homogeneous nucleation				Heterogeneous nucleation
	Linear growth		Diffusion controlled growth		Linear growth
	Instantaneous	Sporadic	Instantaneous	Sporadic	
1D	1	2	1/2	3/2	$1 \leq n \leq 2$
2D	2	3	1	2	$2 \leq n \leq 3$
3D	3	4	3/2	5/2	$3 \leq n \leq 4$

The constant k can be used to provide a quantitative evaluation of the crystallization evolution, since it includes the contribution of both nucleation and crystal growth events. It is directly related with the overall rate of crystallization $\tau_{1/2}^{-1}$ by means of the following equation [60]:

$$K = \left(t_{1/2}^{-1}\right)^n ln2 \approx 0.7\left(t_{1/2}^{-1}\right)^n \qquad \text{Eq. 2-7}$$

where $\tau_{1/2}^{-1}$ is the inverse of the half of the crystallization time, and $\tau_{1/2}$ corresponds to the time needed to achive 50% of the overall crystallization.

Through the Avrami equation, the isothermal crystallization data can be analyzed. There are several different kinds of experimental methods that are commonly used to measure the overall crystallization rate. All of them follow a change in a property that is sensitive to crystallinity, for instance it could be the density of the specific volume. Other frequently used techniques include small-angle x-ray scattering, vibrational spectroscopy, nuclear magnetic resonance, depolarized light microscopy and differential scanning calorimetry (DSC). Each method has a characteristic and different sensitivity to crystallinity. Particuarly, the spherulitic growth rate is measured by either polarized light microscopy or small angle light scattering [63].

Among the aforementioned techniques, DSC is one of most popularly used to follow the crystallization kinetics. That is due to the simplicity by which the data can be fitted to the Avrami Equation [62, 68]. However, two factors are crucial in order to get a good fit: the relative volumetric conversion range chosen and the induction time correction [62, 68].

The Avrami equation can describe overall transformation process until the primary crystallization ends (Vc < 40~ 50%), that is until the impingement of the crystals. Therefore, a reasonable conversion range within the primary crystallization should be chosen to fit the data. From the guidelines of Lorenzo et al. [68], the conversion range between 3 and 20 % is advisable. The initial data points should be neglected due to experimental errors during the first stages of the crystallization process regarding the stabilization of the equipment and the small quantity of heat evolved. And beyond 50 %, the secondary crystallization processes produces non-linear deviations in the Avrami fit due to reorganization process occurring inside the already developed semicrystalline domains [70].

The induction time correction deals with the fact that a certain time may elapse before crystallization starts. In other words, once the isothermal crystallization temperature is reached, there is period of time in which there is not crystallization. This time is called the induction time for the beginning of the crystallization (t_0). In mathematical terms, the Avrami equation is only defined when crystallization starts. Therefore, the experimental induction time must be subtracted from the absolute time. This implies a minor modification into the Avrami classical equation, as follows:

$$1 - V_c(t - t_0) = exp(-k(t - t_0)^n) \qquad \text{Eq. 2-8}$$

And, after applying logarithmic properties to both sides, the following equation is obtained:

$$Log\left[-Ln[1 - V_c(t - t_0)]\right] = Log(k) + nLog(t - t_0) \qquad \text{Eq. 2-9}$$

Now, the Avrami fit can be properly applied to isothermal crystallization data obtained from DSC (or any other technique). First, the relative volumetric fraction (V_c) used in the Avrami equation can be calculated as:

$$V_c = \frac{W_c}{W_c + \frac{\rho_c}{\rho_a}(1 - W_c)} \qquad \text{Eq. 2-10}$$

where W_c is the crystalline mass fraction, and ρ_c and ρ_a are the fully crystalline and fully amorphous polymer densities, respectively. The W_c can be obtained from the integration of the DSC experimental data measured during the isothermal crystallization (as an example see Figure 2.2 for isothermally crystallized PCL at 42 ºC), as follows:

$$W_c = \frac{\Delta H(t)}{\Delta H_{total}} \qquad \text{Eq. 2-11}$$

where $\Delta H(t)$ is the enthalpy variation as function of the time spent at a given crystallization temperature and ΔH_{total} is the maximum enthalpy value reached at the end of the isothermal crystallization process [62] (see Figure 2.2).

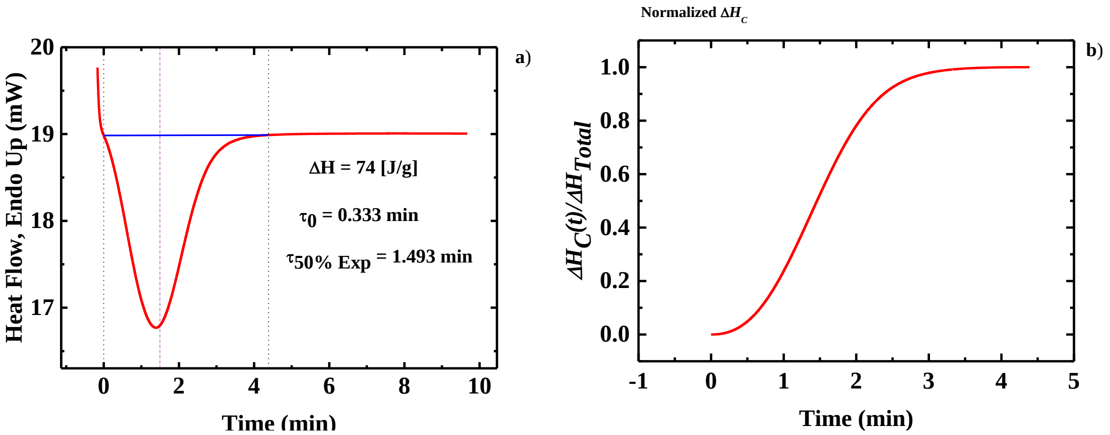

Figure 2.2 a) Isothermal DSC scan of PCL crystallization at 42 ºC. The sample was previously melted at 120 °C for 3 min and then cooled at 60 °C/min to T_c. b) Normalized crystalline mass fraction as a function of time.

Then, the relative volumetric fraction (V_c) as a function of time can be plotted following the Eq. 2-9 to construct the so-called Avrami plot (see Figure 2.3). After applying a linear fit to Eq. 2-9 in the proper range (see red values, between 3 and 20% of conversion in Figure 2.3), the Avrami index n and the overall crystallization rate constant k can be obtained from the slope and the intercept of the fit. A good fit requires R^2 values close to 0.9999.

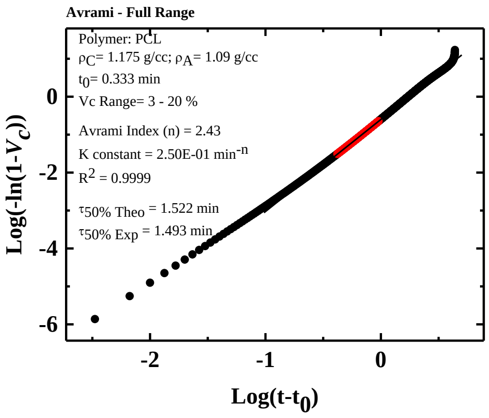

Figure 2.3 Avrami plot of the experimental data (circles) obtained from the isothermal crystallization of PCL at 42 °C. The solid line represents the Avrami fit Eq. 2-9 for a conversion range of 3-20% (red symbols).

With the Avrami parameters (*n* and *k*) estimated, the predicted exotherm of crystallization and the theoretical relative untransformed fraction (i.e. 1-V_c) as a function of time can be constructed and compared to the experimental data. As an example, Figure 2.4 show the superimposition of the theoretical and experimental curves and the excellent quality of the fit for PCL isothermally crystallized at 42 ºC.

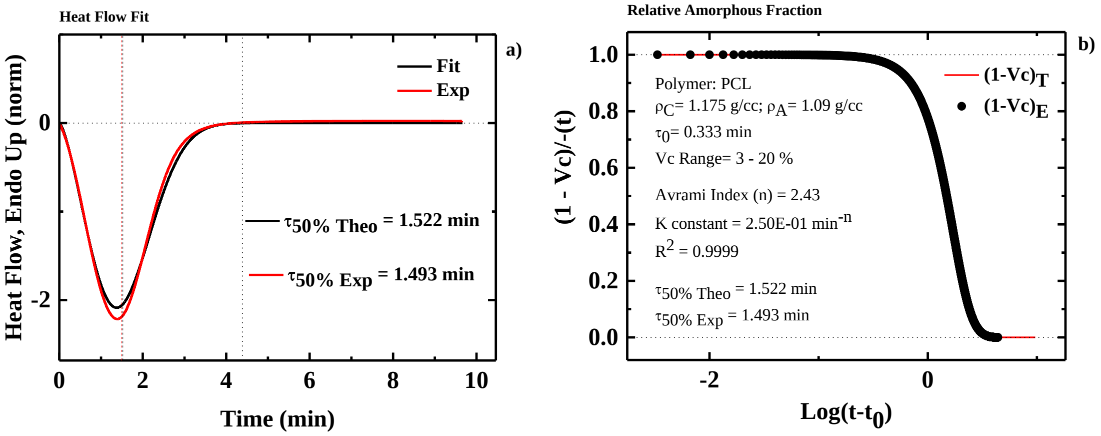

Figure 2.4 a) Isothermal curves of PCL crystallization at 42 ºC. b) Untransformed relative amorphous fraction (1-V_c), as a function of time. Comparison between theoretical Avrami fit and experimental data.

2.1.4 Poly (Lactide), poly (ε-caprolactone) and poly (ethylene oxide)

Among biodegradable and biocompatible polymers, poly (Lactide) (PLA), poly (ε-caprolactone) (PCL) and poly (ethylene oxide) (PEO) are three of the most promising environmentally friendly materials, and the extensive literature published covers a wide scope of aspects, from synthesis and polymerization through physical performance and final applications [71].

Poly (lactide) or Poly(lactic acid)

The increased scientific and industrial interest [71, 72] on PLA relies on its remarkable biodegradability and good processability. It can be processed by extrusion, injection molding, thermoforming, blow moulding, film blowing and melt spinning [73]. PLLA is bioresource and renewable and compared to other bioplastics, it has relatively low price and commercial availability. It is expected that PLLA consumption in 2020 will exceed more than one million tons. Currently, it has been used in many different applications in the agricultural, medical, surgical and pharmaceutical fields as well as in tissue engineering, film packaging, injection moulding products, fabrics, fibers, bottles, cups and disposable and food-contact materials [73]. PLA a linear aliphatic polyester synthesized by ring-opening polymerization of lactide or by polymerization of lactic acid. The lactide monomer is a chiral molecule that exists in two optically active forms; L-lactide and D-lactide [74]. Therefore, the PLA properties are influenced by the stereochemistry. It can be either semicrystalline or amorphous depending on the thermal history and optical purity: the ratio of L to D enantiomer. To be crystalline, the L-lactide content should be higher than 93%; otherwise it is usually amorphous [73]. The crystallization degree of PLA, typically around 37 %, also depends on molecular weight and processing conditions [74].

Semicrystalline PLA is completely biodegradable and compostable under controlled conditions. It undergoes hydrolytic degradation by the random scission of the ester backbone [74]. It has good thermal and barrier properties, high modulus (approximately 4.8 GPa) and good tensile strength [74]. Despite those features, PLA is brittle at room temperature, has a poor elongation at break and it is susceptible of suffering both hydrolysis and pyrolysis at high processing temperatures. For that reason, commercial PLA is typically stabilized against thermal degradation. It has also high rigidity, low impact resistance material with a difficult control of its crystallinity and hydrolysis rate. To overcome these drawbacks different approaches that include copolymerization and blending with other biodegradable polymers, plasticizers and fillers have been used [73].

Mechanical performance, degradation behavior, barrier and optical properties of PLLA are strictly related with the polymer crystallinity. Therefore, it is relevant the understanding of its crystallization behavior [75]. PLA displays different crystalline structures depending on the crystallization conditions. The α-form is the most common crystal type for PLA. Although, a less dense packing α'-form have been detected. The other structures include β and γ-form crystals. The superstructural morphology of PLLA typically consists on non-banded spherulites. Although, others morphologies such as banded spherulites and axialites can be obtained by changing the thermal story, the crystallization conditions (supercooling) or the molecular weight. The glass transition temperature of PLLA is close to 60 ºC and melting temperatures up to 175 ºC have been reported [74]. The melting transition temperature of PLLA depends on the molecular weight as well as the optical purity. At lower molecular weight and increased D-lactide content, the melting temperature decreased. In addition, both cold crystallization and glass transition are also affected by the content of D- enantiomer [75].

In general, the overall crystallization kinetics of PLLA is slow. The crystallization kinetics of PLA is strongly dependent on the optical purity. The degree of crystallinity, nucleation rate, and spherulite growth rate reduce substantially as the optical purity decreases [76]. PLA has the highest rate of crystallization (expressed as the inverse of half-crystallization time), between 100° and 130°C but it displays a discontinuity at around 118 ºC. Also, the crystallization rate decreases as the molecular weight increased. To overcome the retarded crystallization, the addition of nucleating agents and small amounts of stereocomplex crystals has been effective. Commonly, it is reported that PLA crystallization takes place from an instantaneous nucleation into a spherulitic 3D dimension. However, Avrami exponent values ranging from 2 to 3.5 has been reported after fitting the isothermal crystallization data to the Avrami equation [75]. The size of the spherulites changes dramatically whether it is isothermally crystallized from the melt or from a quenched glassy state [76].

Poly(ε-caprolactone)

PCL is one of the earliest biopolymers as it was synthesized by Carothers group in 1930 [77]. It is a hydrophobic, biodegradable and biocompatible polyester that can be synthesized by ring-opening polymerization of ε-caprolactone monomer via anionic, cationic or co-ordination catalysts [78]. The repetitive molecular unit of PCL consists of five nonpolar methylene groups and a single relatively polar ester group [79].

PCL has good solubility in a wide range of organic solvents, high crystallinity (up to 70 % depending on the molecular weight) [80], low melting point, tailored degradation kinetics and mechanical properties, easy processability, and good blend-compatibility. As semicrystalline polymer, PCL exhibits a glass transition around – 60 ºC and a melting temperature ranging between 59 and 64 ºC [74, 78, 80]. Because of this, PCL can be easily processed at relatively low temperatures into wide range of forms such as nanospheres, nanofibers and foams [78]. Due to its very low glass transition temperature, PCL is a very flexible and elastic polymer, with high elongation at break (> 700 %) but low tensile strength (around 23 MPa) [74].

Extensive research has been focused towards the biodegradation features [81] and potential biomedical applications of PCL. In that field, PCL has a proven use on controlled drug-delivery, medical devices (sutures, wound dressing, fixation devices) and tissue enginnering (scaffolds fabrication for bone, cardiovascular, tendon, blood vessel, skin, nerve and cartilage engineering) [78].

PCL can undergo hydrolysis through the labile aliphatic ester bond. Despite that, the hydrolytic degradation rate is slower than that of other biopolymers such as PLA and polyglycolide (PGA). Up to 3 or 4 years for PCL while only few weeks or months for PLA and PGA. For that reason, it has been copolymerized with monomers of highly degradable polylactide and polyglycolide [74, 78, 80]. Functionalization reactions have also been conducted on PCL to increase cell adhesion and improve hydrophylicity and biocompatibility. Blends of PCL with other polymers have been made to improve stress crack resistance, mechanical performance and dyeability and adhesion. Compatibility in PCL polymer blends will depend on composition. PCL biodegradation proceeds under outdoor conditions by living organisms but at a lesser extent inside body environment (*in vivo*) [78].

Early studies on the crystallization behavior of PCL have been followed by dilatometry and optical microscopy [82]. The crystalline growth of PCL was spherulitic and the crystallization exhibited a time dependence nucleation [82]. Clear Maltese cross has been observed for PCL at low supercooling. But as the crystallization temperature decreases, spherulites with banding have been observed for low molecular weight PCL.

The crystallization behavior of PCL also depends on the molecular weight and the structural topology of chains. For instance, Perez et al. demonstrated that linear PCL nucleates and grows slower than analogous linear ones. Besides, as the molecular weight increases, the overall crystallization kinetics reached a maximum. Applying the Avrami fitting to the crystallization kinetics data predicted a 3D dimensional growth with instantaneous nucleation, since the Avrami index of PCLs were around 3.

Poly (ethylene oxide)

Poly(ethylene oxide) (or Poly (ethylene glycol)) market has exhibited a steadily increment during last 5 years. The forecast is that global consumption of PEO will reach 500 KTons by 2020 in the medical, personal care and industrial fields[83]. It is a water-soluble, thermoplastic polymer synthesized by the heterogeneous polymerization of ethylene oxide [84]. PEO with controlled chain length and narrow dispersity is synthesized by living anionic ring-opening polymerization [85, 86]. The repetitive unit is composed of two methylene units and an ether group. It can be obtained in wide range of molecular weight, from very low values to 7×10^{6} g mol^{-1}. PEO has outstanding physical and chemical properties. It is an inert highly crystalline polymer with density values between 1.15 and 1.26 g cm^3. The glass transition temperatures reported are between -80 and -20 ºC, depending on molecular weight. The melting temperatures are around 60 ºC. It has a balanced mechanical performance, with high elongation at break and tensile resistance. For instance, PEO films had ~ 550 % of elongation, 16 MPa of tensile strength and 80 kN/m of impact resistance. PEO has very good solubility in water and common organic solvents at room temperature [85], particularly chlorinated hydrocarbons. However, it also soluble in aromatic hydrocarbons at high temperatures [84]. Due to its advantageous properties, there is high interest in PEO functionalization, blends with other biopolymers and random and block copolymerization [85].

Because of its melting temperature and viscosity, PEO is easily processed as any other thermoplastic by the conventional industrial techniques, such as extrusion, injection molding, blown-films extrusion, among others. As a water soluble and low toxicity polymer, most of the main applications of PEO are related to the personal care, pharmaceutical and biomedical industries. It has been extensively used in denture adhesives, ophthalmic solutions, wound dressings and drugs release systems. It also has a potential use in other products such as flocculants, binders, adhesives and batteries [84].

The PEO grows in a spherulitic structure. The crystallization behavior of PEO has been studied in the light of the crystallization theories. The spherulitic growth rate followed by PLOM was analyzed using the Lauritzen-Hoffman-Miller (LHM) kinetic theory [87]. Wu et al. [87] estimated an end surface free energy of 40 ergs cm^2 for crystallization in regime II for a PEO with a viscosity-average molecular weight of $1.44x10^5$. Although regime transitions have been reported for PEO crystallized in a similar T_c range, the authors did not find such behavior.

2.1.5 Crystallization and morphology of double crystalline AB and ABA diblock and triblock copolymers of poly(ethylene oxide) and poly(ε-caprolactone) (PEO-*b*-PCL)

The morphology, crystal structure and crystallization behavior of AB and ABA block copolymers composed of PEO and PCL have been extensively studied, and several reports and reviews have been published on this matter [1, 21, 88, 89]. Briefly, the PEO-*b*-PCL diblock copolymers exhibit complete melt miscibility [21, 24, 27, 88] and both blocks can crystallize sequentially or coincidentally upon cooling from the melt, since their crystallization temperatures are very similar. Due to this fact, the crystallization order depends on block composition, block molecular weight and molecular architecture. For instance, if the PCL content is higher than the PEO content, the PCL block tends to crystallize first (consequently melting last) and then the PEO block, and viceversa [19, 88]. It has been reported that both blocks can crystallize in a wide composition range [24, 53, 88, 90]. However, if the length of one of the blocks is too short, it may not crystallize, since the crystallization event becomes more difficult. An alternating crystalline lamellar structure of both components is the typical morphology of these copolymers after crystallization.

In general, a reduction in the crystallization and melting temperature of each block as compared to the corresponding homopolymers has been observed, and it is related to the melt miscibility of the PEO and PCL blocks. The reduction in the crystallization temperature become more significant as the content of the block under consideration is reduced [19, 24, 53, 91-93]. Such behavior can be related to a confined crystallization phenomenon induced by the block that crystallizes first over the second block. As a result, a fractionated crystallization behavior could be observed for the confined block [24]. Since these block copolymers are melt miscible, the block that crystallize first fixes the superstructural morphology of the copolymer, inside which the other block will have to crystallize. Therefore, the lower temperature block may be confined by the previously formed lamellar crystals of the block that crystallizes first.

It is interesting to note that the depression in the crystallization temperature of the PCL block is generally more important than in the PEO block, when their content in the block copolymer is reduced [1, 88]. It seems that the PEO block has a larger negative effect on the PCL crystallization. Regarding the melting temperature of each block in the copolymer, their reduction is normally linked with a diluent effect caused by the miscibility of the components, and to the fractioned crystallization. However, some publications report an increase in the melting temperature of the PCL block, even higher than that of the corresponding PCL homopolymer. This fact has been attributed to reorganization phenomena during heating [1, 94, 95].

The crystallization kinetics of these systems has also been studied. Bogdanov et al.[26] reported the isothermal crystallization of a PEO-*b*-PCL block copolymer with 20 % of PEO, in which the PCL block crystallizes at higher temperatures than the PEO block. The PCL block exhibited a crystallization rate and Avrami index values similar to the analogous PCL homopolymer. However, the Avrami index of the PEO block was close to 2. The authors explained this low Avrami index as a two-dimensional lamellar growth of the PEO block over the faces of the previously formed PCL crystals.

More recently, Xue et al.[14] followed the isothermal crystallization of several PEO-*b*-PCL diblock copolymers in which the molecular weight of the PCL block was fixed at 5000 g.mol^{-1} while the length of the PCL block was varied as 3000, 10000, 15000 and 20000 g.mol^{-1}. A one-step crystallization protocol was adopted and the isothermal crystallization was followed by SAXS/WAXS measurements. As it was aforementioned, the block with higher molecular weight crystallized first, and then crystallization of the shorter block started. A lamellar morphology was also confirmed by AFM observations.

AB and ABA block copolymers composed of PEO and PCL crystallize in a spherulitic-type superstructure, regardless of the block composition [19, 21, 22, 88, 96-99]. Inside the spherulites, no evidences of mixed or eutectic crystals have been detected by WAXS, and each block crystallizes inside their own crystalline unit cell. Since these copolymers crystallize from a homogeneous melt, the block that crystallizes first templates the microscale morphology. PLOM characterization revealed that the birefringence patterns of the spherulites change with block composition [21, 22, 88, 96, 97]. In general, as the PEO content is low (18 %) [97] a continuous banding extinction pattern is commonly observed. As the PEO content increases to an intermediate composition (34 – 40, 50 %), double concentric spherulites have been observed [21, 88, 96, 97], in which, the central spherulite may or may not had a banding extinction pattern, and the outer one had a Maltese cross extinction pattern. When the PEO is the major component (66 %), the spherulites exhibited Maltese cross pattern exclusively [97]. After detailed analysis by DSC, WAXS, SAXS, FTIR and PLOM, He et al.[21] proposed that the double concentric morphology observed at intermediate compositions is a result of the growth rate difference between the blocks. However, some authors did not find this unique morphology at intermediate compositions, and regular single spherulites were reported [98].

The recent literature on these block copolymers deals with the crystal morphology obtained from solution crystallization. Van Horn et al.[17] evaluated the structure of double crystalline PEO-*b*-PCL diblock copolymers crystallized from solution employing bright field TEM and electron diffraction experiments (see Figure 2.5). By changing the solvents conditions, it was possible to induce the crystallization of each block. Single crystals of two diblock copolymers of different PCL content were crystallized from *n*-hexanol and amyl acetate. Employing this methodology, only one of the blocks, the one with the highest molecular weight could crystallize, while the other block remained amorphous, tethered to the fold surface of the single crystal. The crystallization of both blocks was achieved by inducing crystal growth through homopolymer crystal seeds. For instance, some homo-PEO crystal seeds were added to a solution of the block copolymer with highest PCL content. The technique was successful to induce the crystallization of the PEO block despite its lower content in the copolymer. A layer structure, with a single PEO crystal in the middle and small crystallites of PCL tethered to the fold surface of the PEO block was obtained (see Figure 2.5). Yu et al.[100] also successfully obtained single crystals of linear diblock and triblock and star-shaped block copolymers of PEG and PCL grown from dilute solutions in n-hexanol. Electron diffraction patterns of the lamellar crystals exhibited the (120) diffracting planes of the monoclinic crystals of PEG, and the (110) and (200) diffracting planes of the PCL orthorhombic crystals. [100].

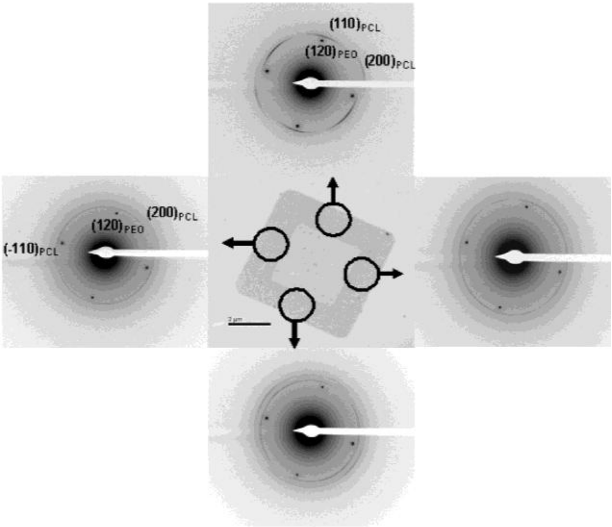

Figure 2.5. TEM bright field image of the homo-PEO single crystal (center) seeded crystallization of EOCL-11 (outer layer) (middle). The darker section indicates the thicker, diblock component. ED patterns of theEOCL-11 crystal for each sector are placed around the central bright field image. Reprinted with permission from Van Horn et al.[17]. © 2010 American Chemical Society.

A recent publication from Li et al.[13] explored the ring-banded morphology in thin films obtained from solution. Maltese cross and three kinds of ring-banded spherulites could be produced in the same copolymer: non- and half- birefringent concentric ringed spherulites and classical extinction banded spherulites, by changing the solution concentration and the evaporation rate (see Figure 2.6). Concentric ring patterns are attributed to a rhythmic variation of the radial lamellar packing along the spherulite radius, while extinction banding patterns are a result of twisted orientation of the lamellae along the radial growth direction. The PCL block fixes the morphology in these block copolymers. However, under specific crystallization conditions (low humidity and slower crystallization rate) dendritic PEO crystals could be formed, besides the PCL concentric ring spherulites (see Figure 2.7). Under these conditions the PEO segment can dominate the crystallization event.

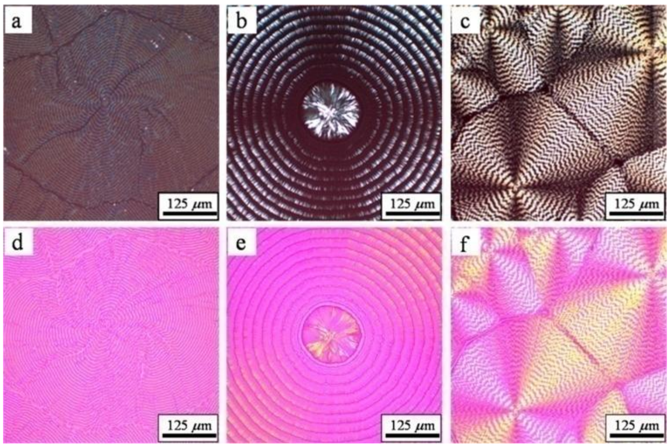

Figure 2.6. POM (a–c) photographs revealing the optical properties of three P(CL$_{24.5K}$EO$_{5.0K}$) ring-banded spherulites formed in solution-cast films at varied drying conditions. (d–f) The corresponding images after adding a λ compensator. The former two concentric ringed spherulites were developed under the same R_e of 1.50 × 10–4 mL h^{-1} at 20 °C but from (a) 5 and (b) 10 mg mL^{-1} solutions, respectively, while the third extinction banded spherulites were emerged upon a rapider R_e of 4.68 × 10–3 mL h^{-1} from 10 mg mL^{-1} solution at 0 °C. Reprinted with permission from Li et al.[13] © 2014 American Chemical Society.

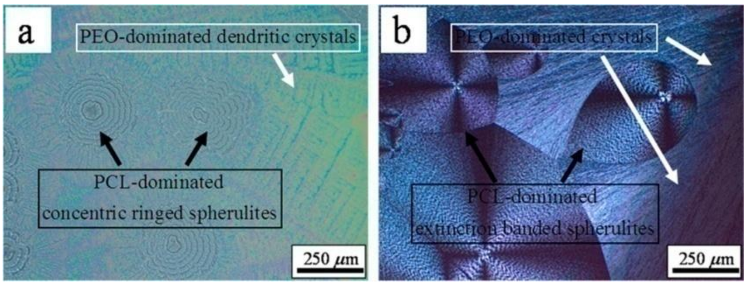

Figure 2.7. OM (a) and POM (b) pictures of P(CL$_{24.5K}$EO$_{5.0K}$) crystals formed by drying a solution-cast film at a low humidity (ca. 15%). The drying environments for (a) and (b) are the same as that of Figures 12b and 12c, respectively. Reprinted with permission from Li et al.[13] © 2014 American Chemical Society.

2.1.6 Crystallization and morphology of double crystalline AB and ABA diblock and triblock copolymers of poly(ethylene oxide) and poly(L-lactide) (PEO-*b*-PLLA)

PEO-*b*-PLLA diblock copolymers crystallize upon cooling from the melt, although, the crystallization ability will depend on block composition and conditions. The PLLA and PEO blocks can crystallize sequentially and independently; each block with its own crystal structure. These diblock copolymers do not exhibit mixed or eutectic crystals containing both PEO and PLLA chains. The crystalline unit cell of PEO is monoclinic while that of PLLA is orthorhombic [33].

The crystallization of PEO-*b*-PLLA diblock copolymers has been a field extensively studied in the past, and several publications and reviews have been published [1, 33-35, 37, 38, 41, 85]. Since PLLA crystallizes at higher temperatures than PEO coming from the melt, the crystallization of the PEO block is influenced by the crystallization conditions of the PLLA block. In this sense, the influence of PLLA crystallization under isothermal or non-isothermal conditions are the two main approaches reported in the literature. In the past, a diluent effect caused by the miscible and molten PEO chains connected to PLLA block has been reported during PLLA isothermal crystallization. In addition, a higher degree of supercooling is observed when the PLLA molecular weight decreases. As a result, PLLA nucleation density and crystallizability also decrease. However, as the crystallization temperature is reduced, molten PEO chains improve the crystallizability of the PLLA block, particularly, when the molecular weight of the block decreases [38, 40]. On the contrary, other authors have reported a retarded PLLA crystallization due to the bonded PEO molten chains [1, 43]. Regarding the PEO block, the previously formed PLLA crystals confine the crystallization of the PEO block. However, if the PLLA block length is reduced, the PEO crystallization rate increases, since PLLA crystals provide nucleating sizes for PEO crystallization [38].

More recently, Xue et al. [33] have followed the isothermal crystallization of each block in a symmetric PEO-*b*-PLLA diblock copolymer through simultaneous SAXS/WAXS measurements. In general, the scattering intensity obtained from SAXS increases with crystallization time during the crystallization of the PLLA block at 100 ºC. In addition, the authors reported that the long period value *L* increased slightly.

After PLLA complete crystallization, the sample was quenched until 40 ºC to crystallize the PEO block, and an important reduction of the *L* value and intensity were observed. The crystallization of the PEO block takes place in the rigid environment of PLLA (with both crystalline and glassy regions at the crystallization temperatures of PEO). Therefore, the diblock copolymer forms a lamellar phase, with alternating layers of the constituent blocks during crystallization. Although, the melt miscibility of these block copolymers has been demonstrated in the past [39, 41, 54, 101-103], Xue et al. [33] claimed that it is not possible to detect whether the melt structure was ordered or not just before the block crystallized since the electron density of amorphous and crystalline phase of PEO and PLLA are very similar.

Zhou et al.[31] and Yang et al.[32] evaluated the effect of the crystallization conditions of the PLLA block on the microphase separation and crystallization behavior of poly(ethylene glycol)-*b*-poly(L-lactide) (PEG-*b*-PLLA) diblock copolymers. With that purpose, both authors also followed a two step-crystallization methodology in which the PLLA block was first fully crystallized, and then, the PEG block was sequentially crystallized in a second step. Whereas, Zhou et al. [31] studied the non-isothermal crystallization behavior of both blocks by changing the cooling rate in the first step (during PLLA crystallization), Yang et al.[32] reported the effect of the crystallization temperature of the PLLA block during its isothermal crystallization. Both authors agreed on the microphase separation induced by the initial crystallization of the PLLA block, and on the confined character of the subsequent crystallization of the PEG block. Since these block copolymers are melt miscible, the microphase separation occurs as the PLLA crystallization takes place.

Some peculiarities could be distinguished as a result of the crystallization conditions imposed. First of all, when the PLLA block was crystallized from the melt at different cooling rates, the PLLA T_c and ΔH (or crystallinity) increased as the cooling rate decreased, as it was expected. A lower cooling rate would provide enough time for the formation of PLLA nuclei and crystallites. But beside this obvious observation, the cooling rate at which the PLLA block was crystallized had a significant influence on the following crystallization of the PEG block. As the cooling rate decreased, the PEG T_c shifted to higher values and two exothermal peaks appeared. That observation indicated a PEG fractioned crystallization behavior that could be a result of different PEG microdomains induced by the microphase separation.

The microphase separation and lamellar structure of these PEG-*b*-PLLA diblock copolymers were not only affected by the cooling rate employed during the first step of the crystallization process. Yang et al.[32] evaluated the influence of the crystallization temperature employed during the isothermal crystallization of the PLLA block. SAXS experiments indicated that the long period values of PLLA lamellar structure increases as the PLLA crystallization temperature increased (see Figure 2.8b). At these temperatures, in which the PEG remains molten, two SAXS peaks were detected. The distinctive first one corresponded to the lamellar structure of PLLA, and the second indicated a microphase separated structure induced by PLLA crystallization. As the PLLA block crystallizes, the amorphous PEG block was rejected from the PLLA crystal front, resulting in an increment in the size of PEG domains. These PEG domains, trapped within the PLLA crystals could contribute to the second SAXS peak. As the PLLA crystallization takes place, two mechanisms might be responsible for the increment of the long period values: a stretching of the PLLA amorphous phase by the PLLA crystals and the increase in volume of the amorphous PEG phase as a result of the segregation induced by PLLA crystallization [104].

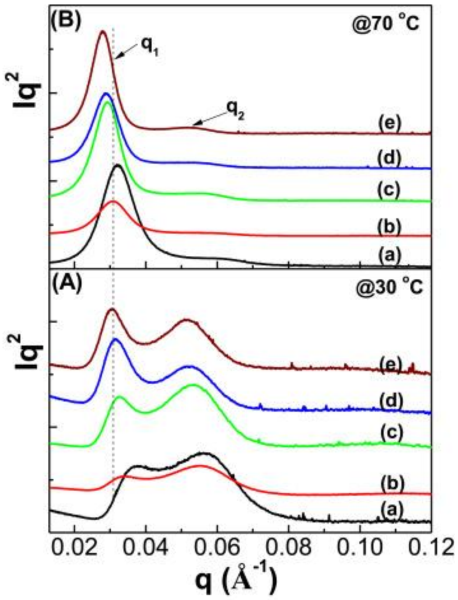

Figure 2.8. Lorentz-corrected 1D SAXS profiles of crystallized PLLA-*b*-PEG copolymer samples with different thermal histories obtained at (A) 30 and (B) 70 °C. PLLA-*b*-PEG copolymers crystallized at different $T_{c,PLLA}$ and the same PEG block crystallization temperature at 30 °C: (a) $T_{c,PLLA}$ = 70 °C, (b) $T_{c,PLLA}$ = 80 °C, (c) $T_{c,PLLA}$ =

90 °C, (d) $T_{c,PLLA}$ = 100 °C, (e) $T_{c,PLLA}$ = 110 °C. Reprinted with permission from Yang et al.[32] © 2015 Elsevier Ltd.

After the crystallization of the PLLA block, the PEG block was crystallized also under isothermal conditions. After PEG crystallization, the relative intensity of the SAXS peaks changed significantly, the second peak became more intense than the first one, and the scattering vector q associated to the first peak changed to higher values (see Figure 2.8a). These results indicated that a lamellar structure belonging to the PEG block was formed inside the interlamellar regions of the PLLA superstructure [32, 104]. WAXS experiments demonstrated that the diffraction peaks of PLLA crystalline structure shifted and the most stable α-form of PLLA was favored after PEG crystallization [104]. Besides SAXS experiments, the transformation of PLLA crystals from α'-form to the more stable α-form after PEG crystallization was also confirmed following the characteristic signals of these crystalline structures by FTIR. A hypothesis to explain this behavior is a possible stretching of the PLLA crystals during the PEG crystallization. However the mechanisms behind the crystalline transformation of PLLA are still not clear [104].

Finally, as it is expected, higher PLLA crystallization temperatures caused an increment in the thickness of PLLA crystalline layer (see Figure 2.9). But also in the domain size of the PEG block. The authors claimed that at higher temperatures the PEG chains were more stretched since they were tethered to the PLLA lamellae, and therefore the PEG domains became bigger. They also claimed that this stretching facilitated the nucleation and growth of the PEG block, which resulted in an increase in the PEG crystallization rate [32]. Summarizing the observations of these authors [31, 32], higher PLLA crystallization temperatures and lower cooling rates for PLLA crystallization promoted bigger PEG microdomains, and in the end, enhanced the crystallization of the PEG block.

Recently, Arnal et al.[30] evaluated the influence of block composition in the crystallization behavior of PEO-*b*-PLLA block copolymers, and self-nucleation experiments were also reported. At higher PLLA content (≥ 80 %), the PEO block exhibited fractionated crystallization in view of the confinement imposed by previously formed PLLA crystals (see Figure 2.10). Fractionated crystallization has been observed in block copolymers with two crystallizable blocks [24, 105-107]. PEO domains without high temperature active heterogeneities are isolated. Therefore, the PEO crystallization takes place at higher supercoolings. If the PLLA content was between 50 and 71 %, the previously formed PLLA crystals had a nucleating effect over the PEO crystallization. On the other hand, the PEO block enhanced the crystallization of the PLLA since the PLLA crystallization temperature increased in a block copolymer with 33 % of PEO. During PLLA crystallization, the PEO block is molten. Thus, the PEO amorphous phase induced a plasticizing action, but also had a nucleating effect over the PLLA crystallization. The enhanced nucleation is result of the donation of heterogeneities coming from the molten PEO phase. The self-nucleation experiments allowed determining a nucleation efficiency of the PEO phase of 33 % [30].

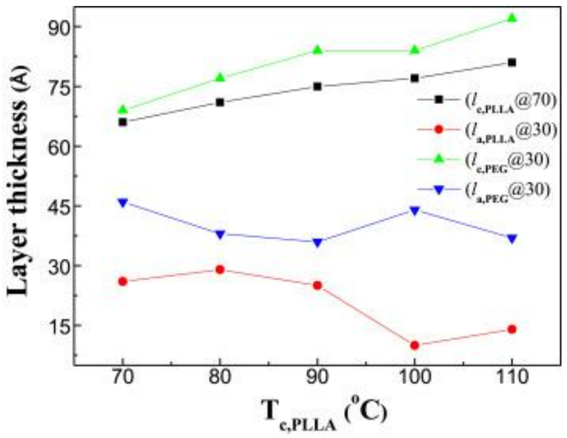

Figure 2.9. $T_{c,PLLA}$ dependent crystalline and amorphous thicknesses of PLLA and PEG blocks in PLLA-*b*-PEG copolymer samples. Reprinted with permission from Yang et al.[32] © 2015 Elsevier Ltd.

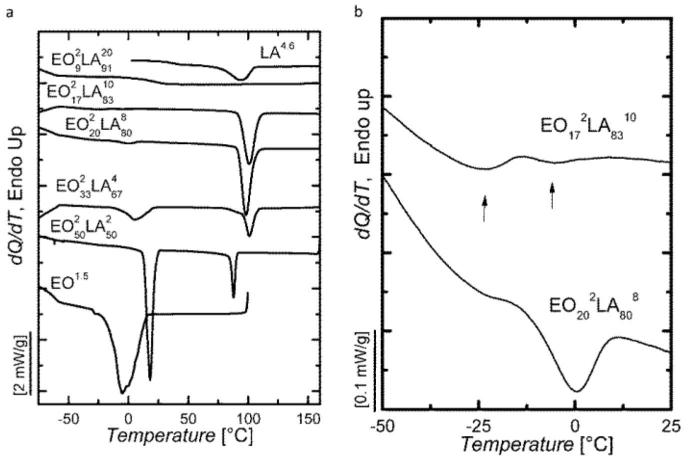

Figure 2.10. (a) DSC cooling scans at 10 °C min^{-1} for homopolymers and block copolymers EO$_x^y$LA$_x^y$ after melting for 3 min at 170 °C. (b) Fractionated crystallization

in DSC cooling scans at 10 °C min^{-1} for block copolymers $EO_{20}{}^{2}LA_{80}{}^{8}$ and $EO_{17}{}^{2}LA_{83}{}^{10}$ after melting for 3 min at 170 °C. Reprinted with permission from Arnal et al.[30]. © 2016 The Royal Society of Chemistry.

The bulk micro-scale morphology is strongly dependent on block composition, as well as, crystallization temperature. Since these block copolymers exhibit melt miscibility [39, 41, 54, 101-103], the superstructural morphology is fixed by the initial crystallization of the PLLA block. Several types of superstructures, such as axialites, dendrites [104] and spherulites have been observed through PLOM and AFM.

Due to their melt miscibility, after the complete crystallization of the PLLA block, the subsequent crystallization of the PEO block do not alter the previous morphology formed by the PLLA crystals. What is observed is a significant change in the birefringence. The superstructures become lighter and brighter after the PEO crystallization. If the sample is remelted to a temperature above the PEO melting temperature but below the PLLA melting, the highly birefringent regions disappear and the morphology remains unchanged on the micrometer scale. This reversibility confirms that the birefringence change account only for the PEO crystallization [104]. This behavior has also been observed in PCL-*b*-PLLA diblock copolymers [4]. Since these copolymers are melt miscible and the PEO chains are chemically anchored to the PLLA block, the PEO phase is unlikely segregated far from the PLLA lamellae. Therefore, the subsequent crystallization of the PEO domains takes place inside the PLLA superstructure. Yang et al. proposed the following sketch to illustrate the possible crystalline domains [104].

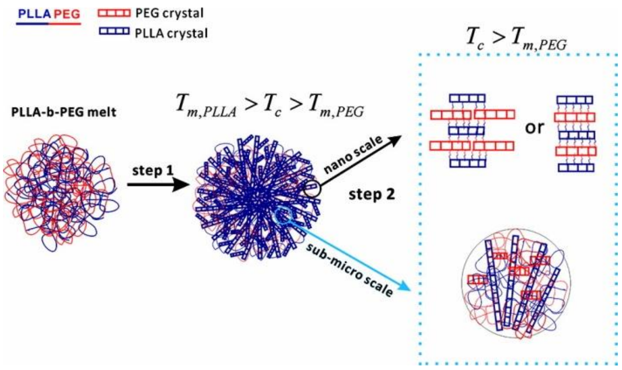

Figure 2.11. Schematic illustration model for mechanism of multilength scales confined crystallization of PEG block in the PLLA-*b*-PEG copolymer. Reprinted with permission from Yang et al. [104]. © 2012 American Chemical Society.

Through AFM, the morphology at the nanoscale can be observed, including lamellar thickness and growth mode of the crystals. However, it should be noticed that the growth mode is also influenced by the sample preparation. In symmetric PEG-PLLA block copolymers reported by Yang et al.[104], the authors indicated that the PLLA crystals grew edge on while those of PEO flat on.

The morphology in thin films is different from that observed in bulk materials, and it also depends on block composition. Arnal et al.[30] studied the morphology of ultrathin films of PLLA-*b*-PEO diblock copolymers, prepared by spin coating, employing AFM and TEM (see Figure 2.12).

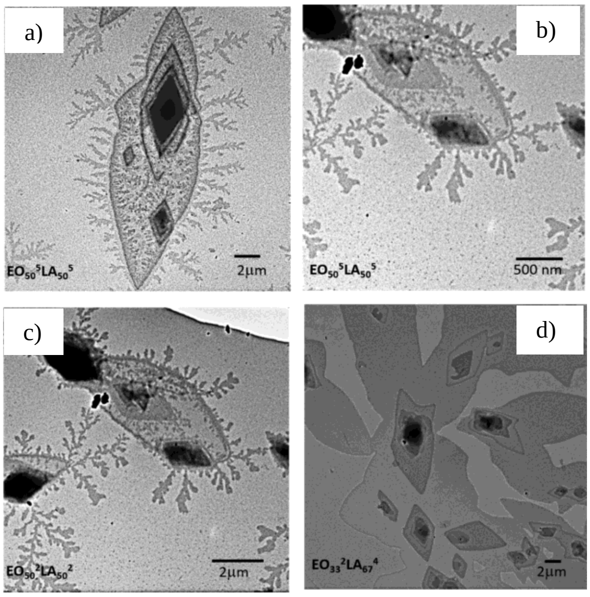

Figure 2.12. TEM observations of single crystals and dendritic crystals for PEO-*b*-PLLA block copolymers, that are far from the 120° value expected for lozenge PLLA type crystals with {110} growing faces. Smaller lozenge shaped crystals, found on top of the lenticular crystals, are constructed by screw dislocations and exhibit 129° angles, a value closer to the 120° reported for PLLA single crystals. The edges of the single crystals tend to be smooth and no striations were observed on their surface. a) $EO_{50}^{5}LA_{50}^{5}$, b) $EO_{50}^{5}LA_{50}^{5}$, c) $EO_{50}^{2}LA_{50}^{2}$, and d) $EO_{33}^{2}LA_{67}^{4}$. The magnification is different from one image to the other and is indicated by a scale bar. Reprinted with permission from Arnal et al.[30]. © 2016 The Royal Society of Chemistry.

After isothermal crystallization from the melt at 100 ºC, PLLA exhibits lozenge shaped single crystals. However, the crystals are better defined when the PEO content is between 29 and 50 %. If the PEO content is reduced below 20 %, distorted PLLA single crystals were observed. A high volume of molten PEO acts as a diluent during the PLLA crystallization. Therefore, the PEO phase can tailor the morphology of the PLLA block. After the subsequent isothermal crystallization of the PEO block at 30 ºC, the morphology observed will also depend on block composition. The block copolymer with 50 % of PEO exhibited a central structure of lozenge shaped PLLA crystals with PEO dendritic crystals that grew on the folding surface and edges of the PLLA single crystals. If the PEO content was reduced to 33 %, no sign of PEO dendritic structures were observed, although an electron diffraction pattern proved the presence of the PEO monoclinic crystals (see Figure 2.12) [30].

2.1.7 Crystallization and morphology of double crystalline AB and ABA diblock and triblock copolymers of poly(ε-caprolactone) and poly(lactide)s (PCL-*b*-PLA)

Extensive literature reports melt miscibility for PCL-*b*-PLA diblock copolymers. In most cases, no evidence of phase separation has been detected by SAXS at temperatures above the melting temperature [1, 5, 6, 8, 46, 50, 51, 101, 108]. Upon cooling from the melt, the PCL-*b*-PLLA block copolymers crystallize forming a lamellar structure and the PLLA block templates the morphology for the subsequent crystallization of the other block. However, in some specific compositions with an increased PLLA content above 44 %, the block copolymers may crystallize from a lamellar microphase separated melt [6]. Similar results have been obtained for other authors [1, 47, 108].

The ability of PCL-*b*-PLLA block copolymers to crystallize was evaluated by Peponi et al.[46] in several block copolymers with different molecular weight and block length of each block. The PLLA block could crystallize provided a minimum molecular weight of 964 g/mol. As the molecular weight of the PLLA block increases above that value, the PLLA crystallinity increased regardless of the block composition, as well as the melting temperature. The former PLLA crystallization greatly hindered the crystallization of the PCL block. As a result, this block required a minimum molecular weight of 2000 g/mol in order to crystallize [46]. Moreover, PLLA cold crystallization process has been reported in several PCL-*b*-PLLA block copolymers [4].

The isothermal crystallization behavior of PCL-*b*-PLLA block copolymers has been extensively studied and reviewed by several authors in the last decades [6, 8, 46, 47, 49-51, 109]. Müller et al.[4-6, 8, 48] have reported the morphology and crystallization kinetics of a wide series of PCL-*b*-PLLA block copolymers as a function of block composition. Since these block copolymers are melt miscible or partially miscible, the PCL has a diluent effect (similar to PEO) in the PLLA phase that leads to a reduction in the PLLA crystallization and melting temperatures, as the PCL content in the diblock copolymer increases.

The isothermal crystallization experiments carried out in two sequential steps by Müller et al. demonstrated that the PLLA block crystallization rate decreased in comparison to the PLLA homopolymer. However, the variation with block composition was only significant for PLLA contents lower than 10 % (see Figure 2.13). On the contrary, the crystallization rate of the PCL block was highly depressed and the supercooling greatly enlarged as the PLLA content increased (see Figure 2.14). In addition, PCL fractioned crystallization occurred when the PCL content was lower than 40 % and the Avrami analysis (*n* ~1) confirmed a homogeneous nucleation process for this block. Since the PCL block had to crystallize inside the interlamellar regions of the previously formed PLLA crystals, the PCL crystallization was confined by the topological restrictions imposed by the covalently linked PLLA block. Additional self-nucleation experiments demonstrated that PLLA crystals had a nucleation effect on PCL crystallization, although that effect did not enhance its crystallization kinetics. Moreover, in block copolymers with less than 7 % of PCL, this block was not able to crystallize [4].

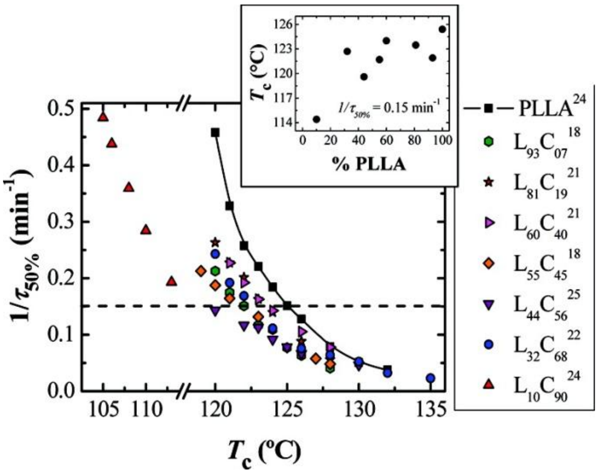

Figure 2.13. Inverse of half crystallization times (1/τ50%) for the PLLA block within the block copolymers. Insert: Isothermal crystallization temperature (Tc) needed to

obtain a value of 1/τ50% = 0.15 min−1 (dashed line in the main figure) versus PLLA content. Reprinted with permission from Castillo et al. [4]. © 2010 American Chemical Society.

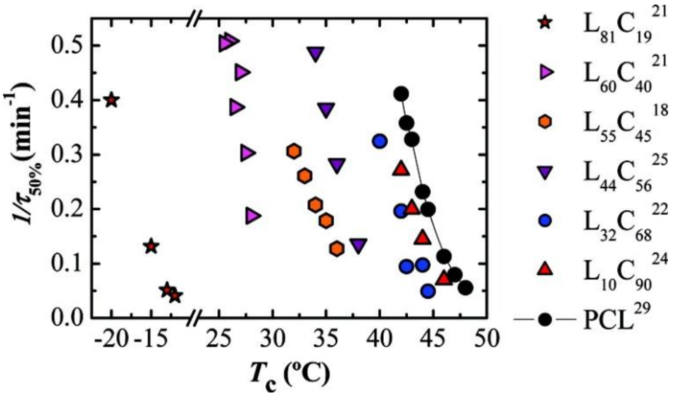

Figure 2.14. Inverse of half crystallization times ($1/\tau_{50\%}$) for the PCL block within the block copolymers. Reprinted with permission from Castillo et al. [4]. © 2010 American Chemical Society.

Regarding the microscale morphology, the superstructures formed upon cooling from the melt have been observed by PLOM [5, 6, 8]. Due to the fact that these copolymers crystallize from a homogeneous melt, the microphase separation is driven by the PLLA crystallization, which is the block that crystallizes at higher temperatures. Therefore, the PLLA block templates the morphology of the block copolymer. Castillo et al. reported the morphology as a function of block composition [4] (see Figure 2.15). At higher PLLA contents, well-defined negative PLLA spherulites with no banding were developed. However, the Maltese cross extinction pattern became diffuse as the PLLA content decreased. When the PLLA content was very low (only 10 %), the superstructure changed from spherulites to axialities. Similar to PEO-*b*-PLLA block copolymers, the subsequent crystallization of the PCL block did not macroscopically change the previously formed superstructure of PLLA, and only a change in the magnitude of the birefringence account for PCL crystallization. Even the axialitic superstructure observed at very low PLLA content (10 %) remained unchanged. This fact indicates that the PLLA block always templates the morphology in these diblock copolymers.

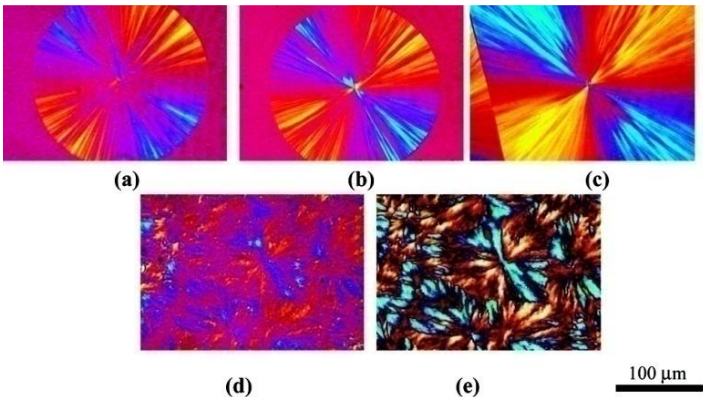

Figure 2.15. Polarized light optical micrographs during isothermal crystallization: (a) PLLA^{24} after 8 min at 140 °C. (b) $L_{81}C_{19}^{21}$, after 10 min at 140 °C. (c) $L_{60}C_{40}^{21}$, after 30 min at 140 °C. (d) $L_{10}C_{90}^{24}$ after 10 min at 100 °C. (e) $L_{10}C_{90}^{24}$ after 3 min at 30 °C. Reprinted with permission from Castillo et al. [4]. © 2010 American Chemical Society.

The morphology of single crystals grown from solution also depends on block composition and crystallization temperature. Casas et al.[48] reported that PLLA developed large crystals with truncated lozenge shape. Also, the lamellar morphology changed from hexagonal to spindle shaped when the crystallization temperature was increased. After a two-step crystallization (in which the PCL block was crystallized after the PLLA isothermal crystallization), small and fringed PCL crystals grew over or close to the PLLA lamellae when the PLLA block crystallization temperature was high (see Figure 2.16).

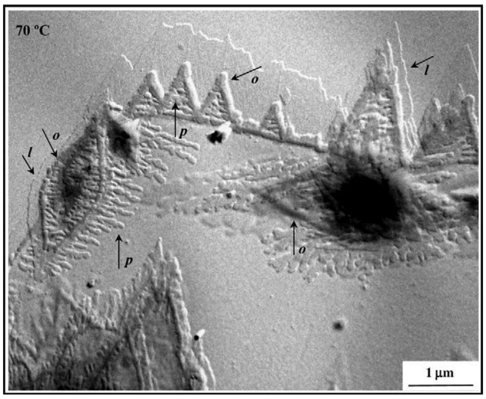

Figure 2.16. Lamellar crystals of $L_{44}C_{56}$ obtained after isothermal crystallizations performed at 70 ºC, which was a higher temperature than the poly(ε-caprolactone) melting point. Arrows labeled *o* and *p* indicate PLLA and PCL crystals, respectively. Reprinted with permission from Casas et al. [48]. © 2011 Elsevier Ltd.

Very recently, Lienard et al.[44] reported the synthesis and characterization of double crystalline cyclic diblock copolymers of poly(ε-caprolactone) and poly(L(D)-lactide) (c(PCL-*b*-PL(D)LA)). The non-isothermal crystallization behavior and the morphology of these novel cyclic copolymers were compared to the analogous linear diblock copolymers. The double crystalline nature of the as-synthesized cyclic copolymers was confirmed by WAXS measurements. However, under the cooling and heating rates employed in the non-isothermal DSC measurements, it was not possible to obtain a double crystalline copolymer in view of the slow crystallization of the PLA component. Double crystalline materials can be obtained by employing very slow cooling rates or by isothermal crystallization. In fact, PLOM observations during the isothermal crystallization of the cyclic copolymer at 100 ºC (a temperature in which only the PL(D)LA block crystallizes) and then at 30 ºC (a crystallization temperature for PCL) proved their double crystalline nature upon cooling from the melt. At 100 ºC, a distorted spherulitic morphology was formed by the crystallization of PL(D)LA block. Once the temperature was cooled down until 30 ºC, the characteristic change in the magnitude of the birefringence was observed as a result of the PCL crystallization. Although SAXS measurements in the melt were not presented, the authors claimed that these cyclic block copolymers are most likely melt miscible based on what is reported in the literature for analogous linear ones. Therefore, the phase separation and morphology was a result of the PL(D)LA crystallization, that templates the subsequent crystallization of the PCL block [44].

2.1.8 ABC block terplymers of poly(ethylene oxide), poly(ε-caprolactone) and poly(L-lactide)

Only recently a few publications have reported a new generation of ABC triblock and ABCBA pentablock terpolymers composed of poly(ethylene oxide), poly(ε-caprolactone) and poly(L-lactide) synthesized employing different novel routes [110-115]. As the analogous diblock copolymers, the interest of triblock terpolymers of PEO, PCL and PLLA relies in their potential applications in the biomedical field. For this reason, features such as, biodegradation, self-assembly in aqueous solution, drug-release behavior, and cytotoxicity have been studied [112-114]. Due to their amphiphilic nature, these terpolymers can form micellar structures [112]. In addition, these PEO-*b*-PCL-*b*-PLLA triblock terpolymers have been considered as templating materials. Several nanostructures, such as bicontinuous gyroids, hexagonally packed cylinders, spherical micelle structures and closed-loop mesoporous structures have been obtained after templating phenolic resins employing these triblock terpolymers [116].

However, the crystallization behavior and morphology of terpolymers that contain three different potentially crystallizable blocks is a very new field of research, and only four reports have been published so far dealing with this matter [20, 110, 113, 117]. Comparing to double crystalline diblock copolymers, the crystallization behavior of triblock terpolymers with three crystallizable blocks is expected to be more complex. The understanding of their triple crystalline nature is particularly relevant, since the biodegradation features of these novel PEO-*b*-PCL-*b*-PLLA terpolymers will be affected by the coexistence of three crystalline phases and one mixed amorphous phase inside a mixed crystalline superstructure. These phases will exhibit different packing densities, as a result of three different chemical structures and block lengths.

Sun et al. [113] reported the synthesis of PEO-*b*-PCL-*b*-PLLA triblock and PLLA-*b*-PCL-*b*-PEO-*b*-PCL-*b*-PLLA pentablock terpolymers. The authors reported that the terpolymers were crystalline from DSC analysis and WAXS experiments performed at room temperature. The WAXS profiles demonstrated the coexistence of the three crystalline structures. Strong diffraction peaks of PLLA and PEO crystals were observed. However, the diffraction peaks corresponding to the PCL crystals were very weak; suggesting that crystallization of the PCL central block was highly hindered by the PEO and PLLA end blocks. However, the low PCL content in the terpolymers (between ～13-20 %), also accounted for the weak scattering peaks in the WAXS profile. DSC cooling scans of the triblock and pentablock terpolymers performed at 10 ºC.min^{-1} showed that the crystallization temperature of the PEO and PCL blocks overlapped between 10 and 16 ºC, while the PLLA block crystallized at around 83-85 ºC. The subsequent DSC heating scan also showed an overlapped peak between 40-43 ºC corresponding to the melting of the PEO and PCL crystals, and a high temperature melting peak between 105 and 112 ºC corresponding to the PLLA block. The authors calculated the crystallization degree from the crystallization enthalpy. Taken together, the crystallization degree of the PEO-PCL segment in the pentablock terpolymer decreased in comparison with that of the same segment in the triblock terpolymer. On the contrary, the crystallization degree of the PLLA block remained almost the same.

The reduced crystallinity of the PEO-PCL segment in the pentablock further indicated that the previously formed PLLA crystals strongly restricted the subsequent crystallization of the central PCL-PEO block [113]. In contrast, other authors reported PLLA-*b*-PCL-*b*-PEO-*b*-PCL-*b*-PLLA pentablock terpolymers, in which only the PCL and PLLA blocks could crystallize, according to WAXS. If the PCL content increased, only the PCL block crystallized and the other two remained amorphous. Also, the DSC PCL melting temperature decreased as the PLLA content in the terpolymer increased [114]. Therefore, the microstructure has a great influence in the crystallizability of the terpolymers.

The crystallization and melting sequence of PEO-*b*-PCL-*b*-PLLA triblock terpolymers has been reported by Chiang et al.[110] The authors were able to observe the sequential crystallization of each block by employing 10 ºC.min^{-1} as a cooling rate. The sets of samples contain different molecular weights of each block. It is well known that the crystallization kinetics of PLLA is rather slow and depends on molecular weight following a bell shape trend [75]. In order to obtain a terpolymer with a triple crystalline nature, the PLLA block must have a suitable size. For instance, Chiang et al.[110] reported that when PLLA block molecular weight was 1000 g.mol^{-1}, this block remained amorphous after cooling at 10 ºC.min^{-1}. A PLLA crystalline phase was obtained when the molecular weight of the PLLA block was 6300 g.mol^{-1}. In general, as the PLLA molecular weight increases, the low chain mobility reduces the crystallizability of PLLA [75].

The thin film morphology obtained after crystallization from melt and solution was studied by Chiang et al.[110] After a one-step melt crystallization performed by quenching the sample directly to 90, 45 or -10 ºC, flat on PLLA, flat on PCL and edge-on PEO single crystals were obtained (see Figure 2.17). At 90 ºC, only PLLA lozenge-shaped single crystals were formed (Figure 2.17a). In contrast, not well-defined crystals were obtained for PCL and PEO at 45 and -10 ºC, respectively, as a result of the vitrified PLLA matrix that obstructed the crystallization of the other two blocks. In contrast, when a two step or a three step sequential crystallization protocol was employed, well-defined single crystals of the PEO and PCL blocks were directed by the first crystallization of the PLLA block (see Figure 2.18). During PLLA crystallization at 90 ºC, the PEO and PCL amorphous chains were excluded onto the surface of PLLA single crystals. As a result, the subsequent crystallization of the other two blocks was confined by the PLLA crystals, and the final morphology was determined by the first-crystallization event [110].

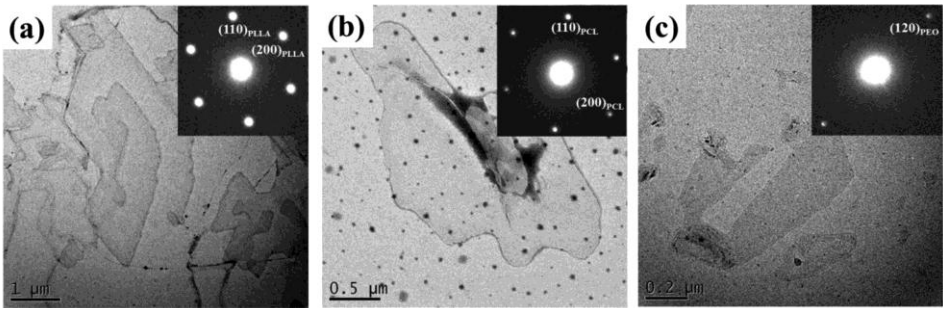

Figure 2.17. TEM micrographs and the corresponding SAED patterns of the PEO5-PCL3-PLLA6 thin films after melt crystallization at (a) 90, (b) 45, and (c) −10 °C for 3 h. Reprinted with permission from Chiang et al.[110]. © 2015 American Chemical Society.

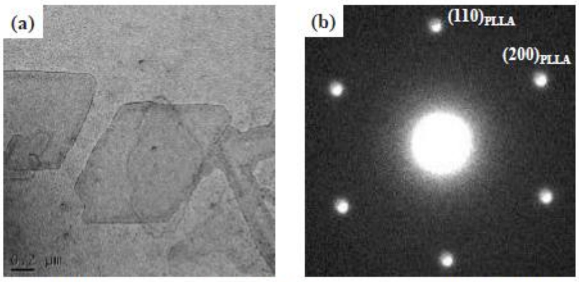

Figure 2.18. (a) TEM micrograph and (b) the corresponding SAED pattern of the PEO5-PCL3-PLLA6 thin film after two step crystallization, *i.e.*, 90 ºC → 45 ºC. After RuO_4 staining the dark region is PEO and the bright region is PCL and PLLA. The crystallization time at each step is 3 h. Reprinted with permission from Chiang et al.[110]. © 2015 American Chemical Society.

2.2 EXPERIMENTAL PART

2.2.1 Materials

The homopolymers, diblock copolymers and triblock terpolymers under study were kindly provided by Prof. Nikos Hadjichristidis, head of the Polymer Synthesis Laboratory from King Abdullah University of Science and Technology. The structure of the PLLA, PCL and PEO homopolymers, PCL-*b*-PLLA diblock copolymers and PEO-*b*-PCL-*b*-PLLA triblock terpolymers are presented in Figure 2.19.

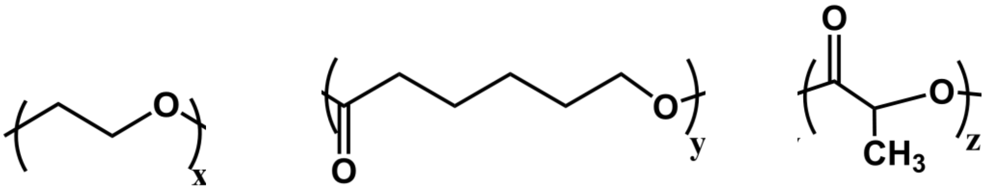

PEO **PCL** **PLLA**

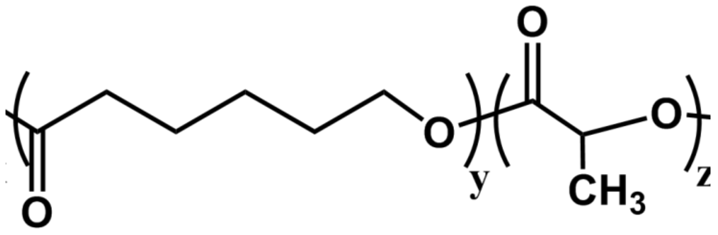

PCL-*b*-PLLA diblock copolymer

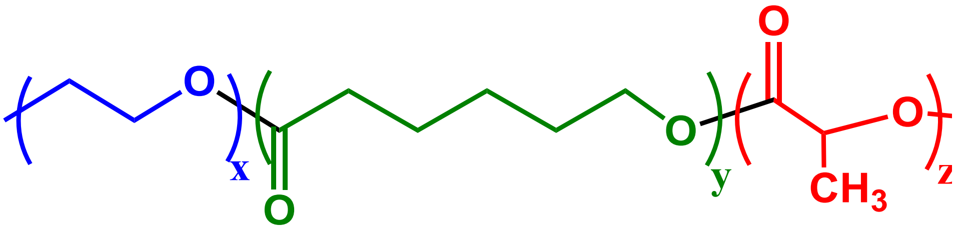

PEO-*b*-PCL-*b*-PLLA triblock terpolymer

Figure 2.19 Chemical structure of the PLLA, PCL and PEO homopolymers, PCL-*b*-PLLA diblock copolymers and PEO-*b*-PCL-*b*-PLLA triblock terpolymers

The PEO-*b*-PCL-*b*-PLLA triblock terpolymers were synthesized, as previously described, by one-pot sequential organocatalytic ring-opening polymerization of ethylene oxide (EO), ε-caprolactone (CL) and L-lactide (LLA) using a phosphazene base, 1-tert-butyl-2,2,4,4,4-pentakis(dimethylamino)-$2\lambda^5$,$4\lambda^5$-catenadi(phosphazene) (t-

BuP_2), as a single catalyst for the three monomers [111]. The scheme of the synthesis is presented in Figure 2.20. After the polymerization of the second monomer (CL), the reaction solution was divided into two approximately equal parts. Then, different amount of LLA was added into each part to form the third block. In this way, it was ensured that the triblock terpolymers have the same lengths of PEO and PCL blocks (4600 g mol^{-1} for PEO and 6800 g mol^{-1} for PCL), and different lengths of PLLA blocks (4700 and 8500 g mol^{-1}, respectively). Size exclusion chromatography (SEC) revealed that the triblock terpolymers had relatively low molecular weight distributions (ĐM < 1.20), and the nuclear magnetic resonance spectra (1H NMR) represented all the characteristic signals of the expected macromolecular structure, including the main bodies of the three blocks, end groups and groups linking different blocks [111]. Due to the use of PEO standards, the number-average molecular weight (M_n) of the PEO block obtained by SEC analysis was considered the absolute value, which was then used to calculate the M_ns of the other blocks from the 1H NMR spectra (values given above). The two triblock terpolymer samples used in this study are named herein as $PEO_{29}PCL_{42}PLLA_{29}^{16.1}$ and $PEO_{23}PCL_{34}PLLA_{43}^{19.9}$.

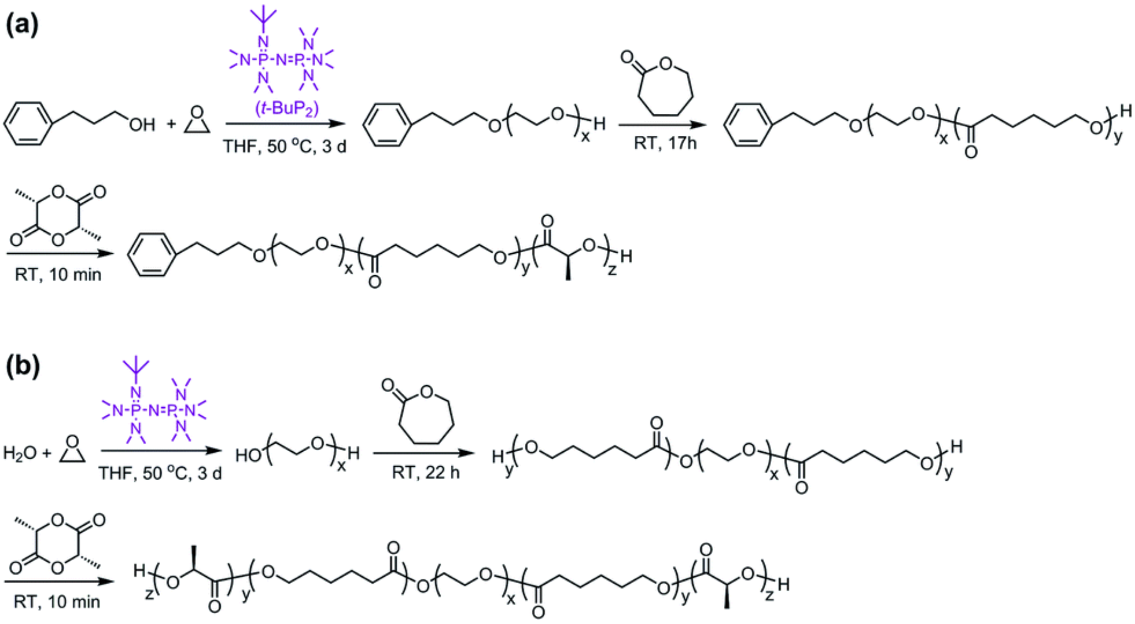

Figure 2.20 Schematic illustration of one-pot sequential polymerization of ethylene oxide, ε-caprolactone and L-lactide catalysed by t-BuP_2 toward (a) the triblock terpolymer using 3-phenyl-1-propanol as an initiator and (b) the pentablock terpolymer using water as an initiator.

All the samples are described in Table 2.2 . The subscript numbers represent the weight fractions of the blocks calculated from the M_ns and the superscript numbers, the molecular weight of the entire sample.

Table 2.2. Block molecular weight (M_n) and polidispersity index (PDI) of the terpolymers, diblock copolymers and homopolymers.

Sample code	M_n PEO block (g mol^{-1})	M_n PCL block (g mol^{-1})	M_n PLLA block (g mol^{-1})	PDI (Mw/Mn)
PEO^{4}	3800	-	-	1.03
PCL^{7}	-	7000	-	1.10
$PLLA^{4.6}$	-	-	4600	1.10
$PLLA^{8.6}$	-	-	8600	1.12
$PCL_{59}PLLA_{41}{}^{11.2}$	-	6600	4600	1.21
$PEO_{29}PCL_{42}PLLA_{29}{}^{16.1}$	4600	6800	4700	1.10
$PCL_{43}PLLA_{57}{}^{15.4}$	-	6600	8800	1.16
$PEO_{23}PCL_{34}PLLA_{43}{}^{19.9}$	4600	6800	8500	1.18

2.2.1 Small angle X-Ray scattering (SAXS) characterization of the PEO-*b*-PCL-*b*-PLLA triblock terpolymers

The large-scale structure was investigated by Small Angle X-Ray Scattering (SAXS) at the Material Physic Center in San Sebastian-Donostia. Experiments were performed on a Rigaku 3-pinhole PSAXS-L equipment operating at 45 kV and 0.88 mA. The MicroMax-002+ X-Ray Generator System composed by a microfocus sealed tube source module and an integrated X-Ray generator unit produces CuK_α transition photons of wavelength $\lambda = 1.54$ Å. The scattered X-Rays are detected on a two-dimensional multiwire X-Ray Detector (Gabriel design, 2D-200X). With a 200 mm diameter active area, this gas-filled proportional type detector offers ca. 200 micron resolution. The azimuthally averaged scattered intensities were obtained as a function of wave vector q ($q= 4\pi*\sin\theta/\lambda$, where 2θ is the scattering angle). Reciprocal space calibration was done using silver behenate as standard. The samples were placed in a Linkam

Scientific Instruments THMS 600 temperature controller (range: -196 to 600 ºC, stability < 0.1 ºC) at a distance of 2 m from the detector, covering a q-range: $0.1 \leq q \leq 1.5$ nm^{-1}. Flight path and sample chamber were under vacuum. Experiments were conducted at room temperature, 80 ºC and 140 ºC with measuring times of 5 min.

2.2.2 Non-Isothermal crystallization of the PEO-*b*-PCL-*b*-PLLA triblock terpolymers evaluated by differential scanning calorimetry (DSC)

A Perkin Elmer DSC Pyris 1 was employed to perform DSC measurements of the triblock terpolymers. Samples of approximately 3 mg were encapsulated in aluminum pans and tested under ultra-high purity nitrogen atmosphere. The instrument was previously calibrated with an indium standard. The thermal program employed for all samples was as follows: an initial heating run from 25 to 160 ºC at 20 ºC min^{-1}, keeping the sample for 3 min at that temperature to erase the thermal history, followed by a cooling scan down to -20 ºC at 1 ºC min^{-1}, and a second heating scan up to 160 ºC at 20 ºC min^{-1}.

2.2.3 Non-Isothermal crystallization of PEO-*b*-PCL-*b*-PLLA triblock terpolymers evaluated by wide angle X-Ray scattering (WAXS)

In-situ WAXS measurements were carried out at the beamline BL16B1 in the Shanghai Synchrotron Radiation Facility (SSRF). The wavelength of the radiation source was $\lambda = 1.2398$ Å. Scattering patterns were collected using a MAR 165 detector with a resolution of 2048×2048 pixels (pixel size: 79×79 μm^2). The sample-to-detector distance was 178 mm, and the effective scattering vector q range was 5~21 nm^{-1}. The temperature profile was controlled by a Linkam TST350 stage. To avoid degradation, all experiments were carried out under nitrogen atmosphere. The triblock terpolymer samples were first heated to 160 ºC and kept at that temperature for 3 min to erase possible thermal history. During cooling at 5 ºC min^{-1}, scattering patterns were collected in-situ to monitor the non-isothermal crystallization process. The acquisition time for each pattern was 9 s, yielding a temperature resolution of 1 ºC. All the X-ray patterns were corrected for detector noise, air scattering and sample absorption. The two dimensional scattering patterns were integrated radially to one dimensional intensity profiles using the program Fit2D.

2.2.4 Morphological observations of the microscale structure by polarized light optical microscopy (PLOM)

The crystalline microscale morphology of the diblock copolymers and triblock terpolymers was observed by polarized light optical microscopy (PLOM). Films were prepared by melting the sample between a glass slide and a cover slip employing a Mettler Toledo FP82HT hot stage plate. Samples were observed in a Leitz Aristomet microscope with crossed polarizers and making use of λ wave plate to determine the sign of the spherulites. The thermal protocol applied was as follows: once the sample was melted at 160 ºC inside the hot stage, it was kept at this temperature for 3 min. Then, it was quickly cooled down sequentially to the isothermal crystallization temperature of each block.

2.2.5 Thermal treatments to study the lamellar structure

The $PEO_{23}PCL_{34}PLLA_{43}^{19.9}$ triblock terpolymer and the analogous $PCL_{43}PLLA_{57}^{15.4}$ diblock copolymer were selected in order to study the lamellar structure by X-Ray scattering and Atomic Force Microscopy (AFM). With that purpose, each block in the copolymer and terpolymer was previously crystallized employing two particular thermal protocols. For the X-Ray experiments, the samples were crystallized inside DSC pans making use of a Perkin Elmer DSC Pyris 1 calorimeter.

In the two thermal protocols, the first step consisted in melting the sample at 160 °C for 3 min to erase thermal history.

In the first protocol (T1), the sample was cooled down from the melt at 20 ºC min^{-1} until 0 ºC and then heated up to the crystallization temperature of the PLLA block (T_c PLLA) at 60 ºC min^{-1}. Then, the sample was kept at this temperature for 1 h to induce the PLLA block crystallization until saturation. Finally, it was quenched to 25 ºC at 100 ºC min^{-1}.

In the second protocol (T2), a two steps sequential crystallization was conducted. The sample was also cooled down from the melt until 0 ºC and then heated up to T_c PLLA at 60 ºC min^{-1}, and kept at this temperature for 1 h. Then, it was cooled down to T_c PCL at 60 ºC min^{-1}, and kept at this temperature for 1 h to isothermally crystallize the PCL block. Finally, the sample was quenched to 25 ºC at 100 ºC min^{-1}. The crystallization temperatures employed in the two protocols for each particular sample are presented in Table 2.3.

Table 2.3 Crystallization temperatures employed in the thermal treatments.

Sample code	Method	T_c PLLA block (ºC)	T_c PCL block (ºC)
$PCL_{43}PLLA_{57}^{15.4}$	1	81.0	-
	2	81.0	49.5
$PEO_{23}PCL_{34}PLLA_{43}^{19.9}$	1	81.0	-
	2	81.0	50.0

After the crystallization treatment, a subsequent heating scan was additionally recorded in the DSC a 5 ºC min^{-1} under ultra-high purity nitrogen atmosphere. The instrument was previously calibrated with an indium standard.

2.2.6 Morphological observation of the lamellar structure by atomic force microscopy (AFM)

The morphology of the $PCL_{43}PLLA_{57}^{15.4}$ and $PEO_{23}PCL_{34}PLLA_{43}^{19.9}$ samples, obtained after the two thermal protocols described in section 2.2.5, was observed by AFM. A Bruker Multimode 8 Multimode scanning probe microscope equipped with a Nanoscope V controller was employed. The figures were acquired in tapping mode using microfabricated silicon tips/cantilevers (cantilever spring constant, k = 42 N/m, and resonance frequency, f_o = 320 kHz, Bruker). Height and phase images of lamellae were collected simultaneously and were subjected to a first-order plane-fitting procedure to compensate for sample tilt. The micrographs size was in a range of 0.5 to 7 μm. The samples were prepared by spin-coating into a homogeneous thin film on a mica substrate from chloroform solution (50 mg/mL). Then, the two thermal protocols were performed on each sample as described previously (see Table 2).

2.2.7 Simultaneous SAXS/WAXS characterization of the lamellar structure

X-Ray experiments were conducted in the $PCL_{43}PLLA_{57}^{15.4}$ and $PEO_{23}PCL_{34}PLLA_{43}^{19.9}$ samples that were previously crystallized following the two thermal protocols described in section 2.2.5. The samples were tested inside DSC pans. In-situ simultaneous SAXS/WAXS measurements were carried out at the beamline BL11-NCD in the ALBA Synchrotron Radiation Facility (Cerdanyola del Valles, Barcelona, Spain). The wavelength of the radiation source was $\lambda = 0.9999$ Å. SAXS scattering patterns were collected using an ADSC Q315r detector with a resolution of 3070x3070 pixels (pixel size: 102 μm^2). The sample-to-detector distance was 6388.5 mm, covering a scattering vector q range from 0.2 to 2.5 nm^{-1}. The tilt angle was 0°. WAXS patterns were recorded using a Rayonix LX255-HS detector with a resolution of 1920x5760 pixels (pixel size: 40 μm^2). The sample-to-detector distance was 126.8 mm, the effective scattering vector q range was 8-22 nm^{-1}, and the tilt angle 30°. The calibration was performed employing silver behenate and Cr_2O_3 standards. The temperature profile was controlled by a Linkam Scientific Instruments THMS600 stage coupled to a liquid nitrogen cooling system. The previously crystallized samples were heated from 25 to 160 ºC at 5 ºC min^{-1}. Scattering patterns were collected in-situ to monitor the evolution of the microphase separation on heating. The acquisition time for each pattern was 6 s, yielding a temperature resolution of 0.5 ºC. The two dimensional scattering patterns were integrated radially to one dimensional intensity profiles using the program DAWN, as a function of the inverse scattering vector, $q = 2\pi/d = 4\pi \sin \theta/\lambda$.

2.2.8 Isothermal crystallization of the PCL-*b*-PLLA diblock copolymers and PEO-*b*-PCL-*b*-PLLA triblock terpolymers followed by DSC

The isothermal crystallization of each block in the diblock copolymers and terpolymers described in Table 2.2 was studied separately. In all cases, preliminary tests were performed to assure that the block under study did not crystallize during the scans previous to the isothermal step. Several crystallization temperatures were employed and the crystallization process of each block as function of time was recorded.

The PLLA block

The sample was first melted at 160 ºC during 3 min and next cooled down until 0 ºC at 20 ºC min^{-1} (to improve the nucleus density of the PLLA block). Then, it was heated up to the PLLA crystallization temperature (T_c) at 60 ºC min^{-1}. The sample was isothermally crystallized until saturation and finally it was heated again from T_c to 160 ºC at 20 ºC min^{-1}.

The PCL block

To study the crystallization kinetics of the PCL block, two different approaches were employed: two step and one step crystallization. In the first one, the PLLA block was first crystallized until saturation as it was described previously. At those temperatures, the PCL and the PEO blocks are molten. After PLLA crystallization was completed, the sample was rapidly cooled at 60 ºC min^{-1} until the PCL crystallization temperature. Then, the PCL block was isothermally crystallized until saturation and finally, the sample was heated again at 20 ºC min^{-1}.

In the second approach, the crystallization process was carried in one step. The sample was first melted at 160 ºC during 3 min. After that, it was cooled down at 60 ºC min^{-1} until the PCL crystallization temperature and isothermally crystallized until saturation. Finally, the subsequent heating scan a 20 ºC min^{-1} was recorded.

The PEO block

The isothermal crystallization of the PEO block in the terpolymers was followed employing a three step thermal protocol. After melting the sample during 3 min at 160 ºC, the PLLA block was crystallized until saturation as previously described. Then, the sample was rapidly cooled down, and the PCL block was fully crystallized at a temperature high enough to keep the PEO block molten. After PCL crystallization was completed, the sample was quenched again until PEO crystallization temperature. The PEO block was allowed crystallizing until saturation. Finally, the subsequent heating scan a 20 ºC min^{-1} was recorded.

2.2.9 Isothermal crystallization of the PLLA block in a PCL-*b*-PLLA diblock copolymer and a PEO-*b*-PCL-*b*-PLLA triblock terpolymer followed by simultaneous SAXS/WAXS

The $PCL_{59}PLLA_{41}^{11.2}$ diblock copolymer and the $PEO_{29}PCL_{42}PLLA_{29}^{16.1}$ triblock terpolymer were selected to follow the crystallization of the PLLA block by in-situ simultaneous SAXS/WAXS. The measurements were carried out at the beamline BL11-NCD in the ALBA Synchrotron Radiation Facility (Cerdanyola del Valles, Barcelona, Spain). The samples were tested inside DSC pans and the scattering of an empty DSC pan was subtracted from the data. The wavelength of the radiation source was $\lambda = 1$ Å. WAXS scattering profiles were recorded using a Rayonix LX255-HS detector with a resolution of 1920x5760 pixels (pixel size: 44 μm^2). The sample-to-detector distance was 132.6 mm, the effective scattering vector q range was 8-22 nm^{-1}, and the tilt angle 21.2°. SAXS patterns were collected using an ADSC Q315r detector with a resolution of 3070x3070 pixels (pixel size: 102 μm^2). The sample-to-detector distance was 6495.0 mm, covering a scattering vector q range from 0.1 to 2.7 nm^{-1}. The tilt angle was 0°. The calibration was performed employing silver behenate and Cr_2O_3 standards. The temperature profile was controlled by a Linkam Scientific Instruments THMS600 stage coupled to a liquid nitrogen cooling system. The crystallization protocol was the same described in section 2.2.8 for the PLLA block. The acquisition time for each pattern was 6 s. The two dimensional scattering patterns were integrated radially to one dimensional intensity profiles using the program pyFAI, as a function of the inverse scattering vector, $q = 2\pi/d = 4\pi \sin \theta/\lambda$.

2.3 RESULTS AND DISCUSIONS

2.3.1 Standard SAXS characterization of the PEO-*b*-PCL-*b*-PLLA triblock terpolymers

SAXS experiments of both triblock terpolymers were performed at room temperature (RT), 80 and 140 ºC and the resulting patterns are shown in Figure 2.21. SAXS patterns were taken during heating, so the disappearance of scattering peaks is a result of the melting of each block in the terpolymer. At 140 ºC, both triblock terpolymers are in the melt state, according to previous DSC measurements (see also below). Figure 2.21a shows that no reflection was observed at 140 ºC for the $PEO_{29}PCL_{42}PLLA_{29}^{16.1}$ sample while the other triblock terpolymer exhibits a single very broad and weak reflection at this temperature (Figure 2.21b). Both observations indicate that the terpolymers are most likely miscible in the melt. The broad reflection of the $PEO_{23}PCL_{34}PLLA_{43}^{19.9}$ sample at 140 ºC can be ascribed to a correlation hole effect[8, 118, 119] that produces broad signals in the scattering pattern of block copolymers with a homogeneous melt morphology. Similar observations have been previously reported in literature for miscible or weakly segregated di and triblock copolymers.[6, 8]

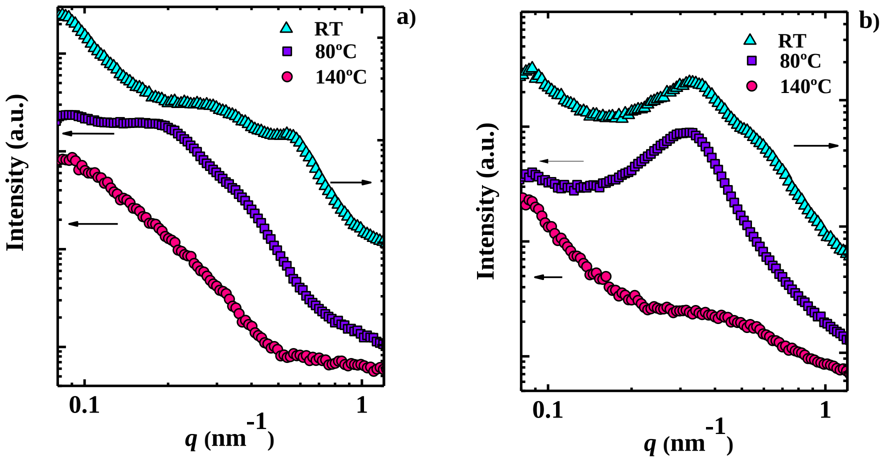

Figure 2.21 SAXS patterns taken at different temperatures on heating of a) $PEO_{29}PCL_{42}PLLA_{29}^{16.1}$ and b) $PEO_{23}PCL_{34}PLLA_{43}^{19.9}$

For instance, a homogeneous melt have been detected by SAXS for PCL-*b*-PLLA [6, 8, 46], PEO-*b*-PLLA [34] and PCL-*b*-PEO copolymers [1]. In diblock copolymers, microphase segregation in the melt can be predicted by calculating the segregation strength, i.e., the product of χN, on the basis of the mean-field theory [120, 121]. The parameter χ is the Flory-Huggins interaction parameter and N the polymerization degree. According to this theory, if the χN value is ≤ 10 the entropic terms prevail and the system will exhibit a disorder-homogeneous melt. Since our samples are *ABC*-type triblock terpolymers, estimating their miscibility through this theory becomes more complicated because, to our knowledge, experimental determination of the χ value for any of the diblocks in the terpolymer has not been reported so far. Thus, a rough estimation of χ [35, 51, 122] and χN parameter for each pair of blocks *AB*, *BC* and *AC* has been calculated using the solubility parameters of PEO, PCL and PLLA reported in the literature [35, 51]. The values obtained are compiled in Table 2.4. The low χN values (≤ 10) of the pairs in both samples could be used as an approximate indication of a low melt-segregation level in the triblock. Thus, although the calculated values might not fully represent the interactions in the whole triblock terpolymer, it would be expected that PEO, PCL and PLLA blocks would be miscible or weakly segregated in the melt. These calculations are in line with our SAXS results and support our contention that the two triblock terpolymers employed here are miscible in the melt. As already mentioned in the introduction, PEO-*b*-PCL [18, 21, 24, 27, 88] and PEO-*b*-PLLA [1, 34, 35, 41, 101, 123] diblock copolymers are reported to be miscible in the melt [1], while PCL-*b*-PLLA copolymers are known for exhibiting either a miscible [6, 8, 46, 49, 51, 124] or weakly segregated [5, 50, 101, 124] behaviour, depending on composition and PLLA block M_w.

Table 2.4. Values of χ and segregation strength parameter χN calculated for different diblock copolymer pairs at different temperatures. Such diblock copolymer pairs can be considered precursors or parts of the chain of thePEO-*b*-PCL-*b*-PLLA triblock terpolymers.

Sample	Temperature (ºC)	PEO-PCL		PCL-PLLA		PEO-PLLA	
		χ	χN	χ	χN	χ	χN
PEO$_{29}$PCL$_{42}$PLLA$_{29}^{16.1}$	160	-	-	1.86x10^{-2}	2.32	2.90x10^{-4}	0.04
	90	2.81x10^{-2}	3.59	2.22x10^{-2}	2.77	3.46x10^{-4}	0.05
	50	3.15x10^{-2}	4.01	-	-	-	-
	41	3.24x10^{-2}	4.14	2.56x10^{-2}	3.20	4.00x10^{-4}	0.05
	25	3.42x10^{-2}	4.37	2.70x10^{-2}	3.37	4.22x10^{-4}	0.06
PEO$_{23}$PCL$_{34}$PLLA$_{43}^{19.9}$	160	-	-	1.86x10^{-2}	3.30	2.90x10^{-4}	0.05
	90	2.81x10^{-2}	3.59	2.22x10^{-2}	3.94	3.46x10^{-4}	0.06
	50	3.15x10^{-2}	4.01	-	-	-	-
	41	3.24x10^{-2}	4.14	2.56x10^{-2}	4.55	4.00x10^{-4}	0.07
	25	3.42x10^{-2}	4.37	2.70x10^{-2}	4.79	4.22x10^{-4}	0.08

SAXS scattering peaks observed at room temperature and 80 ºC suggest a periodic lamellar microdomain structure with long-range order [89]. For instance, in PEO-*b*-PCL diblock copolymers, their structure consists of alternating crystalline lamella of each component with amorphous layers in between [89]. This alternating lamellar structure has also been reported on PLLA-*b*-PEO / PLLA-*b*-PEG and PLLA-*b*-PCL copolymers (see [1, 125] and references therein), which are all miscible or weakly segregated in the melt. Thus, it is possible that a similar but even more complicated morphology (i.e., with the presence of three different lamellar crystal types within the spherulites) exists in these terpolymers. The existence of mixed spherulites will be demonstrated below by Polarized Light Optical Microscopy (PLOM) experiments.

2.3.2 Non-Isothermal crystallization of PEO-*b*-PCL-*b*-PLLA triblock terpolymers and the corresponding diblock copolymers and homopolymers evaluated by DSC

The morphology of the samples is in direct relationship with their thermal behaviour. Thus, DSC analysis was performed in order to evaluate if the blocks in the terpolymers are able to crystallize under standard cooling conditions. First of all, Figure

2.22 exhibits the DSC heating scan of the samples as-synthesized. Three clear endothermic peaks are observed in both samples. Since the typical melting temperatures of PLLA as homopolymer and in block copolymers are between 80 and 180 ºC [123], the highest temperature peak is assigned to the melting of PLLA crystals. Then, the other two lower temperature peaks must correspond to the melting of PEO, PCL, or both PEO/PCL crystals.

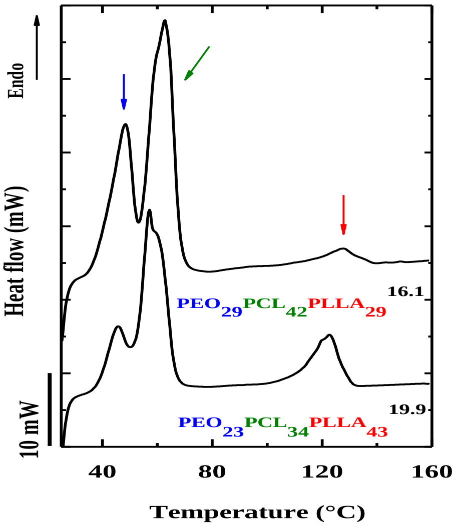

Figure 2.22 First DSC heating scans of as obtained reactor powders of the indicated triblock terpolymers at 20 ºC min-1.

After melting, the subsequent cooling scans were recorded at 1 ºC min^{-1}. Several tests were carried out to establish the ideal cooling rate to achieve the crystallization of the blocks. From this analysis, a low cooling rate is needed to accomplish this goal (see Appendix, Figure 6.1, 6.2, 6.3 and 6.4).

Figure 2.23, shows three well defined exothermic peaks that are due to the crystallization from the melt of the blocks. The PLLA block crystallizes first upon cooling from the melt at around 70 ºC. After PLLA block crystallization, upon further cooling, the following blocks to crystallize are either PEO or PCL. Similar results have been reported recently in similar PEO-*b*-PCL-*b*-PLLA terpolymers obtained by a different synthetic pathway [126].

In PEO-*b*-PCL diblock copolymers the sequence of crystallization depends on copolymer composition. For instance, when PCL is the major component, this block crystallizes first and then the PEO block. The opposite behaviour is observed when the

PEO content is higher.[89] Thus, further analyses by WAXS are needed in order to properly identify the order in which PCL and PEO blocks crystallize from the melt.

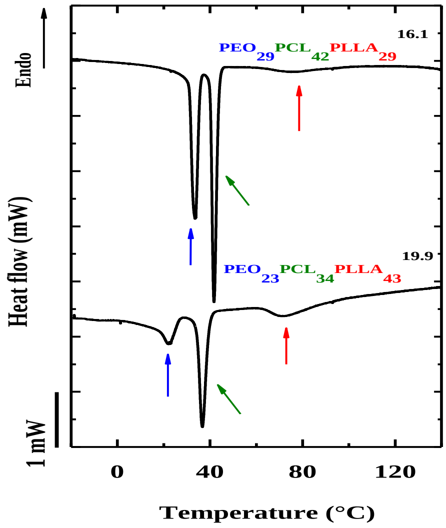

Figure 2.23 DSC cooling scans at 1 ºC min^{-1} after melting at 160 ºC for 3min.

The second DSC heating scans of the triblock terpolymers (after the cooling shown in Figure 2.23) are shown in Figure 2.24. The melting of the PLLA block clearly takes place around 120 ºC, identified by a broad endothermic peak with a minor low-temperature shoulder. This shoulder is a common observation and it has been reported before for PLLA homopolymers. Such double melting behaviour has been ascribed to a recrystallization-melting mechanism leading to the formation of a more stable crystalline phase [4, 127-129]. This typical behaviour has also been observed in PLLA-containing diblock copolymers with PCL [49] and PEO [35, 40, 42]. Other works on PLLA based diblock [4, 124] and *ABA*-type triblock [101] copolymers did not observe this minor shoulder.

Another interesting observation is the absence of the typical cold crystallization peak of PLLA block during heating, which has been usually reported for PLLA block copolymers.[4, 6, 8, 49] The appearance of this peak depends on the length of the PLLA block, copolymer composition and cooling conditions. Since the cooling rate employed here was very low (1 ºC min^{-1}), the PLLA block is able to crystallize until saturation under this condition and additional crystallization does not occur during the heating scan.

In our triblock terpolymers, the PEO and PCL crystals melt between 40 and 60 ºC. A double peak endotherm located between these temperatures indicates the melting of these blocks, but which one occurs first will be elucidated by WAXS analysis below.

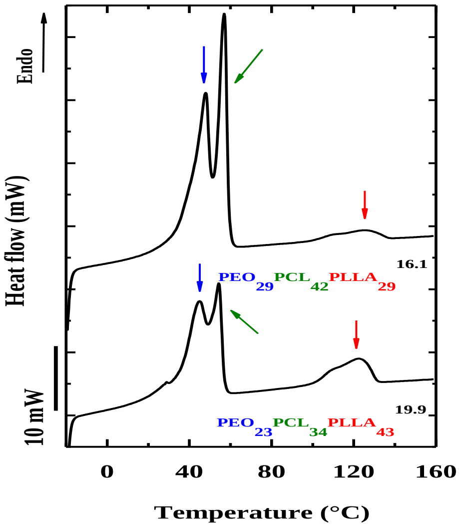

Figure 2.24 Subsequent DSC heating scans at 20 ºC min^{-1} after cooling at 1 ºC min^{-1} (shown in Figure 2.23).

2.3.3 Non-Isothermal crystallization of PEO-*b*-PCL-*b*-PLLA triblock terpolymers evaluated by WAXS

The local structure of both samples was investigated by WAXS experiments performed on cooling and the resulting patterns are shown in Figure 2.25 and Figure 2.26. The patterns confirm beyond any doubt the triple crystalline nature of these novel *ABC*-type triblock terpolymers. The reflections pointed out in those figures clearly reflect that each block crystallizes separately in an independent unit-cell structure. The PEO, PCL and PLLA crystals co-exist together in the terpolymer at low temperatures. The indexation reported in Table 2.5 agrees well with the assignments widely published in the literature for PEO, PCL and PLLA crystals within diblock copolymers.[6, 8, 22, 35, 49, 101, 130]

Taking for example the PEO$_{29}$PCL$_{42}$PLLA$_{29}^{16.1}$ terpolymer (see Figure 2.25), the two peaks at 11.73 and 13.37 nm^{-1} correspond to 100/200 and 203 reflections of the α form of PLLA. The very strong peak and the small shoulder close to it located at 14.96 and 15.37 nm^{-1} belong to 110 and 111 reflections of PCL respectively, along with the 200 reflection at 16.56 nm^{-1}. And, since the PLLA 203 peak coincides with the PEO

120 reflection, the evidence that the PEO block is able to crystallize is the small shoulder that belong to 112/032/132/212 reflection of PEO crystals located at 16.33 nm^{-1}. The PEO$_{23}$PCL$_{34}$PLLA$_{43}^{19.9}$ terpolymer also displays the 010 and 210 PLLA reflections at 10.44 and 15.56 nm^{-1}, respectively.[6, 8, 22, 35, 49, 101, 130] The values of the 2θ angles reported in Table 2.5 were obtained from the scattering vector q and the typical CuK$_{\alpha}$ radiation (λ = 1.54 Å). According to literature, PLLA and PCL crystallize in an orthorhombic system while the PEO does it in a monoclinic structure.[22, 40]

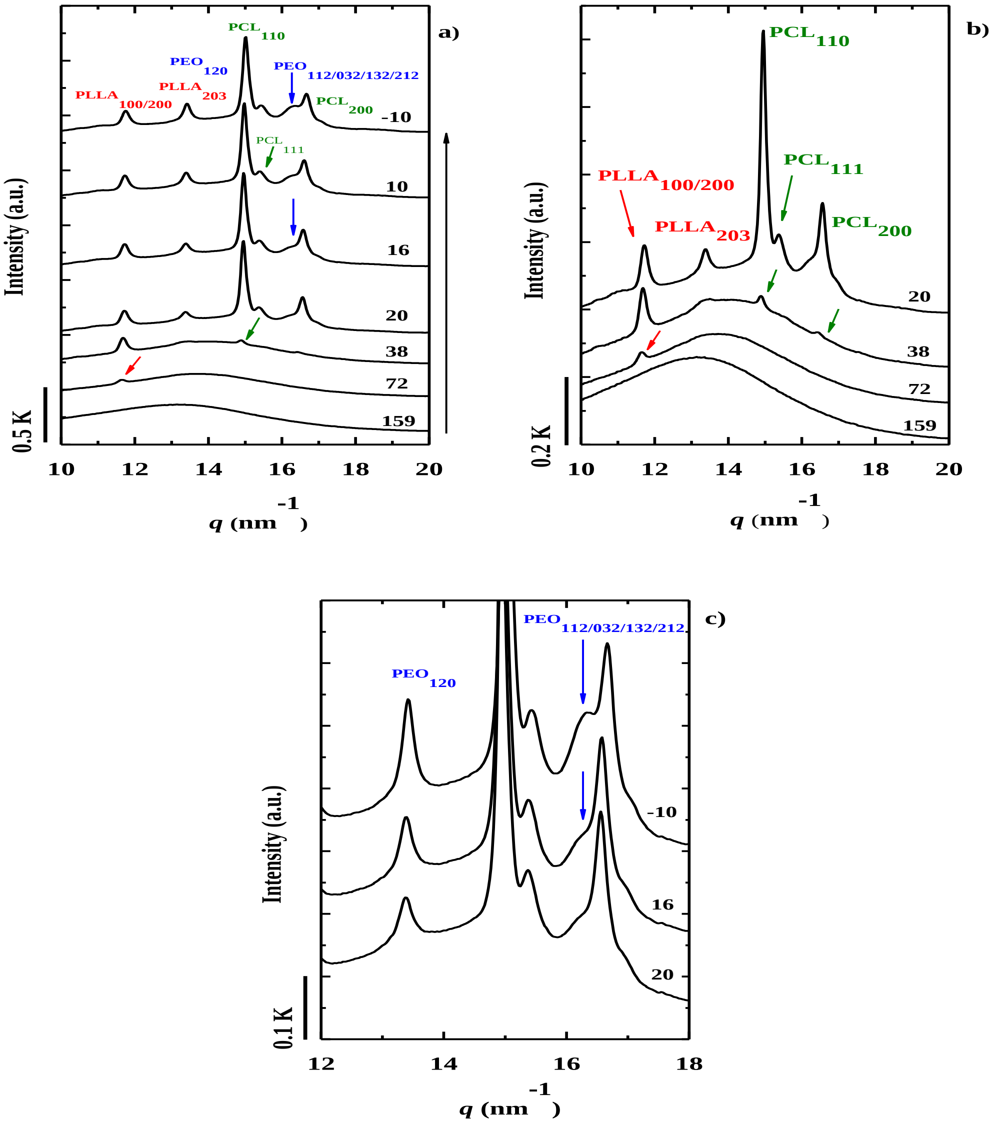

Figure 2.25 a) WAXS pattern taken at different temperatures during cooling from the melt at 5 ºC min^{-1} of PEO$_{29}$PCL$_{42}$PLLA$_{29}^{16.1}$. Peak assignment and structural features of each block are indicated in more detail in: b) PLLA and PCL and c) PEO.

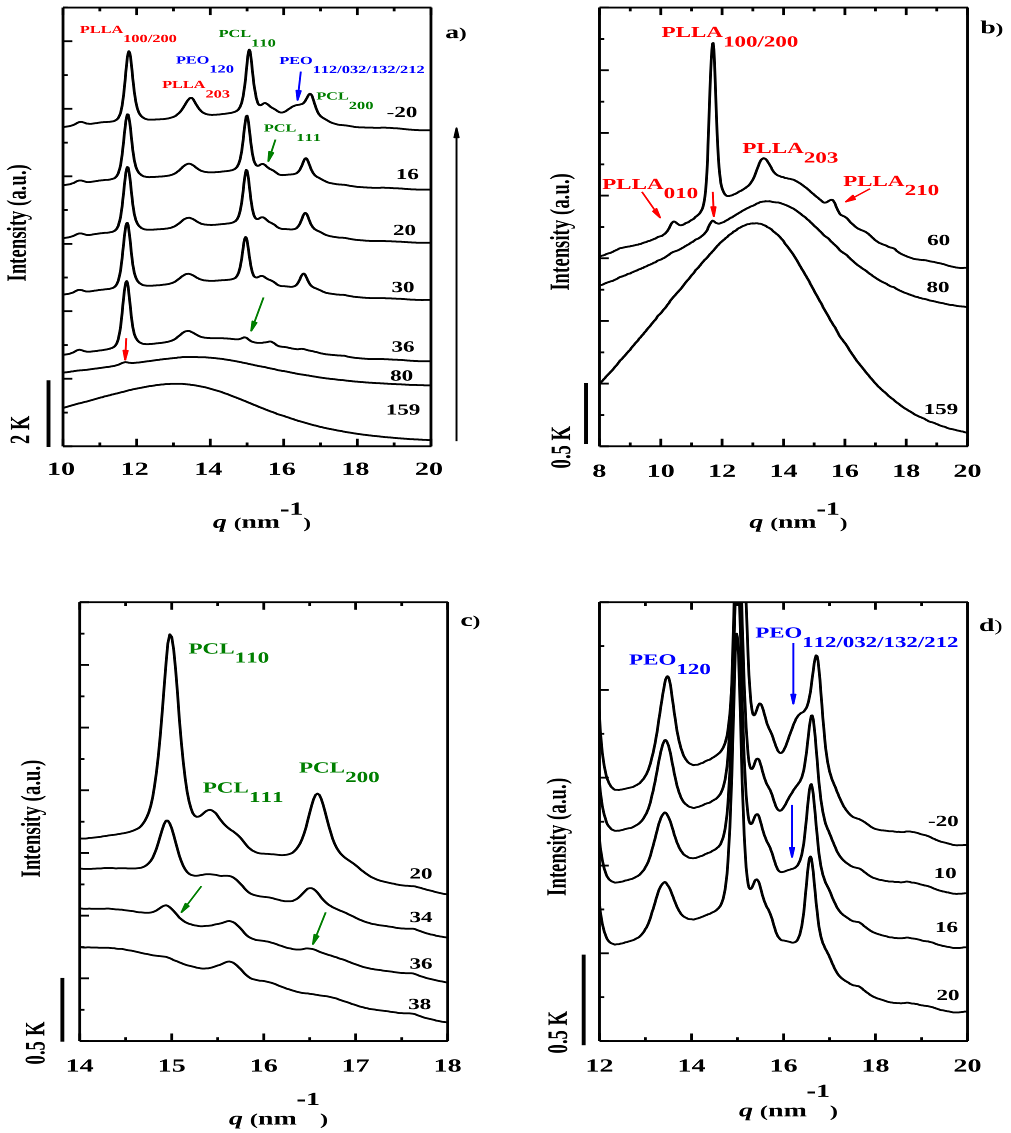

Figure 2.26 a) WAXS pattern taken at different temperatures during cooling from the melt at 5 ºC min^{-1} of $PEO_{23}PCL_{34}PLLA_{43}^{19.9}$. Peak assignment and structural features of each block are indicated in more detail in: b) PLLA, c) PCL and d) PEO.

The WAXS analysis also confirms that the crystallization sequence is as follows: the PLLA block crystallizes first, as it was expected (see Figure 2.25b and Figure 2.26b); then, the PCL block (see Figure 2.25b and Figure 2.26c), and, finally, the PEO block starts to crystallize at 16 ºC in both terpolymers (see Figure 2.25c and Figure 2.26d). A similar sequential crystallization has been reported for PEO-*b*-PCL-*b*-PLLA terpolymers prepared by a different synthetic route and with different molecular weights.[126]

Two modes of melt crystallization may occur in block copolymers: break-out crystallization and confined crystallization, depending on the segregation strength.[1, 105, 125] Since these triblock terpolymers are miscible in the melt, according to our SAXS evidence, the initial crystallization of the PLLA block templates the morphology by forming superstructural aggregates, like spherulites (as will be demonstrated below).[1, 125]

Table 2.5. WAXS indexation of the PEO-*b*-PCL-*b*-PLLA triblock terpolymers.

Sample	Reflections	q_{max} (nm^{-1})	D (nm)	2θ [a] (º)
$PEO_{29}PCL_{42}PLLA_{29}^{16.1}$	PLLA $_{110/200}$	11.73	0.54	16.5
	PLLA $_{113/203}$	13.37	0.47	18.9
	PCL $_{110}$	14.96	0.42	21.1
	PCL $_{111}$	15.37	0.41	21.7
	PCL $_{200}$	16.56	0.38	23.4
	PEO $_{120}$	13.41	0.47	18.9
	PEO $_{112/032/132/212}$	16.33	0.38	23.1
$PEO_{23}PCL_{34}PLLA_{43}^{19.9}$	PLLA $_{010}$	10.44	0.60	14.7
	PLLA $_{100/200}$	11.69	0.54	16.5
	PLLA $_{203}$	13.35	0.47	18.9
	PLLA $_{210}$	15.56	0.40	22.0
	PCL $_{110}$	14.98	0.42	21.2
	PCL $_{111}$	15.42	0.41	21.8
	PCL $_{200}$	16.58	0.38	23.5
	PEO $_{120}$	13.48	0.47	19.0
	PEO $_{112/032/132/212}$	16.36	0.38	23.2

[a] The values of 2θ correspond to the typical CuK_{α} radiation ($\lambda = 1.54$ Å).

The previously crystallized PLLA block will restrict the crystallization of the other two blocks creating an alternating lamellar template that confines the amorphous PLLA chains together with the molten PCL and PEO blocks. Despite interlamellar confinement in the intra spherulitic domains of PLLA block spherulites, Figure 2.25b and Figure 2.26b and c indicate that the PCL block can crystallize upon further cooling.

In PEO-*b*-PCL diblock copolymers the order of crystallization also depends on the copolymer composition. He et al. found that PCL crystallizes first when the PCL content was 43 % or higher, but if the PCL content is 36 % or less the PEO is the one who crystallizes first [89]. Similar results were reported by Sun et al.[16] and Wei et al.[28] in PEO-*b*-PCL diblock and PCL-*b*-PEG-*b*-PCL triblock copolymers, respectively. Hence, the main reason for the order of crystallization observed in our triblock terpolymers is the larger PCL content within them.

After the PCL block crystallization, the PEO block chains have no other choice but to crystallize inside the limited spaces left in between PLLA block and PCL block lamellae. The confinement imposed by these two previously formed lamellar crystals will hinder its crystallization, and this is the reason why the intensity of the PEO reflections in both triblock terpolymers is not sharp. WAXS experiments during heating allow assigning the melting behaviour shown in Figure 2.24 to the sequential fusion of all three corresponding blocks. Patterns exhibited in Figure 2.27 clearly demonstrate that, in both triblock terpolymers, PEO crystals melt first, as indicated with the blue arrow (see colour figure for reference), then PCL and finally the PLLA block.

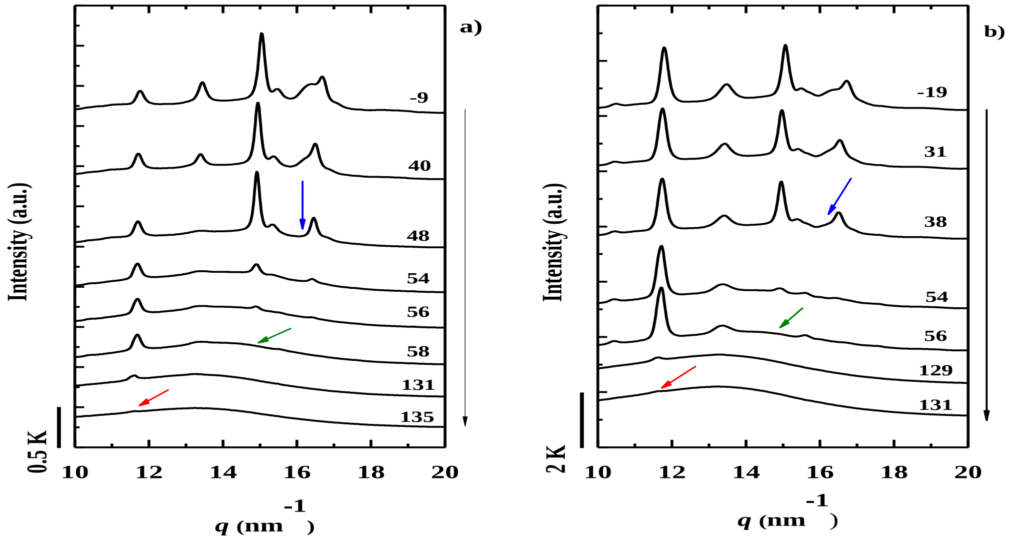

Figure 2.27 WAXS pattern taken at different temperatures during subsequent heating at 5 ºC min^{-1} of a) $PEO_{29}PCL_{42}PLLA_{29}^{16.1}$ and b) $PEO_{23}PCL_{34}PLLA_{43}^{19.9}$.

2.3.4 DSC thermal transitions of PEO-*b*-PCL-*b*-PLLA triblock terpolymers during non-isothermal crystallization

The results of our WAXS analysis, allows proper assignment of the thermal transitions observed by DSC to each the corresponding block. We have assigned a colour code (in the web version of our manuscript), to easily identify the crystallization and melting of each block in the DSC traces presented in Figure 2.22, Figure 2.23 and Figure 2.24, and in all WAXS diffractograms above: red for PLLA block, green for PCL block and blue for PEO block. The characteristic thermal properties obtained by DSC are presented in Table 2.6, Table 2.7 and Table 2.8.

Comparing thermal properties from WAXS and DSC, the results follow a similar general trend, in spite of the fact that they were conducted at different cooling and heating rates. The PLLA block in the triblock terpolymers presented here crystallizes around 70 ºC. Typical melt crystallization temperatures of PLLA blocks in miscible or weakly segregated diblock copolymers are between 80 and 115 ºC [1, 4, 6, 8, 35, 42, 49]. A similar situation is observed with the melting point of the PLLA block, it is lower in the triple crystalline triblock terpolymers than in the diblock copolymers previously studied in the literature (see Table 6.1 in Appendix). In partially miscible block copolymers both PLLA crystallization and melting temperatures decrease when the PLLA content is lower, as a result of a diluent effect of the molten PEO and PCL chains or for compositions where PLLA is a minor component (less than 20%) a confinement effect can also lead to lower crystallization temperatures. This has been the most common observation in PLLA-*b*-PCL [1, 4, 6, 46, 49, 131] and PLLA-*b*-PEO [1, 35, 37, 42, 101] diblock copolymers.

Table 2.6. Thermal properties of the triblock terpolymers obtained from DSC 1st heating scan at 20 ºC min^{-1}.

Sample	T_m PEO^{1st} (°C)	ΔH_m PEO^{1st} (J/g)	T_m PCL^{1st} (°C)	ΔH_m PCL^{1st} (J/g)	T_m PLLA^{1st} (°C)	ΔH_m PLLA^{1st} (J/g)
$PEO_{29}PCL_{42}PLLA_{29}^{16.1}$	48.4	102	62.8	66	127.5	23
$PEO_{23}PCL_{34}PLLA_{43}^{19.9}$	45.8	46	57.2	104	122.5	33

Table 2.7. Thermal properties of the triblock terpolymers obtained from DSC cooling scan at 1 ºC min^{-1}.

Sample	T_c PEO (°C)	ΔH_c PEO (J/g)	T_c PCL (°C)	ΔH_c PCL (J/g)	T_c PLLA (°C)	ΔH_c PLLA (J/g)
$PEO_{29}PCL_{42}PLLA_{29}^{16.1}$	33.5	-108	41.7	-73	75.0	-16
$PEO_{23}PCL_{34}PLLA_{43}^{19.9}$	22.1	-53	36.7	-63	72.3	-22

Table 2.8. Thermal properties of the triblock terpolymers obtained from DSC 2nd heating scan at 20 ºC min^{-1}.

Sample	T_m PEO^{2nd} (°C)	ΔH_m PEO^{2nd} (J/g)	T_m PCL^{2nd} (°C)	ΔH_m PCL^{2nd} (J/g)	T_m PLLA^{2nd} (°C)	ΔH_m PLLA^{2nd} (J/g)
$PEO_{29}PCL_{42}PLLA_{29}^{16.1}$	48.0	126	56.9	66	112.0 - 124.5	20
$PEO_{23}PCL_{34}PLLA_{43}^{19.9}$	45.0	112	54.2	45	112.1 - 121.8	28

The crystallization and melting enthalpies of the PLLA block are highly reduced in the triblock terpolymers, as compared to analogous PLLA-b-PCL diblock copolymers reported previously. For example, $L_{44}C_{56}^{25}$ and $L_{55}C_{45}^{18}$ have PLLA ΔH_m values of 82 and 69 J/g respectively [4], while in the triblock terpolymers those values are reduced to 20 and 28 J/g (see Table 2.8). Also, PLLA ΔH_c and ΔH_m values in the triblock slightly reduce as the PLLA content reduces. These results indicate that the crystallization ability of the PLLA block is affected by the presence of the two molten covalently bonded PCL and PEO blocks.

The PCL block crystallization and melting temperatures decrease as its content in the triblock terpolymers reduces, as it was expected (see Table 2.7 and Table 2.8). The crystallinity values follow a similar trend. Comparable results have been reported by Castillo et al. in PLLA-*b*-PCL diblock copolymers [4]. The reduced crystallinity of the PCL block accounts for the restriction imposed by the previous crystallization of the PLLA block that limits the PCL block lamellae to form in between the lamellar stacks of PLLA and the amorphous phase of the triblock terpolymer.

Finally, PEO is the last block to crystallize. Thus, its crystallization ability will be affected by the previous crystallization of both PLLA and PCL blocks. Nevertheless, the crystallization temperature of the PEO block in both terpolymers is relatively high, a fact that could be due to the nucleating actions of both PLLA and PCL crystals. This means that the PEO block is not undergoing the classical crystallization in confined isolated domains, where typically crystallization temperatures can be depressed to values below -30 ºC, as nucleation changes from heterogeneous to homogeneous and dominates overall crystallization kinetics (see references [105, 132, 133]).

Despite the crystallization temperature of the PEO block is not significantly affected, its degree of crystallinity is much reduced as compared to analogous PEO chains of equivalent lengths in diblock copolymers or even in homopolymers [42, 89]. This is probably a result of a slower crystallization kinetics of the PEO block (the last to crystallize upon cooling) when it is a part of the triple crystalline triblock terpolymer.

2.3.5 Morphology of the PEO-*b*-PCL-*b*-PLLA triblock terpolymers

Solid-state morphology of block copolymers is a reflection of their composition, crystallization behaviour, miscibility level and the degree of microphase separation driven by the crystallization process [134]. Polarized light optical microscopy (PLOM) observations have been performed on cooling from the melt in order to detect the sequential crystallization and superstructural organization of the terpolymers.

Figure 2.28 exhibits the morphology of both terpolymers as a function of selected temperatures at which each block crystallizes according to DSC and WAXS. First, the melt was quenched to 100 ºC. At this temperature the PLLA block crystallizes, while the other two blocks remain molten. Secondly, a quench was made to 39 ºC, a temperature at which PCL can crystallize and lastly, a final quench was carried out to room temperature where the PEO block can also crystallize.

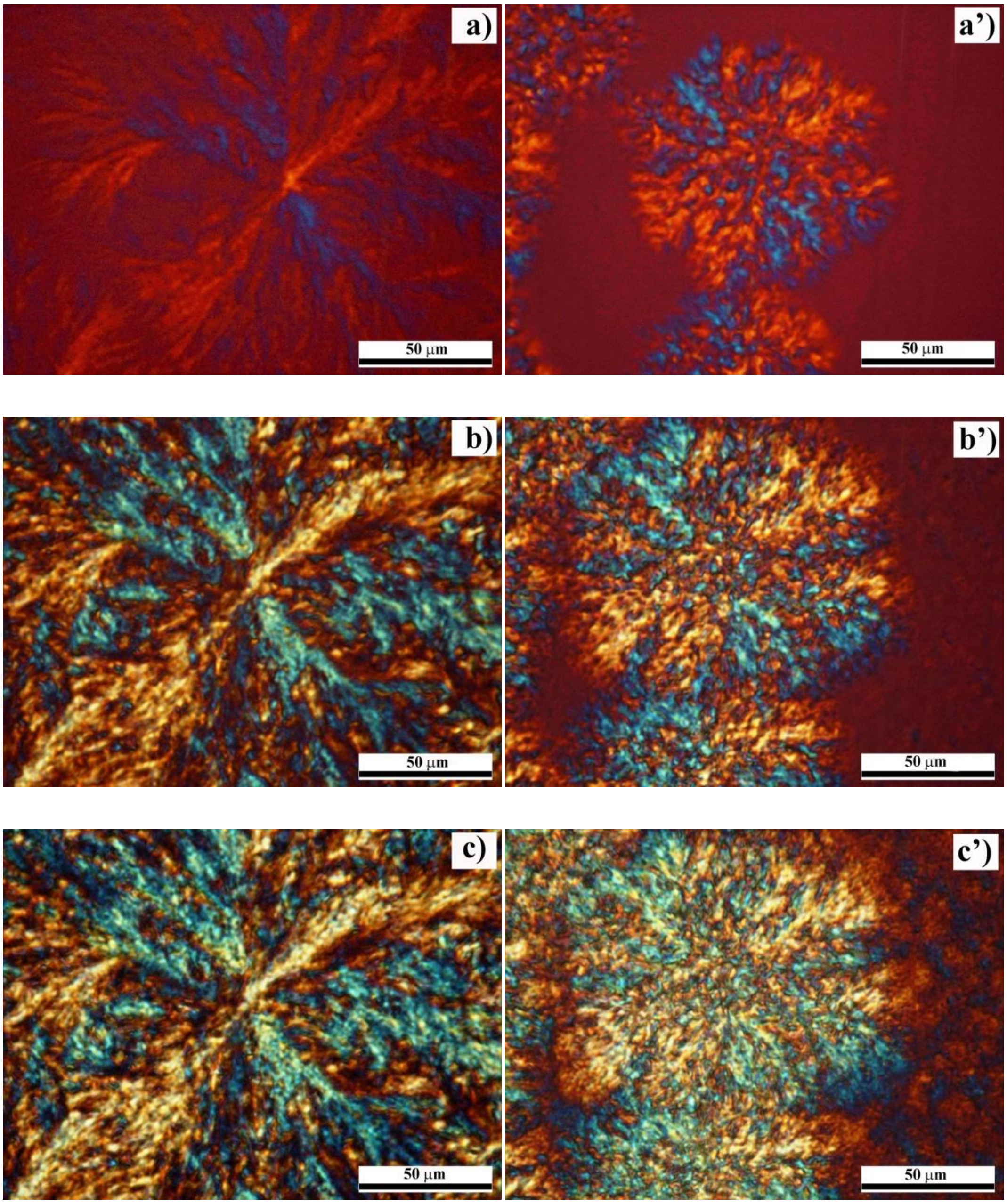

Figure 2.28 PLOM Micrographs taken at a) a') 100 ºC, b) b') 39 ºC and c) c') room temperature of $PEO_{29}PCL_{42}PLLA_{29}^{16.1}$ (left side) and $PEO_{23}PCL_{34}PLLA_{43}^{19.9}$ (right side). Scale bar 50 µm.

Figure 2.28 shows that the superstructure formed by PLLA in both triblock terpolymers is irregular and that banding extinction patterns are not observed. In block copolymers, the morphological evolution is influenced by the sample thickness, crystallization temperature and block composition [1, 34, 125, 135]. In many PEO-*b*-PCL, PCL-*b*-PLLA and PEO-*b*-PLLA diblocks copolymers, morphological changes with temperature and composition have been observed: from well-defined Maltese cross spherulites and concentric spherulites to spherulites with continuous banding extinction patterns [34, 35, 42, 49, 89]. For instance, PEO-*b*-PLLA diblock copolymers with PLLA content between 71 and 32 % exhibit PLLA banded spherulites [123]. However, based on the observations of Huang et al.[35] in the same diblock copolymers, the branching morphology developed as PLLA content in the terpolymers is lower (see Fig 8a, left) might be a result of the richer PCL-PEO amorphous phase that surrounds the proximity of the PLLA lamellae and disturbs further growth in their immediate vicinity [35]. Hence, the microphase separation driven by PLLA block crystallization is affected by the proportion of the three phases in the terpolymers.

The PLLA block crystalline superstructure created at 100 ºC templates the morphology for the subsequent crystallization of the PCL and PEO blocks. Fig. 8b and b' shows that PCL crystallization takes place at 39 ºC without altering significantly the superstructure of the previously crystallized PLLA block. The spherulities remain negative. However, the magnitude of the birefringence changes. Clear color changes and a new intense brightness account for the newly formed PCL block lamellar crystals within the PLLA block spherulite. Such intraspherulitic crystallization occurs within the interlamellar regions and as a result mixed spherulites are formed. The interlamellar regions are composed of a mixture of PLLA, PCL and PEO chains in the amorphous state. When the sample is quenched again to room temperature, quadrant colors become even lighter and brighter as a result of the PEO block crystallization inside the intra-spherulitic regions (see Figure 2.28c and c'). These observations in the $PEO_{29}PCL_{42}PLLA_{29}^{16.1}$ and $PEO_{23}PCL_{34}PLLA_{43}^{19.9}$ triblock terpolymers are very similar to those reported on PCL-*b*-PLLA [1, 6, 8, 49] and PEO-*b*-PLLA [37, 41, 42] diblock copolymers. However, in the terpolymer case, unique triple crystalline superstructures are formed with potentially very interesting properties.

Further evidences of the periodic lamellar structure of these micro domains are obtained from SAXS experiments. Table 2.9 reports the long period distance *L* calculated from the q values at the maxima observed at room temperature, in which the three blocks are crystallized, and at 80 ºC, where only the PLLA crystals are present. At room temperature, two maxima are detected in both triblock terpolymers, associated to two average long periods in the sample, while only one maximum is observed for the $PEO_{23}PCL_{34}PLLA_{43}^{19.9}$ at 80 ºC. Further investigation is needed in order to explain the exact origin of the SAXS reflections.

At room temperature both terpolymers have very similar long period values, thus the increase on the PLLA block M_w does not significantly disturb the complex triple lamellar structure present in the terpolymers. However, when temperature is increased to 80 ºC, L increases, as a result of the melting of both PEO and PCL block lamellae. After melting, the amorphous layer thickness becomes wider. This result is clearer in the $PEO_{29}PCL_{42}PLLA_{29}^{16.1}$ triblock terpolymer.

Table 2.9. Long period values L of the $PEO_{29}PCL_{42}PLLA_{29}^{16.1}$ and $PEO_{23}PCL_{34}PLLA_{43}^{19.9}$ triblock terpolymers measured at room temperature and 80 ºC.

Sample	Temperature (ºC)			
	RT		80	
	q_{max} (A^{-1})	L (nm)	q_{max} (A^{-1})	L (nm)
$PEO_{29}PCL_{42}PLLA_{29}^{16.1}$	0.0379	16.6	0.0211	29.8
	0.0566	11.1	0.0350	17.9
$PEO_{23}PCL_{34}PLLA_{43}^{19.9}$	0.0369	17.0	0.0341	18.4
	0.0597	10.5	-	-

2.3.6 Lamellar morphology of the PEO-*b*-PCL-*b*-PLLA triblock terpolymer and PCL-*b*-PLLA diblock copolymer

The nanoscale trilayered morphology of the triple crystalline $PEO_{23}PCL_{34}PLLA_{43}^{19.9}$ triblock terpolymer is the subject of this study. In order to examine the lamellar structure in this terpolymer, and compare it to the analogous diblock copolymer, two thermal protocols were employed to crystallize the blocks in the samples.

In the first thermal protocol (T1) (see Figure 2.29a), the sample was cooled from the melt and then heated to 81 ºC, a temperature at which only the PLLA block can crystallize. During the first cooling scan the PLLA block do not crystallize but it improves its nucleus density. After 1h at 81 ºC, the sample was quenched until 25 ºC. During the subsequent quenching, the other block (for the diblock case, PCL) or blocks (PCL and PEO for the triblock case) crystallize under non-isothermal conditions. The second thermal protocol (T2) is described as follows (see Figure 2.29b): the PLLA block was first isothermally crystallized as in the first protocol. Then, the sample was quenched again until the PCL crystallization temperature, and the crystallization of the PCL block was carried out during one hour. Finally, the sample was quenched again until 25 ºC. During the last quenching, the PEO block might crystallize.

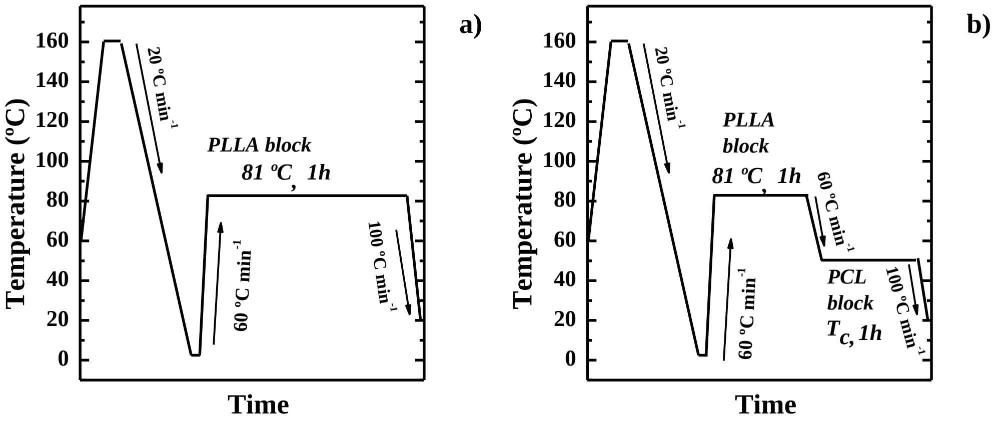

Figure 2.29 Thermals protocols: a) One step (T1) and b) Two steps (T2). The crystallization temperatures employed are reported in Table 2.3.

In Figure 2.30 is depicted the subsequent DSC heating scans of the samples, after the isothermal crystallization in one step (thermal protocol T1) and two steps (thermal protocol T2). In Table 2.10 are reported the thermal properties that correspond to the DSC scans. The PCL block melts at ~ 55 ºC. In the case of the triblock terpolymer, the PEO crystals melt in the same temperature range of the PCL block and for that reason, it is not possible to assign the PEO melting transition with certainty just from DSC. The melting of the PLLA block displayed a double peak (see Figure 2.30b). This double melting peak is a common observation for PLLA homopolymers [4, 127-129] and PLLA blocks in diblock copolymers [35, 40, 42, 49]. It has been ascribed to a reorganization into a more stable crystalline phase (α'/α transition) or to a melting-recrystallization phenomenon. This last one involves the partial melting of PLLA crystals, closely followed by a recrystallization process, and finally, the melting of the recrystallized crystals. In addition, the extension of the double melting peak in the terpolymer differs from the diblock copolymer. The enthalpy area ratio between the peaks is approximately 14 in the diblock copolymer, a value that is higher than the ratio observed in the terpolymer, which was around 4. When a polymer as PLLA is sensitive to undergo melting-recrystallization, cooling the sample at low rates aid the crystallization during cooling, and then less reorganization takes place during the subsequent heating. As result, the double melting peak tends to transform into one (see Figure 6.5 in Appendix). The third possible explanation for the double melting peak is the melting of two crystalline populations of different lamellar thickness. The nature of this double melting behavior will be elucidated later by simultaneous WAXS/SAXS analysis.

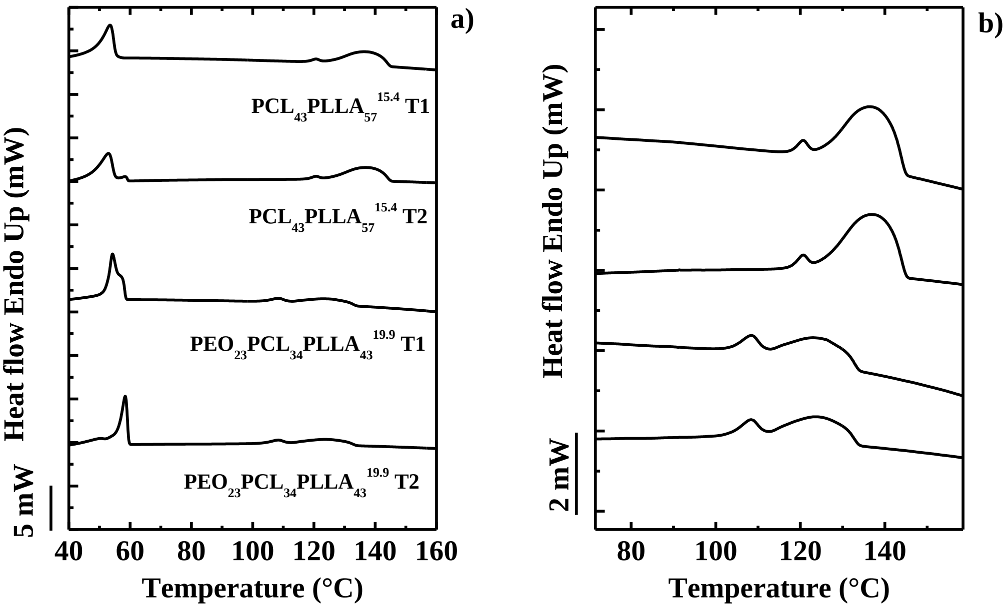

Figure 2.30 a) Subsequent DSC heating scans at 5 ºC min^{-1} after isothermal crystallization in one step (thermal protocol T1) two steps (thermal protocol T2). The crystallization temperatures employed are reported in Table 2.3. b) Zoom of the PLLA melting peak.

Table 2.10. Thermal properties of the samples obtained from DSC 2nd heating scan at 5 ºC min-1.

Sample	Crystallization protocol	T_m PCL (°C)	T_m PLLA (°C)	ΔH_m PCL (J/g)	χ_C PCL (%)	ΔH_m PLLA (J/g)	χ_C PLLA (%)
PCL$_{43}$PLLA$_{57}^{15.4}$	One step (T1)	53.5	120.8 137.3	46	33	36	38
	Two steps (T2)	52.9	120.8 137.7	48	35	34	36
PEO$_{23}$PCL$_{34}$PLLA$_{43}^{19.9}$	One step (T1)	54.3	114.1 124.7	44*	-	31	33
	Two steps (T2)	58.4	111.3 124.1	40*	-	28	30

*The enthalpy value might include the heat of fusion of the PEO block.

In the PEO-*b*-PCL-*b*-PLLA triblock terpolymer, the PLLA block forms spherulitic templates within which the other two blocks crystallized sequentially upon cooling from the melt. Mixed spherulitic superstructures are formed with alternating crystalline and amorphous regions. The interlamellar regions are composed of a mixture of PLLA, PCL and PEO chains in the amorphous state. The crystalline lamellae are composed of PLLA, PCL and PEO and initially one could assume that the lamellae are interdigitated and alternate between them.

To give evidences of this alternating lamellar structure at the nanoscale, the PEO$_{23}$PCL$_{34}$PLLA$_{43}^{19.9}$ triblock terpolymer and the analogous PCL$_{43}$PLLA$_{57}^{15.4}$ diblock copolymer were observed by atomic force microscopy (AFM). AFM phase micrographs corresponding to the PCL$_{43}$PLLA$_{57}^{15.4}$ diblock copolymer observed at 25 ºC, after the application of both protocols, are shown in Figure 2.31. Most of the lamellae observed are clearly edge on, a characteristic that allows approximate measurements of the average lamellar thickness.

A close observation of the microstructure in the AFM micrographs reveals alternated lamellae of different lamellar thickness (see color indications in Figure 2.31 shown as an example). After a large number of measurements, two different lamellar populations were detected by their clearly different sizes and the values of the average lamellar thickness are reported in Table 2.11. After both crystallization protocols (T1 and T2), the average lamellar thickness values were very similar, approximately 15 and 10 nm. Since the PLLA block was crystallized first, the thicker lamellae (red) should correspond to this block, while we hypothesized that the thinner one (green) correspond to the PCL block. In order to prove that both blocks were able to crystallize, WAXS measurements were performed at 25 ºC after completion of both thermal protocols.

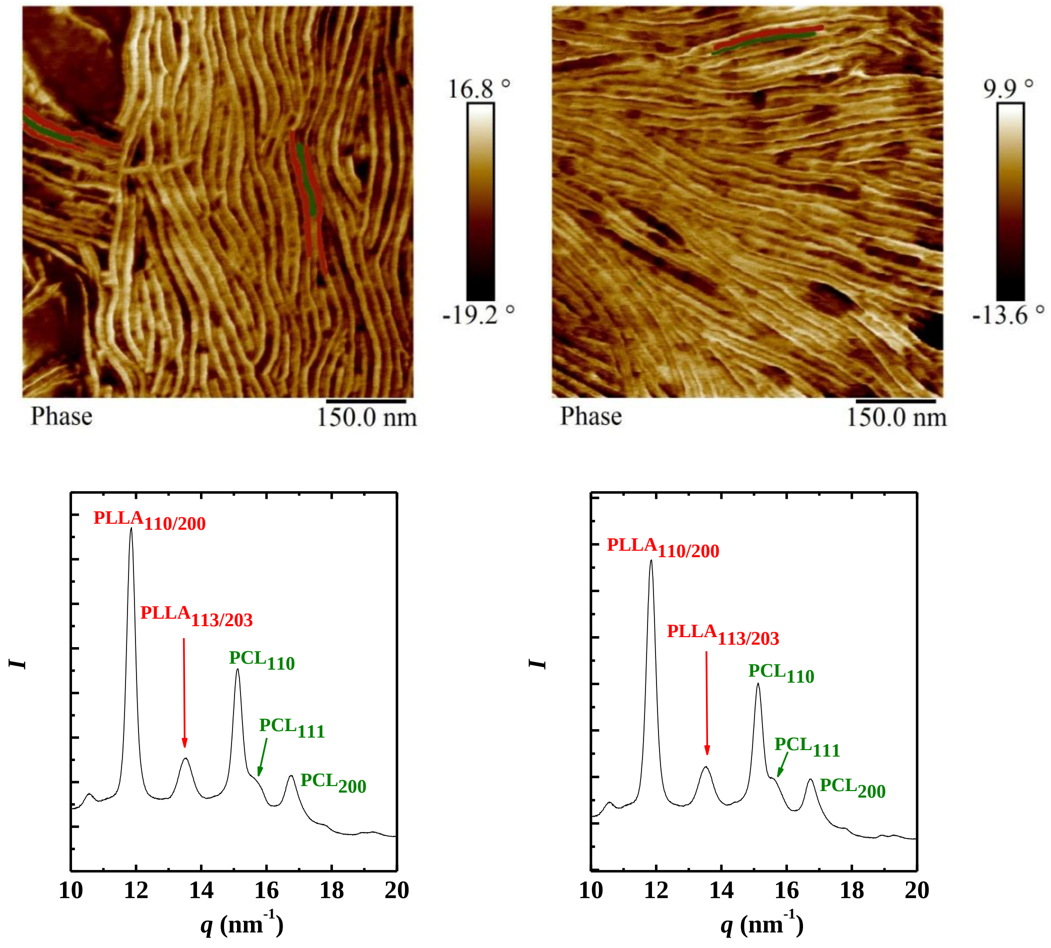

a) b)

Figure 2.31. AFM phase micrographs and WAXS patterns of $PCL_{43}PLLA_{57}^{15.4}$ observed at 25 ºC. Samples were quenched to 25 ºC after isothermal crystallization in a) one step at 81 ºC (thermal protocol T1) and b) two steps: first at 81 ºC and then at 50 ºC (thermal protocol T2).

Table 2.11. Lamellar thickness measured by AFM and long period values measured from SAXS at room temperature.

Sample	Crystallization protocol	Lamellar thickness (AFM) (nm)			Distance between lamellar centers (AFM) (nm)		Long period (SAXS) (nm)	
$PCL_{43}PLLA_{57}^{15.4}$	One step (T1)	15.2 +/- 0.9	10.0 +/- 0.6	-	22.9 +/- 1.9	-	19.9	10.8
	Two steps (T2)	14.5 +/- 0.9	9.0 +/- 0.6	-	22.1 +/- 1.9	-	20.0	11.5
$PEO_{23}PCL_{34}PLLA_{43}^{19.9}$	One step (T1)	15.2 +/- 0.9	9.7 +/- 1.0	-	26.4 +/- 3.1	-	25.3	-
	Two steps (T2)	15.3 +/- 0.9	10.7 +/- 1.0	6.9 +/- 0.8	28.2 +/- 3.3	12.6 +/- 1.8	24.5	12.9

The WAXS patterns included in Figure 2.31 confirmed the presence of both PLLA and PCL crystalline phases after crystallizing the sample in one or two steps. Therefore, the thinner lamellae are most probably PCL block crystals and the morphology consists of PLLA and PCL alternate lamellae with an amorphous mixed layer in between them. Interestingly, the lamellar thickness values were similar regardless the crystallization protocol employed. Since the PLLA block was first crystallized at the same temperature in both protocols, similar lamellar thickness is expected (in this case ～15 nm). However, quenching the sample after PLLA crystallization or isothermally crystallizing the PCL block in a subsequent step did not affect the thickness of the PCL lamellae. Thicker PCL lamellae would be expected as a result of the PCL isothermal crystallization at 49.5 ºC . The similar PCL thickness values might obey to the regular confinement imposed by the PLLA crystals and the inherent fast crystallization kinetics of PCL.

The lamellar structure of PCL-*b*-PLLA diblock copolymers have been observed before by transmission electron microscopy (TEM). However, to our knowledge, AFM observations of these diblock copolymers crystallized from melt (melt-crystallization) have not been reported. A publication from Ho et al.[51] reported melt crystallized and and epitaxially grown crystals observed by TEM. Different subtracts were compared and the samples were crystallized at different temperatures. In those temperatures in which only the PLLA block can crystallize (upon cooling from melt), the authors reported a branching crystalline lamellae composed of PLLA block. Epitaxial crystallization on different subtracts induced a flat-on crystalline morphology of PLLA. However, the authors neglected the crystallinity of PCL block generated at room temperature and considered it trivial. Thus, unlike the double-crystalline alternated lamellar morphology observed by us by AFM, the authors reported a phase separated lamellar structure composed of a flat-on PLLA crystalline layer alternated with an amorphous layer of PLLA and PCL chains. In addition to Ho et al.[51] publication, single crystals grown from solution observed by TEM were reported by Casas et al.[48]. The PLLA block developed large crystals with truncated lozenge shape. After the subsequent crystallization of the PCL block, small and fringed PCL crystals grew over or close to the PLLA lamellae when the crystallization temperature of the PLLA block was high. Complex morphologies were developed depending on the crystallization temperature.

Since the PCL-*b*-PLLA diblock copolymers are able to self-assemble in an alternated ordered crystalline structure, we expected that the addition of a third miscible crystalline block might follow the same trend.

A remarkable view of the triple crystalline nature of the PEO-*b*-PCL-*b*-PLLA triblock terpolymers is given in the AFM micrographs shown in Figure 2.32. In this case, some of the lamellae exhibit a certain degree of tilt (see Figure 4b), i.e., they are not perfectly flat on. To our knowledge, this is the first time a lamellar trilayered structure in a triblock terpolymer is observed by AFM, after melt crystallization. The triblock terpolymer exhibited a wide range of lamellar thicknesses. It was possible to measure three populations of different lamellar thickness (signaled with colors and arrows in Figure 2.32).

The lamellar thickness values of the $PEO_{23}PCL_{34}PLLA_{43}^{19.9}$ triblock terpolymer exhibited in Figure 2.32 are reported in Table 2.11. As in the diblock copolymer, the thicker lamellae were approximately 15 nm. This value is as expected since the molecular weight of the PLLA block in the terpolymer is similar to that in the diblock copolymer; and also, because both samples were first crystallized at the same temperature (81 ºC) and during the same time in both crystallization protocols. Therefore, the 15 nm lamellae in the terpolymer should also correspond to the PLLA block crystals.

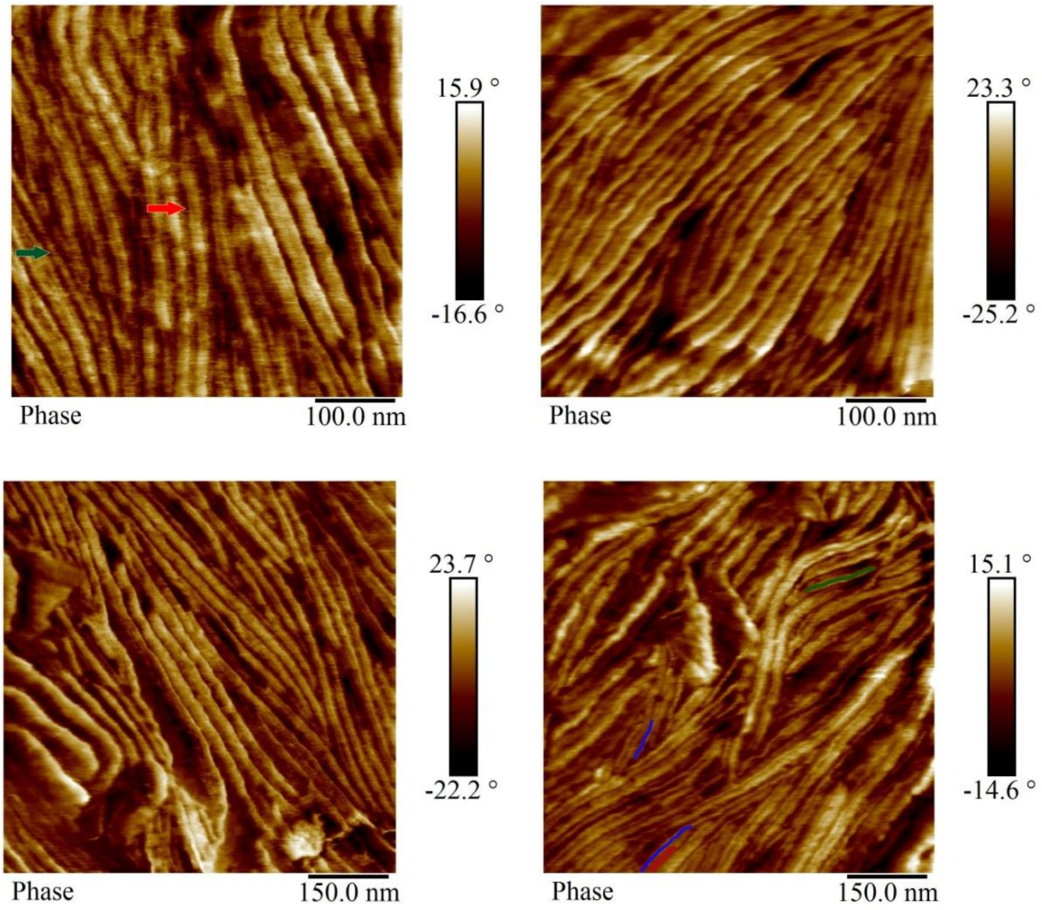

a) b)

Figure 2.32. AFM phase micrographs of $PEO_{23}PCL_{34}PLLA_{43}^{19.9}$ observed at 25 ºC. Samples were quenched to 25 ºC after isothermal crystallization in a) one step at 81 ºC (thermal protocol T1) and b) two steps: first at 81 ºC and then at 50 ºC (thermal protocol T2).

Interestingly, one or two more populations of different lamellar thickness were discriminated after exhaustive measurements. Regardless of the crystallization protocol employed, the second lamellar thickness was around 10 nm, a similar value to that observed in the diblock copolymer for PCL. Since the PCL block had similar molecular weight in both the terpolymer and the diblock copolymer, this result was also expected.

Comparing the two samples crystallized in two steps (thermal protocol T2), the second lamellar thickness of the terpolymer was very close to that of the diblock copolymer because the crystallization temperature in the second step was also very similar (50 ºC). However, an even smaller lamellar thickness was measured in the terpolymer crystallized in two steps (thermal protocol T2) (see Table 2.11 and Figure

2.32b). This third population of lamellae had an average lamellar thickness of ~ 7 nm. Therefore, we hypothesized that the 10 nm and the 7 nm lamellae might correspond to the PCL and PEO lamellae.

When the sample was crystallized in one step (thermal protocol T1), both the PEO and PCL blocks may crystallize simultaneously, during the subsequent quenching after PLLA crystallization. But it is possible that the rapid cooling did not allow the crystallization of the PEO block or did not allow well developed PCL and PEO crystals that could be differentiated from each other. However, in the two steps crystallization protocol (T2) the sample was isothermally crystallized in a second step at 50 ºC, a temperature high enough for the PCL block to crystallize on its own, as the PEO block cannot crystallize. Therefore, well-develop PCL crystals were formed during the isothermal step, and smaller PEO lamellae crystallized during the final subsequent quenching.

In order to prove this hypothesis, a WAXS pattern was taken at 25 ºC, after the two steps (thermal protocol T2) crystallization of the terpolymer. The reflections pointed out in Figure 2.33a confirmed the presence of both PLLA and PCL crystals. However, the $PLLA_{113/203}$ peak coincides with the PEO_{120} reflection. Therefore, it cannot be assured a priori that the PEO block crystallized during the quenching to room temperature. In order to answer this question, the two steps (thermal protocol T2) crystallized diblock copolymer and terpolymer were heated while simultaneous SAXS/WAXS patterns were taken (See Figure 6.6 and 6.7 in Appendix). The intensity ratio between $PLLA_{113/203}$ and $PLLA_{110/200}$ WAXS signals of the $PCL_{43}PLLA_{57}^{15.4}$ diblock copolymer was measured and compared to that of the $PLLA_{113/203}$+PEO_{120} and $PLLA_{110/200}$ signals of the $PEO_{23}PCL_{34}PLLA_{43}^{19.9}$ terpolymer (See Figure 6.8 for the triblock terpolymer in Appendix). The intensity ratio values plotted against temperature are depicted in Figure 2.33b.

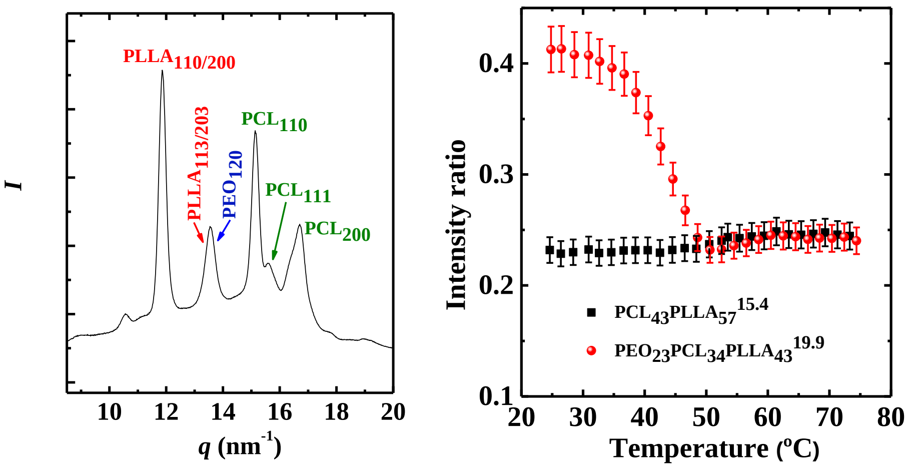

a) b)

Figure 2.33. a) WAXS patterns of $PEO_{23}PCL_{34}PLLA_{43}^{19.9}$ taken at 25 ºC, after isothermally crystallizing the sample in two steps: first at 81 ºC and then at 49.5 ºC (thermal protocol T2). b) Intensity ratio between WAXS signals $PLLA_{113/203}$ and $PLLA_{110/200}$ of $PCL_{43}PLLA_{57}^{15.4}$, and ($PLLA_{113/203}$+PEO_{120}) and $PLLA_{110/200}$ of $PEO_{23}PCL_{34}PLLA_{43}^{19.9}$ during heating after crystallizing the samples in two steps (thermal protocol T2).

If the PEO block in the terpolymer crystallized during the final quenching of the two steps crsytallization protocol (T2), the PEO_{120} crystalline phase reflection would add to the intensity measured at 13.54 nm^{-1} for the $PLLA_{113/203}$ reflection. Figure 2.33b shows that the intensity ratio of the diblock copolymer was almost constant between 25 and 75 ºC, a temperature range in which the PLLA phase remains crystalline. However, the intensity ratio of the terpolymer at 25 ºC is almost twice the value of the diblock copolymer. This confirms the presence of a PEO crystalline phase in the terpolymer. In fact, as the temperature increases, the intensity ratio is reduced until it matches the intensity ratio of the diblock copolymer, at around 50 ºC. The PEO block in the terpolymer melts at 45 ºC, as measured by DSC at 20 ºC min^{-1}[117]. Therefore, the WAXS measurements clearly proved the unique trilamellar structure observed in Figure 2.32b. The three lamellar populations, whose thicknesses are reported in Table 2.11, should correspond to each crystalline phase, most probably, the 15 nm thickness to the PLLA, the 10 nm thickness to the PCL and the 7 nm thickness to the PEO crystalline phases.

As aforementioned, simultaneous SAXS/WAXS measurements were performed for the two steps (thermal protocol T2) crystallized samples during subsequent heating. SAXS/WAXS measurements were also carried out in the one step crystallized samples (thermal protocol T1) and similar behavior was observed (results not shown).

The evolution of the Lorentz corrected SAXS peaks with temperature is shown in Figure 2.34a for the $PCL_{43}PLLA_{57}^{15.4}$ diblock copolymer and in Figure 2.35a for the $PEO_{23}PCL_{34}PLLA_{43}^{19.9}$ triblock terpolymer. The product between the intensity and the square of the scattering vector *q* was plotted versus *q*.

At 25 ºC, the diblock copolymer exhibits two SAXS peaks at $q = 0.31$ and 0.55 nm^{-1}. The long period value of the first scattering peak (20.0 nm) agrees well with the distance from the center of one lamella to the center of the adjacent one, according to AFM micrographs (see 22.1 nm in Table 2.11). At 25 ºC, it was demonstrated by AFM that lamellae of PLLA and PCL crystals alternated to form a large order superstructure in the diblock copolymer. Thus, the observation of two long period values represents the arrangement of the two crystalline sequences of PCL and PLLA blocks.

As the temperature reaches 60 ºC, and PCL crystals melt, the intensity of the first peak increased markedly and the high-*q* peak vanished (see Figure 2.34a and b). The general feature of the SAXS profiles corresponds to a lamellar structure consisting of PLLA lamellae and mixed amorphous layers containing amorphous PLLA and molten PCL chains. The intensity increase of the low-*q* peak at 57 ºC (see black arrow in Figure 2.34a) was attributed to an increment of the electron density difference of the two blocks when PCL was molten. A similar phenomenon has been reported previously in PEO-*b*-PLLA diblock copolymers [33, 104]. A detailed analysis of the SAXS data is carried out below.

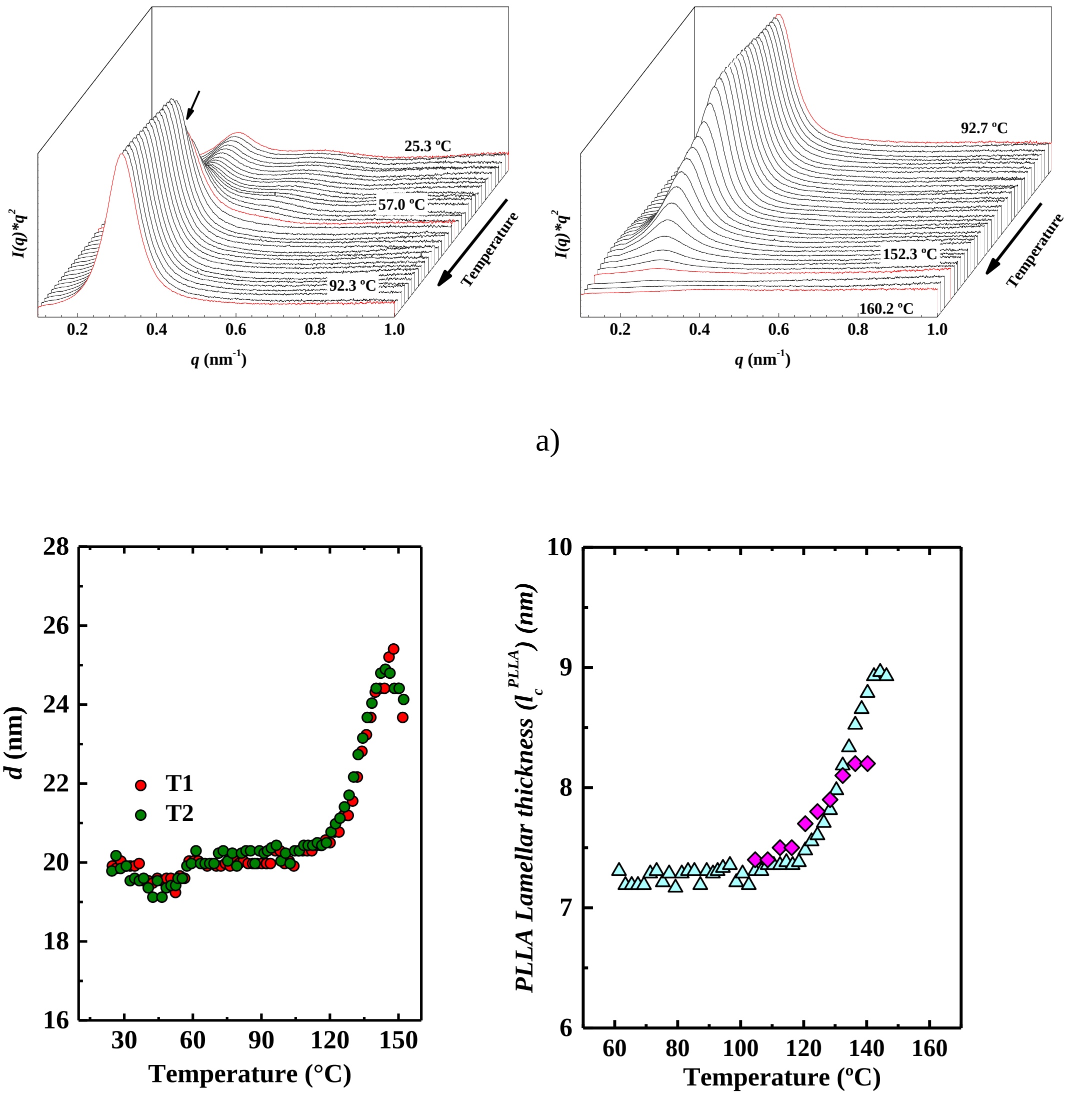

a)

b)

c)

Figure 2.34 a) Lorentz corrected SAXS patterns during heating of $PCL_{43}PLLA_{57}^{15.4}$, after isothermally crystallizing the sample in two steps: first at 81 ºC and then at 49.5 ºC (thermal protocol T2). b) Evolution of the long period values calculated from SAXS measurements during heating, after isothermally crystallizing the sample in one step at 81 ºC (thermal protocol T1) and two steps: first at 81 ºC and then at 49.5 ºC (thermal protocol T2). c) Evolution of the PLLA lamellar thickness during heating, after isothermally crystallizing the sample in two steps: first at 81 ºC and then at 49.5 ºC (thermal protocol T2). Estimation using DSC crystallinity (triangles). Estimation using one dimensional electron density correlation function (rhombs).

From 60 ºC and beyond, the observed lamellar structure corresponded to PLLA crystalline lamellae alternated with a mixed PCL+PLLA amorphous phase inside the interlamellar domains. The lamellar structure parameters of $PCL_{43}PLLA_{57}^{15.4}$ were calculated at 65 ºC and the data is summarized in Table 2.12. Since, only PLLA crystals remained at these temperatures, the long period value (d) can be exclusively related to the lamellar thickness of the PLLA lamellae (l_c^{PLLA}), employing the relation $l = d\ \chi_v$ (being χ_v the volumetric crystalline fraction) [136]. The χ_v value can be approximated to the χ_m (mass crystalline fraction) and can be measured from DSC as follows:

$$\chi_m = \frac{\Delta H_m}{\Delta H_m^{100\%}} \qquad \text{Eq. 2-12}$$

where ΔH_m is the melting enthalpy of the PLLA block normalized by block composition and $\Delta H_m^{100\%}$ is the melting enthalpy of 100 % crystalline PLLA. Even though several $\Delta H_m^{100\%}$ values have been published for PLLA [40, 137], the value of 93.6 J/g have been the most accepted one [46, 49, 75, 138], and thus, it was employed here.

From a DSC heating scan in a sample crystallized under the same conditions, the PLLA χ_m was measured as 36 %. At 65 ºC, the as calculated PLLA lamellar thickness was ~ 7.3 nm (see Figure 2.34c and Table 2.12). This value agrees well with the electron density correlation analysis (Figure 6c), as the system can be described as a two-phase system (see Figure 6.9 in the Appendix). However, this value is very far from the ~ 15 nm value measured in the AFM micrographs (see Figure 2.31b and Table 2.11).

The poor quantitative correspondence between the AFM and DSC/SAXS measurements might obey errors involved in the values obtained by AFM. SAXS is a well-established and very precise technique that allows measuring large range order in a bulk sample (it averages the characteristic scattering of the irradiated sample volume). On the contrary, AFM is a surface characterization technique that scans a definite area of the sample surface, and therefore, it is more sensitive to errors in measurements of the lamellar thickness. Zhou et al.[136] and Trifonova et al.[139] discussed the limitations of the AFM technique. Measuring the lamellar thickness by AFM requires that the lamellae grow strictly edge-on and not tilted to the sample surface. Despite that, lamellar thickness measured from the edge-on view might be slightly overestimated due to tip-sample interactions and tip-imaging artifacts. Depending on the tip shape, some features of the surface (such as the amorphous regions) cannot be properly scanned [139]. Zhou et al.[136] reported that better agreement is observed in lamellar thickness measurements performed by SAXS and TEM rather than by SAXS and AFM. The authors reported that the values from AFM seem to be larger than the values from SAXS and TEM. In our case, the 7.3 nm PLLA lamellae thickness is more reliable. Nevertheless, AFM images directly show the alternating feature of the lamellar morphology.

Having measured the PLLA lamellar thickness and the long spacing of the lamellar structure, it was interesting to determine whether the PLLA and PCL block crystallized in a folded or extended chain conformation. The length of the extended chain (L) in both blocks was estimated by the following equation:

$$L = \frac{M_w^{block}}{N^{RU} M_w^{RU}} c \qquad \text{Eq. 2-13}$$

where M_w^{block} is the molecular weight of the block, M_w^{RU} is the molecular weight of the repetitive unit, c is length of the chain axis and N^{RU} is the number of repetitive units within the c dimension. The PLLA crystal structure includes 10 repetitive units in the c dimension while the PCL crystal structure includes 2. The c dimensions reported for α-form PLLA and PCL are 2.880 [140] and 1.705 [141] nm, respectively. After calculations, the lengths of the PLLA and PCL extended chain were 35.3 and 49.2 nm, respectively (see Table 2.12). These L_{ext} values indicated that both blocks crystallized in a chain-folded conformation, since the lamellar thicknesses measured by AFM at 25 ºC (~ 15 nm for PLLA, ~ 10 nm for PCL) and SAXS at 65 ºC (~ 7.3 nm for PLLA) were considerably smaller. A chain folding number (N_F^{PLLA}) equal to 3 was calculated for the PLLA block employing the following equation [32, 104]:

$$N_F^{PLLA} = \frac{L_{ext}^{PLLA}}{l_c^{PLLA}} - 1 \qquad \text{Eq. 2-14}$$

where l_c^{PLLA} is the PLLA crystalline lamellar thickness calculated from SAXS and DSC crystalline fraction and L_{ext}^{PLLA} is the chain extended length of the PLLA block. The number of folds can be calculated with certainty only for the PLLA block. The lamellar thicknesses of only the PCL lamellae cannot be calculated from SAXS measurements, since the scattering observed correspond to the arrangement of the two crystalline sequences of PCL and PLLA. Following an alternating lamellar model (see Figure 6.9 in Appendix), the thickness of the mixed (PLLA+PCL) amorphous layer (l_a) can be calculated as it follows [32, 104]:

$$l_a = d - l_c^{PLLA} \qquad \text{Eq. 2-15}$$

The data calculated is resumed in Table 2.12.

Table 2.12. Lamellar structure parameters of PCL$_{43}$PLLA$_{57}^{15.4}$ and PEO$_{23}$PCL$_{34}$PLLA$_{43}^{19.9}$ at 65 ºC

Dimension (nm)	PCL$_{43}$PLLA$_{57}^{15.4}$	PEO$_{23}$PCL$_{34}$PLLA$_{43}^{19.9}$
SAXS Long period (d)	20.3	27.5
PLLA crystalline lamellar thickness (l_c^{PLLA})	7.3	8.3
PLLA Chain extended length (L_{ext}^{PLLA})	35.3	34.1
PCL Chain extended length (L_{ext}^{PCL})	49.2	50.7
PEO Chain extended length (L_{ext}^{PEO})	-	18.8
PLLA Chain folding number (N_F)	3	3
PLLA+PCL or PLLA+PCL+PEO amorphous layer thickness (l_a) ($l_a^{PLLA+PCL}$ or $l_a^{PLLA+PCL+PEO}$)	13.0	19.2

The evolution of the as calculated PLLA lamellar thickness with temperature is depicted in Figure 2.34c. The long period remained constant until approximately 120 ºC, after which it increases with temperature. Close to its melting transition, several reorganization phenomena might be taking place. For instance, α'/α crystal transition [130, 142-146] and melt-recrystallization processes have been reported for PLLA [4, 127-129]. In order to elucidate the reason behind the increase in long period, detailed analysis of the corresponding WAXS profiles (See Figure 6.6 in Appendix) taken during heating was performed. All reflections observed corresponded only to the α-form of PLLA. No signals were detected for the α'-form. In addition, the $d_{110/200}$ interplanar distance of the 110/200 distinctive planes of PLLA was measured and plotted against temperature (see Figure 6.10 in Appendix). When α'/α transition occurs, a reduction in the $d_{110/200}$ is observed around 100-120 ºC because the α'-crystals have lower packaging density than α-crystals. In Figure 6.10 in Appendix the $d_{110/200}$

interplanar distance increases steadily and no change was observed at the beginning of PLLA melting. Moreover, the PLLA crystal unit cell dimensions (*a*, *b*, and *c*) were determined at 25, 60, 100 and 120 ºC. No decrease was observed in the lattice dimensions that can be attributed to a change into a more densely packed crystalline structure (see Table 6.2 in Appendix).

The WAXS evidence discussed above conclusively shows that only α-crystals were formed during the isothermal crystallization of the PLLA block within $PCL_{43}PLLA_{57}^{15.4}$ at 81 ºC. It has been reported that PLLA homopolymer forms α'-crystals when it is isothermally crystallized at temperatures below 100 ºC [130, 142-146]. However, the molecular weight of the PLLA block in the diblock copolymer and triblock terpolymer is very low, and because of that a reduced melting temperature at 122 ºC was observed, which is much smaller than the typical $\sim$160 ºC melting temperature of high molecular weight PLLA. Therefore, it is plausible that the PLLA block can form α-crystals at 81 ºC, as the degree of supercooling changes with molecular weight.

The other hypothesis to explain the behavior shown in Figure 6c is the melt-recrystallization phenomenon of the PLLA crystals described before. As depicted in Figure 2.30 and Table 2.10 the $PCL_{43}PLLA_{57}^{15.4}$ sample exhibited a double melting peak at 120.8 and 137.7 ºC. A partial melting of the crystals, closely followed by a subsequent crystallization can take place. This process would contribute to enhance the lamellar thickness near the fusion, and therefore an increase in the long period value would be observed (see Figure 2.34b). To confirm that, an estimation of the lamellar thickness through a one dimensional electron density correlation function (see Figure 6.11 in Appendix) was calculated (rhomb symbols in Figure 2.34c) and compared to the lamellar thickness values estimated by SAXS and DSC crystalline fraction ($l = d\,\chi_c$) (Figure 2.34c). The two calculated data sets for l values overlap in the temperature range evaluated. Therefore, the increase in the long period value beyond 100 ºC, might obey to a thickening process of the lamellae during heating. In addition, the average spacing becomes larger after further increasing the temperature because some of the lamellae are molten.

In the case of the $PEO_{23}PCL_{34}PLLA_{43}^{19.9}$ triblock terpolymer a similar lamellar structure was observed. As in the diblock copolymer, two peaks were observed at 25 ºC, and the second one could not be ascribed to a second order reflection (see green arrows Figure 2.35a). The values of q were 0.26 and 0.49 nm^{-1} (the q ratio was 1.88) and the high-q peak has higher intensity than the low-q peak, which is not usual and indicates a more complex superstructure. Thus, two *characteristic lengths* of 24.5 and 12.9 nm were measured. More analysis is provided in a later section. The first value (24.5 nm) agreed well with the distance from the center of one lamella to the center of the adjacent one measured in the AFM micrographs (see Table 2.11). However, in the triblock terpolymer the alternating lamellar structure was less clear, since lamellae of the three blocks co-exist. Therefore, the long periods observed are an average of the crystalline layers present but they cannot be assigned with certainty to one or the other block. We might speculate that the larger domain spacing should correspond to the PLLA block that crystallized first.

Unlike the diblock copolymer, two transitions occurred at around 50 and 60 ºC (see black arrows in Figure 2.35a) during the subsequent heating scan of the terpolymer. Also, the intensity of the first SAXS peak greatly increased and a small increment in the long period values (d) was observed (see Figure 2.35a and b). These transitions corresponded to the sequential melting of PEO block first and the PCL block later. After 60 ºC, only PLLA block crystalline lamellae remained with interlamellar regions composed of mixed PLLA+PCL+PEO amorphous phase. A shoulder appeared in the first SAXS peak that was not observed for the diblock copolymer (see blue arrows in Figure 2.35a and compare to Figure 2.34a). Since, the q position of this shoulder deviates significantly from $2q_{max}$ of the first SAXS peak (q ratio of 1.63), it should not be a second order peak. In the case of the terpolymer, we can only attribute this feature to the existence of two populations of crystalline lamellae of PLLA with different lamellar thickness after PEO/PCL melting. Finally, an increment in the long period values and PLLA crystalline lamellar thickness took place at around 120 ºC, similar to what it was observed in the analogous diblock copolymer (see Figure 2.35b and c).

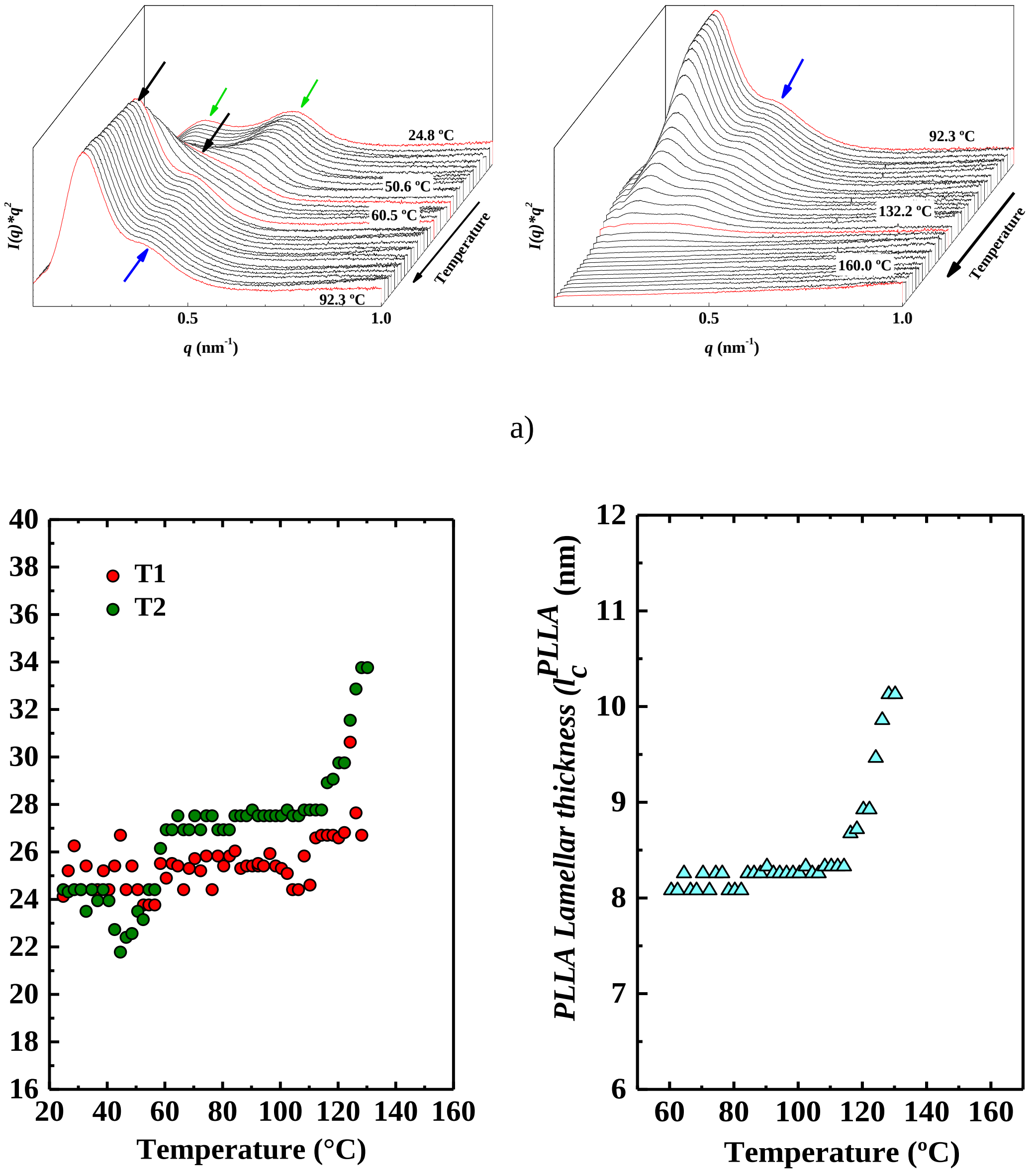

a)

b)

c)

Figure 2.35 a) Lorentz corrected SAXS patterns during heating of PEO$_{23}$PCL$_{34}$PLLA$_{43}^{19.9}$, after isothermally crystallizing the sample in two steps: first at 81 ºC and then at 50 ºC (thermal protocol T2). b) Evolution of the long period values calculated from SAXS measurements during heating, after isothermally crystallizing PEO$_{23}$PCL$_{34}$PLLA$_{43}^{19.9}$ at 81 ºC (T1), and at 81ºC and then 50 ºC (T2). c) Evolution of the PLLA lamellar thickness during heating, after isothermally crystallizing the sample in two steps: first at 81 ºC and then at 50 ºC (thermal protocol T2).

As aforementioned, the nature of the two PLLA melting peaks showed in the DSC curves in Figure 2.30 is related with the evolution of the PLLA structure and the process taking place during heating. PLLA is characterized by a crystal reorganization phenomenon on heating that makes more complex to elucidate the behavior observed by SAXS. The SAXS peaks of the terpolymer exhibit a high-*q* shoulder after PCL/PEO melting that can be a hint of the presence of PLLA lamellae of lower lamellar thickness. These crystals might have been formed in a secondary crystallization process inside the interspherulitic regions, after the impingement of the PLLA spherulites. If it is so, these less stable PLLA crystals will melt first and the second peak should correspond to the melting of PLLA crystals formed during the isothermal step. This could be a reasonable explanation since the enthalpy ratio between the second at the first peak is 4, which might indicates that the content of these less thick crystals is much lower, as they were formed in a secondary process. However, the diblock copolymer does not exhibit a high-*q* shoulder in the SAXS patterns (see Figure 2.34a). Therefore, a second population of PLLA lamellar thickness cannot be assumed at first, even though the DSC curves also show a double melting peak (see Figure 2.30). Although, in the diblock copolymer, the enthalpy ratio is even higher (~ 14), which might indicate that if less thicker crystals are present, their content is even lower and they might not scatter in SAXS. Moreover, melting-recrystallization cannot be dismissed as an additional explanation behind the double melting peak observed in the DSC curves since a thickening of the PLLA lamellae during melting was also estimated. Therefore, both aspects, two lamellar thickness and melting-recrystallization, might be involved in the behavior observed. The reason behind the formation of two lamellar populations requires deeper analysis. In any case, the presence of PLLA lamellae of less lamellar thickness in the terpolymer should be very difficult to observe by AFM because their content should be very low. Therefore, we remain confident that the layered structure observed and measured in Figure 2.32b corresponds to crystalline phases of the three PLLA, PCL and PEO blocks.

Table 2.12 presents the calculated lamellar structure parameters of $PEO_{23}PCL_{34}PLLA_{43}^{19.9}$ at 65 ºC. The PLLA crystalline lamellar thickness was calculated as in the diblock copolymer employing a PLLA χ_m of 30 % (measured by DSC). To calculate the chain extended length of the PEO block in the terpolymer, the PEO crystal structure was taken into account. It has a *c* dimension of 1.948 nm and this dimension includes 7 repetitive units [147].

At 65 ºC, the PLLA crystalline lamellar thickness in the triblock terpolymer was ~ 8.3 nm (see Figure 2.35c and Table 2.12). A value that is similar to the 7.3 nm of the same block in the diblock copolymer. Also, a three-fold chain conformation was estimated for the PLLA block. In addition, the other two PEO and PCL blocks should have also crystallized in a multi-folded conformation, considering the length of the extended chain (see Table 2.12) and the lamellar thickness measured by both AFM and SAXS (see Table 2.11). Similar values of PLLA crystalline lamellar thickness have been reported by Xue et al. [33] in symmetric PLLA-*b*-PEO diblock copolymers. Since the PLLA block in the terpolymer and the diblock copolymer had almost the same molecular weight and the PLLA crystallization temperature was equal in for both samples (81 ºC), a similar lamellar thickness was expected. Also, the size of the mixed amorphous domain (l_a was bigger in the terpolymer than in the diblock copolymer because of the higher concentration of PEO+PCL molten chains at 65 ºC.

After PLLA block crystallization, the crystallization of the constituent blocks occurs inside the mixed amorphous domains. In case of the diblock copolymer, the alternating structure of the PLLA and PCL blocks lamellae can be proposed and demonstrated experimentally by DSC/SAXS/WAXS during melting, as shown above. However, elucidating the alternating lamellar structure within the triblock terpolymer is more complex. After PLLA block crystallization, the mixed amorphous domain contains both PCL and PEO chains. The exact structure of the tri-lamellar packing after these two blocks crystallize in the intervening spaces between PLLA lamellae is very difficult to ascertain. Therefore, we have employed one-dimensional structural models in order to elucidate this complex tri-lamellar self-assembly.

2.3.7 Simulation of SAXS curves

The double crystalline and triple crystalline polymers shown above show complex features in their SAXS curves that are not straightforward to understand in terms of lamellar packing structures. Therefore, the SAXS curves have been simulated to test different structural models. Since both the diblock copolymer and the triblock terpolymer are miscible in the melt, the contribution of microphase separation can be ignored. The whole system can be simplified to be a one-dimensional problem, similar to the case of semicrystalline homopolymers. Thus, it is easy to generate one-dimensional density profiles $\rho(x)$ according to the proposed microstructural models.

According to scattering theory, the intensity $I(q)$ can be calculated numerically from the absolute square of the Fourier transform of the scattering density [148],

$$I(q) = \left| FT[\rho(x)] \right|^2 \qquad \text{Eq. 2-16}$$

Starting from the easier case of the $PCL_{43}PLLA_{57}^{15.4}$ diblock copolymer, it is known that at temperatures above the melting temperature of PCL, the material should have a similar microstructure as the typical semicrystalline homopolymers (two-phase model: one crystalline and one amorphous phase). We assume the crystalline lamellar densities for PLLA and PCL as 1.297 g/cm^3 [149] and 1.146 g/cm^3 respectively [150]. The amorphous phase contains both amorphous PLLA and amorphous PCL chains, we assume the lowest value of the PCL amorphous density as 1.081 g/cm^3 [151]. The average value of the lamellar thickness and long period of PLLA was taken as 7.3 nm and 19.9 nm, respectively, according to the above analysis of the SAXS data. The periodic lamellar structure is described by a paracrystalline lattice, as proposed by Hosemann [152]. In a paracrystalline lattice, the second type of distortions are considered, meaning that the position of a lattice point only depends on the next neighbor position. This results both in lower intensities and a broadening of higher order peaks in SAXS [153]. The lamellar thickness and long period were assumed to have a Gaussian distribution:

$$f(x) = \frac{1}{\sqrt{2\pi\sigma^2}} e^{-\frac{(x-\mu)^2}{2\sigma^2}} \qquad \text{Eq. 2-17}$$

Figure 2.36a presents a density distribution profile assuming a standard deviation for PLLA lamellar thickness of σ = 1.5 nm and one for the long period of σ = 4.0 nm. In this two-phase model, only crystalline PLLA lamellae and interlamellar amorphous layers (constituted by PLLA and PCL mixed amorphous chains) are represented at high temperatures, where PCL is in the melt. For the $PCL_{43}PLLA_{57}^{15.4}$ at lower temperatures when PCL is crystalline, we insert PCL crystalline layers in between the amorphous layers (formed by amorphous PCL and PLLA chains). Figure 2.36b shows an example where the thickness of PCL crystalline layer is fixed at 6.0 nm.

Figure 2.36c shows the calculated Lorentz-corrected intensity curves of the density profiles of the cases represented in Figure 2.36a and b. Compared with the experimental SAXS curves in Figure 2.36d, it is clear that the salient features are essentially reproduced, i.e., when PCL is crystalline the low-q peak is weaker and the high-q peak is stronger. Therefore, the high-*q* peak mainly comes from the correlation of the PCL and PLLA crystalline layers.

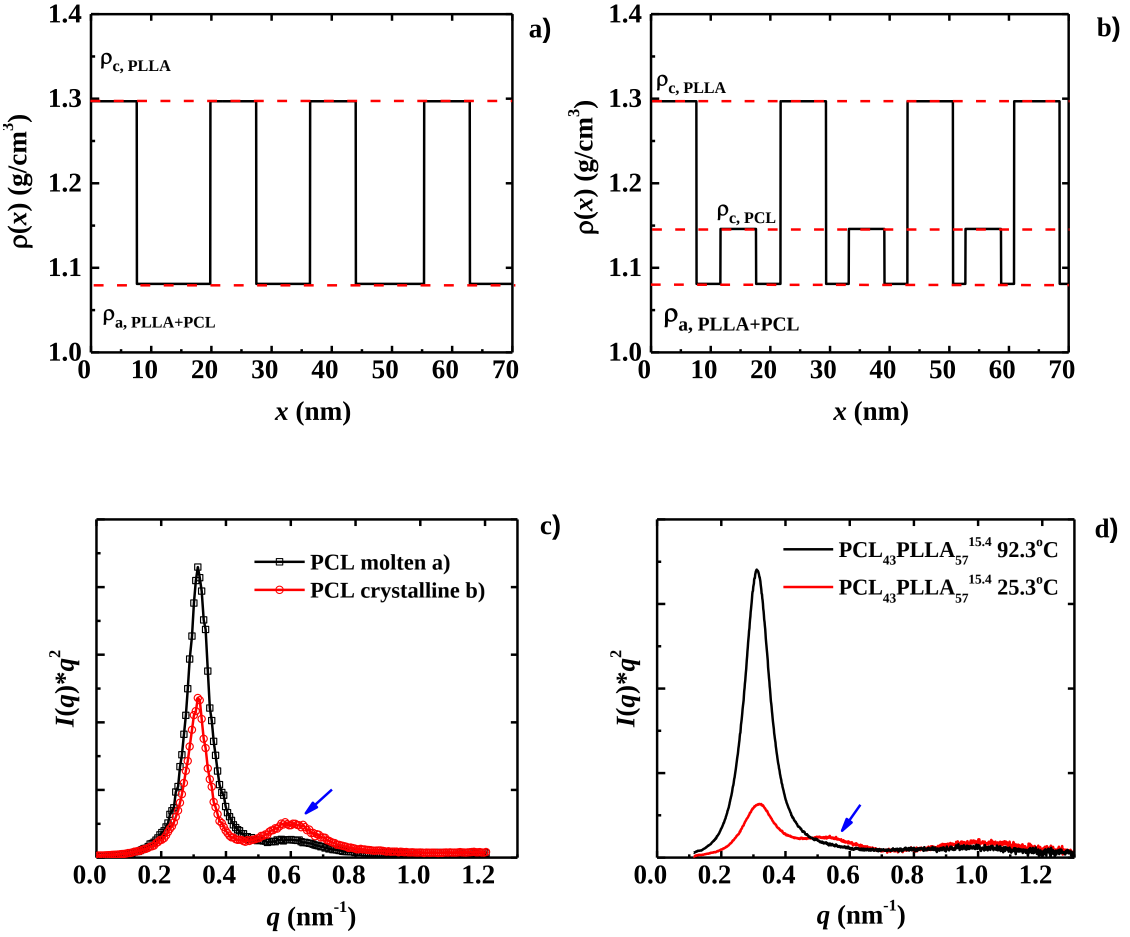

Figure 2.36 a) One-dimensional density profile in a two-phase model, corresponding to the diblock copolymer with molten PCL. b) One dimensional density profile in a three-phase model, corresponding to the diblock copolymer with crystalline PCL. c) Simulated SAXS curves of the density profiles of a) corresponding to molten PCL and b) corresponding to crystalline PCL. d) Experimental SAXS data at 25.3°C and 92.3°C (protocol T2).

The $PEO_{23}PCL_{34}PLLA_{43}^{19.9}$ triblock terpolymer has a more complicated microstructure. It is interesting to test different structural models by comparing simulated SAXS curves with experimental ones. Again, we start with the easiest situation at higher temperatures, where only PLLA is crystalline. Just as we pointed out in the above sections, we have to assume two populations of long period and lamellar thickness of PLLA because the high-q peak deviates significantly from a value equal to twice the low-*q* peak (*q*-ratio is 1.63, above 60ºC). Similar to the diblock copolymers, we assumed a Gaussian distribution of the lamellar thickness and long period of PLLA. The thicker layer is assumed to have a long period of μ = 27.5 nm and σ = 5.5 nm, and the thinner layers is assumed to have a long period of μ = 17.0 nm and σ = 3.4 nm. To simplify the situation, we assume the ratio of the crystalline layer thickness to the long period is fixed at 0.3. Therefore, the lamellar thickness of PLLA has two populations of distribution as well, specifically, μ_1 = 8.3 nm (with σ_1 = 1.6 nm) and μ_2 = 5.1 nm (with σ_2 = 1.0 nm). The population ratio of the thicker layers over the thinner layers is assumed to be 2:1. As shown in Figure 2.37a and c, these parameters reproduce the experimental SAXS curves well.

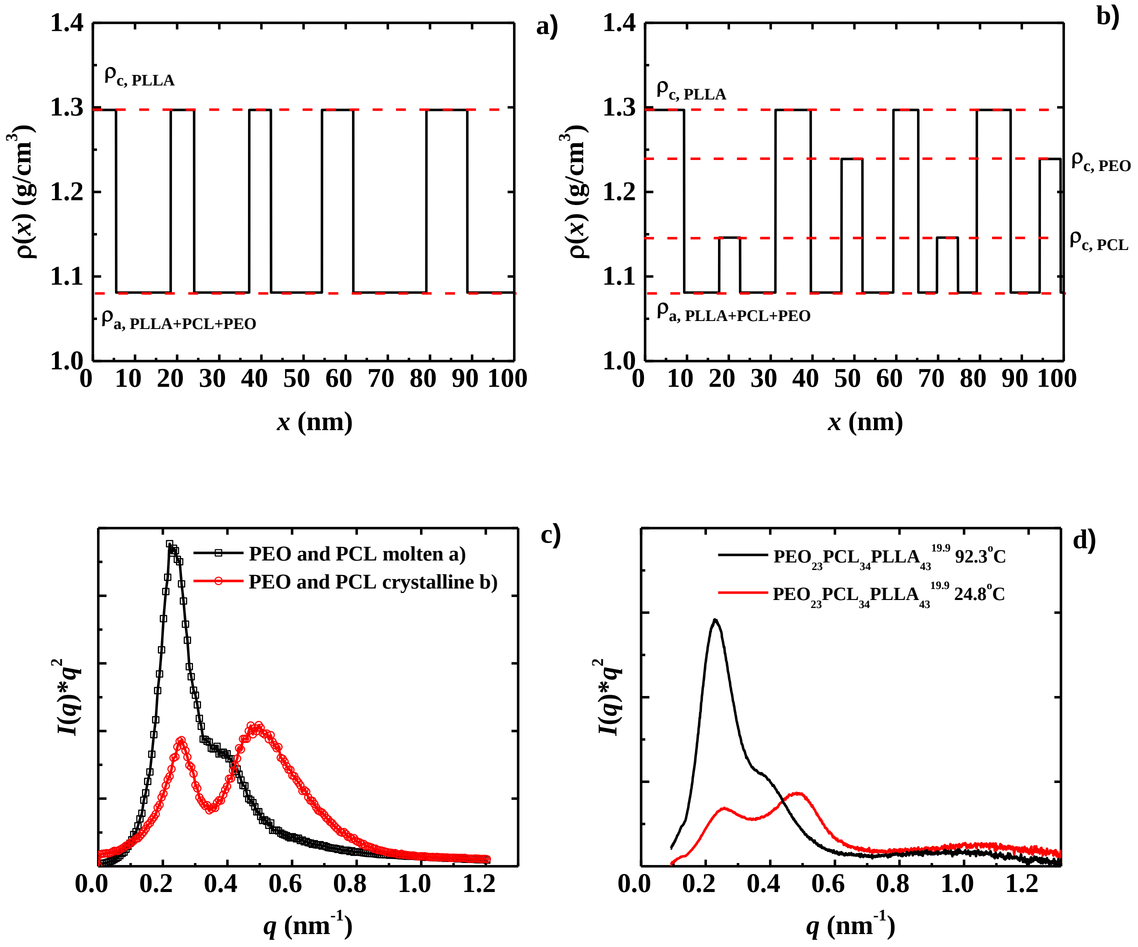

Figure 2.37. a) One dimensional density profile in a two-phase model, corresponding to the triblock copolymer with molten PCL and PEO. b) One dimensional density profile

in a four-phase model, corresponding to the triblock terpolymer with crystalline PCL and PEO. c) Simulated SAXS curves of the density profiles of a) corresponding to molten PCL/PEO and b) corresponding to crystalline PCL/PEO. d) Experimental SAXS data of $PEO_{23}PCL_{34}PLLA_{43}^{19.9}$ at 25.3°C and 92.3°C (protocol T2).

To understand the microstructure of the triblock terpolymers with both PCL and PEO crystalline lamellae, we need to formulate a hypothesis. Because the amorphous layers in between PLLA contains both PEO and PCL, the first question is how many crystalline layers will form in between the PLLA lamellae. If one PCL lamella and one PEO lamella are inserted in between two adjacent PLLA layers, one would expect to see stronger third-order peaks (indeed the simulated curves do show this result). After several trails, we present in Figure 2.37b a random insertion model, in which either a PCL or a PEO crystalline lamella is inserted within the PLLA amorphous layer (i.e., the intelamellar region in between PLLA crystalline lamellae). The density of the PEO crystalline phase is assumed to be 1.239 g/cm^3 [154]. The thickness of the PCL or PEO layer is assumed to be 5.0 nm. As seen in Figure 2.37c, this model roughly reproduces the experimental SAXS curve. We must point out that the purpose of the simulation is to understand the microstructure by comparing the theoretical scattering curves and experimental ones, rather than trying to obtain exact structural parameters. Therefore, many simplifications were carried out including the ignorance of the transition layer at the interface and density fluctuations within the crystalline or amorphous layers. Based on previous analysis, Figure 2.38 shows a schematic illustration of the trilayered lamellar morphology proposed, in which only one lamella of PCL or PEO inserts between two PLLA lamellae in a random fashion.

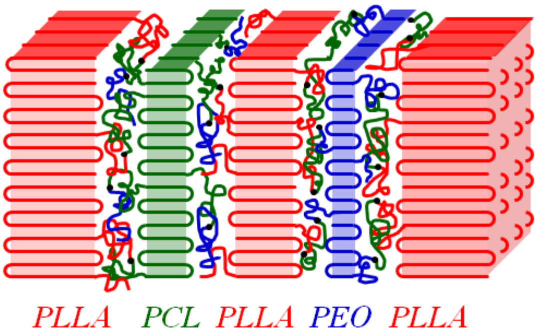

Figure 2.38. Schematic representation of the trilayered morphology in the triple crystalline $PEO_{23}PCL_{34}PLLA_{43}^{19.9}$ triblock terpolymer.

2.3.8 Overall isothermal crystallization kinetics of the PLLA block in the PEO-*b*-PCL-*b*-PLLA triblock terpolymers and PCL-*b*-PLLA diblock copolymers

In order to establish the influence of each block and the environment created in the crystallization behavior of the terpolymers, different crystallization protocols have been applied and the isothermal crystallization of each block have been followed. On studying polymer crystallization kinetics, the two main factors to assess are the crystallization rate and the supercooling.

It is well known that the crystallization kinetics of PLLA is extremely slow [75]. Particularly, it was not possible to follow the isothermal crystallization of the PLLA block in the terpolymers after quenching the sample from the melt. The DSC isothermal signal was too small for the equipment to detect. Therefore, in order to increase the nucleus density of PLLA, the sample was cooled from the melt until 0 ºC and then, rapidly heated up to the PLLA crystallization temperature (see Figure 2.39). In this way, the isothermal cold crystallization of PLLA was followed. During the rapid cooling and heating steps, the PLLA block did not crystallize.

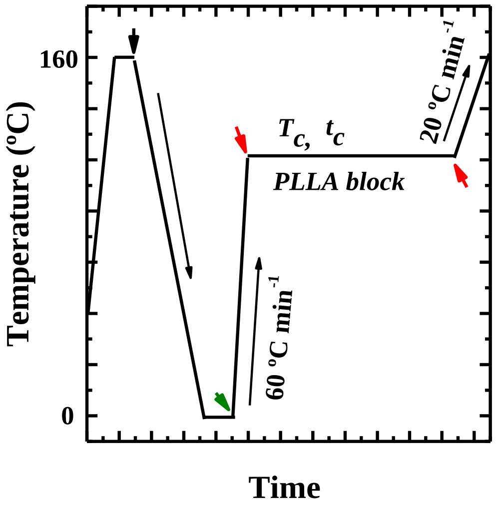

Figure 2.39. Thermal protocol applied to follow the isothermal crystallization behavior of the PLLA block.

Thus, from the DSC isothermal experiments, the inverse half-crystallization time ($1/\tau_{50\%}$) values were determined and plotted against the crystallization temperature. The $1/\tau_{50\%}$ values represent the inverse of the time needed to achieve the 50 % of the total crystalline mass during the isothermal crystallization event, and it is related to the overall crystallization rate. Figure 2.40 compares the overall crystallization kinetics of the PLLA block in both terpolymers to that of the PLLA block in the analogous diblock copolymers. The length of the PLLA block is almost the same in the diblock copolymer and terpolymer. Following the isothermal cold crystallization of the corresponding PLLA homopolymers was not possible due to their very slow crystallization rate. The data in Figure 2.40 represents the left side of the bell-shape curve of the crystallization rate plot. Thus, the crystallization rate of the samples decreased as the crystallization temperature reduces. At temperatures in which the PLLA block crystallizes, the PCL and PEO blocks are melted. The molten PEO and PCL chains caused a strong plasticizing effect on the PLLA crystallization. A higher supercooling was needed in order to crystallize the PLLA block at the same crystallization rate (by extrapolation). The depression in T_c was more notorious as the PLLA content in the terpolymer and the diblock copolymer was reduced (see Figure 2.40, left). In diblock copolymers of PLLA and PCL, and PLLA and PEO, a similar reduction in the PLLA crystallization temperature has been observed as the PLLA content (or molecular weight) decreases [4, 38, 40].

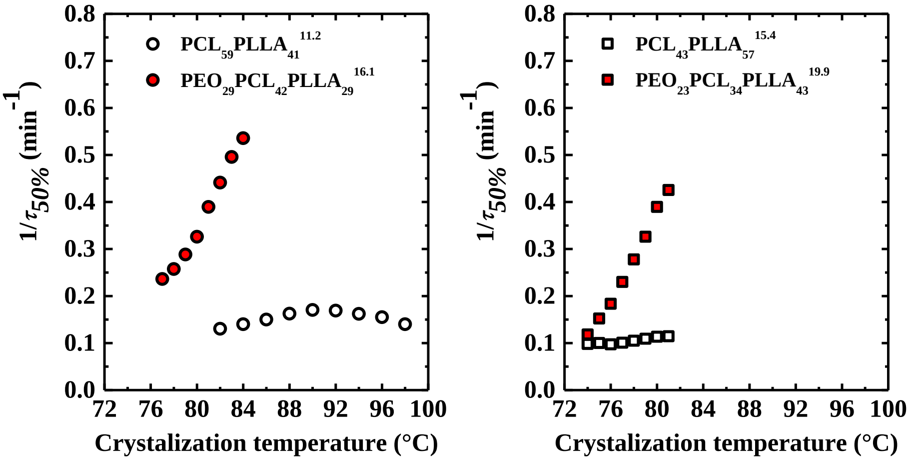

Figure 2.40. Inverse of half crystallization times ($1/\tau_{50\%}$) versus crystallization temperature. Isothermal cold crystallization of the PLLA block within the diblock copolymers and terpolymers indicated.

Surprisingly, the overall crystallization rate of PLLA block was higher in both terpolymers in comparison to the diblock copolymers. This behavior was not as expected, since in PCL-*b*-PLLA diblock copolymers, a decreased PLLA block crystallization rate has been reported [4]. However, the crystallization kinetics reported previously have been followed upon cooling directly from the melt [4]. In this case, it has been followed the cold isothermal crystallization of the PLLA block upon heating from 0 ºC. Therefore, left side of the bell-shape crystallization rate was examined. Particularly in the $PEO_{29}PCL_{42}PLLA_{29}^{16.1}$ triblock terpolymer (see Figure 2.40, left), the higher content of covalently bonded molten phase (PEO + PCL) compared to that in the diblock copolymer (only PCL) caused a strong plasticizing effect, shifting the crystallization rate curve to lower temperatures. Therefore, the increased crystallization rate might be related to the increase in the supercooling. The overall crystallization is the combination of the nucleation and growth event. At high supercoolings (left side of the bell-shape crystallization rate plot depicted in Figure 2.40), the crystallization kinetics is governed by the nucleation rate and diffusion control. A possible explanation for an increased crystallization rate might be an enhanced nucleation, caused by a donation of more active heterogeneities from the molten PEO phase [30]. However, this fact is uncertain. The most plausible explanation should be the presence of the additional high flexible PEO block. The high mobility of the mixed and molten PEO chains might aid the diffusion of the PLLA chains to the crystalline front, enhancing the PLLA crystallization kinetics in the terpolymers.

The phase structure of the samples previous the PLLA isothermal cold crystallization was examined by simultaneous SAXS/WAXS measurements. The PLLA block was crystallized upon heating from 0 ºC up to the PLLA crystallization temperature. During the previous cooling scan down to 0 ºC, the PCL and PEO blocks might crystallize. Then, the PCL or PEO crystals melted in the subsequent heating scan up to the PLLA T_c. The $PCL_{59}PLLA_{41}^{11.2}$ diblock copolymer and $PEO_{29}PCL_{42}PLLA_{29}^{16.1}$ triblock terpolymer were selected to perform simultaneous SAXS/WAXS measurements during the isothermal crystallization step of the PLLA block. The same thermal protocol depicted in Figure 2.39 was applied and the isothermal cold crystallization of PLLA was carried out at 82 ºC until saturation. The Lorentz corrected SAXS curves plotted against time are shown in Figure 2.41a for the $PCL_{59}PLLA_{41}^{11.2}$ diblock copolymer and Figure 2.41b for the $PEO_{29}PCL_{42}PLLA_{29}^{16.1}$

triblock terpolymer. The product between the intensity and the square of the scattering vector (q) was plotted versus q.

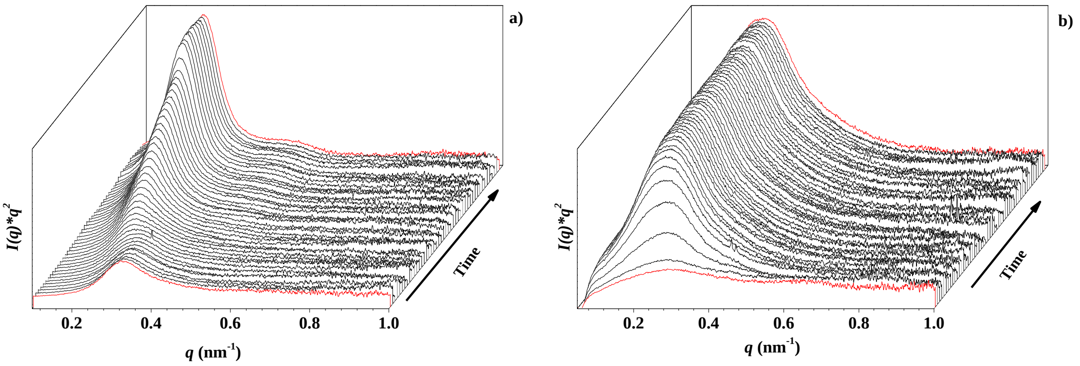

Figure 2.41. Lorentz corrected SAXS patterns during the isothermal cold crystallization of the PLLA block at 82 ºC in a) $PCL_{59}PLLA_{41}^{11.2}$ diblock copolymer and b) $PEO_{29}PCL_{42}PLLA_{29}^{16.1}$ triblock terpolymer.

At zero time, the $PCL_{59}PLLA_{41}^{11.2}$ diblock copolymer exhibited a SAXS peak at q = 0.33 nm^{-1} (see first red curve in Figure 2.41a). The scattering vector is related to the long period (d-spacing) through the equation $d = 2\pi/q^{max}$. This value corresponded to a long period value of 19.1 nm. On the contrary, no scattering was observed in the $PEO_{29}PCL_{42}PLLA_{29}^{16.1}$ triblock terpolymer at the beginning of the isothermal crystallization step (see first red curve in Figure 2.41b). It seems that the crystallization of the PLLA block in the diblock copolymer started from a phase separated structure, while in the terpolymer, the PLLA block started to crystallize from a homogenous phase. To confirm that the samples were completely amorphous before the PLLA crystallization and to determine whether phase separation exists, SAXS/WAXS patterns were selected at specific times of the thermal protocol depicted in Figure 2.39 (see small arrows). The selected frames are shown in Figure 2.42.

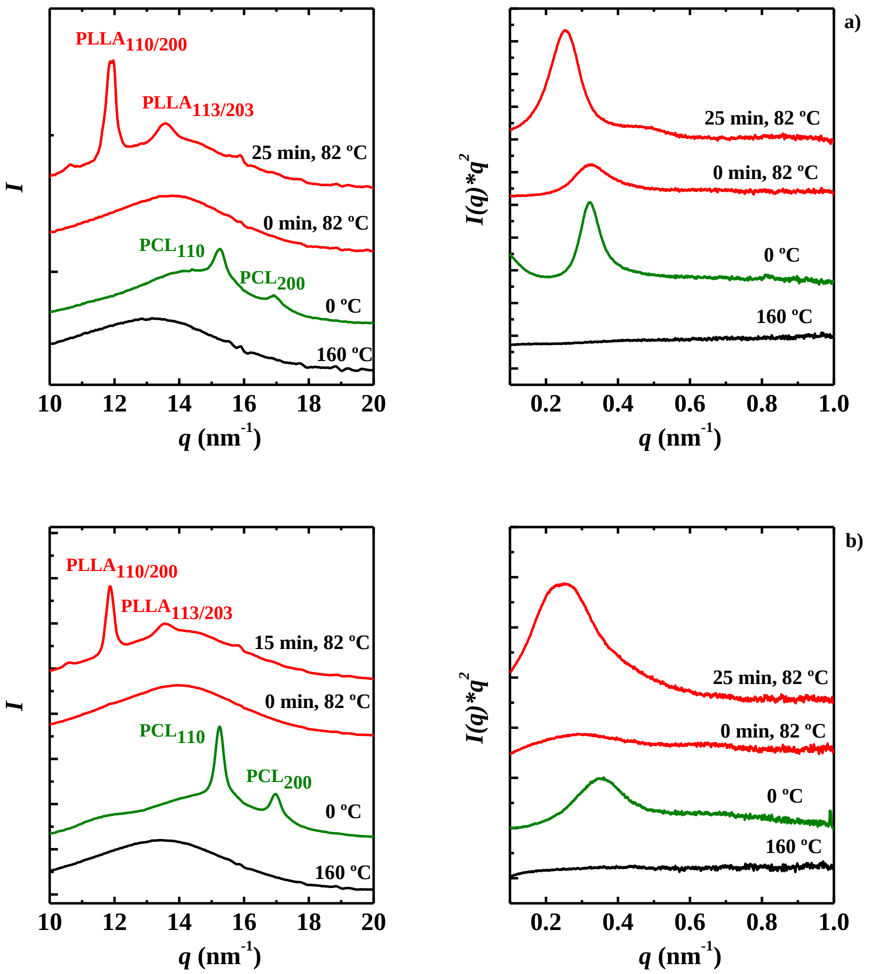

Figure 2.42. WAXS profiles (left) and Lorentz corrected SAXS profiles (right) of a) PCL$_{59}$PLLA$_{41}^{11.2}$ diblock copolymer and b) PEO$_{29}$PCL$_{42}$PLLA$_{29}^{16.1}$ triblock terpolymer.

At 160 ºC, both samples are molten. Thus, the WAXS patterns exhibited the characteristic amorphous halo and no melt structure was observed in the SAXS patterns measured at this temperature. The melt miscibility of PCL-*b*-PLLA diblock copolymers [6, 8, 46, 49, 51, 124] and the specific PEO-*b*-PCL-*b*-PLLA terpolymers [117] studied here has been previously reported. During the cooling until 0 ºC, the PCL block crystallized in both samples (see WAXS profiles at 0 ºC in Figure 2.42). A lamellar structure corresponding to the PCL crystalline lamellae was detected in the SAXS patterns (see the green plots on the right of Figure 2.42). The long period value of the lamellar arrangement was 19.7 and 17.4 nm for the diblock copolymer and terpolymer, respectively. Then, the PCL crystals melted during the subsequent heating scan up to 82 ºC. At the beginning of the PLLA crystallization (zero time) both samples were completely amorphous. No crystalline reflections were observed at this time in the

WAXS plots of Figure 2.42 (left side, bottom red curves). However, the SAXS profile of the diblock copolymer showed a reflection prior to PLLA crystallization that it was absent in the SAXS profile of the terpolymer (see right side in Figure 2.42, bottom red curves). This reflection corresponded to a phase separation at 82 ºC, and described a lamellar structure with a long period of 19.1 nm. This value is similar the one observed at 0 ºC (19.7 nm) when the PCL block was crystallized. Thus, the SAXS reflection at 82 ºC and 0 min might indicate a phase segregation of PCL amorphous lamellar microdomains that were crystalline before and a mixed PCL + PLLA amorphous phase. As a result, the PLLA crystallization initiated in the presence of a phase segregated structure. Due to the rapid heating, it was not possible to achieve a homogeneous phase after the melting of the PCL crystals and amorphous microdomains remained segregated. As for the $PEO_{29}PCL_{42}PLLA_{29}^{16.1}$ triblock terpolymer, the PLLA crystallization started from a homogeneous phase. Perhaps, the high mobility of the molten PEO block might have disrupted any possible segregation of PCL microdomains, and a mixed amorphous phase with molten PCL and PEO chains and amorphous PLLA chains prevailed.

After the PLLA block was completely crystallized, the ordered lamellar phase prior to PLLA crystallization disappeared, as it was substituted by the PLLA crystalline lamellar structure. Similar observations have been reported by Hamley et al.[6, 8] in PLL-*b*-PCL diblock copolymers but in their case the samples were crystallized upon cooling from melt. A transient ordered lamellar structure prior to PLLA crystallization was detected for $L_{60}^{12}C_{40}^{9}$ and $L_{32}^{7}C_{68}^{15}$, similar diblock copolymers to the one reported here. The size of the PLLA crystalline lamellar structure of both samples was similar. The values of the long period were 25.0 and 25.2 nm for the diblock copolymer and terpolymer, respectively. The reason is the similar PLLA block length in both samples (4600 and 4700 g mol^{-1}). In the diblock copolymer, besides the first order reflection at $q = 0.25$ nm^{-1}, a second order reflection was detected at $q = 0.49$ nm^{-1}.

The length (or molecular weight) of the PLLA block in the terpolymers affects its crystallization rate. At the same temperature, as the PLLA block lenght increases the overall crystallization rate reduced slightly (see the terpolymers in Figure 2.40a and b). It has been widely reported that the crystallization rate of PLLA drops greatly as the molecular weight increases [75, 155].

In order to compare the PLLA crystallinity achieved during the isothermal cold crystallization, the degree of crystallinity is plotted against T_c for the terpolymers and corresponding diblock copolymers (see Figure 2.43). In general, isothermally crystallized PLLA undergoes reorganization and melting/recrystallization phenomena during the subsequent heating scan. As a result, a double melting peak is a common observation, in which, the first endotherm corresponds to the isothermally growth crystals, and the second to the melting of the more stable structures formed during a melting/recrystallization event immediately after the first endothermic peak. Some authors [156] claimed that at standard heating rates (i.e. 20 ºC min^{-1}), it is not possible to avoid reorganization during the heating scan previous melting. All the terpolymers and diblock copolymers under study exhibited this characteristic double melting peak. Therefore, to ensure that the crystallinity evaluated corresponds to the isothermal event only, the degree of crystallinity was calculated from the crystallization enthalpy instead of the melting enthalpy.

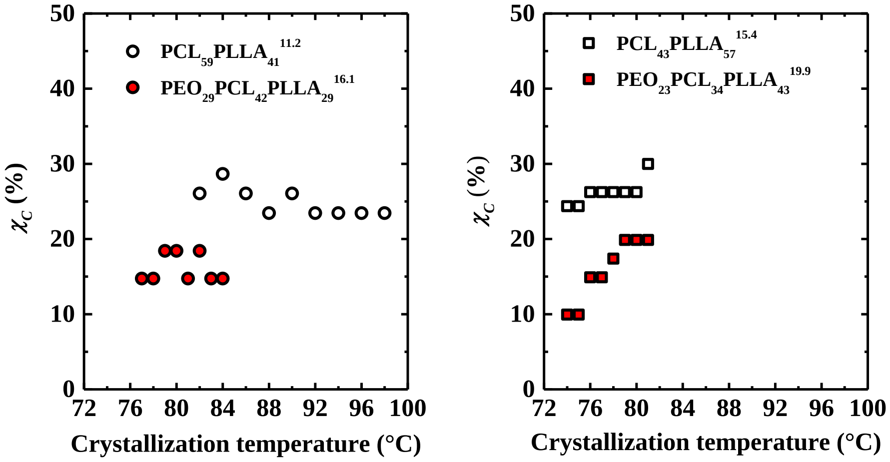

Figure 2.43. Crystallization degree (χ_C) of the isothermally crystallized PLLA block within the diblock copolymers and terpolymers indicated.

Both terpolymers had PLLA crystallization degrees smaller than that of the PLLA block in the corresponding diblock copolymers. The lower crystallinity degree is an indication of the plasticizing effect induced by the molten PCL and PEO chains. In comparison with the quantity of PCL in the diblock copolymers, the content of the molten PEO + PCL phase in the terpolymers is higher (71 and 57 % in the terpolymers versus 59 and 43 % in the diblock copolymers). This fact caused a diluent effect that might have made more difficult the addition of new crystallizable segments on the front of the growing crystal. The crystallization degree in both terpolymers was between 10 and 20 % while in the diblock copolymers was between 20 and 30 %.

The isothermal experimental data obtained from the DSC measurements was fitted to the Avrami equation following carefully the procedure proposed by Lorenzo at al. [68]. The crystallization kinetics in polymers have been described trough several theories [61]. One of them is the "free growth" theory formulated by Göler and Sachs [62, 63, 66, 67] that establishes once a given nuclei is initiated, it grows unrestrained or without the influence of others that may have also been nucleated or growing at the same time [62]. One of the possible solutions to this theory is the Avrami equation, also referred to as the Kolmogorov-Johnson-Mehl-Avrami equation (see Eq. 2-8) [157-161]:

This particular arrangement of the equation takes into account the role of the induction time, t_0, in the fitting. The other parameters are the relative volumetric transformed fraction V_c, the overall crystallization rate constant, k (that includes both contributions of the crystallization process: nucleation and growth), and the Avrami index, n, which is related to the time dependence of the nucleation and the crystal growth geometry. In polymers with spherulitic type morphology (3D structure), the Avrami index expected is between 3 and 4; while in crystals growing in 2D aggregates, such as axialites, the Avrami values would be between 2 and 3. In both cases, the final value will depend on whether the nucleation event is sporadic or instantaneous [61, 63, 162]. The quality of the fitting will depend on the conversion range (V_c) employed since the Avrami equation rarely describes the complete process. In general, the equation fits the process properly until the primary crystallization ends, which is < 40-50 % [62].

The Avrami index values, obtained from fitting the PLLA cold isothermal crystallization data, are plotted in Figure 2.44 against the crystallization temperature. The range of conversion employed in the fit was 3 – 20 %, and the correlation coefficients were always higher than 0.99. The Avrami Index of the diblock copolymers are around 2.5, which is approximately 3. While the values of the terpolymers are in some extend smaller. Particularly, the Avrami index of the terpolymer with the lower PLLA content ($PEO_{29}PCL_{42}PLLA_{29}^{16.1}$) exhibited values close to 1.7. This value agreed well with a crystal growth in 2D dimension. Also, it seems that the nucleation event might be more instantaneous than sporadic in the terpolymers, comparing to the diblock copolymers. The PLOM micrographs depicted in Figure 2.45 confirmed the morphology predicted by the Avrami equation. The $PEO_{29}PCL_{42}PLLA_{29}^{16.1}$ terpolymer exhibited 2D lamellar aggregates like axialites (see Figure 2.45b). But as the PLLA content in the terpolymer (and corresponding block copolymer) increases, the morphology resembled more to spherulites (see Figure 2.45c and d).

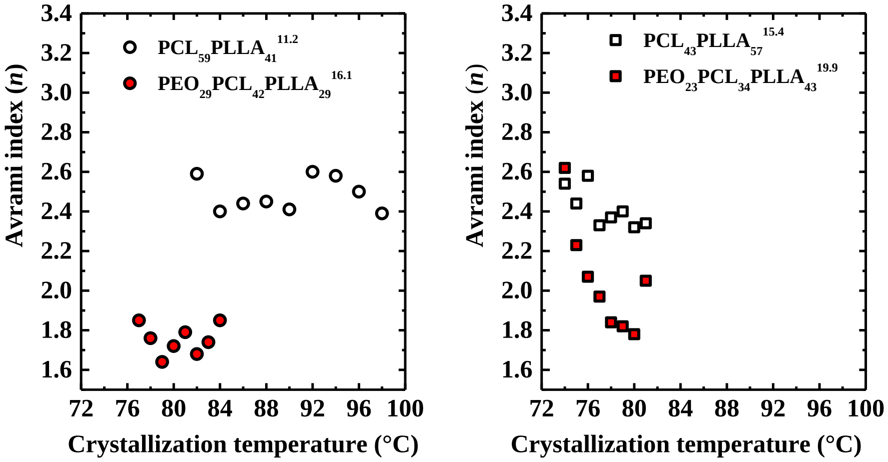

Figure 2.44. Avrami index (*n*) values of the PLLA block within the diblock copolymers and terpolymers indicated.

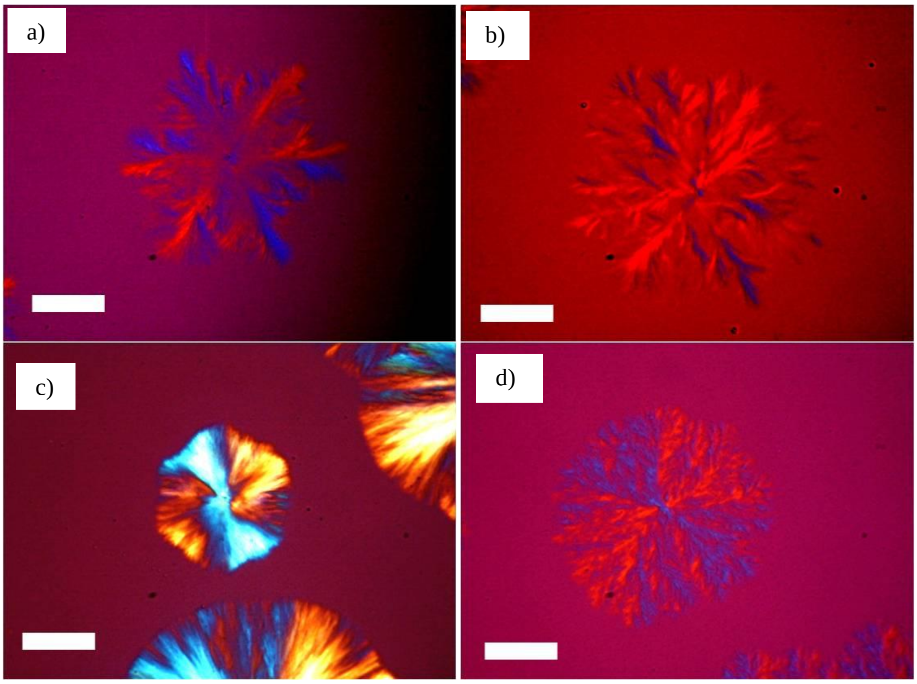

Figure 2.45. PLOM micrographs taken at 100 ºC of (a) $PCL_{59}PLLA_{41}^{11.2}$ and (b) $PEO_{29}PCL_{42}PLLA_{29}^{16.1}$, at 106 ºC of (c) $PCL_{43}PLLA_{57}^{15.4}$, and at 96 ºC of (d) $PEO_{23}PCL_{34}PLLA_{43}^{19.9}$. Scale bar: 50 μm.

2.3.9 Overall crystallization kinetics of the PCL block in the PEO-*b*-PCL-*b*-PLLA triblock terpolymers and PCL-*b*-PLLA diblock copolymers

Since the PLLA block crystallizes first, two different crystallization protocols were employed to follow the crystallization behavior of the PCL block in the terpolymers and diblock copolymers. The results were compared to that of the PCL homopolymer of same molecular weight. In the first one, the PLLA block was first crystallized until saturation, and then, the sample was quenched until the crystallization temperature of the PCL block. The PCL isothermal crystallization was registered. In the case of the terpolymers, the crystallization temperatures chosen were high enough to assure that only the PCL block was crystallizing, while the PEO block remained molten. With this two step crystallization protocol, the effect of the PLLA semicrystalline matrix in the crystallization of the PCL block was evaluated (see

Figure 2.46).

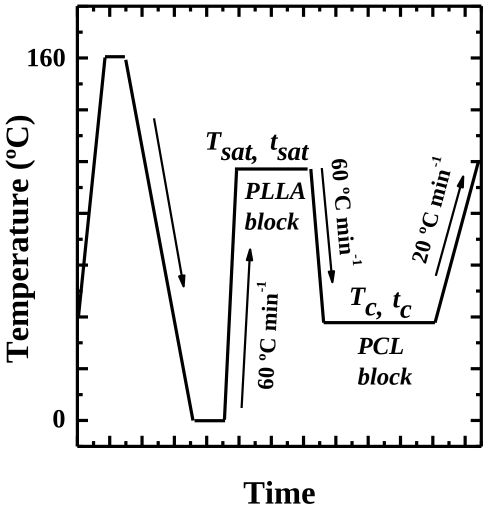

Figure 2.46. Two step crystallization protocol to follow the crystallization of the PCL block with the PLLA phase previously crystallized.

The inverse half-crystallization time ($1/\tau_{50\%}$) values of the PCL homopolymer and the PCL block in the diblock copolymers and terpolymers are depicted in Figure 2.47. Since the PCL block crystallization was followed after quenching from a molten PCL phase, the $1/\tau_{50\%}$ values correspond to the right side of the bell-shape crystallization rate curve. The previously formed PLLA crystals had a nucleating effect on the crystallization of the PCL chains. Therefore, the supercooling needed to crystallize the PCL block decreased. Also, the crystallization kinetics of the PCL block in both terpolymers and diblock copolymers increased, in comparison to the PCL homopolymer. Despite the PCL block had to crystallize inside the interlamellar regions of the PLLA spherulitic superstructure, this fact did not perturbed the PCL crystallization. In a previous publication about PCL-*b*-PLLA diblock copolymers [4], some of us reported a hampered crystallization of the PCL block when the PLLA block was previously crystallized until saturation. Even thought a nucleating effect of the PLLA crystals was demonstrated by self-nucleation experiments, larger supercoolings were needed to crystallize the PCL block and a retarded overall crystallization kinetics was observed. Two of those diblock copolymers had a similar PCL content (40 and 56 %) to that of the copolymers reported here (43 and 59 %). However, the length of the PCL block is different. Besides the nucleating effect of the PLLA crystals, the increase in the crystallization rate shown in Figure 2.47 obeyed to the smaller PCL block length. The molecular weight of the PCL homopolymer and PCL block in the copolymers and terpolymers was 7000, 6600 and 6800 g mol^{-1}, respectively. In contrast, the molecular weight of the PCL block in the diblock copolymers reported previously was 8500 and 14200 g mol^{-1} [4].

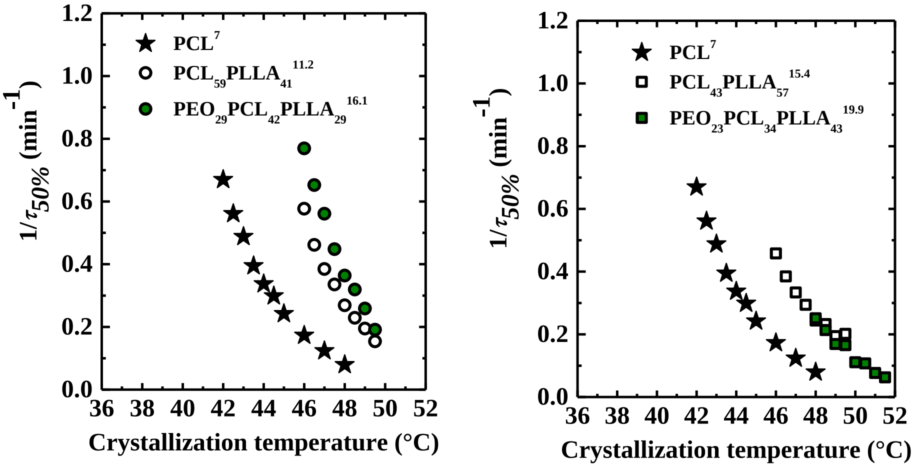

Figure 2.47. Inverse of half crystallization times ($1/\tau_{50\%}$) versus crystallization temperature of the PCL hompolymer and the PCL block within the diblock copolymers and terpolymers, after first isothermally crystallizing the PLLA block until saturation.

At higher PLLA content, the crystallization trend of the PCL block in the terpolymer and the diblock copolymer was the same ($\mathrm{PCL}_{43}\mathrm{PLLA}_{57}^{15.4}$ and

$PEO_{23}PCL_{34}PLLA_{43}^{19.9}$ samples). As the PLLA content reduces (PCL content increases), the crystallization kinetics of the PCL block in the terpolymer was only slightly higher than in the diblock copolymer (see Figure 2.47, left). In the terpolymer, the middle PCL block had one end attached to the PLLA crystals and the other to a molten PEO chain. It seems that the PEO molten block enhanced the crystallization of the PCL block. This suggested that the amorphous PEO chain, chemically bonded to one end of the PCL block, might increased the mobility and diffusion of the PCL chains to the crystallization sites.

The content of PCL did not affect considerably the crystallization kinetics of the PCL block. Only a slight increment in the $1/\tau_{50\%}$ values was observed as the PCL content in the terpolymers increased. The molecular weight of the PCL block is not to take into consideration, since the length values are almost the same as in the PCL homopolymer (7000 g mol^{-1} of the PCL homopolymer, and 6600 and 6800 g mol^{-1}, of the PCL block in both copolymers and terpolymers, respectively).

Despite the enhanced crystallization kinetics, the crystallinity degree of the PCL block in the diblock copolymers reduced, in comparison to the PCL homopolymer (see Figure 2.48). As expected, the crystallinity was even lower as the PCL content in the diblock copolymer reduces (see sample $PCL_{43}PLLA_{57}^{15.4}$ versus $PCL_{59}PLLA_{41}^{11.2}$ in Figure 2.48). Since, the PCL block had to crystallize inside the intraspherulitic regions of the PLLA crystalline superstructure, the amount of amorphous PCL phase that could convert into a crystalline one was highly diminished. The previously formed PLLA crystals restricted the PCL block lamellae to grow in between the lamellar stacks of the PLLA.

On the contrary, the presence of the molten PEO block in the terpolymer contributed to increase the crystallinity of the PCL block; in comparison to the diblock copolymers (see samples $PEO_{29}PCL_{42}PLLA_{29}^{16.1}$ and $PEO_{23}PCL_{34}PLLA_{43}^{19.9}$ in Figure 2.48). In fact, the PCL crystallinity degree in the terpolymer with larger PCL content even matched that of the PCL hompolymer (see Figure 2.48, left). In both terpolymers, the amorphous PEO chains enhanced the cristalizability of the PCL block, increasing the mobility and diffusion of the PCL chains (which are anchored to the PLLA crystals) to the growing PCL crystal front.

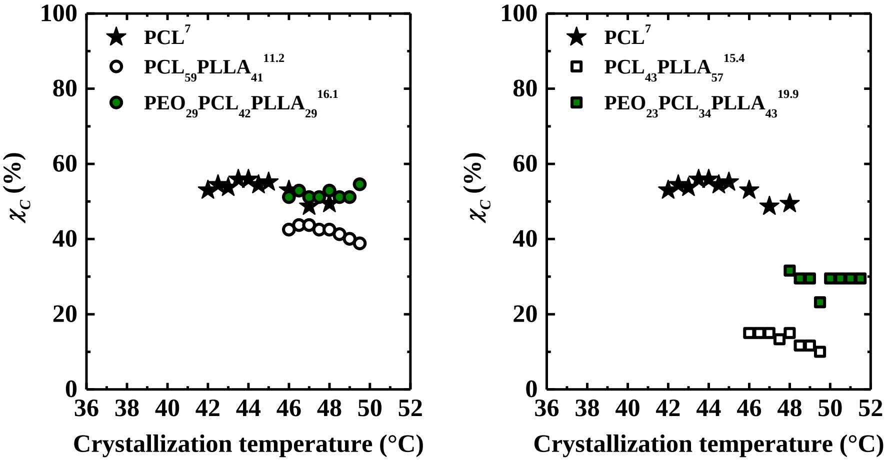

Figure 2.48. Crystallization degree (χ_c) of the PCL block within the diblock copolymers and terpolymers indicated, after first isothermally crystallizing the PLLA block until saturation.

The Avrami fitting was also applied to the experimental data registered during the isothermal crystallization of the PCL hompolymer and the PCL block in the diblock copolymers and terpolymers. The Avrami index values of all the samples were between 2 and 3 (see Figure 6.12 in Appendix).

The crystallization of the PCL block in the terpolymers and block copolymers was also followed employing a one step protocol. The method consisted in quenching the sample from the melt until the crystallization temperature of the PCL block. Then, the PCL isothermal crystallization was registered at that temperature, and finally, the sample was heated again until its melting (see Figure 2.49). Again, in the case of the terpolymers, the crystallization temperatures chosen were high enough to assure that only the PCL block was crystallizing, while the PEO block remained molten. In addition, during the cooling scan the PLLA block did not crystallized. A cold crystallization of the PLLA block took place during the subsequent heating scan, after the melting of the isothermally crystallized PCL crystals. Unlike the two step protocol, in this method the PCL block crystallization was followed while the PLLA phase remained amorphous.

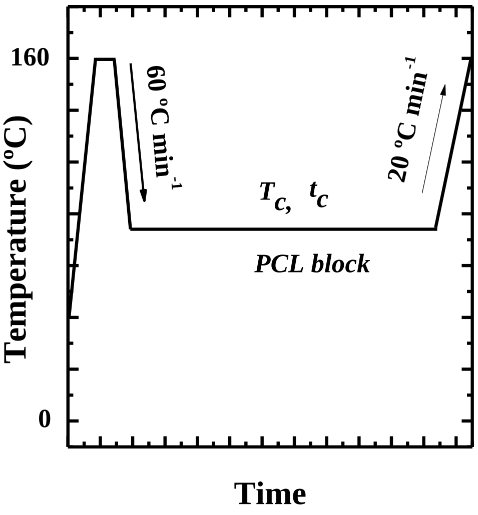

Figure 2.49. One step crystallization protocol to follow the crystallization of the PCL block while keeping the PLLA phase amorphous.

The isothermal crystallization kinetics of the PCL block surrounded by an amorphous PLLA phase is shown in Figure 2.50. Comparing the $1/\tau_{50\%}$ values to those plotted in Figure 2.47, it is clear that the crystallization behavior was completely opposite under this condition. In comparison to the PCL homopolymer, the crystallization rate of the PCL block in the diblock copolymers was highly diminished. While previously formed PLLA crystals caused a nucleating effect, in this case the amorphous PLLA phase induced an anti-plasticizing effect. The PCL block required a larger supercooling in order to crystallize, and the overall crystallization kinetics greatly reduces. These PCL-*b*-PLLA diblock copolymers have been reported to be miscible or weakly segregated in the met. When the sample is quenched from the melt until the PCL crystallization temperature, chains of the PCL and PLLA blocks are mixed together. In order to crystallize, the PCL chains had to demix from this amorphous phase that contains more rigid PLLA chains, and come closer to form a nucleus or to grow in the crystalline front. Therefore, under this condition, the phase separation is driven by the enthalpy of demixing of the constituent blocks during the crystallization of the PCL block. Since this is a miscible system and the glass transition of PLLA is higher than that of PCL, the glass transition in the diblock copolymer probably takes place at higher temperature than in the PCL homopolymer. Therefore, the PCL is probably crystallizing at temperatures that are closer to T_g. As a result, the mobility of the PCL chains should have reduced considerably. In addition, at temperatures in which PCL crystallizes, the chain movements of the more rigid PLLA block had also slowed down, making more difficult the diffusion and crystallization of the PCL chains covalently attached to them.

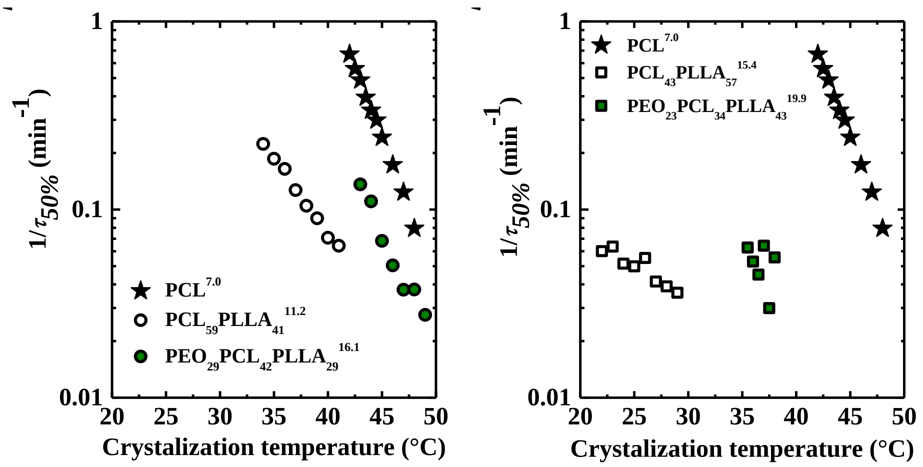

Figure 2.50. Inverse of half crystallization times ($1/\tau_{50\%}$) versus crystallization temperature of the PCL hompolymer and the PCL block within the diblock copolymers and terpolymers, crystallized in one step.

In contrast, when a third block of PEO is attached to PCL-*b*-PLLA copolymers, the crystallization behavior of the middle PCL block became very interesting. From Figure 2.50 it is clear that the overall crystallization rate and crystallization temperature of the PCL block in the terpolymers increased, in comparison to the same PCL block in the analogous diblock copolymers. The middle PCL block crystallized under smaller supercooling in both terpolymers. At the temperatures in which the PCL crystallizes, the PEO block remains molten. As in the two step crystallization protocol, the molten PEO chains enhanced the crystallization ability of the PCL block due to a plasticizing effect. In the terpolymers, the PCL crystallized from a mixed amorphous phase that includes more rigid amorphous chains of PLLA as well as molten PCL and PEO chains. As the crystallization took place, the molten PEO chains increased the mobility and diffusion of the PCL chains to the crystalline front. However and as expected, the $1/\tau_{50\%}$ values did not match those of the PCL homopolymer, even though the crystallization rate of the PCL block in the terpolymers was increased. In the PCL homopolymer, the chains can form nucleus and grow freely from the melt. While in the terpolymers, the PCL chains are covalently attached to more rigid PLLA chains in amorphous state that would hinder the ability of the PCL block to undergo the crystallization process.

Unlike the two step crystallization protocol, the composition affected the crystallization kinetics of the PCL block in the terpolymers and diblock copolymers when they were crystallized in one step. By extrapolating the $1/\tau_{50\%}$ values to higher crystallization temperatures in Figure 2.50, right, it is clear that the crystallization rate became faster as the PCL content increases, comparing both terpolymers and diblock copolymers separately.

2.3.10 Overall crystallization kinetics of the PEO block in the PEO-*b*-PCL-*b*-PLLA triblock terpolymers

Following the crystallization kinetics of the third PEO block was extremely difficult since the crystallization and melting temperatures of both PEO and PCL are very similar. A three step crystallization protocol was the procedure employed to evaluate the crystallization behavior. The PLLA block was first crystallized until saturation, and next, the sample was quenched until the crystallization temperature of the PCL block. Then, the PCL block was crystallized until saturation while the PEO chains remained molten. Finally, the sample was quenched again until the PEO crystallization temperature and the isothermal crystallization was recorded (see Figure 2.51). The purpose of this protocol was to evaluate the effect of the double crystalline PCL/PLLA lamellae formed previously in the subsequent PEO crystallization. The isothermal crystallization of the PEO block in the terpolymers was compared to the analogous PEO hompolymer. Attempts were made to register the crystallization behavior of the PEO block within analogous PEO-*b*-PCL diblock copolymers. However, due to the similarity between the crystallization temperatures of both blocks, it was not possible to isolate the crystallization of one block from the other. In other words, both blocks crystallized simultaneously.

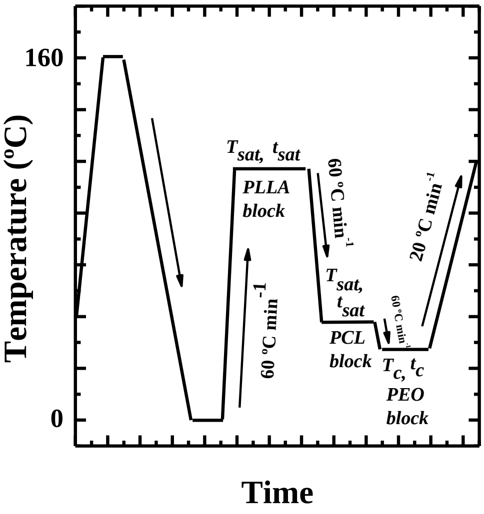

Figure 2.51 Three step crystallization protocol to follow the crystallization of the PCL block with the PLLA phase previously crystallized.

In Figure 2.52 are depicted the half crystallization times ($1/\tau_{50\%}$) of the PEO block in the $PEO_{29}PCL_{42}PLLA_{29}^{16.1}$ triblock terpolymer and the PEO homopolymer. It was not possible to isolate the PEO crystallization from that of the PCL block in the other triblock terpolymer sample. The PEO crystallization rate in the terpolymer highly decreased in comparison to the PEO homopolymer, as well as the crystallization temperature. A higher supercooling was needed to crystallize the PEO block. The previously formed PLLA and PCL rigid crystals created a hard environment that highly confined the crystallization of the PEO block. The theoretical analysis of the SAXS curves employing one-dimensional structural models (see section 2.3.7) suggested that either a lamella of PCL or a lamella of PEO inserted randomly between two adjacent PLLA lamellae, but not both PCL and PEO blocks together. The PEO molten chains (located at the end of the terpolymer) are covalently bonded to the PCL block in the middle. Therefore, the PEO chains had no other choice but to crystallize inside the interlamellar spaces left in between PLLA crystalline lamellae. Thus, the confinement imposed by the previously formed lamellar crystals will hinder PEO crystallization [117]. Evidences of confinement have been reported in PLLA-*b*-PEO block copolymers with short PEO block length or high PLLA content, in which the PLLA block crystallized first [30, 38].

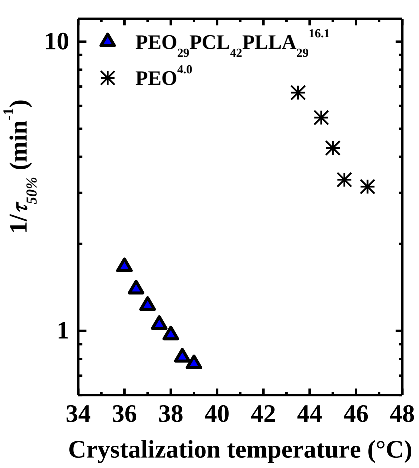

Figure 2.52. Inverse of half crystallization times ($1/\tau_{50\%}$) as function of crystallization temperature for the PEO hompolymer and the PEO block within the $PEO_{29}PCL_{42}PLLA_{29}^{16.1}$ triblock terpolymer.

2.4 CONCLUSIONS

The unique tricrystalline features of novel PEO-*b*-PCL-*b*-PLLA triblock terpolymers were assessed. In these multiphasic systems, three different types of crystalline lamellae coexist within the nanoscale structure. Compared to double crystalline diblock copolymers, the addition of a third crystallizable block makes the morphology and crystallization behavior even more complex. The following conclusions derived from the research:

- The PEO-*b*-PCL-*b*-PLLA triblock terpolymers exhibit a homogeneous melt morphology, as it was confirmed by SAXS.
- The triple crystalline nature and sequential crystallization of the three blocks in PEO-*b*-PCL-*b*-PLLA triblock terpolymers was confirmed by DSC, WAXS and PLOM.
- The three blocks are able to crystallize sequentially and separately upon cooling from the melt at very low cooling rates (1 and 5 ºC min^{-1}).
- The crystallization sequence is as follows. The PLLA block crystallizes first upon cooling from the melt, then the PCL block, and finally the PEO block.
- PLLA block crystallization templates the morphology of the entire triblock terpolymer upon cooling from the melt. The microscale morphology changes with composition. For the triblock terpolymer with a lower PLLA content, the superstructural morphology formed by the PLLA block resembles axialites. But at higher PLLA content, the crystalline superstructure is more similar to spherulites.
- Upon further cooling from the melt, the crystallization of the PCL and PEO blocks do not alter the already formed superstructure. Unique triple crystalline mixed spherulitic superstructures are formed and clear changes in the birefringence reflect the sequential crystallization of each block.
- A remarkable trilamellar self-assembly at nanosacle was confirmed by AFM, after the isothermal crystallization of the PEO-*b*-PCL-*b*-PLLA triblock terpolymers in two steps.

- The trilayered assembly consisted in alternated crystalline lamellae of PEO, PCL and PLLA, of different lamellar thickness, with an amorphous mixed layer in between.

- Theoretical SAXS curves calculated by one-dimensional structural models sugges that only one lamella of PCL or one lamella of PEO inserts randomly between two adjacent PLLA lamellae.

- The PEO and PCL molten chains caused a strong diluent effect (higher supercooling) on the PLLA block crystallization in the terpolymers, as compared to the PLLA block in the diblock copolymers.

- Despite the increased supercooling, the overall crystallization rate of PLLA block was higher in both terpolymers in comparison to the analogous diblock copolymers, although the crystallization degree reduced.

- In PEO-*b*-PCL-*b*-PLLA triblock terpolymers crystallized in two steps (first the PLLA block and then, the PCL block), the previously formed PLLA crystals had a nucleating effect on the PCL crystallization. Thus, the PCL crystallization kinetics increased and the supercooling decreased.

- In PEO-*b*-PCL-*b*-PLLA triblock terpolymers crystallized in one step (quenching from melt until T_c of PCL), the amorphous PLLA matrix caused an anti-plasticizing effect on the PCL crystallization. Thus, the supercooling increased and the overall crystallization kinetics of PCL greatly reduced.

- The presence of the PEO block increased the overall crystallization rate and crystallization temperature of the PCL block in the PEO-*b*-PCL-*b*-PLLA triblock terpolymers, in comparison to the analogous PCL-*b*-PLLA diblock copolymers.

- Following the crystallization of the PEO block after PLLA and PCL fully crystallized was extremely difficult due to the very similar PCL and PEO crystallization temperatures. The PEO crystallization rate highly decreased and the supercooling increased as a result of the confinement imposed by the previously formed PLLA and PCL crystals.

2.5 REFERENCES

[1] R. V. Castillo and A. J. Müller, "Crystallization and morphology of biodegradable or biostable single and double crystalline block copolymers," *Progress in Polymer Science,* vol. 34, no. 6, pp. 516-560, 2009.

[2] S. Li, S. B. Myers, and R. A. Register, "Solid-State Structure and Crystallization in Double-Crystalline Diblock Copolymers of Linear Polyethylene and Hydrogenated Polynorbornene," *Macromolecules,* doi: 10.1021/ma201951j vol. 44, no. 22, pp. 8835-8844, 2011/11/22 2011.

[3] S. B. Myers and R. A. Register, "Crystalline−Crystalline Diblock Copolymers of Linear Polyethylene and Hydrogenated Polynorbornene," *Macromolecules,* doi: 10.1021/ma800759b vol. 41, no. 18, pp. 6773-6779, 2008/09/23 2008.

[4] R. V. Castillo, A. J. Müller, J. M. Raquez, and P. Dubois, "Crystallization kinetics and morphology of biodegradable double crystalline PLLA- b -PCL diblock copolymers," *Macromolecules,* vol. 43, no. 9, pp. 4149-4160, 2010.

[5] E. Laredo *et al.*, "Miscibility in poly(L-lactide)-b-poly(ε-caprolactone) double crystalline diblock copolymers," *European Physical Journal E,* vol. 23, no. 3, pp. 295-303, 2007.

[6] I. W. Hamley *et al.*, "Melt structure and its transformation by sequential crystallization of the two blocks within poly(L-lactide)-block-poly(ε-caprolactone) double crystalline diblock copolymers," *Macromolecular Chemistry and Physics,* vol. 207, no. 11, pp. 941-953, 2006.

[7] A. J. Müller *et al.*, "Self-nucleation and crystallization kinetics of double crystalline poly(p-dioxanone)-b-poly(ε-caprolactone) diblock copolymers," *Faraday Discussions,* vol. 128, pp. 231-252, 2005.

[8] I. W. Hamley *et al.*, "Crystallization in poly(L-lactide)-b-poly(ε-caprolactone) double crystalline diblock copolymers: A study using x-ray scattering, differential scanning calorimetry, and polarized optical microscopy," *Macromolecules,* vol. 38, no. 2, pp. 463-472, 2005.

[9] A. J. Müller *et al.*, "Confinement effects on the crystallization kinetics and self-nucleation of double crystalline poly(p-dioxanone)-b-poly(ε-caprolactone) diblock copolymers," in *Macromolecular Symposia*, 2004, vol. 215, pp. 369-382.

[10] J. Albuerne *et al.*, "Nucleation and crystallization in double crystalline poly(p-dioxanone)-b-poly(ε-caprolactone) diblock copolymers," *Macromolecules,* vol. 36, no. 5, pp. 1633-1644, 2003.

[11] M. Ponjavic, M. S. Nikolic, S. Jevtic, J. Rogan, S. Stevanovic, and J. Djonlagic, "Influence of a low content of PEO segment on the thermal, surface and morphological properties of triblock and diblock PCL copolymers," *Macromolecular Research,* Article vol. 24, no. 4, pp. 323-335, 2016.

[12] Y. Li, J. Zhou, J. Zhang, Q. Gou, Q. Gu, and Z. Wang, "Morphology of poly(ethylene oxide)- b-poly(ε -caprolactone) spherulites formed under compressed CO 2," *Journal of Macromolecular Science, Part B: Physics,* vol. 53, no. 6, pp. 1137-1144, 2014.

[13] Y. Li, H. Huang, Z. Wang, and T. He, "Tuning radial lamellar packing and orientation into diverse ring-banded spherulites: Effects of structural feature and crystallization condition," *Macromolecules,* Article vol. 47, no. 5, pp. 1783-1792, 2014.

[14] F. F. Xue, X. S. Chen, L. J. An, S. S. Funari, and S. C. Jiang, "Confined lamella formation in crystalline-crystalline poly(ethylene oxide)-b-poly(ε-caprolactone) diblock copolymers," *Chinese Journal of Polymer Science (English Edition),* vol. 31, no. 9, pp. 1260-1270, 2013.

[15] F. Xue, X. Chen, L. An, S. S. Funari, and S. Jiang, "Soft nanoconfinement effects on the crystallization behavior of asymmetric poly(ethylene oxide)-block-poly(ε- caprolactone) diblock copolymers," *Polymer International,* Article vol. 61, no. 6, pp. 909-917, 2012.

[16] J. Sun, C. He, X. Zhuang, X. Jing, and X. Chen, "The crystallization behavior of poly(ethylene glycol)-poly(ε- caprolactone) diblock copolymers with asymmetric block compositions," *Journal of Polymer Research,* vol. 18, no. 6, pp. 2161-2168, 2011.

[17] R. M. Van Horn *et al.*, "Solution crystallization behavior of crystalline-crystalline diblock copolymers of poly(ethylene oxide)-block-poly(ε-caprolactone)," *Macromolecules,* Article vol. 43, no. 14, pp. 6113-6119, 2010.

[18] L. Li, F. Meng, Z. Zhong, D. Byelov, W. H. De Jeu, and J. Feijen, "Morphology of a highly asymmetric double crystallizable poly (ε -caprolactone- b -ethylene oxide) block copolymer," *Journal of Chemical Physics,* vol. 126, no. 2, 2007, Art. no. 024904.

[19] C. Hua and C.-M. Dong, "Synthesis, characterization, effect of architecture on crystallization of biodegradable poly(ε-caprolactone)-b-poly(ethylene oxide) copolymers with different arms and nanoparticles thereof," *Journal of Biomedical Materials Research Part A,* vol. 82A, no. 3, pp. 689-700, 2007.

[20] M. Vivas *et al.*, "Synthesis and characterization of triblock terpolymers with three potentially crystallisable blocks: Polyethylene-b-poly(ethylene oxide)-b-poly(ε-caprolactone)," *Macromolecular Symposia,* vol. 239, pp. 58-67, 2006.

[21] C. He *et al.*, "Formation of a unique crystal morphology for the poly(ethylene glycol)-poly(ε-caprolactone) diblock copolymer," *Biomacromolecules,* vol. 7, no. 1, pp. 252-258, 2006.

[22] S. Jiang, C. He, L. An, X. Chen, and B. Jiang, "Crystallization and ring-banded spherulite morphology of poly(ethylene oxide)-block-poly(ε-caprolactone) diblock copolymer," *Macromolecular Chemistry and Physics,* vol. 205, no. 16, pp. 2229-2234, 2004.

[23] M. L. Arnal, F. López-Carrasquero, E. Laredo, and A. J. Müller, "Coincident or sequential crystallization of PCL and PEO blocks within polystyrene-b-poly(ethylene oxide)-b-poly(ε-caprolactone) linear triblock copolymers," *European Polymer Journal,* vol. 40, no. 7, pp. 1461-1476, 2004.

[24] L. Piao, Z. Dai, M. Deng, X. Chen, and X. Jing, "Synthesis and characterization of PCL/PEG/PCL triblock copolymers by using calcium catalyst," *Polymer,* vol. 44, no. 7, pp. 2025-2031, 2003.

[25] M. L. Arnal *et al.*, "Synthesis and characterization of polystyrene-b-poly(ethylene oxide)-b-poly(ε-caprolactone) block copolymers," *Macromolecules,* Article vol. 34, no. 23, pp. 7973-7982, 2001.

[26] B. Bogdanov, A. Vidts, A. Van Den Buicke, R. Verbeeck, and E. Schacht, "Synthesis and thermal properties of poly(ethylene glycol)-poly(ε-caprolactone) copolymers," *Polymer,* vol. 39, no. 8–9, pp. 1631-1636, 1998.

[27] S. Nojima, M. Ono, and T. Ashida, "Crystallization of block copolymers II. Morphological study of poly(ethylene glycol)-poly(ε-caprolactone) block copolymers," *Polymer Journal,* vol. 24, no. 11, pp. 1271-1280, 1992.

[28] Z. Wei, L. Liu, F. Yu, P. Wang, and M. Qi, "Synthesis and characterization of poly(ε-caprolactone)-b-poly(ethylene glycol)-b-poly(ε-caprolactone) triblock

copolymers with dibutylmagnesium as catalyst," *Journal of Applied Polymer Science,* vol. 111, no. 1, pp. 429-436, 2009.

[29] Z. Wei *et al.*, "Nonisothermal crystallization and melting behavior of poly(e-caprolactone)- b-poly(ethylene glycol)-b-poly (e-caprolactone) by DSC analysis," *Journal of Applied Polymer Science,* vol. 114, no. 2, pp. 1133-1140, 2009.

[30] M. L. Arnal *et al.*, "Interplay between poly(ethylene oxide) and poly(l-lactide) blocks during diblock copolymer crystallization," *CrystEngComm,* Article vol. 18, no. 20, pp. 3635-3649, 2016.

[31] D. Zhou *et al.*, "Unusual crystallization and melting behavior induced by microphase separation in MPEG-b-PLLA diblock copolymer," *Polymer,* vol. 80, pp. 123-129, 2015.

[32] J. Yang, Y. Liang, and C. C. Han, "Effect of crystallization temperature on the interactive crystallization behavior of poly(l-lactide)-block-poly(ethylene glycol) copolymer," *Polymer (United Kingdom),* vol. 79, pp. 56-64, 2015.

[33] F. Xue, X. Chen, L. An, S. S. Funari, and S. Jiang, "Crystallization induced layer-to-layer transitions in symmetric PEO-b-PLLA block copolymer with synchrotron simultaneous SAXS/WAXS investigations," *RSC Advances,* Article vol. 4, no. 99, pp. 56346-56354, 2014.

[34] S. Huang, H. Li, S. Jiang, X. Chen, and L. An, "Morphologies and structures in poly(l-lactide-b-ethylene oxide) copolymers determined by crystallization, microphase separation, and vitrification," *Polymer Bulletin,* vol. 67, no. 5, pp. 885-902, 2011.

[35] S. Huang, S. Jiang, L. An, and X. Chen, "Crystallization and morphology of poly(ethylene oxide-b-lactide) crystalline-crystalline diblock copolymers," *Journal of Polymer Science Part B: Polymer Physics,* vol. 46, no. 13, pp. 1400-1411, 2008.

[36] J. Yang *et al.*, "Single crystals of the poly(L-lactide) block and the poly(ethylene glycol) block in poly(L-lactide)-poly(ethylene glycol) diblock copolymer," *Macromolecules,* vol. 40, no. 8, pp. 2791-2797, 2007.

[37] C. Cai, L. U. Wang, and C. M. Donc, "Synthesis, characterization, effect of architecture on crystallization, and spherulitic growth of poly(L-lactide)b-poly(ethylene oxide) copolymers with different branch arms," *Journal of*

Polymer Science Part A: Polymer Chemistry, vol. 44, no. 6, pp. 2034-2044, 2006.

[38] J. Yang *et al.*, "Nonisothermal crystallization behavior of the poly(ethylene glycol) block in poly(L-lactide)–poly(ethylene glycol) diblock copolymers: Effect of the poly(L-lactide) block length," *Journal of Polymer Science Part B: Polymer Physics,* vol. 44, no. 22, pp. 3215-3226, 2006.

[39] C. G. Mothé, W. S. Drumond, and S. H. Wang, "Phase behavior of biodegradable amphiphilic poly(l,l-lactide)-b-poly(ethylene glycol)-b-poly(l,l-lactide)," *Thermochimica Acta,* vol. 445, no. 1, pp. 61-66, 2006.

[40] C. I. Huang, S. H. Tsai, and C. M. Chen, "Isothermal crystallization behavior of poly(L-lactide) in poly(L-lactide)-block-poly(ethylene glycol) diblock copolymers," *Journal of Polymer Science Part B: Polymer Physics,* vol. 44, no. 17, pp. 2438-2448, 2006.

[41] D. Shin *et al.*, "A morphological study of a semicrystalline poly(L-lactic acid-b-ethylene oxide-b-L-lactic acid) triblock copolymer," *Macromolecules,* vol. 38, no. 1, pp. 104-109, 2005.

[42] J. Sun, Z. Hong, L. Yang, Z. Tang, X. Chen, and X. Jing, "Study on crystalline morphology of poly(L-lactide)-poly(ethylene glycol) diblock copolymer," *Polymer,* vol. 45, no. 17, pp. 5969-5977, 2004.

[43] K. S. Kim, S. Chung, I. J. Chin, M. N. Kim, and J. S. Yoon, "Crystallization Behavior of Biodegradable Amphiphilic Poly(ethylene glycol)-Poly(L-lactide) Block Copolymers," *Journal of Applied Polymer Science,* vol. 72, no. 3, pp. 341-348, 1999.

[44] R. Liénard *et al.*, "Synthesis and Characterization of Double Crystalline Cyclic Diblock Copolymers of Poly(ε-caprolactone) and Poly(l(d)-lactide) (c(PCL-b-PL(D)LA))," *Macromolecular Rapid Communications,* vol. 37, no. 20, pp. 1676-1681, 2016.

[45] I. Navarro-Baena, A. Marcos-Fernández, A. Fernández-Torres, J. M. Kenny, and L. Peponi, "Synthesis of PLLA-b-PCL-b-PLLA linear tri-block copolymers and their corresponding poly(ester-urethane)s: Effect of the molecular weight on their crystallisation and mechanical properties," *RSC Advances,* vol. 4, no. 17, pp. 8510-8524, 2014.

[46] L. Peponi, I. Navarro-Baena, J. E. Báez, J. M. Kenny, and A. Marcos-Fernández, "Effect of the molecular weight on the crystallinity of PCL-b-PLLA di-block copolymers," *Polymer,* vol. 53, no. 21, pp. 4561-4568, 2012.

[47] D. Yan, H. Huang, T. He, and F. Zhang, "Coupling of Microphase Separation and Dewetting in Weakly Segregated Diblock Co-polymer Ultrathin Films," *Langmuir,* doi: 10.1021/la202379b vol. 27, no. 19, pp. 11973-11980, 2011/10/04 2011.

[48] M. T. Casas, J. Puiggalí, J. M. Raquez, P. Dubois, M. E. Córdova, and A. J. Müller, "Single crystals morphology of biodegradable double crystalline PLLA-b-PCL diblock copolymers," *Polymer,* vol. 52, no. 22, pp. 5166-5177, 2011.

[49] J. L. Wang and C. M. Dong, "Synthesis, sequential crystallization and morphological evolution of well-defined star-shaped poly(ε-caprolactone)-b-poly(L-lactide) block copolymer," *Macromolecular Chemistry and Physics,* vol. 207, no. 5, pp. 554-562, 2006.

[50] O. Jeon, S. H. Lee, S. H. Kim, Y. M. Lee, and Y. H. Kim, "Synthesis and characterization of poly(L-lactide)-poly(ε-caprolactone) multiblock copolymers," *Macromolecules,* vol. 36, no. 15, pp. 5585-5592, 2003.

[51] R. M. Ho, P. Y. Hsieh, W. H. Tseng, C. C. Lin, B. H. Huang, and B. Lotz, "Crystallization-Induced Orientation for Microstructures of Poly(L-lactide)-b-poly(ε-caprolactone) Diblock Copolymers," *Macromolecules,* vol. 36, no. 24, pp. 9085-9092, 2003.

[52] L. Ostacolo *et al.*, "In vitro anticancer activity of docetaxel-loaded micelles based on poly(ethylene oxide)-poly(epsilon-caprolactone) block copolymers: Do nanocarrier properties have a role?," *Journal of Controlled Release,* vol. 148, no. 2, pp. 255-263, 2010.

[53] S. Zhou, X. Deng, and H. Yang, "Biodegradable poly(ε-caprolactone)-poly(ethylene glycol) block copolymers: characterization and their use as drug carriers for a controlled delivery system," *Biomaterials,* vol. 24, no. 20, pp. 3563-3570, 2003.

[54] D. W. Lim and T. G. Park, "Stereocomplex formation between enantiomeric PLA-PEG-PLA triblock copolymers: characterization and use as protein-delivery microparticulate carriers," *Journal of Applied Polymer Science,* vol. 75, no. 13, pp. 1615-1623, 2000.

[55] H. Danafar, "Applications of copolymeric nanoparticles in drug delivery systems," *Drug Research,* Review vol. 66, no. 10, pp. 506-519, 2016.

[56] X. Guo, L. Wang, X. Wei, and S. Zhou, "Polymer-based drug delivery systems for cancer treatment," *Journal of Polymer Science, Part A: Polymer Chemistry,* Review vol. 54, no. 22, pp. 3525-3550, 2016.

[57] C. Schick and R. Androsch, "New Insights into Polymer Crystallization by Fast Scanning Chip Calorimetry," in *Fast Scanning Calorimetry*, C. Schick and V. Mathot, Eds. Cham: Springer International Publishing, 2016, pp. 463-535.

[58] N. Sbirrazzuoli, N. Guigo, and S. Vyazovkin, "Isoconversional Kinetics by Fast Scanning Calorimetry," in *Fast Scanning Calorimetry*, C. Schick and V. Mathot, Eds. Cham: Springer International Publishing, 2016, pp. 237-257.

[59] G. Strobl, *The Physics of Polymers*. Verlag Berlin Heidelberg: Springer, 2007, pp. 1-518.

[60] D. W. van Krevelen and K. te Nijenhuis, *Properties of polymers*, 4 ed. Amsterdam: Elsevier B.V., 2009.

[61] U. W. Gedde, *Polymer Physics*. London: Chapman & Hall, 1995.

[62] A. J. Müller, R. M. Michell, and A. T. Lorenzo, "Isothermal Crystallization Kinetics of Polymers," in *Polymer Morphology: Principles, Characterization, and Processing*, Q. Guo, Ed. Hoboken, NJ: John Wiley & Sons, Inc, 2016, pp. 181-203.

[63] L. Mandelkern, *Crystallization of Polymers: Volume 2, Kinetics and Mechanisms*. Cambridge University Press, 2004.

[64] L. H. Sperling, *Introduction to physical polymer science*. New Jersey: Wiley Interscience, 2006.

[65] D. M. Sadler and G. H. Gilmer, "Selection of lamellar thickness in polymer crystal growth: A rate-theory model," *Physical Review B,* vol. 38, no. 8, pp. 5684-5693, 09/15/ 1988.

[66] E. Ergoz, J. G. Fatou, and L. Mandelkern, "Molecular Weight Dependence of the Crystallization Kinetics of Linear Polyethylene. I. Experimental Results," *Macromolecules,* doi: 10.1021/ma60026a011 vol. 5, no. 2, pp. 147-157, 1972/03/01 1972.

[67] F. v. Göler and G. Sachs, "Zur Kinetik von Kristallisationsvorgängen," *Physik,* vol. 77, no. 5, pp. 281-286, 1932// 1932.

[68] A. T. Lorenzo, M. L. Arnal, J. Albuerne, and A. J. Müller, "DSC isothermal polymer crystallization kinetics measurements and the use of the Avrami equation to fit the data: Guidelines to avoid common problems," *Polymer Testing,* vol. 26, no. 2, pp. 222-231, 2007.

[69] J. M. Schultz, *Polymer Crystallization*. Oxford, 2001.

[70] F. Azurri, *Melt Crystallization and Polymorphic Transformation in Isotactic Poly (1-butene) based materials* (PhD Thesis). Genova: Universita´Degli Studi di Genova, 2003, pp. 1-388.

[71] A. Jimenez, M. Peltzer, and R. Ruseckaite, *Poly(lactic acid) Science and Technology: Processing, Properties, Additives and Applications*. Cambridge: The Royal Society of Chemistry, 2015, pp. 1-353.

[72] R. Auras, L. T. Lim, S. E. M. Selke, and H. Tsuji, *Poly(lactic acid).Synthesis, Structures, Properties, Processing, and Applications*. Hoboken, NJ, USA: John Wiley & Sons, 2010.

[73] S. Fiori, "Industrial Uses of PLA," in *Poly(lactic acid) Science and Technology: Processing, Properties, Additives and Applications*, vol. 12, A. Jimenez, M. Peltzer, and R. Ruseckaite, Eds. (RSC Polymer Chemistry Series, Cambridge: The Royal Society of Chemistry, 2015, pp. 317-333.

[74] L. S. Nair and C. T. Laurencin, "Biodegradable polymers as biomaterials," *Progress in Polymer Science,* vol. 32, no. 8–9, pp. 762-798, 8// 2007.

[75] A. J. Müller, M. Avila, G. Saenz, and J. Salazar, "Crystallization of PLA-based Materials," in *Poly(lactic acid) Science and Technology: Processing, Properties, Additives and Applications*, vol. 12, A. Jimenez, M. Peltzer, and R. Ruseckaite, Eds. (RSC Polymer Chemistry Series Cambridge: The Royal Society of Chemistry, 2015, pp. 66-98.

[76] D. E. Henton, P. Gruber, J. Lunt, and J. Randall, "Polylactic Acid Technology," in *Natural Fibers, Biopolymers, and Biocomposites*, A. K. Mohanty, M. Misra, and L. T. Drzal, Eds. Boca Raton, FL, USA: Taylor & Francis, 2005.

[77] F. J. v. Natta, J. W. Hill, and W. H. Carothers, "Studies of Polymerization and Ring Formation. XXIII.1 ε-Caprolactone and its Polymers," *Journal of the American Chemical Society,* vol. 56, no. 2, pp. 455-457, 1934/02/01 1934.

[78] M. A. Woodruff and D. W. Hutmacher, "The return of a forgotten polymer—Polycaprolactone in the 21st century," *Progress in Polymer Science,* vol. 35, no. 10, pp. 1217-1256, 10// 2010.

[79] D. E. Perrin and J. P. English, "Polycaprolactone," in *Handbook of Biodegradable Polymers*, A. J. Domb, J. Kost, and D. M. Wiseman, Eds. USA: CRC Press, 1997.

[80] A. L. Sisson, D. Ekinci, and A. Lendlein, "The contemporary role of ε-caprolactone chemistry to create advanced polymer architectures," *Polymer,* vol. 54, no. 17, pp. 4333-4350, 8/2/ 2013.

[81] R. Chandra and R. Rustgi, "Biodegradable polymers," *Progress in Polymer Science,* vol. 23, no. 7, pp. 1273-1335, 11// 1998.

[82] K. R. Chynoweth and Z. H. Stachurski, "Crystallization of poly(ε-caprolactone)," *Polymer,* vol. 27, no. 12, pp. 1912-1916, 1986/12/01 1986.

[83] *Polyethylene glycol (PEG): Market analysis by application (medical, personal care, industrial) and segment forecasts to 2020*. Available: http://www.grandviewresearch.com/industry-analysis/polyethylene-glycol-peg-market

[84] D. M. Back and R. L. Schmitt, "Ethylene Oxide Polymers," in *Encyclopedia of Polymer Science and Technology*: John Wiley & Sons, Inc., 2002.

[85] M. J. Barthel, F. H. Schacher, and U. S. Schubert, "Poly(ethylene oxide) (PEO)-based ABC triblock terpolymers-synthetic complexity vs. application benefits," *Polymer Chemistry,* vol. 5, no. 8, pp. 2647-2662, 2014.

[86] D. H. Richards and M. Szwarc, "Block polymers of ethylene oxide and its analogues with styrene," *Transactions of the Faraday Society,* 10.1039/TF9595501644 vol. 55, no. 0, pp. 1644-1650, 1959.

[87] L. Wu, M. Lisowski, S. Talibuddin, and J. Runt, "Crystallization of Poly(ethylene oxide) and Melt-Miscible PEO Blends," *Macromolecules,* vol. 32, no. 5, pp. 1576-1581, 1999/03/01 1999.

[88] C. He *et al.*, "Study of the synthesis, crystallization, and morphology of poly(ethylene glycol) - Poly(ε-caprolactone) diblock copolymers," *Biomacromolecules,* vol. 5, no. 5, pp. 2042-2047, 2004.

[89] C. He, J. Sun, J. Ma, X. Chen, and X. Jing, "Composition dependence of the crystallization behavior and morphology of the poly(ethylene oxide)-poly(ε-caprolactone) diblock copolymer," *Biomacromolecules,* vol. 7, no. 12, pp. 3482-3489, 2006.

[90] G. A. Abraham, A. Marcos-Fernández, and J. San Román, "Bioresorbable poly(ester-ether urethane)s from L-lysine diisocyanate and triblock copolymers

with different hydrophilic character," *Journal of Biomedical Materials Research Part A,* vol. 76A, no. 4, pp. 729-736, 2006.

[91] Y. K. Choi, Y. H. Bae, and S. W. Kim, "Star-shaped poly(ether-ester) block copolymers: Synthesis, characterization, and their physical properties," *Macromolecules,* vol. 31, no. 25, pp. 8766-8774, 1998.

[92] C. Lu, S. R. Guo, Y. Zhang, and M. Yin, "Synthesis and aggregation behavior of four types of different shaped PCL-PEG block copolymers," *Polymer International,* vol. 55, no. 6, pp. 694-700, 2006.

[93] Z. X. Du, J. T. Xu, Y. Yang, and Z. Q. Fan, "Synthesis and characterization of poly(ε-caprolactone)-b-poly(ethylene glycol) block copolymers prepared by a salicylaldimine-aluminum complex," *Journal of Applied Polymer Science,* vol. 105, no. 2, pp. 771-776, 2007.

[94] S. J. Bae, J. M. Suh, Y. S. Sohn, Y. H. Bae, S. W. Kim, and B. Jeong, "Thermogelling poly(caprolactone-6-ethylene glycol-b-caprolactone) aqueous solutions," *Macromolecules,* vol. 38, no. 12, pp. 5260-5265, 2005.

[95] P. P. Ghoroghchian *et al.*, "Bioresorbable vesicles formed through spontaneous self-assembly of amphiphilic poly(ethylene oxide)-block-polycaprolactone," *Macromolecules,* vol. 39, no. 5, pp. 1673-1675, 2006.

[96] W. Zhu, W. Xie, X. Tong, and Z. Shen, "Amphiphilic biodegradable poly(CL-b-PEG-b-CL) triblock copolymers prepared by novel rare earth complex: Synthesis and crystallization properties," *European Polymer Journal,* vol. 43, no. 8, pp. 3522-3530, 2007.

[97] T. Shiomi, K. Imai, K. Takenaka, H. Takeshita, H. Hayashi, and Y. Tezuka, "Appearance of double spherulites like concentric circles for poly(ε-caprolactone)-block-poly(ethylene glycol)-block-poly(ε-caprolactone)," *Polymer,* vol. 42, no. 7, pp. 3233-3239, 2001.

[98] H. Takeshita *et al.*, "Formation of lamellar structure by competition in crystallization of both components for crystalline-crystalline block copolymers," *Polymer,* vol. 47, no. 24, pp. 8210-8218, 2006.

[99] Z. X. Du, Y. Yang, J. T. Xu, and Z. Q. Fan, "Effect of molecular weight on spherulitic growth rate of poly(ε-caprolactone) and poly(ε-caprolactone)-b-poly(ethylene glycol)," *Journal of Applied Polymer Science,* vol. 104, no. 5, pp. 2986-2991, 2007.

[100] T. Yu *et al.*, "Solution crystallization behavior of linear and star-shaped poly(ethylene glycol)-b-poly(É"-caprolactone) block copolymers," *Chinese Journal of Polymer Science (English Edition),* Article vol. 31, no. 12, pp. 1717-1724, 2013.

[101] G. Maglio, A. Migliozzi, and R. Palumbo, "Thermal properties of di- and triblock copolymers of poly(l-lactide) with poly(oxyethylene) or poly(ε-caprolactone)," *Polymer,* vol. 44, no. 2, pp. 369-375, 2003.

[102] D. Kubies, F. Rypáček, J. Kovářová, and F. Lednický, "Microdomain structure in polylactide-block-poly(ethylene oxide) copolymer films," *Biomaterials,* vol. 21, no. 5, pp. 529-536, 2000.

[103] I. Rashkov, N. Manolova, S. M. Li, J. L. Espartero, and M. Vert, "Synthesis, Characterization, and Hydrolytic Degradation of PLA/PEO/PLA Triblock Copolymers with Short Poly(l-lactic acid) Chains," *Macromolecules,* doi: 10.1021/ma950530t vol. 29, no. 1, pp. 50-56, 1996/01/01 1996.

[104] J. Yang, Y. Liang, J. Luo, C. Zhao, and C. C. Han, "Multilength scale studies of the confined crystallization in poly(l -lactide)- block -poly(ethylene glycol) copolymer," *Macromolecules,* vol. 45, no. 10, pp. 4254-4261, 2012.

[105] A. J. Müller, V. Balsamo, and M. L. Arnal, "Nucleation and crystallization in diblock and triblock copolymers," *Advances in Polymer Science,* vol. 190, pp. 1-63, 2005.

[106] R. V. Castillo *et al.*, "Fractionated crystallization and fractionated melting of confined PEO microdomains in PB-b-PEO and PE-b-PEO diblock copolymers," *Macromolecules,* vol. 41, no. 3, pp. 879-889, 2008.

[107] A. J. Müller, V. Balsamo, M. L. Arnal, T. Jakob, H. Schmalz, and V. Abetz, "Homogeneous nucleation and fractionated crystallization in block copolymers," *Macromolecules,* Article vol. 35, no. 8, pp. 3048-3058, 2002.

[108] J. K. Kim, D. J. Park, M. S. Lee, and K. J. Ihn, "Synthesis and crystallization behavior of poly(L-lactide)-block-poly(ε-caprolactone) copolymer," *Polymer,* vol. 42, no. 17, pp. 7429-7441, 2001.

[109] I. Navarro-Baena, A. Marcos-Fernandez, J. M. Kenny, and L. Peponi, "Crystallization behavior of diblock copolymers based on PCL and PLLA biopolymers," *Journal of Applied Crystallography,* vol. 47, no. 6, pp. 1948-1957, 2014.

[110] Y.-W. Chiang, Y.-Y. Hu, J.-N. Li, S.-H. Huang, and S.-W. Kuo, "Trilayered Single Crystals with Epitaxial Growth in Poly(ethylene oxide)-block-poly(ε-caprolactone)-block-poly(l-lactide) Thin Films," *Macromolecules,* vol. 48, no. 23, pp. 8526-8533, 2015/12/08 2015.

[111] J. Zhao, D. Pahovnik, Y. Gnanou, and N. Hadjichristidis, "Sequential polymerization of ethylene oxide, ε-caprolactone and l-lactide: A one-pot metal-free route to tri- and pentablock terpolymers," *Polymer Chemistry,* vol. 5, no. 12, pp. 3750-3753, 2014.

[112] B. Guillerm *et al.*, "A one-pot two-step efficient metal-free process for the generation of PEO-b-PCL-b-PLA amphiphilic triblock copolymers," *RSC Advances,* vol. 4, no. 20, pp. 10028-10038, 2014.

[113] L. Sun, L. J. Shen, M. Q. Zhu, C. M. Dong, and Y. Wei, "Synthesis, self-assembly, drug-release behavior, and cytotoxicity of triblock and pentablock copolymers composed of poly(ε-caprolactone), poly(L -lactide), and poly(ethylene glycol)," *Journal of Polymer Science Part A: Polymer Chemistry,* vol. 48, no. 20, pp. 4583-4593, 2010.

[114] V. Tamboli, G. P. Mishra, and A. K. Mitra, "Novel pentablock copolymer (PLA-PCL-PEG-PCL-PLA)-based nanoparticles for controlled drug delivery: Effect of copolymer compositions on the crystallinity of copolymers and in vitro drug release profile from nanoparticles," *Colloid and Polymer Science,* vol. 291, no. 5, pp. 1235-1245, 2013.

[115] N. Hadjichristidis, H. Iatrou, M. Pitsikalis, S. Pispas, and A. Avgeropoulos, "Linear and non-linear triblock terpolymers. Synthesis, self-assembly in selective solvents and in bulk," *Progress in Polymer Science,* vol. 30, no. 7, pp. 725-782, 2005.

[116] C. C. Liu, W. C. Chu, J. G. Li, and S. W. Kuo, "Mediated competitive hydrogen bonding form mesoporous phenolic resins templated by poly(ethylene oxide-b-ε-caprolactone-b-L-lactide) triblock copolymers," *Macromolecules,* vol. 47, no. 18, pp. 6389-6400, 2014.

[117] J. K. Palacios *et al.*, "Sequential crystallization and morphology of triple crystalline biodegradable PEO-b-PCL-b-PLLA triblock terpolymers," *RSC Advances,* 10.1039/C5RA25812J vol. 6, no. 6, pp. 4739-4750, 2016.

[118] I. W. Hamley and V. Castelletto, "Small-angle scattering of block copolymers in the melt, solution and crystal states," *Progress in Polymer Science,* vol. 29, no. 9, pp. 909-948, 2004.

[119] L. Leibler, "Theory of microphase separation in block copolymers," *Macromolecules,* vol. 13, no. 6, pp. 1602-1617, 1980.

[120] I. W. Hamley, *The Physics of Block Copolymers*. Oxford Oxford University Press, 1998.

[121] V. Abetz and P. F. W. Simon, "Phase behaviour and morphologies of block copolymers," *Advances in Polymer Science,* vol. 189, pp. 125-212, 2005.

[122] M. Rubinstein and R. H. Colby, *Polymer Physics*. Oxford: OUP 2003.

[123] A. J. Muller, M. Avila, G. Saenz, and J. Salazar, "Crystallization of PLA-based Materials," in *Poly(lactic acid) Science and Technology: Processing, Properties, Additives and Applications*, vol. 12, A. Jimenez, M. Peltzer, and R. Ruseckaite, Eds. (RSC Polymer Chemistry Series Cambridge: The Royal Society of Chemistry, 2015, pp. 66-98.

[124] J. K. Kim, D.-J. Park, M.-S. Lee, and K. J. Ihn, "Synthesis and crystallization behavior of poly(l-lactide)-block-poly(ε-caprolactone) copolymer," *Polymer,* vol. 42, no. 17, pp. 7429-7441, 2001.

[125] S. Huang and S. Jiang, "Structures and morphologies of biocompatible and biodegradable block copolymers," *RSC Advances*, vol. 4, no. 47, pp. 24566-24583, 2014.

[126] Y.-W. Chiang, Y.-Y. Hu, J.-N. Li, S.-H. Huang, and S.-W. Kuo, "Trilayered Single Crystals with Epitaxial Growth in Poly(ethylene oxide)-block-poly(ε-caprolactone)-block-poly(l-lactide) Thin Films," doi: 10.1021/acs.macromol.5b02042, 2015/11/23, 2015.

[127] J. R. Sarasua, R. E. Prud'homme, M. Wisniewski, A. Le Borgne, and N. Spassky, "Crystallization and melting behavior of polylactides," *Macromolecules,* vol. 31, no. 12, pp. 3895-3905, 1998.

[128] Y. Wang and J. F. Mano, "Influence of melting conditions on the thermal behaviour of poly(l-lactic acid)," *European Polymer Journal,* vol. 41, no. 10, pp. 2335-2342, 2005.

[129] M. L. Di Lorenzo, "Calorimetric analysis of the multiple melting behavior of poly(L-lactic acid)," *Journal of Applied Polymer Science,* vol. 100, no. 4, pp. 3145-3151, 2006.

[130] J. Zhang, K. Tashiro, H. Tsuji, and A. J. Domb, "Disorder-to-order phase transition and multiple melting behavior of poly(L-lactide) investigated by simultaneous measurements of WAXD and DSC," *Macromolecules,* vol. 41, no. 4, pp. 1352-1357, 2008.

[131] A. J. Müller, M. L. Arnal, and V. Balsamo, "Crystallization in block copolymers with more than one crystallizable block," in *Lecture Notes in Physics* vol. 714, ed, 2007, pp. 229-259.

[132] A. J. Müller, M. L. Arnal, and A. T. Lorenzo, "Crystallization in Nano-Confined Polymeric Systems," in *Handbook of Polymer Crystallization*, E. Piorkowska and G. C. Rutledge, Eds. Hoboken, New Jersey: John Wiley and Sons, 2013, pp. 347-372.

[133] R. M. Michell and A. J. Muller, "Confined crystallization of polymeric materials," 2015.

[134] S. Li and R. A. Register, "Crystallization in Copolymers " in *Handbook of Polymer Crystallization*, E. Piorkowska and G. C. Rutledge, Eds. Hoboken, New Jersey: John Wiley and Sons, 2013, pp. 327-346.

[135] W. N. He and J. T. Xu, "Crystallization assisted self-assembly of semicrystalline block copolymers," *Progress in Polymer Science,* vol. 37, no. 10, pp. 1350-1400, 2012.

[136] H. Zhou and G. L. Wilkes, "Comparison of lamellar thickness and its distribution determined from DSC, SAXS, TEM and AFM for high-density polyethylene films having a stacked lamellar morphology," *Polymer,* vol. 38, no. 23, pp. 5735-5747, 1997/11/01 1997.

[137] T. Miyata and T. Masuko, "Crystallization behaviour of poly(l-lactide)," *Polymer,* vol. 39, no. 22, pp. 5515-5521, 1998.

[138] E. W. Fischer, H. J. Sterzel, and G. Wegner, "Investigation of the structure of solution grown crystals of lactide copolymers by means of chemical reactions," *Kolloid-Zeitschrift und Zeitschrift für Polymere,* vol. 251, no. 11, pp. 980-990, 1973// 1973.

[139] D. Trifonova, J. Varga, and G. J. Vancso, "AFM study of lamellar thickness distributions in high temperature melt-crystallization of β-polypropylene," *Polymer Bulletin,* vol. 41, no. 3, pp. 341-348, 1998// 1998.

[140] W. Hoogsteen, A. R. Postema, A. J. Pennings, G. Ten Brinke, and P. Zugenmaier, "Crystal structure, conformation and morphology of solution-spun poly(L-lactide) fibers," *Macromolecules,* doi: 10.1021/ma00204a041 vol. 23, no. 2, pp. 634-642, 1990/01/01 1990.

[141] Y. Chatani, Y. Okita, H. Tadokoro, and Y. Yamashita, "Structural Studies of Polyesters. III. Crystal Structure of Poly-[epsi]-caprolactone," *Polym J,* vol. 1, no. 5, pp. 555-562, 1970.

[142] J. Zhang *et al.*, "Crystal Modifications and Thermal Behavior of Poly(l-lactic acid) Revealed by Infrared Spectroscopy," *Macromolecules,* vol. 38, no. 19, pp. 8012-8021, 2005/09/01 2005.

[143] J. Zhang, K. Tashiro, A. J. Domb, and H. Tsuji, "Confirmation of Disorder α Form of Poly(L-lactic acid) by the X-ray Fiber Pattern and Polarized IR/Raman Spectra Measured for Uniaxially-Oriented Samples," *Macromolecular Symposia,* vol. 242, no. 1, pp. 274-278, 2006.

[144] T. Kawai *et al.*, "Crystallization and Melting Behavior of Poly (l-lactic Acid)," *Macromolecules,* vol. 40, no. 26, pp. 9463-9469, 2007/12/01 2007.

[145] P. Pan, B. Zhu, W. Kai, T. Dong, and Y. Inoue, "Effect of crystallization temperature on crystal modifications and crystallization kinetics of poly(L-lactide)," *Journal of Applied Polymer Science,* vol. 107, no. 1, pp. 54-62, 2008.

[146] M. C. Righetti, M. Gazzano, M. L. Di Lorenzo, and R. Androsch, "Enthalpy of melting of α′- and α-crystals of poly(l-lactic acid)," *European Polymer Journal,* vol. 70, pp. 215-220, 9// 2015.

[147] H. Tadokoro, Y. Chatani, T. Yoshihara, S. Tahara, and S. Murahashi, "Structural studies on polyethers, [-(CH2)m-O-]n. II. Molecular structure of polyethylene oxide," *Die Makromolekulare Chemie,* vol. 73, no. 1, pp. 109-127, 1964.

[148] K. Schmidt-Rohr, "Simulation of small-angle scattering curves by numerical Fourier transformation," *Journal of Applied Crystallography,* vol. 40, no. 1, pp. 16-25, 02/01 2007.

[149] T. A. J. Kobayashi , M. Ichiki , A. Oikawa , H. Suzuki , T. Watanabe , E. Fukada , and Y. Shikinami, "Structural and optical properties of poly lactic

acids," *Journal of Applied Physics,* vol. 77, no. 7, pp. 2957-2973, 1995/04/01 1995.

[150] H. Bittiger, R. H. Marchessault, and W. D. Niegisch, "Crystal structure of poly-[epsilon]-caprolactone," *Acta Crystallographica Section B,* vol. 26, no. 12, pp. 1923-1927, 12/15 1970.

[151] V. Crescenzi, G. Manzini, G. Calzolari, and C. Borri, "Thermodynamics of fusion of poly-β-propiolactone and poly-ϵ-caprolactone. comparative analysis of the melting of aliphatic polylactone and polyester chains," *European Polymer Journal,* vol. 8, no. 3, pp. 449-463, 3// 1972.

[152] M. R. Hosemann and S. N. Bagchi, *Direct Analysis of Diffraction*. North-Holland, Amsterdam: Interscience, New York, 1962.

[153] S. Fischer, O. Marti, T. Diesner, and B. Rieger, "Small-Angle X-ray Scattering on Melt-Spun Polypropylene Fibers: Modeling and Data Reduction," *Macromolecules,* vol. 43, no. 11, pp. 5009-5015, 2010/06/08 2010.

[154] B. Wunderlich, *Crystal Structure, Morphology and Defects* (Macromolecular Physics). New York: Academic Press, 1973.

[155] P. Pan, W. Kai, B. Zhu, T. Dong, and Y. Inoue, "Polymorphous crystallization and multiple melting behavior of poly(L-lactide): Molecular weight dependence," *Macromolecules,* vol. 40, no. 19, pp. 6898-6905, 2007.

[156] M. Salmerón Sánchez, V. B. F. Mathot, G. Vanden Poel, and J. L. Gómez Ribelles, "Effect of the Cooling Rate on the Nucleation Kinetics of Poly(l-Lactic Acid) and Its Influence on Morphology," *Macromolecules,* doi: 10.1021/ma0712706 vol. 40, no. 22, pp. 7989-7997, 2007/10/01 2007.

[157] M. Avrami, "Kinetics of Phase Change. I General Theory," *The Journal of Chemical Physics,* doi: 10.1063/1.1750380 vol. 7, no. 12, pp. 1103-1112, 1939/12/01 1939.

[158] M. Avrami, "Kinetics of Phase Change. II Transformation-Time Relations for Random Distribution of Nuclei," *The Journal of Chemical Physics,* doi: 10.1063/1.1750631 vol. 8, no. 2, pp. 212-224, 1940/02/01 1940.

[159] M. Avrami, "Granulation, Phase Change, and Microstructure Kinetics of Phase Change. III," *The Journal of Chemical Physics,* doi: 10.1063/1.1750872 vol. 9, no. 2, pp. 177-184, 1941/02/01 1941.

[160] A. N. Kolmogorov, "Zur Statistik der Kristallisationsvorgänge in Metallen," *Izv. Akad. Nauk SSSR Ser. Mat.,* vol. 1, no. 3, pp. 355-359, 1937.

[161] W. A. Johnson and R. F. Mehl, "Reaction Kinetics in processes of nucleation and growth," *Transactions of American Institute of Mining and Metallurgical Engineers*, vol. 135, pp. 416-458, 1939.

[162] J. M. Schultz, *Polymeric Crystallization*. Oxford, 2001.

CHAPTER III

FAST SCANNING CALORIMETRY

The aim of this chapter is to describe the advantages of the novel Fast Scanning Calorimetry (FSC) technique and give some examples of its use in the study of polymer characterization and isothermal crystallization analysis. To that purpose, a particular set of samples were selected from those studied in Chapter 2. The materials to be evaluated are: PCL, PEO and PLLA homopolymers, a PCL-*b*-PLLA diblock copolymer and a PEO-*b*-PCL-*b*-PLLA triblock terpolymer.

3.1 GENERAL CONCEPTS

3.1.1 Fast Scanning Calorimetry

Conventional processing techniques in polymers, such as casting, extrusion and injection molding, involve very high speed coolings between 1 and 10,000 K s^{-1}. Modern conventional DSC is not able to model the crystallization conditions imposed to polymers during processing, since the typical scanning rates are between 0.1 and 100 K min^{-1}. After processing at such high rates, polymers may exhibit metastable crystalline structures or polymorphic phases. To analyze these metastable structures, a heating scan can be performed in a DSC. However, at the typical low heating rates of a conventional DSC, these metastable or polymorphic structures can undergo reorganization effects during heating that may lead to a misinterpretation of the actual structure before the heating scan [1].

To overcome the aforementioned issues, the novel Fast Scanning Calorimetry (FSC) technique emerged [2, 3]. A widening of the scanning rate range for dynamic calorimetry was in demand in order to properly analyze processing relevant cooling rates, and to study the kinetics of fast transformations and reorganization of metastable materials during heating. FSC expands the scope for phase transformations researches not only for polymers but for a wide range of materials. Particularly in polymers, FSC allows to assess several studies, such as [1]:

- Investigation of reorganization and formation phenomena on heating.
- Determination of the original melt crystallized structure by suppressing reorganization or diffusion on heating.
- Measurement of crystallization kinetics in a wide range of cooling rates and temperatures, upon fast cooling from the melt or fast heating from the glassy state.

- Measurement of isothermal crystallization of undercooled or supercooled liquids.
- Influence of additives on the crystallization behavior with a high degree of supercooling.
- Glass formation and vitrification.
- Simulation of processing conditions at the corresponding cooling rate.

In order to achieve high heating and cooling rates two conditions must be fulfilled: the heat capacity of the calorimeter must be small, and the calorimeter must be surrounded by a gas at very low temperature with a thermal resistance sufficiently small. Higher cooling rates can be attained when the gas temperature decreases and the heat conductivity decreases [1].

The calorimeter must be small in order to reach a very small heat capacity. In other worlds, the related volumes of the calorimeter have to be as low as possible. The novelty in FSC is that the calorimeter is composed of a tinny chip sensor with a thin Si3Nx – membrane in the middle and all the electronic components for the heater and temperature sensor integrated inside. These sensors are fabricated using integrated circuit technology.

Compared to conventional DSC, the FSC instruments has low signal time constant. Due to the particular size of the furnaces in regular DSC, the instrument time constant is between 1 and ten of seconds, and therefore, the possible cooling rates are typically between 0.1 and 100 K min^{-1} [4]. On the contrary, FSC has a very low signal time constant, typically less than 1 ms. This very low constant value allows very high heating and cooling rates, between 30 and 2,400,000 K min^{-1} [1]. Therefore, the FSC and DSC measurements can overlap in a scanning rate range of more than one decade [5].

Due to the very small size of the FSC calorimeter, the sample must fulfill the following requirements [1]:

- The sample needs to be thin in order to avoid big temperature gradients inside the sample.

- To follow fast temperature changes on cooling and heating, the sample must have a good thermal contact to both the calorimeter and the surrounding gas.

- To follow high rates, the sample mass has to be very small. The larger the sample is, the lower is the maximum scan rate that can be used.

3.1.2 The Flash DSC 1 equipment

Mettler Toledo brand commercializes the only FSC available in the market, the Flash DSC 1. The equipment is coupled with a microscope and an optional camera to facilitate the placement of the sample on the sensor, as can be seen in Figure 3.1. The instrument can be used with different types of sensors. However, the UFS1 sensor is the only one commercialized by Mettler Toledo. It has a low signal time constant (less than 1 ms) that allows very high heating and cooling rates. The equipment has excellent sensitivity in a broad range of heating and cooling rates. On heating, the typical rates extend from 0.5 to 40,000 K s^{-1} (30–2,400,000 K min^{-1}). Therefore, the Flash DSC measurements at low rates complement with those obtained from conventional DSC at high rates. Both instruments combined allow covering a heating and cooling rate range of more than seven decades, which is a great advantage in order to cover a wide scope of phenomenological process. The suitable heating rate in the Flash DSC depends on the sample properties, the experimental conditions and the temperature range [1].

Figure 3.1 The Flash DSC instrument from Mettler Toledo

3.1.3 The UFS1 Sensor

The USF 1 sensor consists of microchip embedded in a ceramic support. It contains all the electrical contacts and a membrane in the middle. The microchip sensor is based on MEMS technology (MEMS: Micro-Electro-Mechanical Systems) and it consists of two identical quadratic membranes (two calorimeters), one for the sample and the other for the reference (see Figure 3.2). Therefore, the microchip truly operates like a conventional power compensation DSC but without the need of pans [6]. Each membrane represents a furnace and the temperature difference between the two is kept to zero. The temperature difference between sample side and reference side can be measured using indium [1].

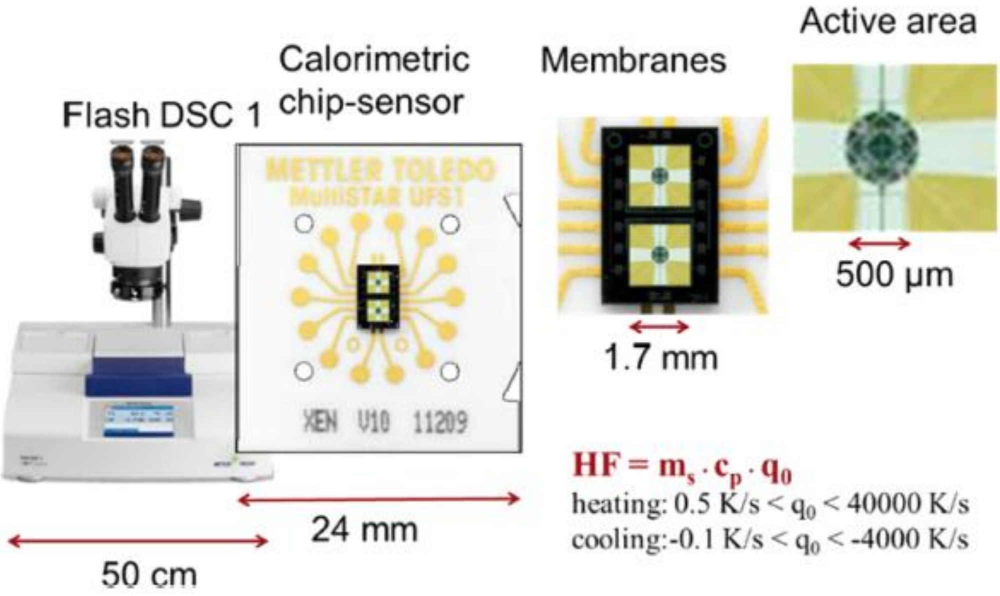

Figure 3.2 Mettler-Toledo Flash DSC 1 and its UFS 1 sensor in different magnifications [7].

The membranes are composed of silicon nitride. Their length and thickness are 1.7 mm and 2µm, respectively, and they are mounted in a silicon frame with a thickness of 300 µm. The effective measurement area is a circle of 0.5 mm of diameter in the middle of each the membrane (see Figure 3.2). It is coated with aluminum in order to achieve a homogeneous temperature profile. These sample area is the actual “furnace”. The temperature of the sample is measured with eight thermocouples [1].

The sensor is fixed with a clamping disc to the support. The temperature measurements on the sensor are performed using thermocouples with a defined reference temperature for the cold junction. The temperature of the sensor support, T_{SS}, is the reference temperature [1].

Many are the sensors that can be used with Flash DSC 1 [8-11]. However, the UFS 1 commercialized by Mettler Toledo comprises several advantages [1]:

- The relatively high thickness of membrane gives to the sensor high robustness.
- The large heating area facilitates the sample positioning.
- Measuring thermal transitions at relatively slow scanning rates, which allow overlapping the evaluations to conventional DSC measurements.
- Measuring of relatively large sample mass.

3.1.4 Features of the Flash DSC 1

The gas

The Flash DSC 1 operates in a wide range of scanning rates. As aforementioned, the surrounding gas is of major importance to achieve very high cooling rates. Nitrogen is the typical gas used and it is sufficiently inert for many samples and experimental conditions. However, other gases are used with the instrument. For instance, argon is typically used for metal samples. It has slightly low heat conductivity and no significant influence on the cooling rate in the high temperature range. Helium has proven to deliver the highest cooling rate possible in the instrument due to its high heat conductivity. However, the maximum use temperature is limited due to the high thermal loss of this gas. The maximum temperature can be increased using a mixture of helium and nitrogen. In general, the gas flow should be set to 50 mL min^{-1} to avoid oxygen contamination [1].

The thermal lag

Unlike conventional DSC instruments, in which the thermal lag (τ_{lag}) between the controlled furnace temperature and the sample temperature is due to the heat transfer between the sensor and the crucible; in the Flash DSC 1 equipment, the τ_{lag} is determined almost exclusively by the sample and its contact to the sensor. The onset temperature of the melting peak (T_{onset}) and the heating rate (β) follows a linear relationship according to the following equation:

$$T_{onset} = T^0_{onset} + \tau_{lag}\beta \qquad \text{Eq. 3-1}$$

where the T^o_{onset} is the onset temperature extrapolated to a heating rate of 0 K s^{-1}.

The typical τ_{lag} values in Flash DSC 1 are between 0.8 and 0.4 ms depending on the sample size and the thermal contact between sample and sensor [1].

Overshooting

During isothermal experiments is mandatory to reach the crystallization temperature at very fast cooling rate, and then stabilize at that temperature as fast as possible without overshooting. In a Flash DSC 1, the crystallization temperature can be reached after about 5.5 ms and the maximum overshoot of the sample temperature can be 0.02 K. Therefore, isothermal process of several tenths of milliseconds can be measured reliably [1].

Temperature Correction

In the Flash DSC 1, the temperature accuracy is smaller than 2 K. In general, errors in the temperature measurement are obtained when the sample size is too thick or too large. For that reason, it is very important to use very small sample mass. The sensor can be calibrated by measuring the melting temperature of known materials. After a sample test, a small piece of the reference material (typically indium) is placed on the sample and the meting temperature is measured. Then, this value can be used to correct the sample temperature [1].

Dynamic Temperature Gradients

In a FSC instrument the sample is positioned directly over the membrane sensor and heated only on the bottom side. Therefore, a temperature gradient is produced inside the sample, between the bottom and the top part. This gradient will be higher as the heating rate and the sample thickness increases and the heat conductivity is lower. The result of a temperature gradient is the shifting of the measured thermal transitions to higher temperatures. Also, the peaks and steps associated to these transitions appear broader. The importance of temperature gradient effects will depend of the sample size, heat capacity and heating rate [1].

If the sample is small and thin, has a simple melting behavior and high thermal conductivity, and the heating rate is above 1000 K s^{-1}, a simple correction of the thermal lag according to Eq.3-1 is sufficient. If the heating rate is below 1000 K s^{-1}, it is not even necessary the correction of the dynamic temperature gradients. These effects become more important in materials with low heat conductivity. For these materials, the sample preparation is crucial. The thermal contact between the sensor and the sample must be as good as possible, the sample mass sufficiently small, around 100 ng, and the sample thickness less than 10 μm. If these requirements are fulfilled, the temperature gradient correction can be neglected, as long as the scanning rates are not higher than 1000 K s^{-1}. Therefore, the sample features and the thermal contact will limit the maximum heating rate. Table 3.1 summarizes the recommended sample mass according to the scanning rate desired for organic materials [1].

Table 3.1 Recommended sample mass according to the scanning rate.

Sample mass (ng)	Scanning rate (K s^{-1})
1000-200	1
500-100	1-30
300-30	30-1000
20	1000-20000
10	>20000

Sample Preparation

In the Flash DSC 1, the sample is usually placed directly on the sensor membrane with the aid of a coupled microscope, or externally, with other techniques. It can be placed in either side of the sensor. If it is needed, the sensors can be placed inside liquids, autoclaves or furnaces in order to put the sample.

The simplest procedure is to place the solid sample directly over the sensor. The sample is cut into very small pieces on a glass slide using knives or scalpels. Then, the glass with the pieces is placed over the sensor and observed with the microscope, in order to check their size. If it is too large, smaller pieces should be cut. To transfer the sample, a very small piece is recovered using a fine hair, and placed in the center of one of the calorimeters with the aid of the coupled microscope (see Figure 3.3). The other calorimeter is left clean since it acts as the reference [1].

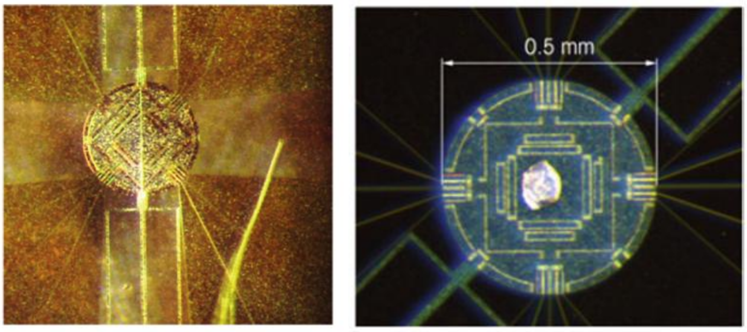

Figure 3.3 Sample area of the UFS 1 sensor. Fine hair to transfer the sample (left), and sample positioned in the center of one of the calorimeters (right) [1].

In some cases, putting a contact medium on the sensor surface, like graphite or oils, is useful to increase the thermal contact between the sample and the sensor, reduce mechanical stresses, prevent possible chemical interaction between the membrane and the sample, and to remove the sample after the measurement. They are also useful to measure the properties of a sample as received during the first heating scan. Oils are more common than graphite as contact medium. They must have high thermal stability, act as a wetting agent of the sensor membrane, no interact with the sample, and no exhibit thermal transitions in the temperature range of interest. The most successful ones are silicon and peanuts oil [1].

The size of the sample will depend of the scan rate desired. For fast scanning rates, the mass of the sample should be small, and viceversa (see Table 3.1). However, large samples could bring some problems. Static internal temperature gradients can be formed and induce additional effects or temperature errors. Additionally, large mass samples can cause mechanical stress on the sensor membrane.

Particularly, polymer samples can be placed by different techniques. For instance, powders or films of less than 10 μm can be put it directly over the sensor. Granulate samples must be cut into small pieces using sharp knives or a microtome with razor blades. Then, a small sample is transferred to the sensor. A good practice prior the test is to melt the polymer at standard rate to create a uniform film over the membrane and optimize the thermal contact between sensor and sample [5]. In testing polymers, the typical mass is between 5 ng and few micrograms. At scan rates above 1000 K s^{-1}, the mass employed is usually around 100 ng. For low rates, below 20 K s^{-1}, several hundred nanograms are preferred [1].

The sample mass can be estimated by different approaches: analyzing the melting enthalpy, ΔH, the heat capacity, C_p, in the melt [12] or the ΔC_p at the glass transition. For instance, the melting enthalpy measured in the Flash DSC 1 can be compared with the one obtained in a conventional DSC, employing the same crystallization protocol. Then, the sample mass, m, can be estimated by the following equation [1]:

$$m = \frac{\Delta H_{FDSC}}{\Delta h} \qquad \text{Eq. 3-2}$$

where ΔH_{FDSC} is the melting enthalpy measured in the Flash DSC 1 and Δh is the melting enthalpy measured in the conventional DSC.

Because polymers have relatively low heat conductivity, the thermal properties and crystallization behavior of a bulk sample (large mass) differ from those of a thin film. For the same reason, high scanning rates requires very small samples. Therefore, it is important to know the critical sample size. This can be done in a simple way by performing the same crystallization protocol in samples of different mass. Once the behavior is reproducible, it can be affirmed that the properties measured correspond to those of the bulk polymer and that will be the minimum sample size [1]. This value will fix the maximum heating rate to measure the bulk properties, according to guidance given in Table 3.1.

3.1.5 Polymer analysis employing FSC

Thermoanalytical techniques have been widely used to study the kinetics of chemical reactions like thermal and thermo-oxidative degradation, decomposition, oxidation and reduction, polymerization, and cross-linking, as well as, physical transformations with temperature, such as crystallization, melting, gelation, vaporization, sublimation, and morphological transitions. The principle is to measure a property, like the heat flow, as a function of temperature (non-isothermal experiment) or as a function of time under constant temperature (isothermal experiment) [13]. DSC is the classical technique to follow the heat flow during these thermal processes. However, the short range of scan rates that can be used limits the scope of the analysis.

Owing to the very fast cooling and heating rates possible in FSC, this technique is highly useful to evaluate several aspects related to the thermal analysis of polymeric materials, including polymer crystallization, reorganization and melting, polymer stability, noncrystalline fraction, glass transition and vitrification [4, 7].

The advantages of FSC faster scanning rates over conventional DSC will be briefly described in the following aspects: reorganization on heating and melting, non-isothermal melt-crystallization and isothermal crystallization kinetics.

Non-isothermal melt-crystallization at different cooling rates

The broad range of cooling and heating rates of FSC allows studying the non-isothermal crystallization upon cooling from the melt. In many polymers, like polyolefins, polyamides and some polyester, it is impossible to obtain completely amorphous samples in a conventional DSC due to their high crystallization kinetics.

However, the crystallization can be suppressed at the very high cooling rates that can be performed in a FSC instrument. The melting or crystallization enthalpy can be analyzed as a function of the scan rate in order to determine the minimum cooling rate to obtain a fully amorphous material. The critical cooling rates to avoid crystallization of some particular polymers are listed in Table 3.2.

However, if the cooling rate decreases, the crystallinity degree increases until it reaches a plateau value indicating the completion of primary crystallization. In other words, the crystallinity is almost independent of the cooling rate at very low cooling rate values [5]. However, in some cases, the crystallinity does not reach a plateau but it keeps increasing to a lesser extent due to a secondary crystallization process [4].

As the cooling rate increases, not only the crystallinity degree reduces but also the crystallization temperature [5]. At a critical cooling rate, the material cannot longer crystallize during cooling. Moreover, polymorphism can be induced and new crystalline phases arise as the cooling rate increases [4, 5]. That is of particular interest from an industrial point of view to establish processing conditions, since most polymer processing techniques involve cooling rates of several hundreds of K s^{-1}, and the properties of the final product will depend on whether the material is amorphous or semicrystalline, the crystallinity degree value, and the type of crystals formed during cooling.

Table 3.2 Critical cooling rates to suppress crystallization from the melt in some polymers.

Polymer	Critical cooling rate to suppress crystallization (K s^{-1})
High-density polyethylene (HDPE) [14]	>1,000,000
Isotactic polypropylene (iPP) [5, 15]	1000
Polyamide 6 (PA6) [16-18]	150, 300, 500
Poly(ethylene terephthalate) (PET) [16, 19]	2, 3
Poly(ε-caprolactone) (PCL) [20]	500
Poly(L-lactic acid) (PLLA) [21]	0.5
Poly(butylene succinate) (PBSu) [22]	70

As the cooling rate increases, not only the crystallinity degree reduces but also the crystallization temperature [5]. At a critical cooling rate, the material cannot longer crystallize during cooling. Moreover, polymorphism can be induced and new crystalline phases arise as the cooling rate increases [4, 5]. That is of particular interest from an industrial point of view to establish processing conditions, since most polymer processing techniques involve cooling rates of several hundreds of K s^{-1}, and the properties of the final product will depend on whether the material is amorphous or semicrystalline, the crystallinity degree value, and the type of crystals formed during cooling.

In order to analyses the crystallization behavior with the scan rate, it is important to start from a truly isotropic melt. Such condition is obtained by variation of the temperature and time of equilibration of the melt prior to the cooling scan. However, in order to obtain a relationship between the cooling rate and the crystallinity achieved, it must be assured that the temperature and residence time of the melt is above the critical values without thermal degradation [4].

Avoiding thermal degradation in FSC is an important issue to take into consideration. Although the residence time to erase thermal history in FSC is very short (only few seconds), heating and cooling the sample repeatedly can cause thermal degradation. A good practice to assure the absence of degradation is to conduct several standard cooling and heating scans prior testing and between tests, and check that the thermal properties have not changed.

Isothermal crystallization kinetics and nucleation

Isothermal crystallization studies consist on crystallizing the sample at a specific constant temperature. To reach that temperature is mandatory to use very fast scan rates to avoid any crystallization prior the isothermal step. The very high speeds available in FSC make it possible to follow the isothermal crystallization kinetics in wide temperature ranges. In some polymers, the whole crystallization window, between T_g and T_m^0, can be evaluated. The analysis can be done upon cooling from the melt (melt crystallization) or re-heating from the glassy state (cold crystallization). In this way, the melt structure prior crystallization at low supercooling differs from that at high supercooling upon heating from a glassy state, and therefore, differences in the primary nucleation mechanism can be evaluated [4].

FSC also allows reducing the time scale of isothermal experiments since it is possible to detect the calorimetric signal at much lower temperatures. For instance, in the isothermal crystallization of polytetrafluoroethylene (PTFE), the time scale of the experiments is about 1 h for DSC measurements and about 0.5 s for FSC measurements [13, 23]. That is one of the major advantages of the FSC instrument for polymer characterization. In many polymers, the minimum half-time of crystallization is lower than a second at specific temperatures. Therefore, the isothermal crystallization cannot be followed by conventional DSC in a wide temperature range.

Nucleation studies can also benefit of the high speed scans of FSC. Cooling a sample from the melt at a very fast rate can suppress the nucleation and a well-defined amorphous state prior to the nuclei-formation step can be obtained. Then, the formation of the nuclei can be induced at different annealing temperatures and times, and finally, the effect of the nucleation on the subsequent cold crystallization kinetics can be assessed. For all these sequences, very high cooling and heating rates are needed. The number of nuclei formed at a pre-defined temperature controls the subsequent semicrystalline morphology after crystallization [4, 20]. FSC is a powerful tool to study the isothermal crystallization kinetics and mechanisms of primary nucleation for many polymers and copolymers at different supercoolings [5, 15, 20, 24-34]. Due to the high scanning rates in FSC, the temperature range of homogeneous nucleation is now accessible in fast crystallizing polymers [7].

Reorganization on heating and melting

Some polymers undergo crystal reorganization phenomena on heating that lead to more stable crystals. Those phenomena include cold crystallization, melt-recrystallization, polymorphic transitions, among others [1]. For instance, during cold crystallization the crystallinity degree of the material increases. Melt-recrystallization is a reorganization phenomenon in which endothermic processes (melting of the existing structure) and exothermic processes (the formation of the new structure) take place simultaneously. Polymorphism involves the transformation of the formed crystals into a different crystalline structure. All these factors affect the final melting of the material.

Therefore, the melting transition observed is not related exclusively to the original structure formed after the crystallization process during cooling. On the contrary, it is a combination of the crystallization and reorganization events that take place on cooling and heating, respectively. Knowing the original thermodynamic stability of the crystals requires suppressing the reorganization processes that occur on heating. However, these phenomena are relatively fast, and suppressing them demands high heating rates that cannot be achieved in conventional DSC. One of the advantages of the FSC instrument is the very high speed scans that it can perform.

That is particularly relevant, when the processing conditions of a material need to be optimized, since the properties of a final product depend on the structure established during processing. For instance, processing techniques like injection molding or film extrusion apply very high supercoolings in few seconds. Under these conditions, less stable crystals can be formed that will tend to reorganize during a subsequent heating. Therefore, to characterize the structural differences in processed materials, the first heating scan of the original sample needs to be recorded without the effect of reorganization phenomena on heating. The critical heating rate to suppress reorganization differs in each polymer [1, 4].

An approach to study reorganization on heating is to cool a sample with specific thermal method, and then record the subsequent heating at increasing scan rates. For instance, an iPP [35] quenched from the melt into the amorphous state exhibited an increase in the T_m value as the heating rate decreases. The cold crystallization and melt-recrystallization into more stable crystals is favored at smaller heating rates. At very high rates, the material no longer cold crystallized and remained amorphous.

However, T_m increases with increasing the heating rate if reorganization is suppressed due to the high heating rate [7, 35]. But, if the heating rate is slow, the reorganization during heating eliminates all structural differences that could be previously created, and the melting remains almost at the same temperature [35]. Therefore, the structural differences created during cooling at different rates can only be detected with the use of sufficiently high heating rates. This is useful information to study the effect of different processing conditions (i.e. cooling rates).

A double-melting peak is a sign of melt-recrystallization in many polymers. This double peak can be transformed into one shifted to higher temperature due to a suppression of the reorganization phenomenon at higher heating rates [36, 37]. Additionally to reorganization suppression, FSC also allows studying superheating of polymer crystals. That is of particular interest since it may help to identify the active mechanisms during polymer melting [4].

Moreover, a good agreement between the equilibrium melting temperature determined by Hoffman-Weeks and Gibbs-Thomson can be established. That is because the secondary process of reorganization and melt-crystallization can be suppressed by ultrafast heating the sample. The zero entropy melting point, determined by extrapolating T_m to zero heating rate, can be used in the Hoffman-Weeks plot [7, 38].

3.2 EXPERIMENTAL PART

3.2.1 Materials

PCL, PEO and PLLA homopolymers, a PCL-*b*-PLLA diblock copolymer and a PEO-*b*-PCL-*b*-PLLA triblock terpolymer were selected to evaluate the FSC technique. The synthesis of these materials has been previously described in Chapter 2. Table 3.3 presents the specific samples chosen.

Table 3.3 Polymer samples evaluated by FSC.

Sample code	M_n PEO block (g mol^{-1})	M_n PCL block (g mol^{-1})	M_n PLLA block (g mol^{-1})	PDI (Mw/Mn)
PEO^{4}	3800	-	-	1.03
PCL^{7}	-	7000	-	1.10
$PLLA^{4.6}$	-	-	4600	1.10
$PCL_{59}PLLA_{41}{}^{11.2}$	-	6600	4600	1.21
$PEO_{23}PCL_{34}PLLA_{43}{}^{19.9}$	4600	6800	8500	1.18

3.2.2 The equipment

The FSC measurements were conducted in a Flash DSC 1 from Mettler Toledo employing a UFS 1 sensor. The maximum cooling and heating rates are 4000 and 40000 K s^{1}, respectively. The operation temperature range is between -100 and 450 ºC. The samples were tested under ultra-high purity nitrogen atmosphere. More features about the equipment are described in Sections The Flash DSC 1 equipment3.1.2 and 3.1.3.

3.2.3 Sampling

A very small piece of the sample was cut on a glass slide. Then, it was positioned in the sensor, in the center of one of the calorimeters, with the aid of a fine hair and the coupled microscope. Next, the sample was melted during 1 s. PCL and PEO were melted at 90 ºC while for PLLA, PCL-*b*-PLLA and PEO-*b*-PCL-*b*-PLLA samples, were melted 160 ºC. At these temperatures, the thermal history is erased (T_{ETH}). Afterwards, the samples were cooled until -90 ºC and heated again several times to create a uniform film and to improve the thermal contact with the sensor.

3.2.4 Standard FSC cooling measurements

The thermal program employed for all samples was as follows: firstly, an initial heating scan from 25 ºC to T_{ETH} at 1000 K s^{-1}, keeping the sample for 0.1 s at that temperature to erase the thermal history. Secondly, a cooling scan down to -90 ºC at cooling rate, CR_i. Finally, a heating scan from -90 to T_{ETH} at 1000 or 2000 K s^{-1}. The procedure was repeated from the second step forward employing different CR_i from 50 to 5000 K s^{-1}.

3.2.5 Standard FSC heating measurements

The thermal program was similar to the one described before, although the sample was cooled at a fixed rate and then heated a different rates as follows. First, the sample was heated from 25 ºC to T_{ETH} at 1000 K s^{-1}, keeping it for 0.1 s at that temperature to erase the thermal history. Then, it was cooled down to -90 ºC at 2000 K s^{-1}. Finally, the sample was heated from -90 to T_{ETH} at different heating rates from 2000 to 20000 K s^{-1}.

3.2.6 Isothermal crystallization measurements upon cooling from melt employing FSC

Using the Flash DSC 1, it was not possible to detect exothermal signal during the isothermal step of crystallization. Therefore, a step crystallization program was employed to follow the crystallization in time. The detailed procedure is described in reference [39]. Briefly, the sample was quenched from the melt at very high rate (2000 K s^{-1} was cooling rate chosen based on the analysis presented later in Section 3.3.1) to the first crystallization temperature, T_{c1}. Then, it was held at this temperature for a given crystallization time, t_1. Afterward, the sample was heated from T_{c1} to the T_{ETH} at 2000 K s^{-1}. From the last heating scan, the melting enthalpy was determined, and it was assumed to be equal to the crystallization enthalpy evolved during the isothermal crystallization step at t_1. This procedure was repeated for several isothermal crystallization times, until enough data were collected to determine the isothermal crystallization kinetics at T_{c1} as function of time (around 40 points). The entire procedure was repeated successively at another crystallization temperature, T_{ci}.

3.2.7 Isothermal crystallization measurements upon heating from the glassy state employing FSC

The isothermal crystallization was measured at 0 ºC following the step crystallization methodology described earlier but upon heating from the glassy state. The sample was quenched from the melt until -90 ºC at 2000 K s^{-1}. Then, it was heated from -90 ºC to T_c (i.e. 0 ºC) at very fast heating rate (2000 and 15000 K s^{-1} were the selected heating rates based on the analysis presented later in Sections 3.3.1 and 3.3.2). Then, it was held at this temperature for a given crystallization time, t_i. Afterward, the sample was heated from T_c to the T_{ETH} at 2000 K s^{-1}. Again, this procedure was repeated for several isothermal crystallization times, t_i.

3.2.8 Annealing prior isothermal crystallization upon heating from the glassy state employing FSC

This approach follows the procedure described previously in Section 3.2.7 with a modification. An annealing step was introduced prior the isothermal step. The sample was quenched from the melt until -90 ºC at 2000 K s^{-1}. Then, it was heated from -90 ºC to the annealing temperature, T_a (i.e. -63 ºC) at 2000 K s^{-1}, and held at this temperature for a 1 s. Afterward, the sample was heated from T_a to T_c (i.e. 0 ºC) at 40000 K s^{-1}, and kept at this temperature for a given crystallization time, t_i. Finally, the sample was heated from T_c to the T_{ETH} at 2000 K s^{-1}. This procedure was repeated for several isothermal crystallization times, t_i.

3.3 RESULTS AND DISCUSSION

PCL, PEO and PLLA homopolymers as well as a PCL-*b*-PLLA diblock copolymer and a PEO-*b*-PCL-*b*-PLLA triblock terpolymer were selected and measured by FSC to get knowledge about the advantages of the technique for particular experiments. Several examples will be given in the following sections.

3.3.1 Non-isothermal melt-crystallization at different cooling rates of PCL, PEO and PLLA homopolymers and PCL-*b*-PLLA diblock copolymer

The critical cooling rate to suppress the crystallization upon cooling from the melt was determined for some selected samples. This parameter is of particular relevance to conduct isothermal crystallization studies. PEO^4 and PCL^7 samples were cooled at different rates between 50 and 5000 K s^{-1} and heated at 1000 and 2000 K s^{-1}. In Figure 3.4 and Figure 3.5 are plotted the subsequent heating scans corresponding to each cooling rate for PEO^4 and PCL^7 samples. To simplify, only selected heating scans are presented. During the cooling scan, the exothermal crystallization signal was not observed at any cooling rate. The subsequent heating scans show a glass transition at around -60 ºC, a cold crystallization peak and a melting peak. The cold crystallization peak increases with the cooling rate in both samples. Because of the their fast crystallization kinetics, both PEO^4 and PCL^7 are able to crystallize completely during cooling at low cooling rates (50 and 100 K s^{-1}) and, therefore, no cold crystallization is observed in the subsequent heating scan. But as the cooling rate increases, the crystallization is hampered and the material partially crystallizes during the cooling and partially cold crystallizes during the heating. Moreover, PCL^7 was heated a two different rates after the non-isothermal crystallization. Increasing the heating rate from 1000 to 2000 K s^{-1} did not suppress the cold crystallization of the sample (see Figure 3.5a and b).

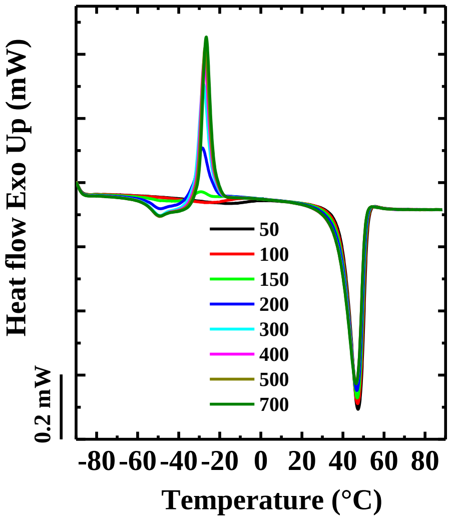

Figure 3.4 Subsequent FSC heating scans of PEO^4 at 1000 K s^{-1}, after cooling at rates from 50 to 700 K s^{-1}.

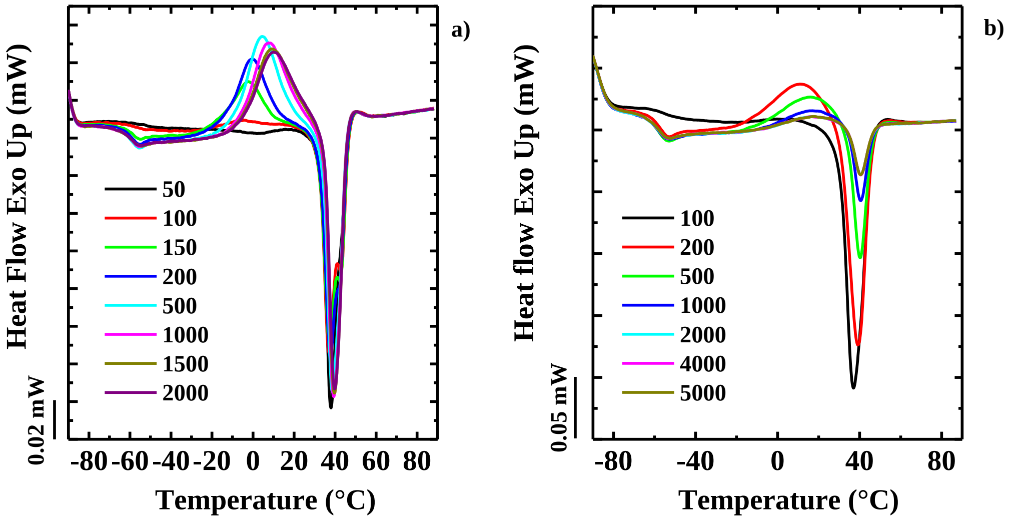

Figure 3.5 Subsequent FSC heating scans of PCL^7, after cooling at rates from 50 to 5000 K s^{-1}. a) Heating rate: 1000 K s^{-1} b) Heating rate: 2000 K s^{-1}.

The difference between the melting enthalpy and the cold crystallization enthalpy (ΔH_m-ΔH_{cc}) was calculated and plotted against the cooling rate to establish the critical cooling rate to avoid crystallization during cooling (see). As the cooling rate increases the enthalpy difference reaches to zero (see Figure 3.6a and b). This value is reached at 700 K s^{-1} for PCL^7 and at 400 K s^{-1} for PEO^4. During cooling at these particular rates, the material is not able to crystallize and it does it entirely during heating. Thus, after cooling the samples at any rate above these critical values, both

PEO and PCL are completely amorphous. A critical cooling rate value of 500 K s^{-1} was reported by Zhuravlev et al. in a PCL of 20000 g mol^{-1} [20]. In comparison to the PCL^{7} sample, whose molecular weight is 7000 g mol^{-1}, the lower critical cooling rate observed by these authors obeyed to the higher molar mass of their PCL. Cooling the samples at rates beyond the critical rate avoids the crystallization but also hinders the nucleation process [8].

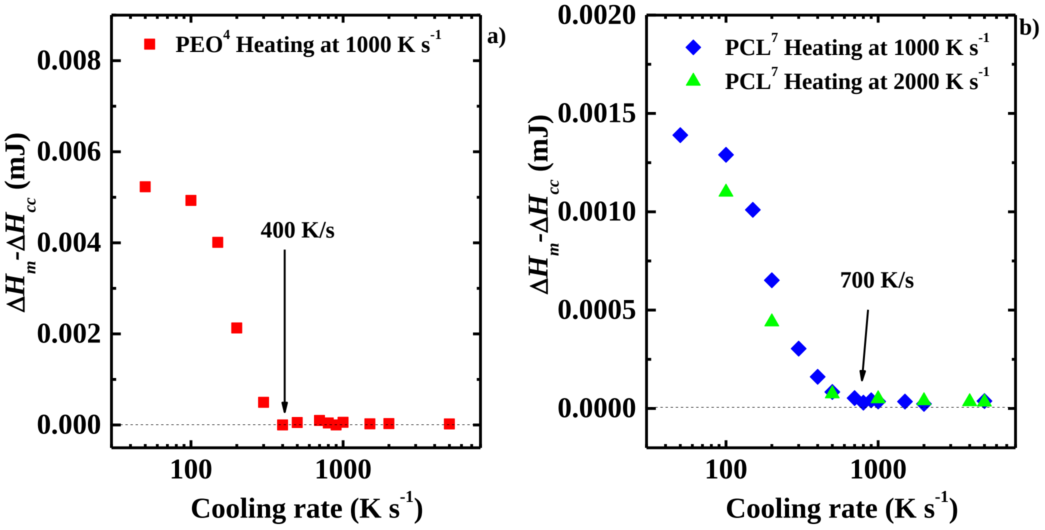

Figure 3.6 Enthalpy change as a function of the previous cooling rate of a) PEO$^{4.6}$ and b) PCL^{7}.

The PLLA$^{4.6}$ sample was also cooled at different rates between 50 and 5000 K s^{-1} and heated at 1000 and 2000 K s^{-1}. The selected subsequent heating scans plotted in Figure 3.7 evidence the crystallization kinetic differences between PLLA and both PCL and PEO. No melting peak was observed during the heating scans (see Figure 3.7a). PLLA is well known for its slow crystallization kinetics [40]. Therefore, it remained amorphous after cooling and heating at all the scanning rates evaluated. The enthalpic relaxation corresponding to the glass transition took place at around 60 ºC. As the cooling rate increases, the T_g values slightly shift to higher temperatures (see Figure 3.7b). This behavior has been observed in PS thin films and bulk PS [41].

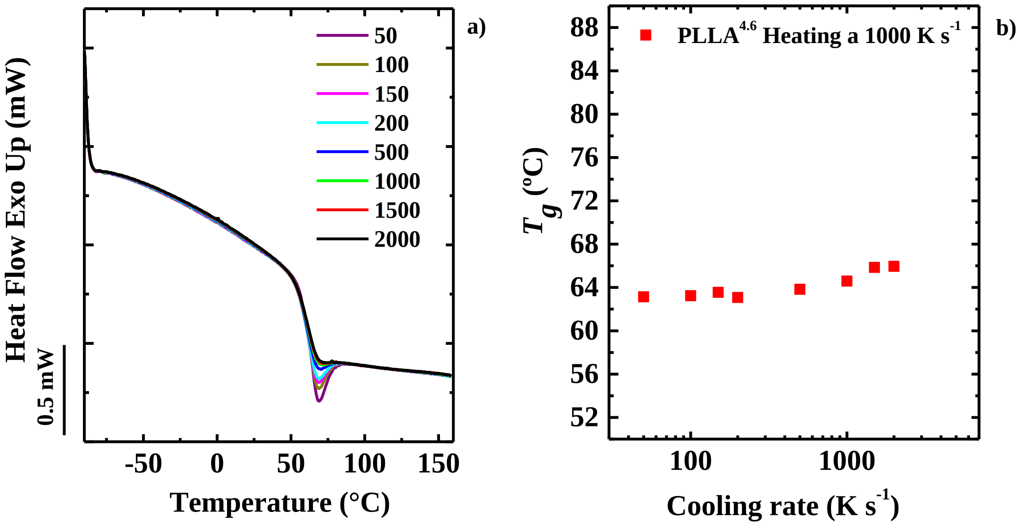

Figure 3.7 a) Subsequent FSC heating scans of PLLA$^{4.6}$ at 1000 K s^{-1}, after cooling at rates from 50 to 2000 K s^{-1}. b) Glass transition temperature (T_g) as a function of the previous cooling rate.

The PCL$_{59}$ PLLA$_{41}$$^{11.2}$ diblock copolymer was selected to evaluate the influence of different cooling rates in the subsequent melting behavior of a diblock copolymer. The sample was cooled at rates between 100 and 4000 K s^{-1}. The heating scans plotted in Figure 3.8 demonstrated that the diblock copolymer is always amorphous on cooling since no melting peak was observed. Although no clear, it appears to be two thermal transitions at around -50 and 55 ºC. This diblock copolymer is melt miscible, as it was proven by SAXS measurements in the melt. Therefore, it is expected to observe a single glass transition at a temperature in between of the T_g of both homopolymers, which are around at -60 ºC for PCL and 60 ºC for PLLA. The low temperature transition might be related to the glass transition. Unfortunately, the glass transition of pure PLLA takes place at the same range of melting of pure PCL. Therefore, it is difficult to properly identify what is the process taking place at around 55 ºC (see black arrow in Figure 3.8).

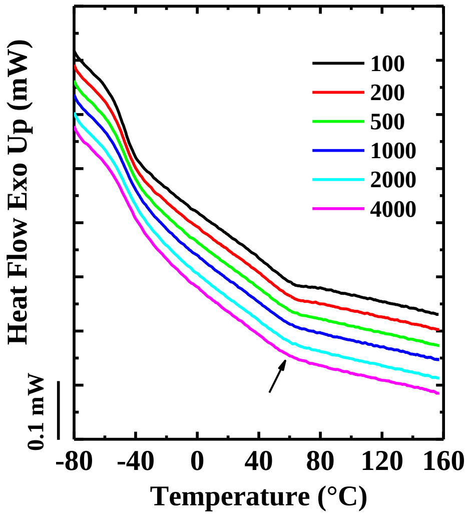

Figure 3.8 Subsequent FSC heating scans at 2000 K s^{-1} of $PCL_{59}PLLA_{41}^{11.2}$, after cooling at rates from 100 to 4000 K s^{-1}.

3.3.2 Reorganization suppression during heating at different heating rates

The high speeds of FSC are useful to avoid cold crystallization and reorganization phenomena during heating. To exemplify this advantage, PCL^7 was cooled at 2000 K s^{-1}, a cooling rate that proved to suppress the crystallization during cooling. Then, the sample was heated at several rates between 2000 and 20000 K s^{-1}. The FSC heating scans are plotted in Figure 3.9. At 2000 K s^{-1}, the PCL^7 is able to cold crystallize and melt afterwards. But, as the heating rate increases, the cold crystallization is suppressed and the material stays amorphous. Surely, above 8000 K s^{-1}, the PCL^7 sample does not crystallize during heating. Wurm et al. [8] reported a suppresion of cold crystallization at 18000 K s^{-1} in a PCL of lower molecular weight (1400 g mol^{-1}). Schawe et al. [35] reported a completely amporphous iPP at heating rates beyond 20000 K s^{-1}. Establishing the critical cooling and heating rates to avoid cristalization and nucleation is relevant to conduct isothermal crystallization analysis.

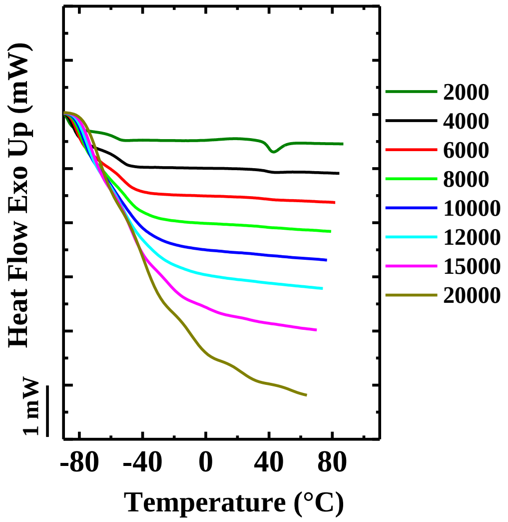

Figure 3.9 Subsequent FSC heating scans of PCL[7] at several rates, from 2000 to 20000 K s^{-1}, after cooling at 2000 K s^{-1}.

3.3.3 Isothermal crystallization from melt and glassy state of PCL and PCL-*b*-PLLA diblock copolymer

The FSC technique was employed to evaluate the isothermal crystallization of the PCL[7] homopolymer and the $PCL_{59}PLLA_{41}^{11.2}$ diblock copolymer at a specific temperature. Two different approaches were conducted to follow the crystallization: upon cooling from the melt and upon heating from the glassy state (see Figure 3.10). From the analysis of the previous Sections 3.3.1 and 3.3.2, proper cooling and heating rates to suppress crystallization during cooling and heating scan were selected. In the case of the isothermal melt crystallization, the samples were always cooled at 2000 K s^{-1} (see Figure 3.10a). For the isothermal cold crystallization, both samples were cooled first at 2000 K s^{-1} to -90 ºC. Then, PCL[7] and PCL_{59} $PLLA_{41}^{11.2}$ were heated from the glassy state at 15000 K s^{-1} and 2000 K s^{-1}, respectively, prior to the isothermal step (see Figure 3.10b). These employed heating rates were selected based on the previous analysis presented in Section 3.3.1 and 3.3.2. The subsequent melting scan was recorded at 2000 K s^{-1}. The crystallization temperature selected was 0 ºC. The samples were crystallized until very long times to assure the complete crystallization of the material (see Figure 3.11a and b). At 0 ºC, the PCL can crystallize. However, due to its fast kinetics, the PCL isothermal crystallization cannot be followed in a conventional DSC at such low temperatures. Here is where the fast speed rates of FSC become highly useful.

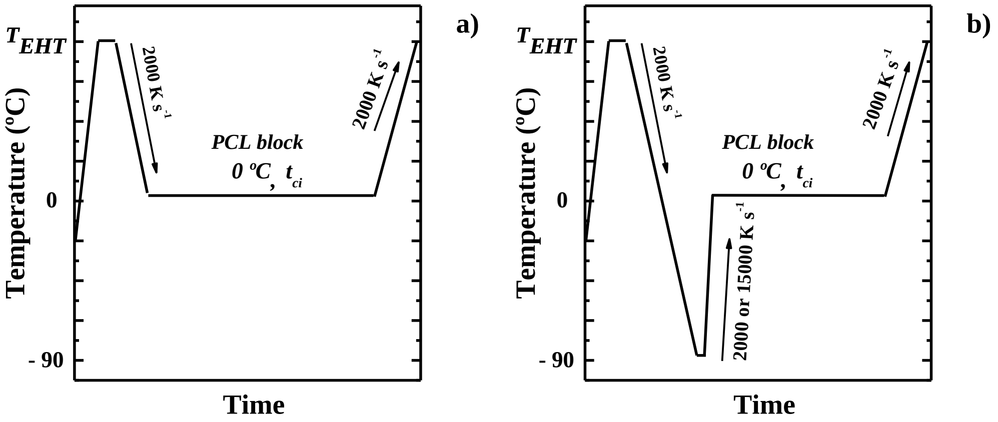

Figure 3.10 Thermals protocols employed to follow the isothermal crystallization at 0 ºC. a) Upon cooling from the melt and b) Upon heating from the glassy state.

The isothermal crystallization of the PCL^{7} homopolymer and the $PCL_{59}PLLA_{41}^{11.2}$ diblock copolymer at 0 ºC is depicted in Figure 3.11. The PCL^{7} homopolymer crystallizes at faster rate when the sample is previously quenched to the glassy state (see Figure 3.11c). As expected, quenching the sample to -90 ºC, a temperature below PCL glass transition increases the nucleus density of the material. As a consequence, the PCL crystallization kinetics is enhanced.

At 0 ºC only the PCL can crystallize. Therefore, the PCL block will crystallize surrounded by an amorphous PLLA matrix in the $PCL_{59}PLLA_{41}^{11.2}$ diblock copolymer. Figure 3.11d shows that the PCL block crystallized at the same rate regardless the thermal protocol applied. The nucleus formation during quenching is a dynamic process. It is possible that the amorphous PLLA matrix hampered the nucleus development. As a result, the nucleus density of the PCL was not further enhanced after quenching the sample to the glassy state.

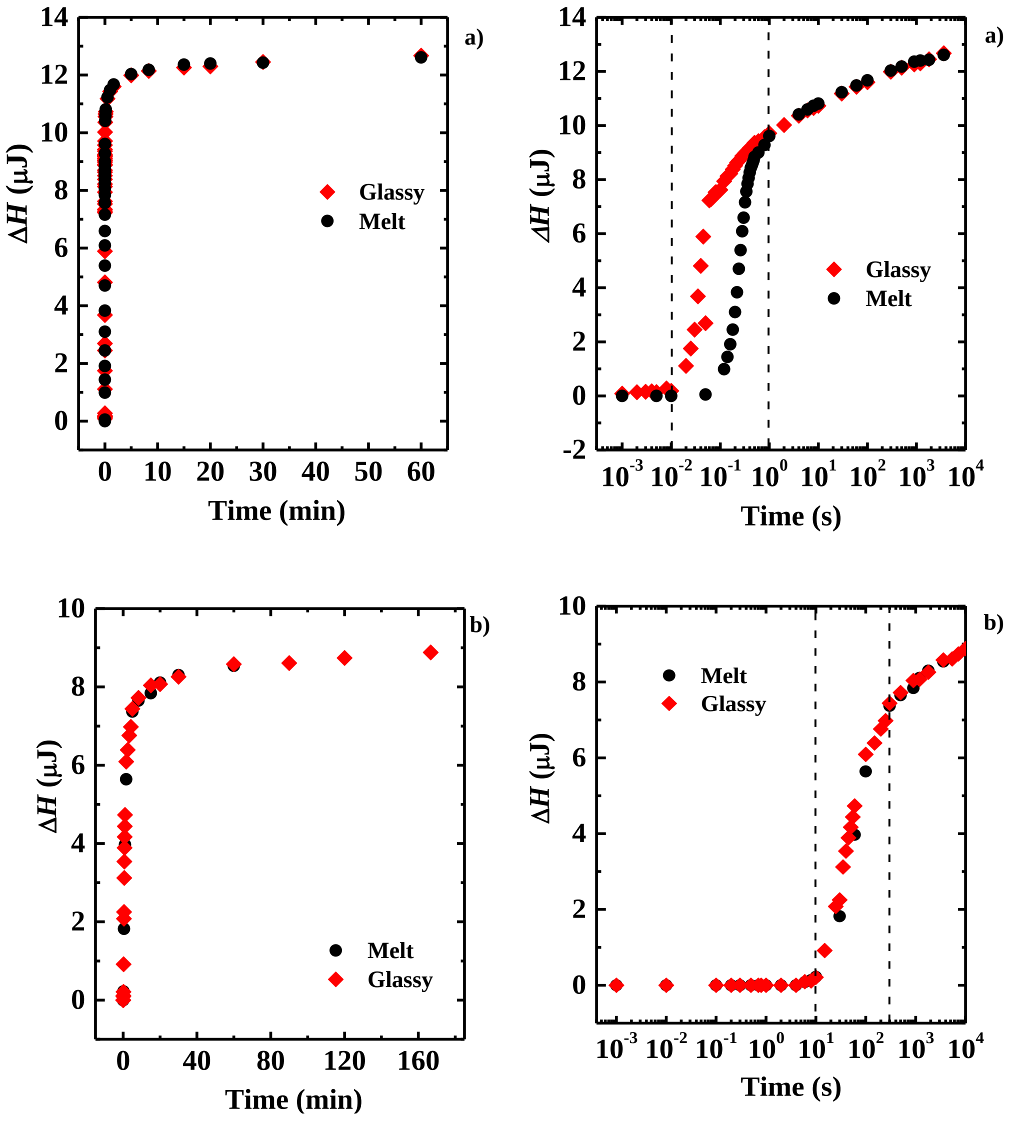

Figure 3.11 Melt enthalpy as function of time after isothermal crystallization at 0 °C of a) PCL^{7} and b) $PCL_{59}PLLA_{41}^{11.2}$.

Since not difference was observed in the crystallization kinetics of the PCL block, an annealing protocol was applied to try to improve the nucleus density (see Figure 3.12). The sample was first quenched at 2000 K s^{-1} until -90 °C. Then, it was heated up to -63 °C at 2000 K s^{-1} and kept at this temperature for 1 s. After that, it was heated again at 2000 K s^{-1} to the crystallization temperature (T_c = 0 °C). The isothermal crystallization kinetics after an additional annealing step is depicted in Figure 3.13 and compared to the behavior observed upon heating from the glassy state. The enthalpy was normalized by the mass because two different samples were used.

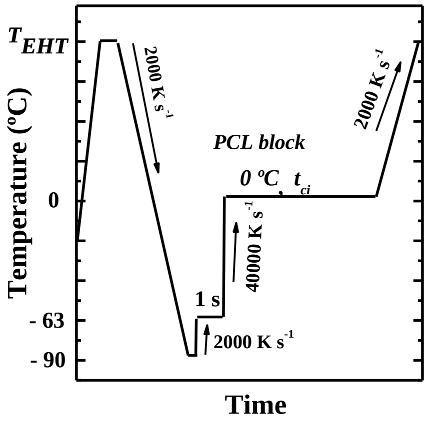

Figure 3.12 Annealing protocol employed to follow the isothermal crystallization upon heating from the glassy state.

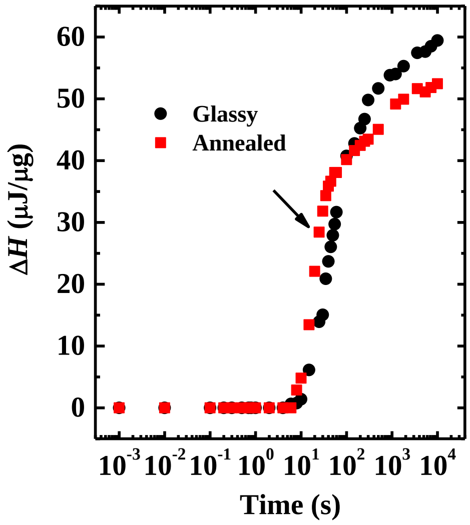

Figure 3.13 Melt enthalpy as function of time after isothermal crystallization at 0 °C of $PCL_{59}PLLA_{41}^{11.2}$.

The annealing step of 1 s at -63 °C did not contribute to enhance significantly the crystallization kinetics of the PCL block in the $PCL_{59}PLLA_{41}^{11.2}$ diblock copolymer. A very small reduction of the crystallization time was obtained (see black arrow in Figure 3.12). The annealing temperature was selected taking into consideration the research in nucleation and crystallization of a pure PCL from Zhuravlev et al. [20] This PCL had a T_g of -73 °C. The authors found the fastest nucleation rate at -63 °C. However, it is possible that this annealing temperature is too low to improve the nucleation of the PCL block in a great manner, since the $PCL_{59}PLLA_{41}^{11.2}$ is a miscible diblock copolymer and its glass transition should take place at much higher temperatures.

In comparison to the PCL^7 homopolymer, the PCL block in the $PCL_{59}PLLA_{41}^{11.2}$ diblock copolymer clearly crystallized at a lower rate, (see dot lines range in Figure 3.11c and d). The reduction in the crystallization kinetics obeyed to the anti-plasticizing effect caused by the amorphous PLLA matrix. The behavior observed agrees well with the isothermal melt crystallization followed by conventional DSC and discussed in Chapter 2, Section 2.3.9. It is interesting the range of supercooling that was possible to study with both techniques. With conventional DSC, the crystallization temperatures evaluated were relatively high, between 34 and 41 ºC. With FSC, a higher supercooling is possible and the crystallization was followed 0 ºC. At this temperature, the PCL block is surely crystallizing at temperatures closer to the T_g of the copolymer, and therefore, the mobility of the PCL chains reduce significantly. In addition, the amorphous PLLA matrix hampers the diffusion of the PCL chains to the crystalline front.

3.3.4 Isothermal crystallization kinetics from melt of PCL, PCL-*b*-PLLA diblock copolymer and PEO-*b*-PCL-*b*-PLLA triblock terpolymer

The high speed scans of FSC allow following the isothermal crystallization kinetics in the whole range of supercooling, providing that the critical cooling rate have been established previously. Thus, the bell shape tendency of the overall crystallization kinetics with the crystallization temperature can be studied. To follow the isothermal crystallization, PCL^7 and $PCL_{59}PLLA_{41}^{11.2}$ were cooled from melt at 2000 K s^{-1} until a T_{ci}. As it was established in Section 3.3.1, at this rate the samples do not crystallize during cooling. Then, the sample was kept at this temperature for a specific time, t_{ci}, to induce the crystallization. Finally, the subsequent heating scan was recorded at 2000 K s^{-1} (see Figure 3.14). At the crystallization temperatures chosen, only PCL can crystallize while PLLA remains amorphous. In this way, the crystallization behavior of the PCL block in the copolymer can be compared to that of the PCL homopolymer.

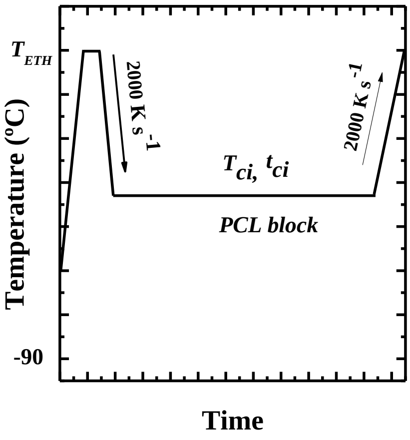

Figure 3.14 Thermal protocol employed to follow the isothermal crystallization upon cooling from the melt.

In Figure 3.15 and Figure 3.16 are plotted the normalized enthalpy as function of time spent at several crystallization temperatures of the PCL^{7} homopolymer and the PCL block in the PCL$_{59}$PLLA$_{41}$$^{11.2}$ diblock copolymer. From the data in these figures, it is obtained the inverse half-crystallization time ($1/\tau_{50\%}$) as a measure of the overall crystallization kinetics (see Figure 3.17).

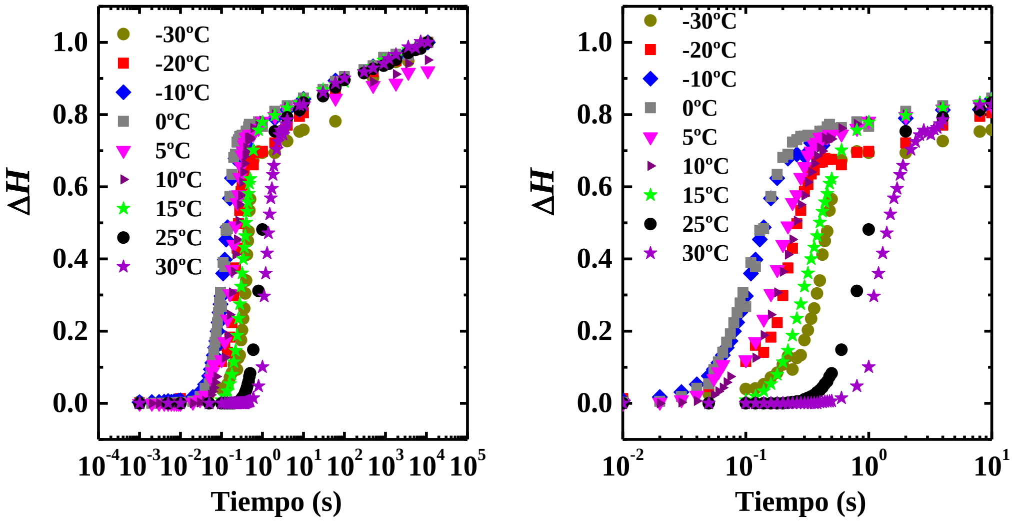

Figure 3.15 Melt enthalpy as function of time after isothermal crystallization of PCL^{7} at several T_c.

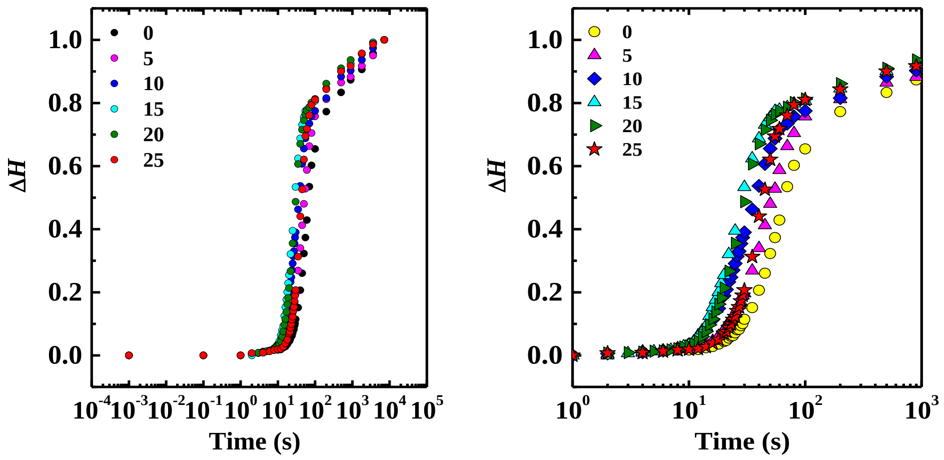

Figure 3.16 Melt enthalpy as function of time after isothermal crystallization of $PCL_{59}PLLA_{41}^{11.2}$ at several T_c.

Figure 3.17 compares the overall crystallization kinetics of the PCL block in the $PCL_{59}PLLA_{41}^{11.2}$ diblock copolymer to that of the PCL homopolymer. The length of the PCL block is almost the same of the homopolymer. The data in Figure 3.17 represents the complete bell shape curve of the crystallization rate plot. Thus, the crystallization rate of the samples first increases, and then decreases, as the crystallization temperature reduces. After quenching from the melt, the PCL block crystallizes surrounded by an amorphous PLLA matrix. The behavior observed in Figure 3.17 agrees well with the isothermal crystallization kinetics studied by conventional DSC and discussed in Chapter 2, Section 2.3.9. However, the advantage of FSC measurements is that the isothermal crystallization can be measured in the complete crystallization window, and hence, both the nucleation and diffusion control over the overall crystallization kinetics can be assessed.

First, the crystallization kinetics of PCL block in the copolymer was reduced in a great extend (see the right scale of Figure 3.17a). Additionally, the supercooling need it to crystallize the PCL block in the copolymer increased in comparison to the PCL homopolymer. As aforementioned, that behavior is a consequence of the anti-plasticizing effect induced by the surrounding PLLA matrix in amorphous state. The shrinkage of the bell shape curve to higher crystallization temperatures indicates an increase of the glass transition temperature, as it would be expected in this kind of miscible diblock copolymers. Because, PCL melting and PLLA glass transition takes place in the same range of temperature, it was difficult to assess the glass transition of this material. Thus, this result is of major importance, since it gives an indication that the glass transition may occur at higher temperature.

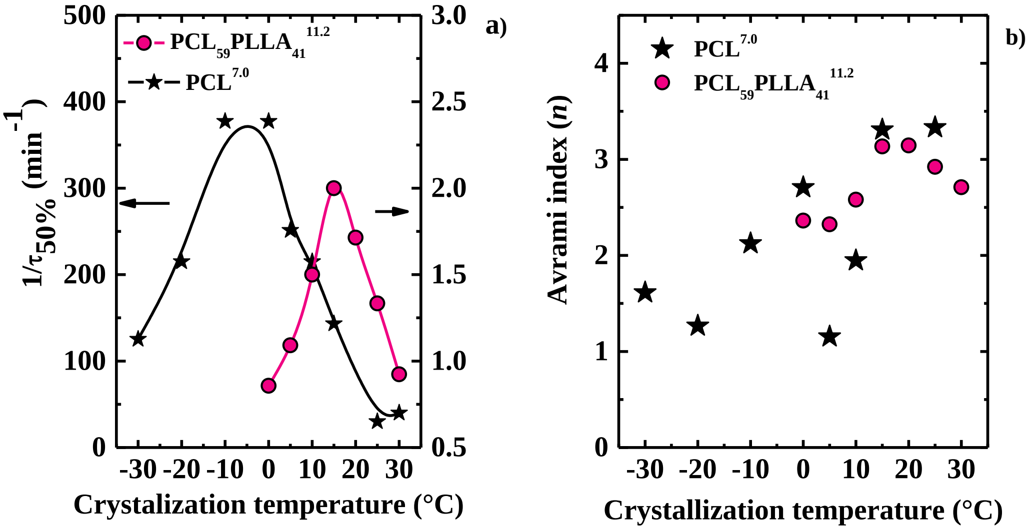

Figure 3.17 a) Inverse of half crystallization times ($1/\tau_{50\%}$) versus crystallization temperature of the PCL^7 hompolymer and the PCL block within the $PCL_{59}PLLA_{41}{}^{11.2}$ diblock copolymer, measured by FSC (the lines are intended to guide the eye). b) Avrami index (*n*) values of the samples.

The results depicted in Figure 3.17 a give an evidence to support the argument given in Section 3.3.3. At 0 ºC, the PCL block in the diblock copolymer crystallizes at high supercooling, at the left side of bell shape curve. Even though the nucleation rate is expected to be high at very low T_c, the PCL block crystallization kinetics highly reduces because this temperature is probably closer to the T_g of the copolymer, and therefore the mobility and diffusion of the PCL chains is highly restricted. On the contrary, at 0 ºC, the PCL homopolymer crystallizes at its maximum rate aided by the thermodynamic forces of the secondary nucleation.

The FSC experimental data can be fitted to the Avrami equation to construct the so-called Avrami plot and estimate the Avrami index (*n*), as it was previously described in Chapter 2, Section 2.1.3. The *n* values exhibited the tendency expected with the crystallization temperature (see Figure 3.17b). For the PCL homopolymer, the Avrami index is between 1 and 2 as T_c decreases. At large supercooling, the nucleation is more instantaneous and the crystal tends to grow in one or two dimensions. At high T_c (small supercooling), the Avrami index is between 3 and 4, which indicate a more sporadic nucleation and a 3D spherulitic crystal growth. For the PCL block in the copolymer, the tendency is similar. Although compared with PCL homopolymer, it seems that the nucleation event might be more sporadic than instantaneous.

The isothermal crystallization of the PCL block in a triblock terpolymer was also followed by FSC. The sample selected was $PEO_{23}PCL_{34}PLLA_{43}^{19.9}$, and the chosen temperature, 15 ºC. At this temperature both PEO and PCL can crystallize but the step crystallization protocol employed (and described in Section 3.2.6) allows separating the crystallization behavior of each block. Figure 3.18 shows the same behavior measured by conventional DSC and already discussed in Chapter 2, Section 2.3.9. The overall crystallization kinetics of the PCL block in the terpolymer reduces compared with PCL^7 homopolymer.

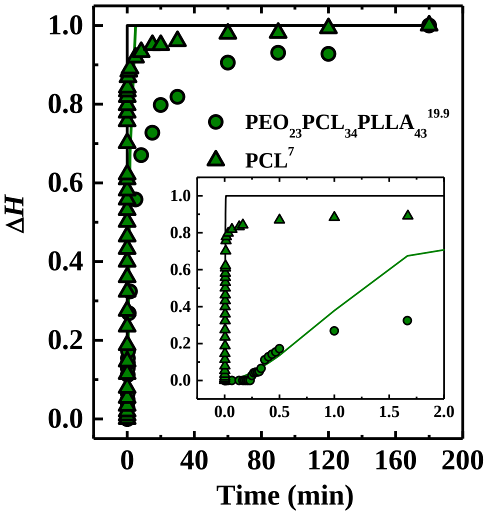

Figure 3.18 Melt enthalpy as function of time after isothermal crystallization at 15 ºC of PCL^7 and $PEO_{23}PCL_{34}PLLA_{43}^{19.9}$.

3.4 CONCLUSIONS

- The very high speeds of FSC allow obtaining completely amorphous materials upon cooling from the melt. The critical cooling rates to suppress crystallization in PCL^{7} and PEO^{4} were 700 and 400 K s^{-1}, respectively.
- The $PLLA^{4.6}$ homopolymer and the PCL_{59} $PLLA_{41}^{11.2}$ diblock copolymer are always amorphous on cooling from the melt at all the scanning rates evaluated.
- The high scanning rates available in FSC are able to suppress cold crystallization during heating. The critical heating rate measured in PCL^{7} was 8000 K s^{-1}. At any heating rate beyond this value, the PCL^{7} is always amorphous.
- The FSC technique is highly useful to study the isothermal crystallization kinetics of polymers in the whole range of supercooling and under different thermal protocols. Those include upon cooling form melt, upon heating from the glassy state and annealing prior an isothermal step.
- With FSC, it is possible to study the bell shape tendency of the overall crystallization kinetics with temperature in fast crystallizing polymers, such as PCL.
- The isothermal crystallization kinetics of the PCL^{7} homopolymer is enhanced after quenching the sample to the glassy state.
- The isothermal crystallization kinetics of the PCL block in the $PCL_{59}PLLA_{41}^{11.2}$ diblock copolymer remained equal upon cooling the sample from the melt or heating from the glassy state. The crystallization rate was only slightly improved, after annealing the sample prior to the isothermal step.
- Compared to the PCL^{7} homopolymer, the PCL block in the $PCL_{59}PLLA_{41}^{11.2}$ diblock copolymer exhibited a high reduction in the overall crystallization kinetics and a larger super cooling, upon cooling from melt.
- Due to the high speed scanning of FSC, it was possible to determine the complete crystallization window for PCL^{7} and the PCL block in $PCL_{59}PLLA_{41}^{11.2}$. A shrinkage of the bell shape curve toward higher crystallization temperatures was observed for the PCL block within the diblock copolymer. Therefore, an increase in the T_g of the diblock copolymer compared to that of the PCL^{7} homopolymer can be inferred.

- The Avrami index values could be evaluated in the wide spectra of crystallization temperatures. In this way, the time of the nucleation could be related to T_c. At large supercoolings, the nucleation is more sporadic and because of that values between 1 and 2 were determined for PCL[7]. On the contrary, at small supercoolings the index values were between 3 and 4.

3.5 REFERENCES

[1] J. E. K. Schawe and S. Pogatscher, "Material Characterization by Fast Scanning Calorimetry: Practice and Applications," in *Fast Scanning Calorimetry*, C. Schick and V. Mathot, Eds. Cham: Springer International Publishing, 2016, pp. 3-80.

[2] S. A. Adamovsky, A. A. Minakov, and C. Schick, "Scanning microcalorimetry at high cooling rate," *Thermochimica Acta,* vol. 403, no. 1, pp. 55-63, 2003/06/26/ 2003.

[3] S. Adamovsky and C. Schick, "Ultra-fast isothermal calorimetry using thin film sensors," *Thermochimica Acta,* vol. 415, no. 1, pp. 1-7, 2004/06/07/ 2004.

[4] C. Schick and R. Androsch, "New Insights into Polymer Crystallization by Fast Scanning Chip Calorimetry," in *Fast Scanning Calorimetry*, C. Schick and V. Mathot, Eds. Cham: Springer International Publishing, 2016, pp. 463-535.

[5] J. E. K. Schawe, "Influence of processing conditions on polymer crystallization measured by fast scanning DSC," *Journal of Thermal Analysis and Calorimetry,* vol. 116, no. 3, pp. 1165-1173, 2014// 2014.

[6] E. van de Kerkhof and P. P. W. van Grinsven, "Thermoanalytical Instrument ", 2009.

[7] A. Toda, R. Androsch, and C. Schick, "Insights into polymer crystallization and melting from fast scanning chip calorimetry," *Polymer,* vol. 91, pp. 239-263, 2016/05/17/ 2016.

[8] A. Wurm *et al.*, "Crystallization and homogeneous nucleation kinetics of poly(ε-caprolactone) (PCL) with different molar masses," *Macromolecules,* vol. 45, no. 9, pp. 3816-3828, 2012.

[9] R. Splinter, A. W. van Herwaarden, I. A. van Wetten, A. Pfreundt, and W. E. Svendsen, "Fast differential scanning calorimetry of liquid samples with chips," *Thermochimica Acta,* vol. 603, pp. 162-171, 2015/03/10/ 2015.

[10] I. A. van Wetten, A. W. van Herwaarden, R. Splinter, R. Boerrigter-Eenling, and S. M. van Ruth, "Detection of sunflower oil in extra virgin olive oil by fast differential scanning calorimetry," *Thermochimica Acta,* vol. 603, pp. 237-243, 2015/03/10/ 2015.

[11] A. W. van Herwaarden, "Overview of calorimeter chips for various applications," *Thermochimica Acta,* vol. 432, no. 2, pp. 192-201, 2005/07/15/ 2005.

[12] E. Zhuravlev and C. Schick, "Fast scanning power compensated differential scanning nano-calorimeter: 2. Heat capacity analysis," *Thermochimica Acta,* vol. 505, no. 1-2, pp. 14-21, 2010.

[13] N. Sbirrazzuoli, N. Guigo, and S. Vyazovkin, "Isoconversional Kinetics by Fast Scanning Calorimetry," in *Fast Scanning Calorimetry*, C. Schick and V. Mathot, Eds. Cham: Springer International Publishing, 2016, pp. 237-257.

[14] A. A. Minakov and C. Schick, "Ultrafast thermal processing and nanocalorimetry at heating and cooling rates up to 1MK∕s," *Review of Scientific Instruments,* vol. 78, no. 7, p. 073902, 2007/07/01 2007.

[15] F. De Santis, S. Adamovsky, G. Titomanlio, and C. Schick, "Isothermal Nanocalorimetry of Isotactic Polypropylene," *Macromolecules*, vol. 40, no. 25, pp. 9026-9031, 2007/12/01 2007.

[16] V. Mathot *et al.*, "The Flash DSC 1, a power compensation twin-type, chip-based fast scanning calorimeter (FSC): First findings on polymers," *Thermochimica Acta,* vol. 522, no. 1, pp. 36-45, 2011/08/10/ 2011.

[17] I. Kolesov, D. Mileva, R. Androsch, and C. Schick, "Structure formation of polyamide 6 from the glassy state by fast scanning chip calorimetry," *Polymer,* vol. 52, no. 22, pp. 5156-5165, 2011/10/13/ 2011.

[18] G. Vanden Poel, D. Istrate, and V. Mathot, "Full-Temperature-Range Crystallization Rates of Polyamides by Fast Scanning Calorimetry as Key to Processing," in *Fast Scanning Calorimetry*, C. Schick and V. Mathot, Eds. Cham: Springer International Publishing, 2016, pp. 611-632.

[19] R. Androsch, C. Schick, and A. M. Rhoades, "Application of Tammann’s Two-Stage Crystal Nuclei Development Method for Analysis of the Thermal Stability of Homogeneous Crystal Nuclei of Poly(ethylene terephthalate)," *Macromolecules,* vol. 48, no. 22, pp. 8082-8089, 2015/11/24 2015.

[20] E. Zhuravlev, J. W. P. Schmelzer, B. Wunderlich, and C. Schick, "Kinetics of nucleation and crystallization in poly(ε-caprolactone) (PCL)," *Polymer,* vol. 52, no. 9, pp. 1983-1997, 2011.

[21] R. Androsch, H. M. N. Iqbal, and C. Schick, "Non-isothermal crystal nucleation of poly (l-lactic acid)," *Polymer,* vol. 81, pp. 151-158, 2015/12/16/ 2015.

[22] D. G. Papageorgiou, E. Zhuravlev, G. Z. Papageorgiou, D. Bikiaris, K. Chrissafis, and C. Schick, "Kinetics of nucleation and crystallization in poly(butylene succinate) nanocomposites," *Polymer,* vol. 55, no. 26, pp. 6725-6734, 2014/12/15/ 2014.

[23] N. Bosq, N. Guigo, E. Zhuravlev, and N. Sbirrazzuoli, "Nonisothermal Crystallization of Polytetrafluoroethylene in a Wide Range of Cooling Rates," *The Journal of Physical Chemistry B,* vol. 117, no. 12, pp. 3407-3415, 2013/03/28 2013.

[24] R. Androsch and M. L. Di Lorenzo, "Kinetics of crystal nucleation of poly(L-lactic acid)," *Polymer,* vol. 54, no. 26, pp. 6882-6885, 2013/12/13/ 2013.

[25] D. Mileva, R. Androsch, D. Cavallo, and G. C. Alfonso, "Structure formation of random isotactic copolymers of propylene and 1-hexene or 1-octene at rapid cooling," *European Polymer Journal,* vol. 48, no. 6, pp. 1082-1092, 2012/06/01/ 2012.

[26] A. Mollova, R. Androsch, D. Mileva, C. Schick, and A. Benhamida, "Effect of Supercooling on Crystallization of Polyamide 11," *Macromolecules,* vol. 46, no. 3, pp. 828-835, 2013/02/12 2013.

[27] R. Androsch, A. M. Rhoades, I. Stolte, and C. Schick, "Density of heterogeneous and homogeneous crystal nuclei in poly (butylene terephthalate)," *European Polymer Journal,* vol. 66, pp. 180-189, 2015/05/01/ 2015.

[28] M. Pyda *et al.*, "Melting and crystallization of poly(butylene terephthalate) by temperature-modulated and superfast calorimetry," *Journal of Polymer Science Part B: Polymer Physics,* vol. 44, no. 9, pp. 1364-1377, 2006.

[29] C. Silvestre, S. Cimmino, D. Duraccio, and C. Schick, "Isothermal Crystallization of Isotactic Poly(propylene) Studied by Superfast Calorimetry," *Macromolecular Rapid Communications,* vol. 28, no. 7, pp. 875-881, 2007.

[30] D. Mileva and R. Androsch, "Effect of co-unit type in random propylene copolymers on the kinetics of mesophase formation and crystallization," *Colloid and Polymer Science,* vol. 290, no. 5, pp. 465-471, 2012// 2012.

[31] D. Cavallo, L. Gardella, G. C. Alfonso, D. Mileva, and R. Androsch, "Effect of comonomer partitioning on the kinetics of mesophase formation in random copolymers of propene and higher α-olefins," *Polymer,* vol. 53, no. 20, pp. 4429-4437, 2012/09/12/ 2012.

[32] M. van Drongelen, T. Meijer-Vissers, D. Cavallo, G. Portale, G. V. Poel, and R. Androsch, "Microfocus wide-angle X-ray scattering of polymers crystallized in a fast scanning chip calorimeter," *Thermochimica Acta,* vol. 563, pp. 33-37, 2013/07/10/ 2013.

[33] D. Cavallo, L. Zhang, G. Portale, G. C. Alfonso, H. Janani, and R. G. Alamo, "Unusual crystallization behavior of isotactic polypropylene and propene/1-alkene copolymers at large undercoolings," *Polymer,* vol. 55, no. 15, pp. 3234-3241, 2014/06/25/ 2014.

[34] R. Androsch and M. L. Di Lorenzo, "Crystal Nucleation in Glassy Poly(l-lactic acid)," *Macromolecules,* vol. 46, no. 15, pp. 6048-6056, 2013/08/13 2013.

[35] J. E. K. Schawe, "Analysis of non-isothermal crystallization during cooling and reorganization during heating of isotactic polypropylene by fast scanning DSC," *Thermochimica Acta,* vol. 603, pp. 85-93, 2015/03/10/ 2015.

[36] J. R. Sarasua, R. E. Prud'homme, M. Wisniewski, A. Le Borgne, and N. Spassky, "Crystallization and melting behavior of polylactides," *Macromolecules,* vol. 31, no. 12, pp. 3895-3905, 1998.

[37] M. L. Di Lorenzo, "Calorimetric analysis of the multiple melting behavior of poly(L-lactic acid)," *Journal of Applied Polymer Science,* vol. 100, no. 4, pp. 3145-3151, 2006.

[38] A. Toda, K. Taguchi, K. Nozaki, and M. Konishi, "Melting behaviors of polyethylene crystals: An application of fast-scan DSC," *Polymer,* vol. 55, no. 14, pp. 3186-3194, 2014/06/19/ 2014.

[39] V. Balsamo, N. Urdaneta, L. Pérez, P. Carrizales, V. Abetz, and A. J. Müller, "Effect of the polyethylene confinement and topology on its crystallisation within semicrystalline ABC triblock copolymers," *European Polymer Journal,* vol. 40, no. 6, pp. 1033-1049, 2004/06/01/ 2004.

[40] A. J. Müller, M. Avila, G. Saenz, and J. Salazar, "Crystallization of PLA-based Materials," in *Poly(lactic acid) Science and Technology: Processing, Properties, Additives and Applications,* vol. 12, A. Jimenez, M. Peltzer, and R. Ruseckaite, Eds. (RSC Polymer Chemistry Series, Cambridge: The Royal Society of Chemistry, 2015, pp. 66-98.

[41] D. Cangialosi, A. Alegría, and J. Colmenero, "Cooling Rate Dependent Glass Transition in Thin Polymer Films and in Bulk," in *Fast Scanning Calorimetry,*

C. Schick and V. Mathot, Eds. Cham: Springer International Publishing, 2016, pp. 403-431.

CHAPTER IV

DOUBLE CRYSTALLINE PP/PA6 BLENDS WITH NANOSILICA AND COMPATIBILIZER AGENTS: MORPHOLOGY, THERMAL AND MECHANICAL PROPERTIES

4.1 GENERAL CONCEPTS AND STATE OF ART

The subject of compatibilization in inmiscible polymer blends is very extensive. Many are the strategies to surpass the inherent incompatibility in polymers blends of different chemical nature, which is of the main requirements to obtain a new material with good balance between morphology and performance. In this section, a brief description of polypropylene (PP) and polyamide 6 (PA6) will be presented. Then, general concepts about polymer blend features and compatibilization approaches will be described, with particular attention to the PP/P6 inmiscible blend. Special emphasis will be given to the use of rigid nanoparticles not as reinforcement agents but as interfacial stabilizers.

4.1.1 Polypropylene

Polypropylene (PP) is a semicrystalline thermoplastic polyolefin with wide spectra of applications and products. It is one of the most widely consumed polymers (global demand for PP totaled 55.1 million tonnes in 2013) [1] because of its low monomer cost, low manufacturing cost, and attractive properties. Its main features, such as mechanical, chemical resistance, good optical properties and low density (typically around 0.90 g cm^3), make PP a highly versatile polymer with wide spectra of applications in packaging, films, fibers, fabrics, injection molded pieces, and in shoes, toys and automobile industries. Additionally, PP can be processed by almost all the common processing techniques such as compression and injection molding, extrusion, rotational molding, film, blow molding, thermoforming, among others [2].

Polypropylene structure is composed of saturated aliphatic chains with propylene as repetitive unit. Typically, it is synthesized through Ziegler – Natta catalysis. But since the 90’s decade, metallocene catalyst has also been employed to improve the regularity of the polymer [2].

Commercial grades of PP include homopolymers, block copolymers, random copolymers, rubber modified blends and grafted PP. The PP homopolymers are classified according to the tacticity as isotactic, syndiotactic and atactic, being isotactic polypropylene (iPP), one of the most commercial significance. In iPP, all of the methyl groups have the same configuration with respect to the polymer backbone [3]. iPP is a highly crystalline polyolefin with high melting temperature (around 160 - 168 ºC under normal analysis conditions), softening point, rigidity, hardness, modulus and tensile strength. These properties would depend on molecular weight, crystal structure, lamellar size and crystallinity (amorphous and crystalline phase content) as well as additives and processing conditions. For instance, an increase in the molecular weight causes a decrease in the tensile strength, stiffness and hardness but an increase in the impact strength. On the other hand, the modulus, yield stress, oxygen and moisture barrier resistance, and hardness increase with increasing crystallinity [3].

iPP has high chemical resistance to most strong mineral acids and bases. It is soluble in high boiling aliphatic and aromatic hydrocarbons at high temperature. Therefore, it exhibits an exceptional stain resistance that makes it suitable for battery applications. It has also an outstanding resistance to water and other inorganic environments[3].

As disadvantages, PP is sensitive to suffer oxidation and thermal degradation at high temperature due to the reactivity of the tertiary carbon in the main chain. The thermal degradation leads to chain scission rather than cross-linking, causing brittleness in the material. For that reason, antioxidants are commonly added to PP. In addition, PP exhibits a low impact resistance, especially at low temperatures due to its glass transition around 0 ºC. Regarding the rheological properties, PP is more non-newtonian than polyethylene since the apparent viscosity declines more rapidly as the shear rate increases [2].

iPP exhibits polymorphism, which is the tendency to crystallize into different crystallographic forms depending on crystallization conditions. In iPP, the dominant crystalline structure is the α-form. Other structures include the β-, γ -, and mesomorphic (smectic) forms. As other semicrystalline polymers, iPP crystallizes in the form of spherulites, and depending on the crystallization conditions, the dimensions of spherulites can vary from a few micrometers to 100 µm, or larger. Optical and mechanical properties depend on the dimension and number of spherulites, which can be modified by adding nucleating agents [3].

Additives in PP include fillers, rubbers, pigments, carbon black, and nucleating agents. The last ones are particularly used to improve the optical properties of PP since nucleating agents induce smaller crystal size as well as higher crystallization temperatures, flexural resistance and less rigidity. In regard to fillers, calcium carbonate and talc are the most used. Between those two, it is reported that calcium carbonate filled grades have higher thermal stability, impact and fatigue strength, brighter color but lower stiffness. However and in general, fillers tend to reduce the tensile strength [2]. The following table resumes some of properties of PP.

Table 4.1 Physical properties of an iPP [3]

Property	Value	ASTM test method
Melt Flow index, g/10min	12	D1238
Tensile yield strength, MPa	34	D638
Elongation at yield, %	10	D638
Flexural modulus, MP	1400	D790
Izod impact strength, J/mg	35	D256
Rockwell hardness, R scale	88	D785
Deflection temperature under laod at 455 kPa	92	D648

4.1.2 Polyamide 6

Polyamides (PA) are thermoplastic semicrystalline polymers obtained from condensation reactions. They were the first engineering plastics, early developed by Carothers group in 1935, and later, commercially produced by Du Pont in 1939 with the trade name Nylon. PA are used in fibers, textiles, adhesives, rubbers, injection molded parts and engineering applications in automotive and electronic/electrical fields. Other uses involve cable sheathing, piping, films, packaging for foodstuffs and pharmaceutical products, molded mechanical parts such as gears and valve seats, among others [4, 5]. Currently, the most consumed polyamides are PA6 and PA66 [6]. The PA6 is synthesized through an opening polycondensation reaction of caprolactam ring or self-condensation of ω-aminocaproic acid (see Figure 4.1 and Figure 4.2). Among them, caprolactam monomer is preferred because it is easier to produce and to purify [4].

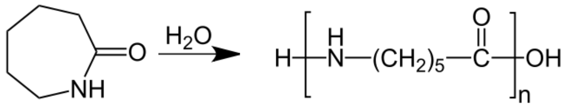

Figure 4.1 Opening of caprolactam ring [4].

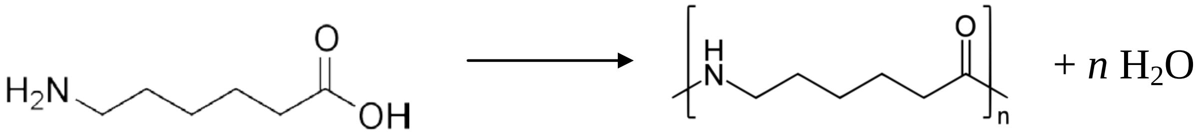

Figure 4.2 Self-condensation of ω-aminocaproic acid [4].

PA are chain flexible polymers with a structural regularity composed of repetitive methylene and amide polar groups in the main chain. Particularly, the PA6 has five methylene groups for each amide bond. This amide group reduces the electrical insulation but increases the resistance to swelling and dissolution in hydrocarbons, as well as the interchain attraction and the stiffness and heat deformation resistance. As a disadvantage, the amide group also increases the water absorption [4].

They are commonly processed by extrusion, injection molding, rotomolding and blow molding as the general purpose polymers. But PA based parts are also obtained by the more special reaction injection molding technique [5].

Most of PA properties are affected by humidity because they are highly hygroscopic materials [4]. PA can also form intermolecular hydrogen bonds. Because of these high intermolecular attractions, PA can develop high crystallinity and melting points, usually above 200 ºC [4]. As the degree of crystallinity is higher, the water absorption is lower, and hence, the humidity will affect less the properties of the polymer. Different crystals structures are developed in polymers with odd and even number of methylene groups. The regular spatial alignment of amide groups allows a high degree of hydrogen bonding when chains are aligned together, with all the oxygen atoms in one molecule adjacent to the amino group of the second molecule [4, 5]. As a consequence, the polymer exhibits higher melting temperature. Moreover, as the number of methylene groups in the main chain reduces, the density increases and the mechanical performance is better (high tensile strength, rigidity, hardness and creep resistance). However, the melting point reduces and the plasticizing effect of water absorption increases when not all the amine and carboxi groups can form intermolecular hydrogen bonds because off an odd number of methylene groups [4, 6].

Because of their crystallinity, PA have high tensile, flexural, compressive, and shear strength [5]. They are also tough above their T_g due to their aliphatic chain segments who give them flexibility in the amorphous zones [4]. PA6 exhibits higher yield stress and tensile strength than other PA. That is because PA6 only has five methylene groups for each amide bond. However, the plasticizing effect caused by the absorbed water induces a reduction in the hardness, tensile strength and modulus, but an increase in the impact resistance and the elongation at break [4, 5].

Regarding the glass transition, dried PA exhibit T_g around 50 ºC but the value can drop until 0 ºC due to water absorption. Therefore, under general service conditions, the T_g of nylons appears to be below room temperature, and the materials exhibits some flexibility in spite of their high crystallinity. [4].

PA has very low thermal expansion coefficient and stable thermal conductivity with temperature. They exhibit very low solubility (only soluble in formic acid, glacial acetic acid, phenols and cresols) and high chemical resistance to esters, alkyl halides, glycols and alkalis. PA6 has good fatigue and abrasion resistance that make the material suitable for use in, for example, unlubricated bearings and intermeshing gears [5]. Environmental exposure causes PA6 degradation because it is highly sensitive to UV radiation. As a consequence, fragility, color changes, yellowness and loss of superficial gloss is observed in this polymer. They also suffer oxidative degradation at high temperatures. PA are good electrical insulators at low frequencies provided a dry environment at room temperature [4, 6]. Some of the physical properties of PA6 are shown in Table 4.2

Table 4.2 Physical properties of PA6* [5]

Property	Value	ASTM test method
Specific gravity	1.13	D792
Water absorption, wt% 24 h	1.6	
Melting point,	215	D2117
Tensile yield strength, MPa	81	D638
Elongation at break, %	50–150	D638
Flexural modulus, MP	2800	D790
Izod impact strength, J/m*g*	55–65	D256
Rockwell hardness, R scale	119	D785
Deflection temperature under laod		D648
At 0.5 MPa	185	
At 1.8 MP *f*	75	
Dielectric strength, kV/mm		D149
Short time	17	
Step by step	15	
Dielectric constant		D150
At 60 Hz	3.8	
At 10^3 Hz	3.7	
At 10^6	3.4	

*Dry as Molded

4.1.3 Polymer blends

Polymer blending is an effective and economic way to combine the desirable properties of different polymers into a new material. It has been increasingly developed for the last 80 years and the exponential increment in the number of patents and literature accounts for that. The combination of two or more polymers with different physical properties holds several advantages [7-9]:

- Development of an improved new material with synergistic properties and without developing new monomers and/or polymerization routes.
- A particular set of properties can be tailor-designed to meet a specific need or application.

- Less time-consuming strategy to obtain new improved materials.
- Low cost and easy processing techniques. Polymer blending usually makes use of common processing machines, such as twin-screw extruders, which are considered standard industrial equipment.
- A wide range of properties can be obtained by merely changing the blend composition.
- Cost reduction with little or no loss of properties.
- Improvement of the material processability by optimizing processing features such as melt viscosity, softening temperature, etc.

Melt blending is the most widely used methodology in research and industry. Due to the high viscosities of polymers, dispersing one polymer into another can be best achieved by intense mechanical stirring in compounders at elevated temperatures; when all the components are in the molten state. The dispersion of the second phase is attained by a shear mechanism that will lead to the final morphology [9].

The phase morphology is a key aspect in the production of new materials with improved properties. During blending, the shape, size and spatial distribution of the dispersed phase is influenced by several factors, such as the shear rate, surface tension, viscosity ratio, processing conditions (time and temperature), blend composition and interfacial properties (miscibility and compatibility) [7].

At the initial stage of mixing the dispersed domains are big. Since the shear stresses are larger than the interfacial ones, the dispersed drops are deformed and stretched into long thin threads. If the local radius of the thread becomes sufficiently small, interfacial (“Rayleigh”) disturbances grow on the thread and cause the breakup of these threads into small drops. At a certain diameter, these small drops may be stretched and broken again until no further stretching takes place or may coalesce after collide against each other (see Figure 4.3) [7]. Therefore, the final morphology is a result of two competitive and opposite mechanisms: break-up and coalescence.

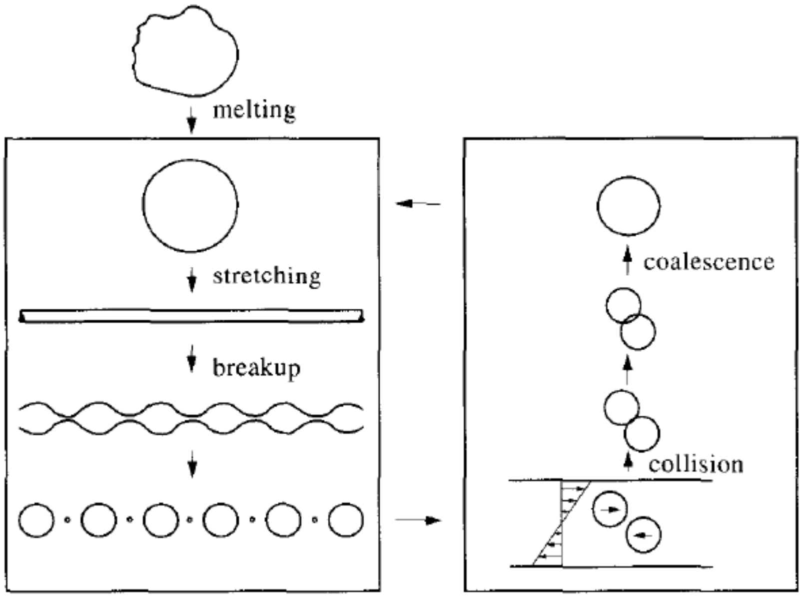

Figure 4.3 Scheme of the breakup and coalescence mechanisms that take place during the melt blending of two polymers [7].

The dispersion of the minority phase is ruled by several factors. In first place, the blending equipment and processing conditions. Co-rotating twin-screw extruders have proven to be the most effective blending machines. In addition, processing conditions such as blending temperature, screw speed, residence time and screw type play an important role in the development of the phase morphology [7]. Moreover, the morphology is also influenced by blend composition. As the concentration of the minor phase increases, the final morphology is a result of a competition between breakup and coalescence mechanisms. However, at low contents of the minority phase, a breakup mechanism is favored and dictates the final particle size [7]. Finally, the phase morphology is strongly governed by the interfacial interactions and the miscibility level between the phases.

Polymer blends can be miscible, compatible or immiscible. An immiscible blend is also an incompatible one. The final physical properties and mechanical performance will be strictly related to the miscibility or compatibility between the components. Miscible blends exhibit a homogenous phase at nanometer scale with a single glass transition. Both polymer components lose part of their intrinsic features and the final mechanical performance of the blend is in between of the ones showed by the neat polymers. On the other hand, immiscible blends show two glass transitions at the same temperature of the corresponding neat polymers. Moreover, these blends exhibits complete phase separation, sharp interface and nonuniform coarse phase morphologies as a result of the relatively low entropy of mixing between the phases. Because the final properties of the blend are strongly related to the morphology, a poor and irreproducible mechanical performance is commonly observed. In the middle, partially miscible (a small part of one blend component is dissolved into the other) and compatible blends also exhibit a phase separation but with a fine morphology that results in good physical properties [7-9]. The best known and most frequently observed morphologies in compatible and inmiscible polymer blends are: (i) a dispersion of one polymer into the matrix of the other polymer; and (ii) a co-continuous two-phase morphology [7]. Typically, immiscible polymer blends with asymmetric compositions (e.g., 90/10, 80/20 or 70/30) exhibit sea-island morphologies with large droplet sizes.

One of the main influential factors that govern the compatibility is the interfacial adhesion. Poor or lack of adhesion is a result of high interfacial tension between the two immiscible phases. A poor interfacial adhesion plus a large size morphology impoverishes mechanical properties such as strength and toughness [8]. Therefore, immiscible blends are useless without being efficiently compatibilized [7]. A compatibilized blend has finer phase morphology and the improved affinity promotes higher stress transfer between the phases, enhancing the mechanical properties of the new material [9]. Besides improving the mechanical performance, compatibilization has also been used to enhance flow and barrier properties [9].

Polymer blends have a wide range of opportunities in the automotive, electronic and electrical field. In addition, the packaging industry as well as, sports and recreation equipment, and medical device industries can have significant usage of nanostructured polymer blends and composites. Secure data storage is another area where polymer nanostructured materials hold some promises [9]. Thus, scientific and industrial efforts have been toward overcome incompatibility in polymer blends.

4.1.4 Brief description of the crystallization behavior in immiscible polymer blends

The addition of a second component, either in the molten or solid state, can affect the crystallization process of the polymeric matrix, including both nucleation and crystal growth. In addition, the crystallization behavior of the dispersed phase can also be modified en comparison to the neat polymer. These are the most important factors that influence the crystallization and nucleation events [10-12]:

- Molecular structure and molecular mass of the components.
- Blend composition.
- Type and degree of dispersion of the phases in the melt state.
- Phase interactions (e.g., nature of the interface, migration of nuclei, etc.).
- Crystallization conditions (e.g., T_c, cooling rate, etc.).
- Physical crystallization environment (surrounded by melt or solidified material).

All the aforementioned factors affect the crystalline development of the polymer blend, causing changes in the nucleation density, the spherulitic growth rate and overall crystallization kinetics, crystallinity degree and semicrystalline morphology. Among them, the physical state of the second phase at the moment of crystallization is of major importance [10].

In double crystalline immiscible polymer blends, the crystallization behavior will be influenced by the crystallization order of the phases. Considering the second phase, the two possible scenarios are: the crystallization of the dispersed drops takes place at lower temperature than that of the polymer matrix, or the opposite, the dispersed drops crystallize first and then the polymer matrix.

In the first scenario, the matrix crystallizes first at high temperature in presence of molten dispersed drops. Hence, some impurities and nuclei might migrate from one phase to the other during the melt-mixing process, changing the nucleation density of the components. Additionally, the interface may enhance the nucleation, mostly due to highly ordered structures in supercooled melt droplets. These phenomena may increase the heterogeneous nucleation of the matrix, and shifting of T_c to higher temperatures can be observed in some cases. However, the crystal growth rate, G, is generally not affected. As result, the crystallization behavior of the matrix is only governed by nucleation. In regards to the subsequent crystallization of the dispersed droplets surrounded by a solidified matrix, heterogeneous nucleation, induced by the solid matrix, or fractionated crystallization might take place. The last one will be described later on [10].

In the second scenario, the dispersed phase crystallizes at higher temperature than the matrix. Hence, the droplets will crystallize surrounded by a molten phase. Afterward, the subsequent crystallization of the matrix will take place in the presence of solidified droplets of the second phase. These solid droplets can act as efficient nucleating agents for the polymer matrix, shifting the T_c to higher temperatures. Also, epitaxial crystallization at the interfaces sporadically occurs. However, it has been reported that finely dispersed solidified domains can increase the melt viscosity of the matrix in such a way that the crystallization rate decreases. In general, the melting behavior of the polymer matrix remains unaffected [10]. Regarding the second phase, as it crystallizes first, the size of dispersed droplets plays a major role in its crystallization behavior. Two phase morphology-dependent phenomena: coincident and fractionated crystallization can arise [10].

When the size of the dispersed crystallizable domains falls below certain limit, the crystallization behavior drastically changes. Instead of two well separate crystallization exotherms located at the T_c of each bulk component, a single or multiple crystallization peaks are observed. Two phenomena can take place. On one hand, first formed semicrystalline droplets can have a nucleating effect over the crystallization of the polymer matrix. As a consequence, a shifting toward higher temperatures is observed in the T_c of the matrix. One the other hand, a fine dispersion of the second phase can shift its T_c toward lower temperatures than that of the neat polymer (due to fractionating). As the crystallization temperature of the matrix and dispersed phase increases and reduces, respectively, both crystallization events may overlap and a *coincident crystallization* takes place [10].

The dispersed phase can also crystallize in a fractionated manner. That is in several crystallization events taking place at different temperatures, all of them lower than that of the T_c of the bulk polymer. Upon cooling from melt, the minor phase can exhibit *fractionated crystallization* provided that it is dispersed into sufficiently small droplets. This phenomenon is the result of the lack of heterogeneities required for the nucleation at the expected temperature. In other words, when the number of finely dispersed droplets exceeds the number of available heterogeneities, the nucleation activity across the dispersed phase is different. Thus, none or only part of the dispersed droplets can crystallize at their bulk T_c and larger undercoolings are required to crystallize the smallest drops. When the drop size is reduced beyond a certain value, it may no longer have a nucleus for heterogeneous nucleation, and it may crystallize by a homogenous mechanism at much lower T_c. This can result in a change of the crystal polymorphic form. However, the melting temperature of dispersed phase is not significantly affected [10-12].

4.1.5 Brief description of the mechanical performance in immiscible polymer blends

Most polymers are combined in polymer blends to obtain new materials with an improved mechanical performance, with particular interest in the impact strength, stiffness and elongation at break. Two types of tests are used to evaluate the mechanical performance in polymer blends: high speed impact experiments and low deformation rate tests. The last one includes tensile, compressive and bending tests.

In general, the first sign of immiscibility or bad compatibility is poor mechanical properties. In tensile testing, the yield stress, the tensile strength (stress at break) and the maximum elongation at break can be dramatically decreased due to a poor adhesion between the phases in the solid state. Likewise, the impact strength is worse than the neat components and the material can fail in a brittle manner. Polymer materials can be ductile or brittle depending on the failure mechanism. In polymer blends, the breaking phenomenon is governed by the failure mechanism of the polymer matrix. Ductile polymer matrixes mainly fail through a shear yielding mechanism in which the energy of crack initiation is high but the crack propagation energy is low. Glassy matrixes fail through a crazing mechanism. However, crazes formation have also been observed in semycristalline polymers such as PP [13]. In this case, both crack initiation as well as propagation energy are low [11].

4.1.6 Morphology refinement and compatibilization approaches in inmiscible polymer blends

Because of nearly all polymer pairs form immiscible blends, a compatibilization strategy needs to be implemented in order to obtain an improved mechanical performance. The three main roles of any compatibilizer are: 1) reducing the interfacial tension that leads to an enhancement of the interfacial adhesion and a reduction of the droplet size of the dispersed phase; 2) stabilizing the dispersed phase by suppressing coalescence; and 3) promoting an effective stress transfer between the phases, leading to an improvement of blend performance [9, 11].

The use of a compatibilizer modifies the interface. During the blending process, compatibilizers reduce the interfacial tension between the two components and retard the formation of Rayleigh disturbances on the threads of the dispersed phase [8, 9]. As the interfacial tension reduces, the deformation stress exceeds the interfacial stress. As result, the stretching of the drops proceeds, leading to threads with smaller diameter, and ultimately, to smaller size droplets and finer dispersion [7]. The compatibilizer should also ensure a stable morphology. In other words, the morphology formed during the blending process should remain optimum during post-processing (forming) stages [11]. Finally, an enhanced interfacial adhesion in the solid state promoted by the compatibilizer will assure a proper mechanical performance [9]. The size of the dispersed particles can give a first idea about the compatibilizer efficiency. Usually, an average particle size in the sub-micron range can be achieved [7]. The dispersed phase size plays a crucial role on the mechanical properties of the blends because the lower the particle size, the higher will be the contact surface between the two polymers [8].

Several compatibilizers, such as block copolymers, reactive compatibilizing agents and nanoparticles, have been developed in the last few decades [7, 11, 14-18]. Block copolymers have been used as interfacial modifiers. One block is miscible with one component of the blend while the second block is miscible with the other one. If the chains of each block deeply diffuse inside their corresponding phase, in a way that enough chain entanglement takes place, the interfacial adhesion will be enhanced. As aforementioned, a good interfacial adhesion is required for a proper stress transfer from one phase to the other and to prevent the crack growth until catastrophic failure [7]. A block copolymer has the advantage of being a tailor made compatibilizer. However, it requires copolymerization routes that might not be always plausible.

Besides, block copolymers, the good compatibilization features of grafted polymers are also well-known [7]. They represent the biggest volume of polymeric compatibilizing agents. Most of modified polymers are miscible with one blend component, but contain attached functional groups that enhance the compatibility with the other component. These groups can react with the functional groups present in the polymer dispersed phase, creating chemical bonds between the two phases. This approach has been called reactive compatibilization. It is a well-known method based on the in-situ formation of a block or graft copolymer across the interface during the melt mixing. As a result, well-dispersed and stabilized morphologies are obtained [7, 9].

Using grafted polymers has a few advantages. First, many kind of polymers can be functionalized and the functional groups can be attached to the polymer chains by easy melt grafting reactions employing peroxides. Second, the grafted copolymer forms specifically at the site needed, which is at the interface of the immiscible polymer blend. However, the functionalities must have a suitable reactivity in order to react across the melt interface, during the short blending time. In addition, the covalent bond generated at the interface must be sufficiently stable to survive post-processing stages [7].

The most common functional groups included in modified compatibilizing agents are maleic anhydride (MA), primary and secondary amines, carboxylic acid, groups capable of interchange reactions, groups capable of ionic interactions, hydroxyl groups and heterocyclic groups. Polyolefins, such as polypropylene and polyethylene, modified with MA are the largest group of polymeric compatibilizers. Thermoplastic elastomers like styrenic block copolymers are the second largest one [9].

The third compatibilization strategy, after adding block copolymers and compatibilizing agents, is the addition of nanofillers. Envisaging nanoparticles or nanofillers, not as reinforcing agents but as compatibilizers (or interfacial modifiers) is a novel approach, and it would be discuss more extensively in section 3.1.7.

The PP/PA (or PA/PP) inmiscible blend stabilized with compatibilizing agents

The PP/PA6 blend has been a well studied system during the past decades. The interest relies on the versatility of the pure materials. PP is a low cost polymer with good overall mechanical performance and moisture resistance but shows relatively poor heat resistance. PA has good processabiliy and high mechanical strength and modulus but it is significantly affected by the absorption of water. It is also a notch-sensitive thermoplastic owing to the low resistance to crack propagation. PA is frequently blended with polyolefins, such as PP to improve material properties, lower water absorption and reduce material cost [19].

PP and PA6 form immiscible blends with very poor mechanical performance, due to the poor of interfacial adhesion between the phases [19]. Historically, one of the most used compatibilization strategies involves the addition of compatibilizing agents functionalized with MA or acrylic acid (AA). The most commonly used are PPgMA, PEOgMA, SEBSgMA, EPRgMA and EPDMgMA [19-21]. Moreover, the combined effect of using both maleated polyolefins and maleated rubbers has also been evaluated [20].

Maleated polypropylene (PPgMA) is the most frequently employed compatibilizer agent in the immiscible PP/PA6 blend. It was first reported by Ide and Hasegawa in 1974 [22]. The compatibilization mechanism goes through an in-situ grafting reaction during the reactive melt blending process [19]. The amine end groups of PA chains react with the succinic anhydride groups in the PPgMA, forming a grafted copolymer at the interface through an imide bond (see Figure 4.4). This bond creates strong links between the two phases.

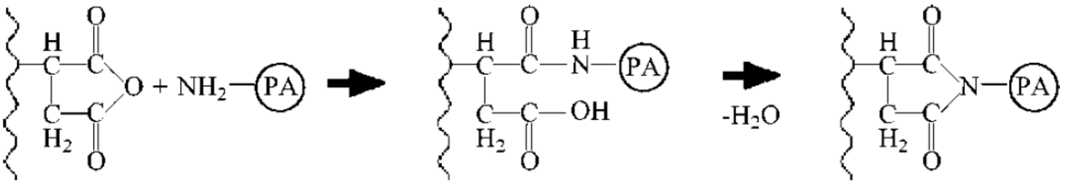

Figure 4.4 Reaction between a succinic anhydride group and a PA6 amine terminal group.

The coupling reaction proceeds very quickly. The amine chain end generally prefers to locate at the interface, because such a chain conformation is more probable. The MA units are highly polar and therefore, unstable in the non-polar PP phase. Thus, the MA pendant groups tend to segregate to the interface and get in contact with the polar amino chain end of PA. Both reactive sites concentrate near the interface and provide a favorable situation for the coupling reaction [23]. In order to a proper compatibilization, PPgMA must have a suitable grafting degree. If the MA content is too small, not enough grafted copolymer is formed at the interface to reduce the interfacial tension and stabilize the PA6 dispersed phase [7].

Liu et al.[24] evaluated the phase morphology in PP/PA6 70:30 blends compatibilized with a maleated thermoplastic elastomer. They confirmed the in-situ formation of the grafted copolymer at the interface by FTIR. The addition of 6 % of the compatibilizer causes a fine dispersion of the PA6 drops. The drops size further decreases as the content the content of the compatibilizer increased. The optimal compatibilizer concentration was 18 %. Beyond this value, the drops size remains almost similar. Thus, the maleated elastomer was successful in decreasing the interfacial tension and inhibiting the coalescence of the dispersed phase. The SEM micrographs demonstrated an enhanced interfacial adhesion. The final morphology is a core-shell structure composed of PA6 inside the core and the maleated elastomer surrounding it.

Zeng et al.[19] studied the effectiveness of two compatibilizing agents in PP/PA6 of different compositions. The PPgMA has proven to be a better compatibilizer agent than the PEOgMA. A stronger interfacial adhesion is formed at the interface when PPgMA is used. They proposed that a too large interfacial adhesion might impoverish the mechanical properties. As the interfacial adhesion is stronger, the interfacial debonding becomes more difficult. In order to obtain a good mechanical performance, the polymer matrix should undergo yielding and plastic deformation. If the interfacial debonding occurred at high stress level and the energy stored in the matrix is too high, the rupture could take place rapidly without leaving time for matrix deformation [19]. From SEM analysis of the surface fracture, it seems that the PP/PPgPA/P6 blend has few debonded particles but several matrix cracks. If the interfacial bonding strength is too high, the matrix around the PA6 particles is restrained and therefore the fracture takes place in brittle manner.

The PP/PA blends exhibit the fractionated and coincident crystallization behaviors described in Section 3.1.4. In these blends the PA6 phase crystallizes first surrounded by a molten PP phase. Moon et al.[25] evaluated the effect of increasing the PPgMA content on the crystallization of PP/PA6 70:30 blend. As the content of compatibilizing agent increases, the tension interfacial and the droplet size reduces causing a coincident crystallization of both phases. The T_c of PA6 reduced while the T_c of PP remained almost the same. Similar results were obtained by Tang et al. [26] in blends of PPgMA/PA6 of different composition, although PA6 exhibited fractionated crystallization in several steps.

Different types of compatibilizers were evaluated in PP/PA6 (and its mirror PA6/PP compositions) blends by Ikkala et al.[27] and Holsti-Miettinen et al.[28]. Two blend compositions and compatibilizer contents, and five compatibilizers with maleic anhydride, fumaric acid, and glycidyl functionalities: PPgMA, SEBSgMA, FAgEBA, GMAgEEA, were evaluated. Except for PPgMA, the other compatibilizing agents form an immiscible interlayer between the PA6/PP phases that encapsulated the PP and highly reduced the droplet size. As the content of PP decreases, the fractionated crystallization behavior became more evident. In the opposite PP/PA6 blends, the PA6 droplets had a nucleating effect over PP crystallization when PPgMA was used, but no significant effect was observed with the other compatibilizers. Coincident crystallization of the PA6 phase took place due to the reduction of the droplet size.

4.1.7 Binary polymer blends stabilized with rigid nanoparticles

Lately, extensive research has been focused on the potential use of nanoparticles, such as clays [29-33], carbon nanotubes (CNT) [34-36] and nanosilica (NS) [37-43], not as reinforcement agents but as compatibilizers or stabilizers in immicible polymer blends, and recent reviews have reported on this subject [17, 18, 44, 45]. This approach is based on the behavior of liquid Pickering emulsions that are stabilized by solid particles located at the interface between two immiscible liquids [17, 46]. The first report on using nanoparticles as stabilizers was done by Gubbels et al.[47, 48] in PE/polystyrene (PE/PS) blends mixed with carbon black particles.

The added nanoparticles to a polymer blend can be located within the polymer matrix, inside the dispersed phase, or at the interface (or at several locations at the same time) (see Figure 4.5). When the preferential location is at the interface, nanoparticles induced morphological changes and can act as solid emulsifiers that stabilize the droplets of the dispersed phase [17, 34-36, 40-42, 45, 49, 50]. The final interfacial location is due to thermodynamic and kinetic factors. The particles surface chemistry and the polarity of the polymers will determine the affinity between components, and therefore, the migration of the nanoparticles from the less affine phase to the interface, or to the second more affine phase [17]. For instance, in PP/EVA blends mixed with hydrophilic and hydrophobic NS [40], the final location agrees with the affinity of the components involved. The hydrophilic NS located at the EVA phase and the hydrophobic NS tended to migrate to the interface. However, shear induced dispersion and collisions between nanoparticles and dispersed droplets are believed to be the most efficient mechanisms to determine the final location of the nanoparticles [40]. As a result of all these factors, a fine-tuned morphology with a significant reduced droplet size and droplet size distribution has been observed in a wide range of immiscible blends [17, 18, 44, 45].

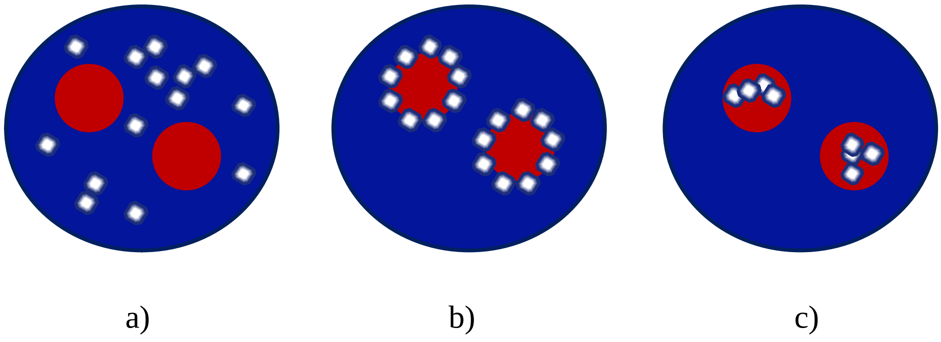

Figure 4.5 Representation of possible locations of rigid particles in binary polymer blends. Inside the a) matrix, b) interface and c) dispersed phase.

It has been reported that the reduction of the droplet size is probably due to two factors: 1) a reduction of the interfacial tension and 2) the fact that nanoparticles surrounding the droplets create a physical barrier that stabilize and avoid their coalescence [18, 45]. However, previous results have shown that nanoparticles act more as physical stabilizers and less as classical compatibilizers or interfacial tension modifiers [37, 51]. In addition to these two factors, other mechanisms have been considered as responsible for the refinement of the morphology by using nanoparticles, such as a change of the viscosity of the phase (or phases) where NP are included, the establishment of a physical network at a percolation threshold, and strong polymer chain – filler interactions [18, 45].

The morphology of binary polymer blends stabilized with rigid particles strictly relates with their physical performance, rheological behavior [30, 34, 41-43, 51-58], mechanical properties [45, 53, 57-59] and crystallization behavior [12, 37]. All the literature to be presented henceforth regards with how the addition of rigid particles affects the morphology, physical and mechanical properties when the particles are mostly or exclusively located at the interface.

In a PE/PA 80:20 blend mixed with organoclays [55], the preferential location of the nanoparticles at the interface caused a reduction of the droplet size as result of their solid-like barrier effect that ultimately inhibits the coalescence. In the blend with the mirror composition, 20:80, the organoclay is located both in the PA matrix and in the interface. The presence of the nanoparticles increases the viscosity of the matrix, leading to break-up of the PE domains. Thus, the final drop size is a result of both breakup mechanism and coalescence barrier effect [55]. Similar results were obtained by Hong et al.[60, 61] in PBT/PE blends with organoclays.

The fractionated crystallization behavior, as widely reported in inmiscible and compatibilized blends, has also been observed in polymer blends stabilized with nanofillers [12, 37, 62-64]. Again, it is consequence of the refined droplet size obtained after nanoparticles addition. Chen et al. and Li et al. reported fractionated crystallization behavior of the PP dispersed phase in PP/PS 20/80 blends stabilized with hydropobic and hydrophilic NS [62, 63]. Moreover, both types of nanoparticles showed a heterogeneous nucleation effect on pure PP as reflected by the increase in the T_c. Compared to hydrophilic nanoparticles, the hydrophobic ones were more efficient in both reducing the size of PP droplets and in promoting their fractionated crystallization behavior. Additionally, the authors claim that an increase in the hydrophilic NS content promoted the heterogeneous nucleation of the PP phase due to an enlargement of the droplet size and a possible swallow of NS particles into the PP droplets. In another approach of the same authors [62, 63], a higher refinement of the domain size and more profound fractionated crystallization phenomenon were observed when both hydropobic and hydrophilic NS where simultaneously added to the blend. The effect was more notorious when the content of hydrophobic nanoparticles was higher than that of hydrophilic ones.

Despite the fact that fillers refine the droplet size, the mechanical performance has not been largely improved, in particular when the nanoparticles locate preferentially at the interface [45]. For instance, Borah et al.[65] reported a reduced impact resistance in blends of PE and EMA with organoclay particles.

Similar results were obtained by Entezam et al. [66] and Chen et al. [33]. They found a deficient mechanical performance in PP/PET and PS/acrylonitrile-butadiene-styrene (PS/ABS) blends mixed with organoclay particles located at the interface. The Young’s modulus increased moderately but the tensile strength remained the same [66] while the tensile energy and elongation at break highly reduced [33]. There was not a proper stress transfer between the matrix and dispersed phase. However, a report from Xiang et al. [67] showed an increase of $\sim$ 168 % in the elongation at break in PE/PA6 blends mixed with functionalized CNT in which some of the nanotubes were at the interface. Additionally, a slightly increase in the yield stress was achieved despite that the reduction of the droplet size was rather small. The authors attributed the enhanced ductility to a nano-bridge effect of the nanotubes located at the interface, which prevents the crack initiation and crack propagation along the interfaces under the stress load [67].

In regard to NS particles as stabilizers, Elias et al.[42] and Zhang et al. [57] reported a refined morphology of PP/ polystyrene (PS) blends due to de addition of hydrophilic and hydrophobic NS. Elias et al.[42] showed that hydrophilic NS tends to locate at the PS dispersed phase while the hydrophobic NS was mostly located at the interface and in the PP matrix. After applying the Palierne model to this blends, they concluded that stabilization mechanism by hydrophilic NS is the reduction of the interfacial tension whereas the hydrophobic NS acted more as rigid layer that avoids coalescence of the PS droplets. On the other hand, Zhang et al. [57] proposed three possible explanations for the decreased PS particle size: (1) enhanced compatibility caused by the adsorption of both PP and PS molecules onto the surface of NS particles, which possess very large specific surface area, (2) increased viscosity ratio caused by the introduction of NS particles, which retards the coalescence of the dispersed PS drops, and (3) enhancing the bending energy of the interface due to the stiff NS particles. From those, the increased viscosity ratio is one of the more plausible. However, the location of NS at the interface seems not stable thermodynamically. The authors detected that at large mixing times, the polymer system tends to reach the equilibrium state and the droplet size increased. This observation suggested that the process is controlled by kinetics rather than thermodynamic factors. Despite the droplet size reduction, the tensile strength remained similar while the impact resistance of the blends was reduced. Only a small improvement was observed in the flexural properties (strength, ～8 % and modulus, ～20 %). They attributed the results to a stress concentration effect.

The PP/PA (or PA/PP) inmiscible blend stabilized with rigid nanoparticles.

A novel approach to modify and stabilize the morphology of the well-known PP/PA polymer blend is the use of NS instead of a compatibilizing agent. Dubois et al. [38, 39] and Müller et al. [37, 51, 68] have studied several aspects, such as the chemical nature of the NS, the NS content and the processing conditions. For instance, two NS with different chemical nature, one hydrophilic and the other hydrophobic have been considered. Laoutid et al.[38, 39] evaluated the efficiency of both type of NS to fine-tune the morphology and properties of a PA6/PP 80:20 blend. The presence of PP domains or NS did not induced a nucleating effect over the PA6. The final location of the NS particles depends on the affinity with the polymer phases. The hydrophilic NS located mainly at the PA6 matrix due to the polar interactions between this phase and the nanoparticles. On the contrary, the hydrophobic NS placed at the interface avoiding the coalescence of the drops, and, as expected, the droplet size of the minor phase was strongly reduced. However, the addition of at least 5 % of NS was needed in order to properly stabilize the blend and reduce the droplet size. Up to about 90% reduction have been detected in these PP/PA (or PA/PP) blends modified with NS [51]. Finally, the thermal stability of the PA/PP blends containing hydrophobic NS seems slightly higher than that of the neat polymers [38].

Laoutid et al.[37] also evaluated the crystallization behavior of the PP matrix in PP/PA and PP/polycarbonate (PP/PC) blends stabilized with NS. In these blends, the PA crystallizes first and PC undergoes its glass transition before PP crystallization. The addition of the nanoparticles highly refined the droplet size and induced fractionated crystallization behavior of the PA dispersed phase. Both, crystalline PA and rigid PC droplets caused a nucleating effect over PP crystallization. However, the PA droplets produced higher nucleation density than the addition of PC or both PC and silica nanoparticles. The authors demonstrated that the nanosilica did not produce any significant nucleation of PP. Despite that fact, the higher nucleation density was obtained in the PP/PA blend stabilized with the nanoparticles. Therefore, the enhanced dispersion of this blend represents the determining factor for the higher nucleating rate of PA. In addition, the crystal growth rate was not affected by the addition of PA, PC or their combination with silica nanoparticles. Thus, the nucleation event is the one responsible for the differences in overall crystallization kinetics among the blends. The refined morphology obtained by the addition of NS enhanced the overall crystallization kinetics of the PP matrix in the PP/PA blend [37].

Former studies [38, 39, 51] proved the good stabilization qualities of the hydrophobic NS. The nanoparticles are effective to stabilize 80:20 PP/PA6 blends (and their mirror composition (i.e., 20/80)) regardless of the processing conditions employed to prepare or to post-process the blend. The preferential location of NS at the interface, creating a physical barrier that avoided coalescence, promoted the stabilization of the minor phase and droplet size reduction.

Particularly, increasing the extrusion time does not modify the blend morphology, and therefore, the thermodynamic factors might have prevailed over the kinetic ones [38, 39]. In addition, hydrophobic NS provides a fine-tune morphology that remains stable after post-processing stages such as compression molding, film extrusion or injection molding [51]. For instance, in a PP/PA6 blend, the hydrophobic NS was highly efficient in stabilizing the PA minor domains into droplets during film extrusion. The droplet morphology was virtually identical to that produced by compression or injection molding [51].

Besides the preferred localization of NS nanoparticles at the interface (acting as a solid barrier and stabilizing the size of the droplets), Fenouillot et al. [69] have pointed out other factors that might be responsible for the final morphology and reduced particle size: a reduction of the interfacial energy; a change in viscosity ratio between the polymers because of NS presence in one of the phases; and a limitation of the droplets or matrix motions because of the formation of a physical network between the particles [17]. Rheological analysis under linear and non-linear conditions have been conducted in order to elucidate changes in interfacial energies or inhibition of movements at molecular levels in PP/PA6 blends.

Novel rheological experiments (small and large amplitude oscillatory shear (SAOS) and (LAOS)) in compatibilized and uncompatibilized PP/PA6 blends mixed with NS have shown that the nanoparticles does not significantly affect the interfacial tension between the phases and therefore NS does not act as a compatibilizer [51, 68]. The lack of adhesion between the phases is not improved by NS addition. Therefore, the reduction of droplet size, observed with the addition of NS particles, is a consequence of the anticoalescence action of nanoparticles at the interface, rather than a compatibilizing effect that would reduce the interfacial tension. A suspension-like behavior is observed for the PP/PA blends in the presence of the NS particles. This behavior is related to the location of the particles surrounding the PA droplets. Experiments carried out in the nonlinear regime applying a large strain (known as LAOS) showed a significant increase of the Q (nonlinearity response) value in the PP/PA6/NS blend with the smallest particle size, far away from the one observed in pure PP and unfilled blends. As the size of the droplets reduces, the interface area increases, bringing about a larger nonlinear response [68]. Additionally, the PP/PA6 blends stabilized with NS exhibited higher elastic module than the analogous unfilled ones, as expected. Induced coalescence experiments, performed under slow shear flow, demonstrated that the addition of a compatibilizer or NS particles suppress efficiently the coalescence phenomenon. Because of that, the size of the droplets remained unchanged after the blends were submitted to flow [68]. These experiments proved the high efficiency of NS particles to stabilize the dispersed phase when they are located at the interface. When the droplets are surrounded by solid nanoparticles creating a physical barrier, the coalescence of the drops during collisions is less favored [68] (see Figure 4.6). The results agree well with the unchanged morphology observed after post-processing. The following scheme exemplifies the anticoalescence action of the NS particles [38].

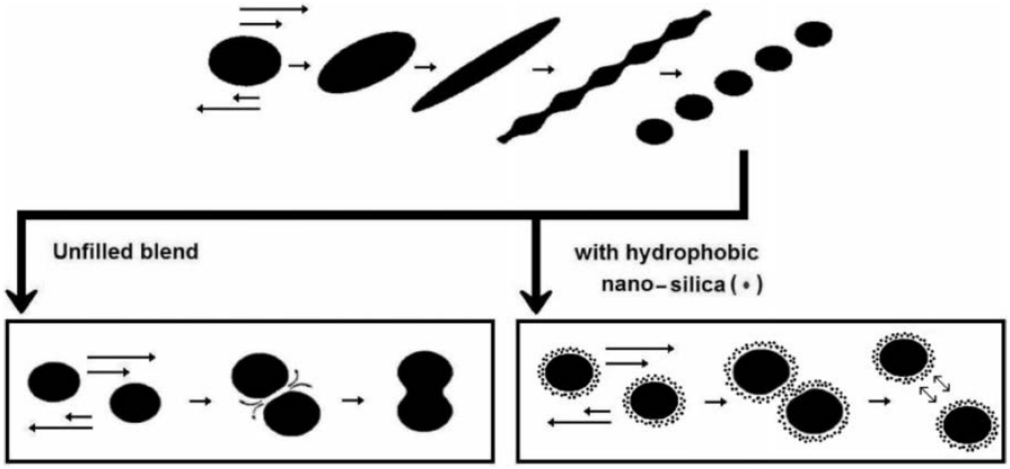

Figure 4.6 Representation of the action of hydrophobic silica nanoparticles against coalescence in PA/PP immiscible polymer blend [39].

In general, the PP/PA6 blends stabilized with hydrophobic and hydrophilic NS exhibits deficient mechanical properties [37-39, 51]. Only a report in a PA/PP 80:20 blend showed an important improvement in the Young’s modulus and elongation at break after the addition of 5 % of hydrophobic NS, as compared to the addition of hydrophilic NS [38].

Even though a fine-tuned morphology is obtained after the addition of NS, it seems that rigid NS nanoparticles reduce the size of the dispersed phase droplets, but act as stress concentrators without any improvement in interfacial adhesion. The addition of 5 % of hydrophobic NS to an uncompatibilized PP/PA6 blend further deteriorates the already poor mechanical performance of this blend. The Young’s modulus remained almost the same as the neat PP but the elongation at break highly reduces. Despite the fact that the PP/PA6 blend underwent the yielding point, the material failed after 6 % of deformation. The authors attributed the deficient properties to the lack of adhesion between the phases. As a semicrystalline material, the PA6 contraction might induce the interface separation [37]. As expected, changing the preparation method or post-processing technique does not significantly affect or improve the poor mechanical performance obtained with the NS addition. In spite of being excellent stabilizers at the interface, they do not promote an effective stress transfer between filler and matrix. The PP/PA6/NS blend has a droplet type dispersed phase with signs of poor adhesion, so de-cohesion is probably involved in the plastic deformation mechanism [51].

4.1.8 Binary polymer blends stabilized with both rigid nanoparticles and compatibilizer agents

Not so many publications [32, 58, 70-74] report the combined effect of adding compatibilizing agents and different types of nanofillers to inmiscible blends. Bose et al. observed fractionated crystallization of PA6 phase in 20/80 PA6/ABS blends mixed with a compatibilizing agent (styrene-maleic anhydride copolymer (SMA)) and CNT [75] The authors found that the content of SMA and SMA modified CNT plays a key role in governing the fractionated crystallization phenomenon. It seems that increasing the concentration of SMA in the blends leads to the finer size distribution of PA6 droplets as compared to the uncompatibilized PA6/ABS blends. As a result, some heterogeneities were active at specific high supercoolings. On the contrary, CNT act as hetero-nucleation sites, and as a result the crystallization temperatures increases. Additionally, the crystallinity degree of PA6 phase decreased in the uncompatibilized and SMA compatibilized blends. However, the incorporation of CNT modified with SMA increased the PA6 crystallinity, which may be due to the heterogeneous nucleation provided by the CNT [75].

Sinha-Ray et al. evaluated the effect of adding organoclays to PP/PS blends. The presence of 5 % of organoclay at the interface did not enhance significantly the Young's modulus, in comparison to the unfilled blend. However, a remarkable increase of ～ 60 % was observed when PPgMA was used instead of PP as polymer matrix. However, the strength resistance and elongation at break drastically diminished regardless the type of matrix or the content of the organoclay, in most cases. Hence, the refined morphology did not lead to better mechanical properties [32].

The effect of the type of compatibilizer has been evaluated by Scaffaro et al.[58, 74]. Three different compatibilizing systems: ethylene-co-acrylic acid copolymer (EAA), PE modified with acrylic acid (HDAA) and ethylene-co-glycidyl methacrylate copolymer (EGMA) did not significantly improved the mechanical properties of PE/PA6 blends filled with organoclay. The compatibilized blends exhibited a better impact resistance and tensile strength than the uncompatibilized ones (between 60 and 190 % of improvement). However, further addition of organoclay provided similar properties to those of the unfilled and uncompatibilized blend.

Istrate et al.[76] reported an improved mechanical performance in PS/PP blends compatibilized with PPgMA and mixed with organoclays. The expected droplet size reduction was observed. However, in this case, the organoclay particles were not only at the interface but also in the two phases. The authors reported an enhanced mechanical performance: impact strength and both tensile and flexural modulus increased [76]. Nevertheless, the improved properties obeyed more to a reinforcement effect of the organoclay particles than to a stabilizing role.

CNT were successfully distributed at the interface of PC/ABS blends compatibilized with ABSgMA. Chen et al.[72] demonstrated that this preferential location provided an effective conductive pathway. With very small CNT content, the electrical resistivity was very low. The addition of only 0.1 wt% CNT decreased the electrical resistivity from about 10^{14} Ω m to 10^{7} Ω m. Further increasing the CNT content induces even further decrease in electrical resistivity. The addition of the comaptibilizing agent decreased the interfacial tension between the phases and aided the migration of the CNT toward the interface.

In particular, very few publications have evaluated the effect of NS particles with compatibilizing agents. Yang et al. [71, 77] evaluated PP/EPDM and PPgMA/EPDM 80:20 blends mixed with hydrophilic and hydrophobic NS. The authors found an increase in the impact strength only when hydrophilic NS was used, and the blend was prepared in two steps. They attributed this behavior to the possible formation of a filler network structure that lead to a super toughened blend with Izod impact strength higher than that of the PP/EPDM blend without NS. However, the morphology obtained is not clear. It seems that many NS particles agglomerate at the interface but the dispersion is not good. In addition, the tensile properties were not reported and, EPDM is already a good toughening phase for PP.

4.2 EXPERIMENTAL PART

4.2.1 Materials

Isotactic polypropylene (PP) from Repsol (Isplen PP070G2M, MFI (230 ºC / 2.16 kg) = 12 g 10^{-1} min) and polyamide 6 (PA6) from Lanxess (Durethan B 30 S, MFI (260 °C / 5.0 kg) = 102 g 10^{-1} min), were used as polymer matrix and dispersed phase, respectively. Two nanosilica (NS) were employed. The first one is a fumed silica (SiO_2) from CABOT (CAB-O-SIL TS 530D, average particle (aggregate) length of ca. 200-300 nm) treated with hexamethyl disilazane, which gives it a hydrophobic character (denoted in this work as PHO). The other one is a SiO_2 from Skyspring Nanomaterials (6852 HN) modified with epoxy groups to increase its hydrophilicity (denoted PHI). Two polypropylene grafted with maleic anhydride (PPgMA) (DuPont Fusabond P353 and P613) of different grafting level were employed as compatibilizer agents. The grafting level was measured by FTIR and the values obtained were 1.20 % and 0.24 %. Thus, the level of grafting was indicated as high ($PPgMA_H$) for the compatibilizing agent with 1.20 % and medium ($PPgMA_M$) for the one with 0.24 %.

4.2.2 Nanocomposites preparation

Melt compounding of the 80/20 PP/PA6 blend with hydrophobic and hydrophilic NS was performed in a Collins ZK 25T co-rotating twin screw extruder (L/D ratio: 18 and screw diameter: 25mm). The temperature profile was 200-210-230-240 °C in the extrusion zone and the screw rotation rate was 40 rpm. The PP/PA6 ratio was 80:20 and the compatibilizer content was fixed at 10 wt.% with respect to the dispersed PA6 phase in all the samples. First, the PP and PA6 were mixed with a fixed content of both NS and compatibilizer agents. Then, a second set of samples were prepared with $PPgMA_H$ and a decreasing content of PHO. Also, a PP/PA6 sample without NS was prepared for comparison purposes. In addition, a PP/PPgMA sample without PA6 and NS was prepared for contact angle measurements. Prior to extrusion, NS nanoparticles and PP, PPgMA and PA6 pellets were dried for 24 h at 80 °C under vacuum. Table 4.3 summarizes the compositions of the samples. The number at the end of the designation indicates the NS content determined after TGA tests.

Table 4.3 Composition of the samples.

Sample designation	Compatibilizer agent	NS type	Composition (% wt.) [a]				
			PP	PA6	PPgMA	NS[b]	NS[c]
PP/PA6	-	-	80.0	20.0	-	-	-
PP/PPgMA$_M$/PA6	PPgMA$_M$	-	80.0	20.0	2.00	-	-
PP/PPgMA$_H$/PA6	PPgMA$_H$	-	80.0	20.0	2.00	-	-
PP/PPgMA$_H$/PA6/PHI 3.8	PPgMA$_H$	PHI	74.5	18.6	1.86	5.0	3.8
PP/PPgMA$_H$/PA6/PHO 3.7	PPgMA$_H$	PHO	74.5	18.6	1.86	5.0	3.7
PP/PPgMA$_H$/PA6/PHO 1.6	PPgMA$_H$	PHO	76.5	19.1	1.91	2.5	1.6
PP/PPgMA$_H$/PA6/PHO 0.9	PPgMA$_H$	PHO	77.3	19.3	1.93	1.5	0.9

[a] Calculated using the ratio PP/PPgMA/PA6 80:2:20.
[b] Theoretical NS content.
[c] Experimental NS content determined by TGA.

4.2.3 Thermogravimetry analysis (TGA)

The NS content was determined in a Q500 TA Instruments TGA analyzer under nitrogen atmosphere. The sample mass was about 6 mg. Before testing, the samples were dried overnight. A heating run was carried out from 40 to 800 ºC at 10 °C min^{-1}.

4.2.4 Morphological observations by means of scanning electron microscopic (SEM) and transmission electron microscopy (TEM)

The morphology of PA6 dispersed phase in the samples was observed by Scanning Electron Microscopic (SEM) using a HITACHI S-2700 microscope at 25 kV. Prior to observation, the samples were cryogenic fractured and coated with gold in a Bio-Rad SC500 sputter coater. Measurements of PA6 droplets diameter was performed to 100 particles. Number (d_n) and volume (d_v) average diameters, polydispersity (D) and average droplet number per cm^3 (N_i) were calculated using the following equations [78, 79]:

$$\boldsymbol{d_n} = \frac{\sum \boldsymbol{n_i d_i}}{\sum \boldsymbol{n_i}} \qquad \text{Eq. 4-1}$$

$$\boldsymbol{d_v} = \frac{\sum \boldsymbol{n_i d_i}^{4}}{\sum \boldsymbol{n_i d_i}^{3}} \qquad \text{Eq. 4-2}$$

$$\boldsymbol{D} = \frac{\boldsymbol{d_v}}{\boldsymbol{d_n}} \qquad \text{Eq. 4-3}$$

$$X_v = \frac{X_p/\rho_d}{X_p/\rho_d + \frac{1-X_p}{\rho_m}} \qquad \text{Eq. 4-4}$$

$$N_i = \frac{X_v 1cm^3}{\frac{\pi}{6}(d_n)^3} \qquad \text{Eq. 4-5}$$

where n_i is the number of droplets “i” of diameter d_i, X_p is the weight fraction of the minor phase, X_v is the volume fraction of the minor phase, ρ_d is the density of dispersed phase and ρ_m is the density of matrix.

Dispersion of NS in the polymer matrix was evaluated by transmission electron microscopy (TEM) employing a TECNAI G2 20 TWIN (FEI) microscope with an acceleration voltage of 200 keV. The samples were cut by ultramicrotomy using a Leica EMFC 6.

4.2.5 Contact angle measurements and surface and interfacial tension calculation

Contac angles of PP, PA6, PHO and a mixture of PP+PPgMA were measured at room temperature in a CAM 100 goniometer (KSV) employing water and ethylene glycol as liquids. Polymeric specimens were prepared by injection molding employing a Battenfeld BA 230E machine at 240ºC. The PHO specimen was prepared by compression molding (2 min, 9 ton.) at room temperature. All specimens were dried 24 h under vacuum at 80 ºC before measurement. A 5.0 µL of liquid was dropped onto the surface of the sample and the contact angle was measured. The values were averaged out over 40 measurements.

To calculate the interfacial tension, the surface tension of the different phases (PP, PP+PPgMA, PA6 and PHO-NS) was calculated first using the widely employed harmonic-mean method of Wu [80-82]. From the following equations, the polar (γ^p) and dispersive (γ^d) components of the surface tension, as well as, the surface tension (γ_S) were obtained:

$$(1+\cos\theta_1)\gamma_1 = 4\left[\frac{\gamma_1^d\gamma_S^d}{\gamma_1^d+\gamma_S^d}+\frac{\gamma_1^p\gamma_S^p}{\gamma_1^p+\gamma_S^p}\right] \qquad \text{Eq. 4-6}$$

$$(1+\cos\theta_2)\gamma_2 = 4\left[\frac{\gamma_2^d\gamma_S^d}{\gamma_2^d+\gamma_S^d}+\frac{\gamma_2^p\gamma_S^p}{\gamma_2^p+\gamma_S^p}\right] \qquad \text{Eq. 4-7}$$

$$\gamma_S = \gamma_S^p + \gamma_S^d \qquad \text{Eq. 4-8}$$

where θ_1 and θ_2 are the contact angles of liquid 1 (water) and liquid 2 (ethylene glycol) on the sample, respectively. The values of γ^p and γ^d for the liquids are reported in the literature [83]. After the surface tension of each polymeric component and NS were calculated, the interfacial tension between two phases (1 and 2) was determined employing the following equation:

$$\gamma_{12} = \gamma_1 + \gamma_2 - \frac{4\gamma_1^d\gamma_2^d}{\gamma_1^d+\gamma_2^d} - \frac{4\gamma_1^p\gamma_2^p}{\gamma_1^p+\gamma_2^p} \qquad \text{Eq. 4-9}$$

4.2.6 Infrared spectroscopy

FTIR transmission spectra of samples were collected after 32 scans in a Thermo Scientific NICOLET 6700 spectrometer. Sample films were prepared by compression molding and tested after dried overnigt at 80 ºC under vacuum.

4.2.7 Thermal analysis through diferential scanning calorimetry (DSC)

Samples of approximately 3 mg were encapsulated in aluminum pans and tested in a Perkin Elmer DSC Pyris 1 under ultra-high purity nitrogen atmosphere. The instrument was previously calibrated with an indium standard. All the samples were dried before testing for 24 h at 80 ºC under vacuum. The thermal protocols employed to study the crystallization behavior of the samples are described below.

Standard DSC experiments

All the samples in Table 1 were tested employing standard DSC measurements. The thermal program was as follows: an initial heating run from 20 to 240 °C at 20 °C min^{-1} keeping the sample for 3 min at that temperature to erase the thermal history, followed by a cooling scan down to -20 °C at 20 °C min^{-1}, and a second heating scan up to 240 °C also at 20 °C min^{-1}.

Self-nucleation experiments

Some samples from Table 1 were selected to conduct self-nucleation (SN) experiments to the PA6 dispersed phase. The self-nucleation thermal protocol was first proposed by Fillon et al. [84, 85] and has been extensively used by Müller et al. who have recently published a review about the technique [86]. The aim is to produce self-nuclei by partial melting of a standard crystalline state [87]. The thermal protocol is described as follows: (a) erasure of previous thermal history and crystalline memory by heating the sample up to 235 ºC for 3 min; (b) controlled cooling down to 50 ºC at 20 ºC min^{-1} to create a standard crystalline state (the sample was kept at 50 ºC for 3 min); (c) heating up to a self-nucleation temperature (T_s) at 20 ºC min^{-1}; (d) isothermal step at T_s for 3 min; (e) DSC cooling scan from T_s down to 50 ºC at 20 ºC min^{-1} to record the effect of the thermal treatment at T_s on the PA6 crystallization (the sample was kept at 50 ºC for 3 min); and (f) DSC heating scan from 50 ºC up to 235ºC, to record the PA6 melting after the entire treatment.

From the SN experiments, the *Domains* of Self-Nucleation can be determined. Depending on the T_s chosen, the polymer can melt entirely, only self-nucleate or self-nucleate and anneal. If the T_s is high enough, the polymer melts completely and no crystalline memory is left (the crystallization (T_c) and melting (T_m) temperatures remain unchanged). Those T_s temperatures belong to *Domain I*.

In *Domain II*, the melt is no longer isotropic and two possible situations can be considered. In the high temperature range within *Domain II*, the melt retains some residual chain segmental orientation, or crystalline memory that causes self-nucleation. In the low temperature range within *Domain II*, small fragments of crystals remain that cannot be annealed during the time spent at T_s [86].

When the T_s is low enough, the material melts only partially and a significant amount of crystals remain unmolten. These unmolten crystals can anneal during the 3 min holding time at Ts. A characteristic annealing peak will then appear in the subsequent melting scan, revealing *Domain III.*

4.2.8 Mechanical properties. Tensil and Impact experiments

Tensile and Izod impact resistance properties were measured following ASTM D638 and ASTM D256, respectively. Tensile (Type IV) and impact specimens were prepared by injection molding employing a Battenfeld BA 230E machine at 240ºC. All specimens were tested after 48 h. Tensile testing measurements were performed employing an INSTRON 5569 universal machine at 50 mm/min and the values were averaged out over 5 valid measurements. Impact specimens were notched in an INSTRON-CEAST AN50 notching machine and Izod impact resistance was measured in a CEAST 6548/000 pendulum instrument. The values were averaged out over 7 valid measurements.

4.2.9 Barrier properties

Permeability tests were performed on compression molded films. Carbon dioxide permeability measurements were carried out using a permeation cell assembled in our laboratory, similar to other devices described in literature [88, 89]. The gas permeability coefficient was calculated from the slope in the plot of permeated pressure versus time, *dp/dt* (Torr/s), at steady state, by the following equation:

$$P = 10^{10}\,\frac{(dp/dt)LVT_{STP}}{p_A p_{STP} T A} \qquad \text{Eq. 4-10}$$

where P is the permeability coefficient in barrer, V is the volume of the downstream chamber (in our case 16.8122 cm^3), A is the effective area of the film (1.8 cm^2), L is the thickness of the membrane (cm), T_{STP} and p_{STP} are the standard temperature and pressure (273 K and 76 cm Hg), p_A is the pressure of the penetrant gas in the upstream chamber (Torr) and T is the temperature at the measurement (298 K). The measurements have been performed at 25 °C and at 1 atm. The values were averaged out over 3 valid measurements. The sample thickness was ~ 160 μm.

Oxygen permeability measurements were carried out in a MOCON OX-TRAN 2/21 (USA) equipment in accordance with ASTM D3985 and ISO 15105-1.2. The measurements were performed at 23 °C, 1 atm and 0 % relative humidity. The films were dried at 70 °C for at least 5 days under vacuum before running the experiments. More details about the permeation cells and experimental methods are reported in previous works [90]. The sample thickness was 143 μm for pure PP and ~ 160 μm for the blends. The values were reproducible.

4.3 RESULTS AND DISCUSIONS

4.3.1 Morphology of the PP/PA6 blends with and without nanosilica and compatibilizer agents

Figure 4.7a, b and c show the sea island morphology expected in these immiscible blends, in which PA6 droplets are dispersed inside the PP matrix. The spherical morphology of the PA6 phase is the most thermodynamically stable one. The immiscible nature of PP/PA6 blend is evident in Figure 4.7a. The morphology observed is very heterogeneous with a broad particle size distribution (see Table 4.4). The presence of holes accounts for the lack of adhesion between the phases, which is characteristic of immiscible polymer blends. As it is well established, the blend immiscibility and phase separated morphology results from the different polarities of PP (apolar) and PA (polar) blend components [7, 37, 91].

In order to overcome coarse morphology and lack of adhesion in inmiscible polymer blends, several strategies have been reported in the literature [7], including the addition of compatibilizing agents or nanoparticles [17, 18, 44, 45]. Some authors have previously reported the positive effect of adding nanosilica to improve the morphology of a PP/PA6 80:20 blend [37, 51]. A reduction in the particle size of the PA6 phase was observed. Therefore, the combined effect of adding both compatibilizing agent and silica nanoparticles is evaluated.

First, a refined morphology was obtained when a compatibilizing agent was added to the PP/PA6 blend. Both particle sizes (d_n and d_v) and particle size distribution (D) exhibited a remarkable reduction (see Figure 4.7b, c and d. and Table 4.4) in comparison with the uncompatibilized blend. This observation is expected since PPgMA is a well-known compatibilizing agent for PP/PA6 blends [20]. Comparing the two compatibilizing agents employed, $PPgMA_H$ proved to be more effective since the particle size and distribution of the PA droplets in this blend ($PP/PPgMA_H/PA6$) were smaller than those of the blend with the medium grafting level compatibilizer ($PP/PPgMA_M/PA6$). This result is a consequence of the higher grafting level of the $PPgMA_H$ compatibilizing agent.

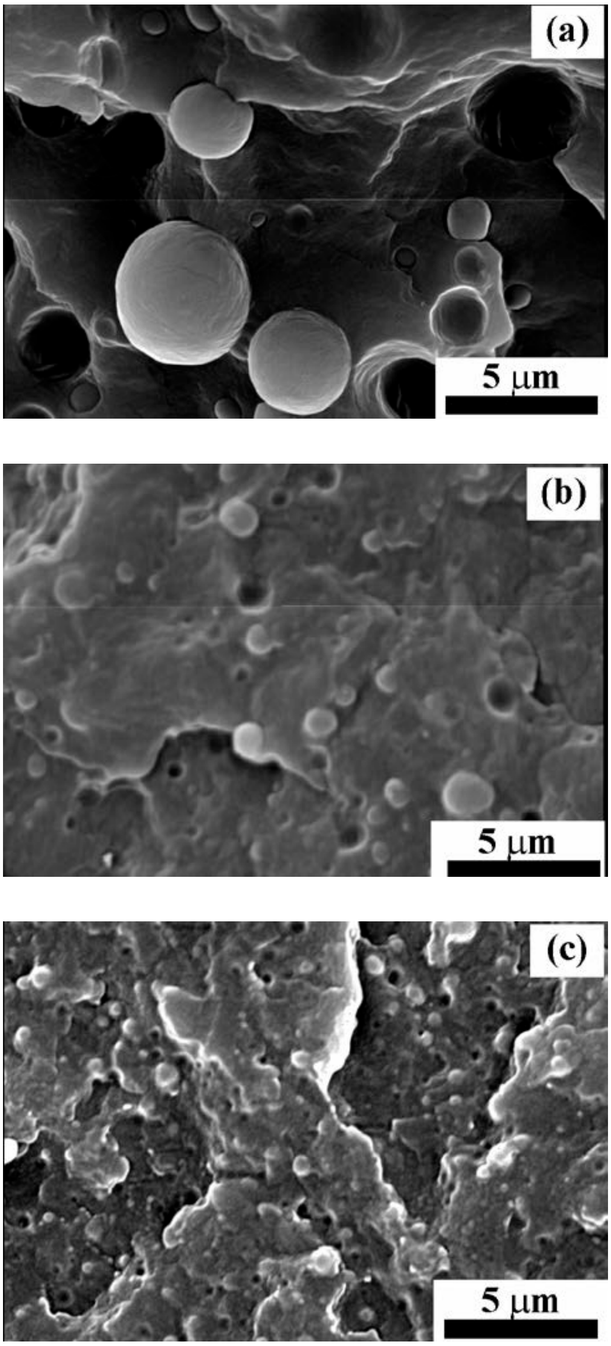
(a)
5 μm
(b)
5 μm
(c)
5 μm

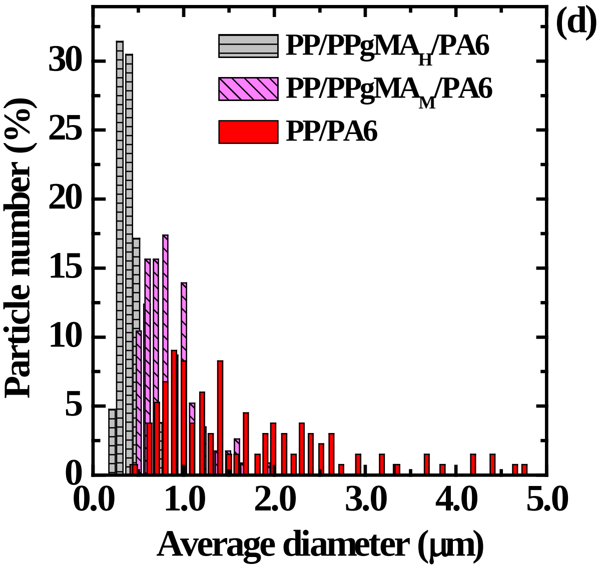

Figure 4.7 Scanning electron microscopy images of a) PP/PA, b) PP/ PPgMA$_M$/PA6 and c) PP/ PPgMA$_H$/PA6 blends. d) Particle size histogram of the aforementioned blends.

Since the PP/PA6 blend compatibilized with the PPgMA$_H$ agent exhibited a smaller particle size and distribution, this blend was chosen to study NS addition. Two types of NS, one hydrophilic (PHI) and another hydrophobic (PHO), were added to this blend in order to observe the combined effect of both NS and PPgMA on the final morphology. The NS content in both blends was ~4 %.

Table 4.4. Number-average (d_n) and volume-average (d_v) diameters, particle size distribution (D) and average droplet number (N_i) of the blends.

Sample	d_n (μm)	d_v (μm)	D	N_i x 10^{-11} (cm^{-3})
PP/PA6	1.67	3.31	1.98	1
PP/PPgMA$_M$/PA6	0.86	1.19	1.38	5
PP/PPgMA$_H$/PA6	0.41	0.52	1.27	47
PP/PPgMA$_H$/PA6/ PHI 3.8	0.51	0.76	1.48	22
PP/PPgMA$_H$/PA6/ PHO 3.7	0.20	0.38	1.89	357
PP/PPgMA$_H$/PA6/PHO 1.6	0.35	0.53	1.52	71
PP/PPgMA$_H$/PA6/PHO 0.9	0.63	0.76	1.19	12

The morphology of both samples, PP/PPgMA$_H$/PA6/PHI 3.8 and PP/PPgMA$_H$/PA6/ PHO 3.7, is depicted in the SEM micrographs of Figure 4.8a and b. The addition of the hydrophilic NS (PHI) did not cause any significant change on the morphology of the compatibilized blend (see Table 4.4). However, the addition of hydrophobic NS (PHO) reduced the PA6 droplet size significantly (see Table 4.4 and Figure 4.8c). In fact, comparing with the uncompatibilized PP/PA6 blend, a reduction of ~88 % of the droplet size was obtained, due to the combined effect of the high grafting level compatibilizing agent (PPgMA$_H$) and hydrophobic silica nanoparticles (PHO). Also, the presence of holes is less frequent, which indicates that some improvement on the adhesion between the phases might have been also accomplished.

The large reduction in average particle size and its distribution for the PP/PPgMA$_H$/PA6/ PHO 3.7 blend, as compared to the other depicted in Figure 4.8, is caused by the preferred location of the NS nanoparticles at the polymer-polymer interface, as confirmed by the TEM images shown in Figure 4.9. Similar morphologies have been previously reported [37, 51] in uncompatibilized PP/PA6/NS blends and for other types of immiscible blends [40-42].

Figure 4.9a shows that hydrophobic NS nanoparticles are located inside the PP matrix and also surrounding the PA6 droplets. The SEM image inset in Figure 4.8b also provides evidence of this preferential location of the particles at the interphase (as signaled with an arrow). Since the nanoparticles are located at the interphase, they act as physical barriers that prevent the coalescence of the dispersed PA6 droplets during melt mixing (see arrows in Figure 4.9a). Therefore, the combination of NS nanoparticles and a compatibilizing agent had a synergistic effect on refining the PP/PA6 blend morphology. While PPgMA$_H$ improves the adhesion and compatibilization between the phases, reducing the droplet size, the NS nanoparticles, especially the hydrophobic ones, contribute to stabilize the PA6 phase into even smaller droplets by preventing coalescence during melt mixing.

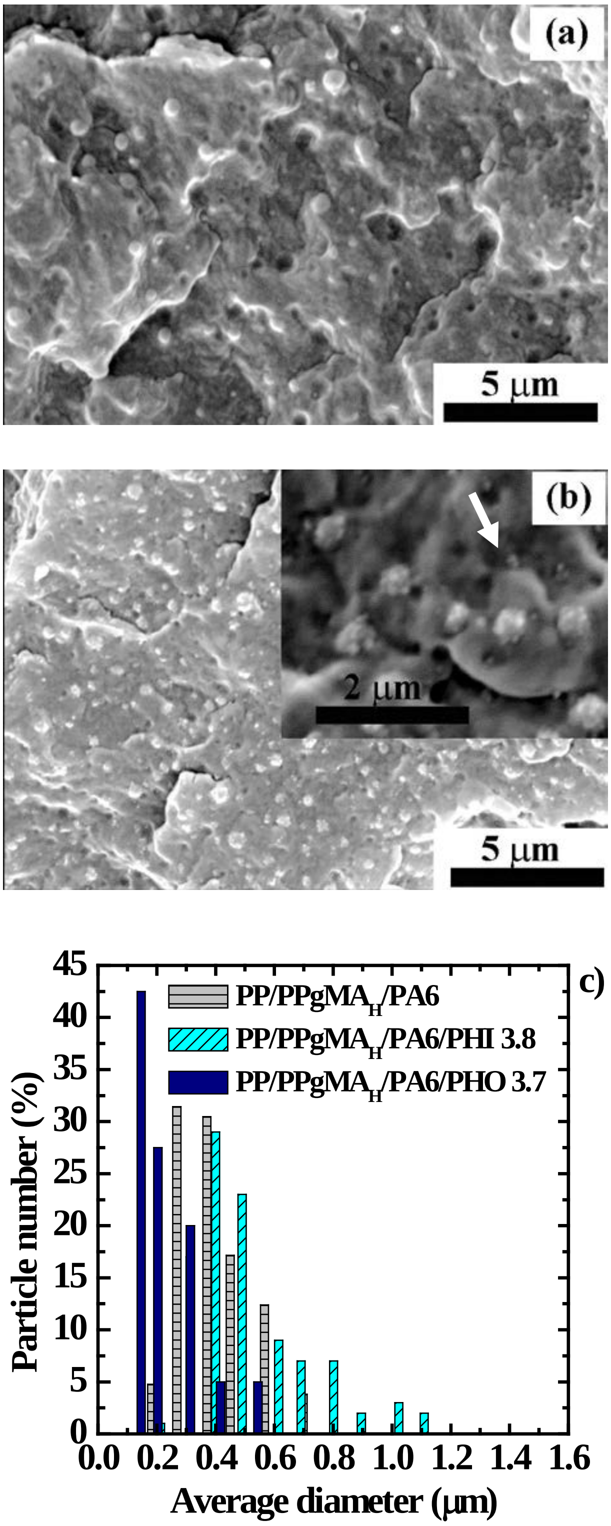

Figure 4.8 Scanning electron microscopy images of a) PP/PPgMA$_H$/PA6/PHI 3.8, b) PP/PPgMA$_H$/PA6/PHO 3.7 blends. c) Particle size histogram of the aforementioned blends compared to the analogous one without NS.

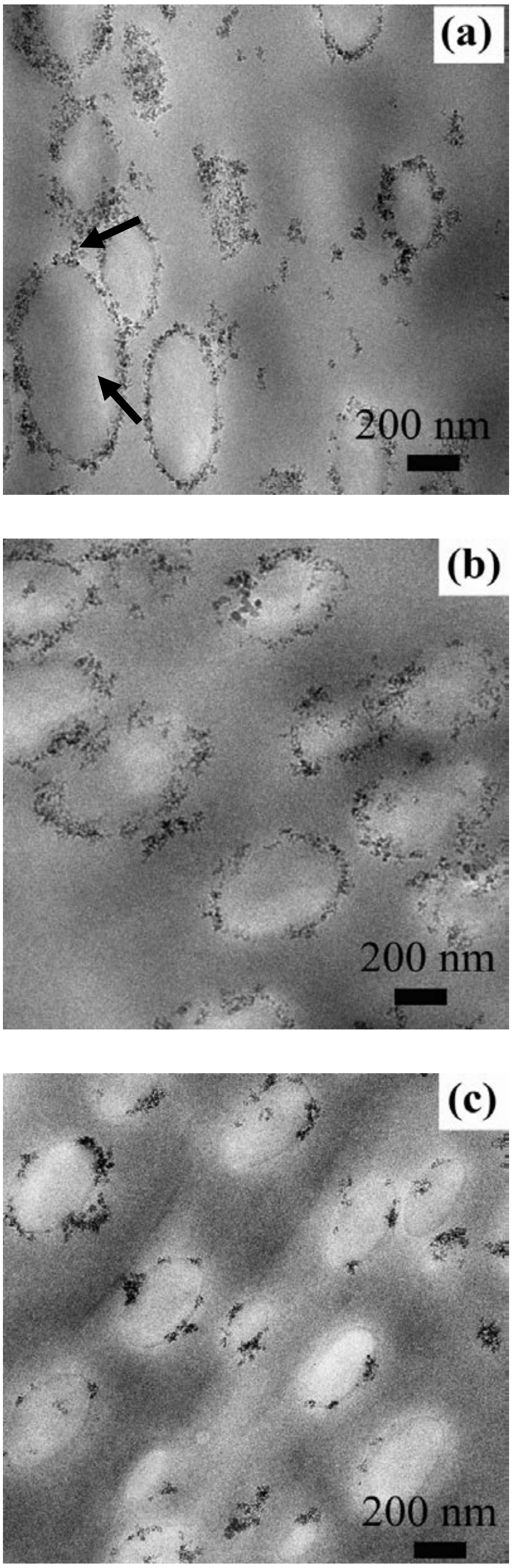

Figure 4.9 Transmission electron microscopy images of blends with decreasing PHO nanosilica content: a) PP/ PPgMA$_H$/PA6/PHO 3.7, b) PP/ PPgMA$_H$/PA6/PHO 1.6 and c) PP/ PPgMA$_H$/PA6/PHO 0.9.

In view of the results obtained above, it is interesting to evaluate the effect of NS content on blend morphology. To this purpose, two additional blends with a reduced PHO-NS content were prepared. Hydrophobic NS was chosen since its effect on the droplet size reduction was more significant, in comparison with hydrophilic NS. The morphology of these two new samples is shown in Figure 4.9b and c, and the droplet size and droplet size distribution values are shown in Table 4.4. As the PHO-NS content was reduced, the droplet size increased (see Figure 4.10). The TEM micrographs of Figure 4.9 demonstrate that the polymer-polymer interphase became less saturated with nanoparticles as the PHO-NS content was lower. At the lowest NS content, some PA6 droplets were not even surrounded by NS. Thus, NS nanoparticles were not able to stabilize and avoid coalescence of the droplets effectively, and as a consequence, droplet size increased. Similar observations have been reported by other authors in different systems [39].

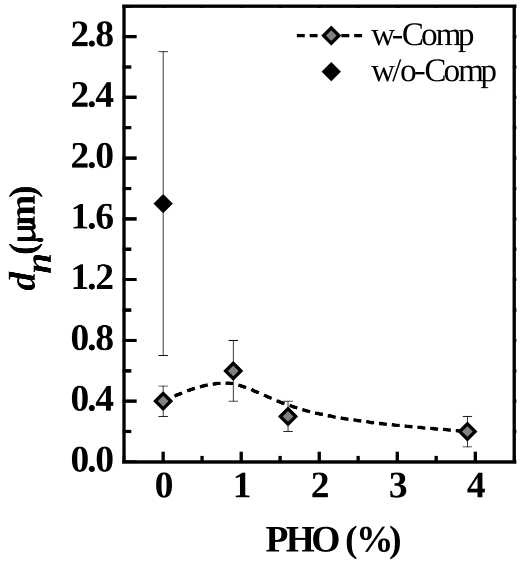

Figure 4.10 Particle size vs PHO nanosilica content in the blends with (w) and without (w/o) compatibilizer agent.

The reasons for the final location of nanoparticles (inside the polymer matrix, at the interface or inside the dispersed phase) remain a subject of high interest [17, 49]. Since kinetic, rheological and thermodynamic factors, as well as mixing conditions and polymer-filler interactions are closely related to the final morphology, it might be difficult to elucidate which is the main factor involved.

The final location of the nanoparticles is induced by particle migration in the molten state and under shear. It will also depend on which of the phases the particles are initially located. Some authors [17] have propose that the viscosity ratio between the phases may control the particle distribution when the interfacial tension between the two polymers is not too high. However, if the viscosities of each phase are similar, the interfacial energy between the particles and the polymers would be a factor of major importance.

In order to address the importance of thermodynamic interactions between the blend components, surface and interfacial tension between pair components in the blends were estimated by contact angle measurements and the harmonic-mean equations proposed by Wu (see equations 6 through 9 above) [80, 81]. The values are presented in Table 4.5 and Table 4.6.

Table 4.5 Surface Tension of PP, PA6, PHO and the mixture PP/PPgMA

Sample	γ^d	γ^p	γ
PP	14.0	12.0	26.0
PA6	12.0	31.7	43.7
PP/PPgMA$_M$	9.6	24.5	33.7
PP/PPgMA$_H$	13.5	19.8	33.3
PHO	0.8	13.8	14.6

Table 4.6 Interfacial Tension between pair components of the blends

Pairs	Interfacial tension (mN/m)
γPP-PA	9.0
γPP/PPgMA$_M$ -PA	1.3
γPP/PPgMA$_H$ -PA	2.8
γPP/PPgMA$_M$ -PHO	10.1
γPP/PPgMA$_H$ -PHO	12.5
γPA-PHO	16.9
γPP-PHO	12.0

An interfacial tension value of 9.00 mN/m was obtained for the PP-PA6 system, which is very close to other values reported in the literature [92]. Once the compatibilizing agent was added, the interfacial tension between the phases was highly reduced (from 9.00 to 1.30 and 2.81 mN/m). This reduction was expected since the compatibilizing agents play two main roles: 1) they reduce interfacial tension and, as a consequence, break up the droplets during mixing, and 2) they stabilize the blend avoiding the subsequence coalescence of the droplets [17]. Therefore, the reduced interfacial tension of this blend promoted the reduction of the PA6 droplet size observed in Figure 4.7b and c. The compatibilizing action of PPgMA in PP/PA blends has been reported extensively [21, 24, 93]. The interfacial compatibilization of the PPgMA is a consequence of the reaction between the anhydride group grafted on PPgMA and the terminal amine group of PA6. The formed graft copolymer is immiscible in both phases and thus locates at the interphase, acts as an emulsifier and reduces the interfacial tension. Through FTIR experiments, the compatibilizing role of PPgMA can be evaluated. Figure 4.11 shows the FTIR spectra of selected PP/PA6, PP/PPgMA$_H$/PA6 and PP/PPgMA$_H$/PA6/PHO 3.7 blends. The characteristic peaks of PA6 in the uncompatibilized blend appear at 3296 cm^{-1} (stretching of the NH bond in amide II), 1637 cm^{-1} (bending of the NH bond in amide I) and 1542 cm^{-1} (bending of the NH bond plus stretching of CN bond in amide II) [24]. The slight shift of these bands observed in the compatibilized blends could be indicative of the interactions promoted by the compatibilizing agent.

The resulting interfacial tension values between the PHO-NS and the polymers in the blend are very interesting. The surface tension of PHI-NS could not be measured due to the very high hydrophilic nature of this nanoparticle. From results of

Table 4.6, the PHO-NS particles will prefer to remain in the PP matrix and not inside the PA6 droplets, since the interfacial tension value between the PHO and PP is lower. The chemical modification of the NS surface with hexamethyl disilazane makes it more hydrophobic and therefore promotes specific interactions with the apolar PP matrix. For this reason, Figure 4.9a shows that some NS particles are within the PP matrix while none can be observed inside the PA6 phase.

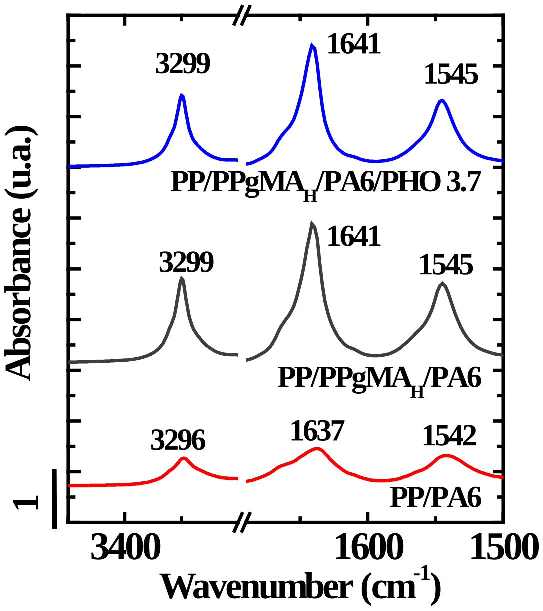

Figure 4.11 FTIR spectra of PP/PA6 and PP/PPgMA$_H$/PA6, and PP/PPgMA$_H$/PA6/PHO 3.7 blends.

Additionally, PHO-NS particles mostly accumulated at the PP/PA6 interface in all the systems, but this fact is probably related to kinetic factors. The final location of the nanoparticles will depend on the balance between kinetic and thermodynamic effects. It is possible that nanoparticles diffusion from the PP matrix towards the interface was promoted by shear induced collisions during melt mixing [17]. Since most of NS particles are located at the polymer-polymer interface and less in the PP matrix it can be speculated that the kinetic effects prevailed over the thermodynamic ones in the final location of the particles. A similar result was obtained for all the systems examined.

4.3.2 Non-isothermal crystallization behavior and self-nucleation experiments of the PP/PA6 blends with and without nanosilica and compatibilizer agents

The morphology analyzed previously significantly affects the physical properties of the blends. In this section, the effect of droplet size on the crystallization behavior of the PA6 phase will be addressed.

The characteristic thermal properties obtained during heating and cooling scans by DSC are presented in Table 4.7, Table 4.8 and Table 4.9. The blends display the separate melting of PP and PA6 expected from immiscible blends. The melting point values do not significantly vary in comparison with those of the homopolymers (see Table 4.7, Table 4.8).

After the samples were melted and their thermal history was erased, they were cooled down and their crystallization behavior recorded as shown in Figure 4.12. Under the non-isothermal conditions applied, PA6 and PP homopolymers crystallized with well defined exotherms that peak at 187.7 ºC and 111.8 ºC respectively.

The PP/PA6 blend and the compatibilized PP/PPgMA$_M$/PA6 and PP/PPgMA$_H$/PA6 blends displayed two well-separated exothermic peaks that belong to the crystallization of each phase. The high temperature peak corresponds to the crystallization of the PA6 droplets, which sometimes is not easy to see with the scale employed in Figure 4.12a. Therefore, a close up is presented in the high temperature range in Figure 4.12b. The low temperature exotherms correspond to the crystallization of the PP matrix.

The PA6 crystallization temperature in these blends remained unchanged except in the case of the PP/PPgMA$_H$/PA6 sample, in which it was slightly reduced. However, the PP matrix exhibited an increase in its crystallization temperature of 6-9 ºC. The increase observed can be explained by a nucleating effect induced by the previously crystallized PA6 droplets.

Regarding the normalized crystallization enthalpy (i.e., the values are normalized with respect to the amount of crystallizing phase under consideration), the PP phase exhibited similar values to that of the neat polymer (within the experimental error of the measurement). However, the PA6 droplets crystallization enthalpy in the blends was notably reduced (see Table 4.9). Once the NS nanoparticles were added to the blends, the reduction in the PA6 crystallization enthalpy was even larger. A closer look to the crystallization of the PA6 phase in the blends with PPgMA and NS shows that the exothermic peak of PA6 was highly reduced in size (see Figure 4.12b) and even disappeared in the sample with the lowest PA6 droplet sizes (PP/PPgMA$_H$/PA6/PHO 3.7, see Table 4.9). In fact, a clear correlation between the PA6 crystallization enthalpy (in the temperature range of 130-240 ºC) and droplet size was found and it is illustrated in Figure 4.13, where the crystallization enthalpy is plotted against the d_n value of the PP/PA6 blend and the blends with PPgMA$_H$ and PHO-NS.

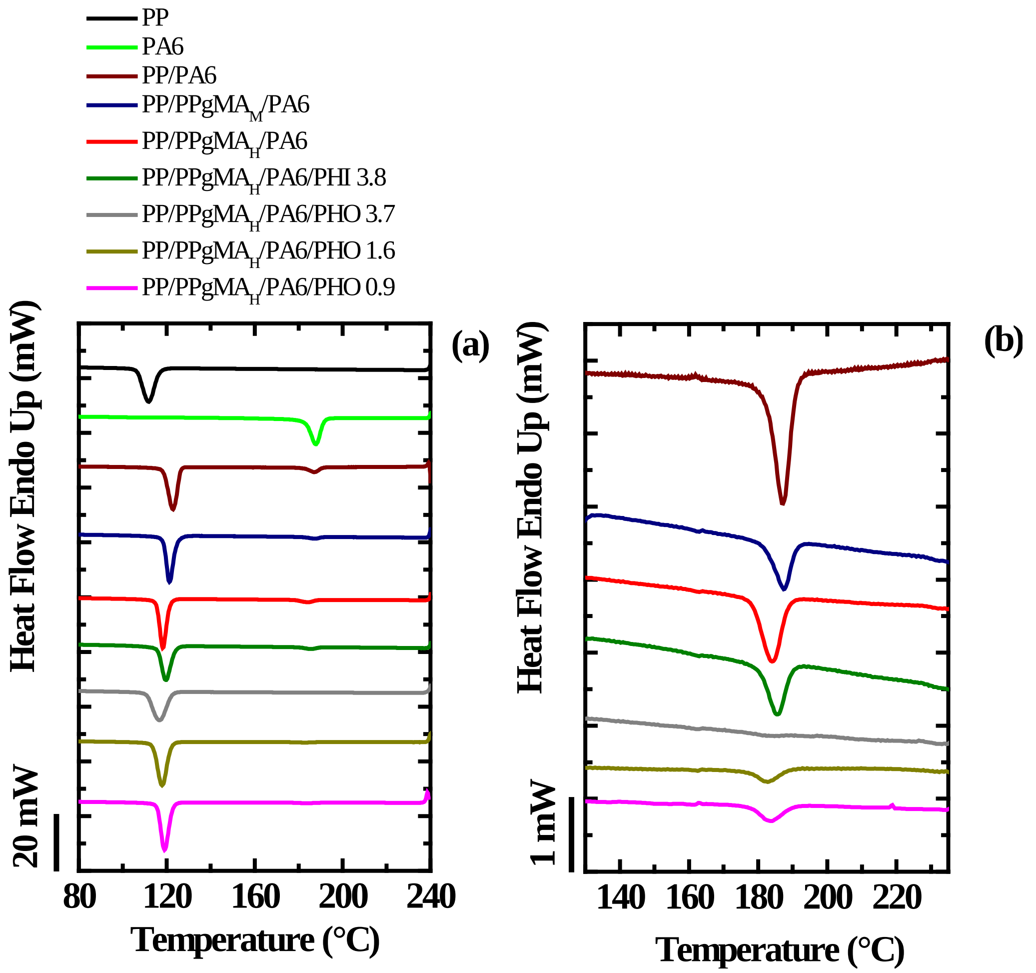

Figure 4.12 DSC cooling scans of the indicated blends at 20 ºC min^{-1} after melting at 240 ºC for 3 min.

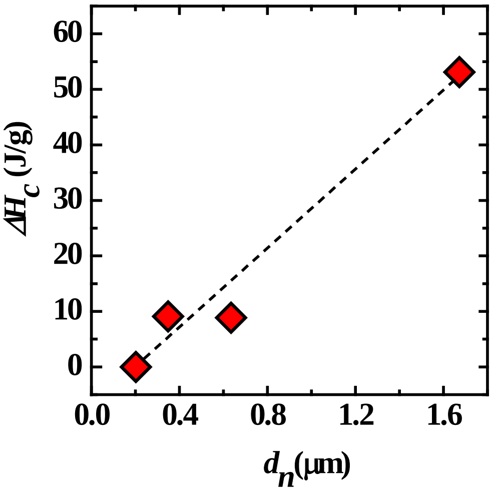

Figure 4.13 PA6 crystallization enthalpy (in the temperature range 130-240 C) vs droplet size (d_n) in the PP/PA6 blend and blends with PPgMA$_H$ and PHO-NS.

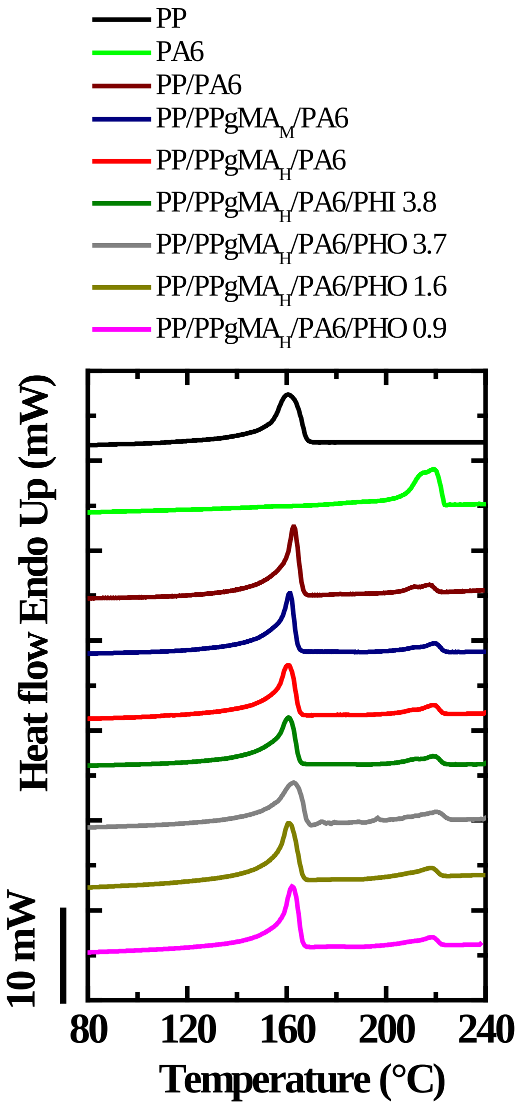

Figure 4.14 Second DSC heating scans of the indicated blends at 20 ºC min^{-1}.

The fact that the PA6 droplets in the PP/PPgMA$_H$/PA6/PHO 3.7 blend do not show any crystallization signal in the 130-240 ºC range (the usual crystallization temperature range for PA6) does not mean it cannot crystallize at all during cooling from the melt. A sub-micron size should not prevent the crystallization of the PA6 droplets [94]. Therefore, the PA6 droplets should have crystallized during cooling at lower temperatures than usual and the exothermic signal could be simply overlapped with that of PP crystallization. The evidence supporting this is given by the second heating scans depicted in Figure 4.14. A small but distinctive higher temperature endothermic peak accounts for the melting of the PA6 crystals. And since no cold crystallization is observed during heating, crystallization of PA6 droplets must have occurred during cooling. In fact, if the PA6 crystallinity degrees obtained from the first and second DSC heating scans are compared, similar values (within the experimental error of the measurements) are obtained in each blend (see Table 4.8), even in the blend in which no crystallization peak was observed (PP/PPgMA$_H$/PA6/PHO 3.7). Therefore, the crystallization of the PA6 did take place but not at the temperature expected for PA6. This behavior is typical of fractioned crystallization [12, 78, 95-97].

Comparing the data summarized in Table 4.8 and Table 4.9, it can be seen that the observed PA6 crystallization enthalpy is significantly lower than its melting enthalpy. Thus, other crystallization events must have taken place during cooling. What this means is PA6 crystallized in a fractioned fashion, in two or more crystallization events that occurred at lower temperatures but got overlap with the PP crystallization

Table 4.7 Thermal properties of PP in the blends obtained from DSC 1st and 2nd heating scan at 20 ºC min^{-1}.

Sample	T_m PP ^{1st} (°C)	ΔH_m PP^{1st} (J/g)	χ_c ^{1st} (%)	T_m PP ^{2nd} (°C)	ΔH_m PP^{2nd} (J/g)	χ_c ^{2nd} (%)
PP	165.8	80	39	160.7	83	40
PP/PA6	164.0	100.7	49	163.0	99	48
PP/PPgMA$_M$/PA6	163.8	106	51	161.1	96	47
PP/PPgMA$_H$/PA6	164.8	91	44	160.4	92	45
PP/PPgMA$_H$/PA6/PHI 3.8	162.4	102	49	160.8	92	44
PP/PPgMA$_H$/PA6/PHO 3.7	164.5	80	38	162.8	100	48
PP/PPgMA$_H$/PA6/PHO 1.6	163.0	87	42	161.0	104	50
PP/PPgMA$_H$/PA6/PHO 0.9	167.1	95	46	162.1	100	48

Table 4.8 Thermal properties of PA6 in the blends obtained from DSC 1st and 2nd heating scan at 20 ºC min^{-1}.

Sample	T_m PA6 ^{1st} (°C)	ΔH_m PA6^{1st} (J/g)	χ_c ^{1st} (%)	T_m PA6 ^{2nd} (°C)	ΔH_m PA6^{2nd} (J/g)	χ_c ^{2nd} (%)
PA6	220.9	62	33	219.3	72	38
PP/PA6	218.1	54	29	217.4	66	35
PP/PPgMA$_M$/PA6	220.9	68	36	219.6	62	33
PP/PPgMA$_H$/PA6	218.9	56	30	218.9	57	30
PP/PPgMA$_H$/PA6/PHI 3.8	219.9	67	36	218.9	60	32
PP/PPgMA$_H$/PA6/PHO 3.7	220.9	58	31	219.9	72	38
PP/PPgMA$_H$/PA6/PHO 1.6	219.3	63	33	218.0	66	35
PP/PPgMA$_H$/PA6/PHO 0.9	218.7	62	33	218.7	60	32

Table 4.9 Thermal properties of PP and PA6 in the blends and nanocomposites obtained from cooling scan at 20 ºC min^{-1}.

Sample	T_c PP (°C)	ΔH_c PP (J/g)	T_c PA6 (°C)	ΔH_c PA6 (J/g)
PP	111.8	-85.7	-	-
PA6	-	-	187.7	-63
PP/PA6	122.9	-99.3	187.2	-53
PP/PPgMA$_M$/PA6	121.2	-97	187.4	-22
PP/PPgMA$_H$/PA6	118.2	-93	184.0	-31
PP/PPgMA$_H$/PA6/PHI 3.8	118.2	-97	185.3	-24
PP/PPgMA$_H$/PA6/PHO 3.7	116.5	-99	-	-
PP/PPgMA$_H$/PA6/PHO 1.6	117.8	-105	182.8	-9
PP/PPgMA$_H$/PA6/PHO 0.9	119.0	-103	183.8	-9

Fractioned crystallization is a well-known phenomenon reported in immiscible polymer blends with a fine dispersion of a crystallizable phase [38, 64, 65]. It occurs when the number of dispersed droplets (in this case, PA6 droplets) is higher than the number of active heterogeneities present in bulk PA6. When the material is dispersed into droplets, some droplets will contain the active heterogeneities that can activate nucleation of PA6 at the usual supercoolings of bulk PA6. However, there will be others that may only contain less active heterogeneities and also some droplets that do not contain any heterogeneity (clean droplets). Less active heterogeneities can only trigger nucleation at larger supercoolings and clean droplets with no heterogeneous nuclei can only nucleate at extreme supercoolings (near T_g). As a result, the material could display a series of crystallization exotherms, reflecting the different types of droplet populations that nucleate at different supercoolings.

For instance, the PP/PPgMA$_H$/PA6/PHO 3.7 blend that exhibited the smallest droplet size and no crystallization peak during cooling was the sample with the highest average droplet number per cm^3 (357 x 10^{11} droplets/cm^3, see Table 4.4). A polymer like PA6 has a typical number of highly active heterogeneities in the range of 10^7 heterogeneties/cm^3. This means that there are 4 orders of magnitude more PA6 droplets that active heterogeneities available, hence the number of droplets that can contain highly active heterogeneities is very small (in relative terms) and their crystallization cannot be detected by the DSC. Therefore, most of the crystallization of the droplets must be occurring at much lower temperatures and it is probably overlapped with the crystallization of the PP matrix. A fractionated crystallization phenomenon has also been reported by other authors [12]. For instance, Chen et al. [98] observed fractionated crystallization in PP/PS 20/80 blends with hydrophobic NS nanoparticles surrounding dispersed PP droplets. Similar to our results, the authors found that fractioned crystallization became more pronounced as the NS content was higher (and the droplet size reduced).

In order to prove the hypothesis that the lack of active heterogeneous nuclei in every PA6 droplet was the reason for the fractioned crystallization behavior observed, self-nucleation experiments were conducted (as described in the Experimental Section) on selected samples; including this particular blend: PP/PPgMA$_H$/PA6/PHO 3.7. Morales et al. [99] employed for the first time the self-nucleation technique to that purpose and many others researchers followed them [78, 96, 100-102]. Consider Figure 4.15, in which the cooling scans from the indicated T_s and the subsequent heating scans of this blend are plotted (only the temperature range in which the crystallization and melting transitions of PA6 occur are shown for clarity).

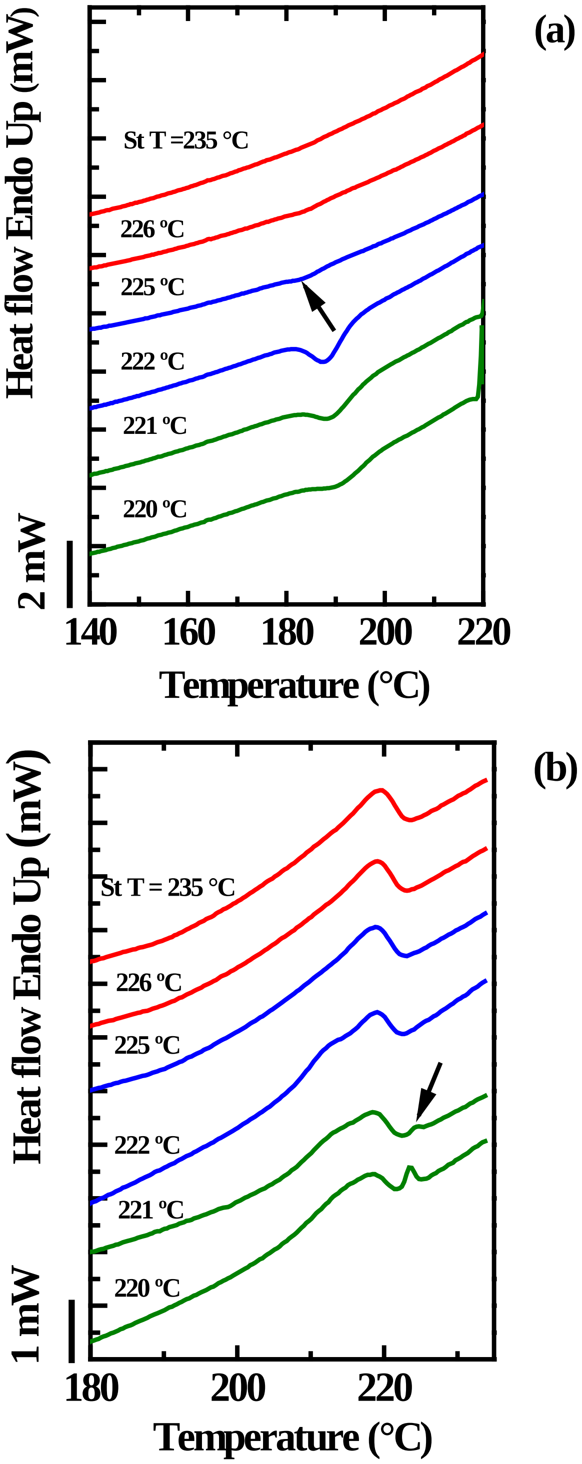

Figure 4.15 Self-nucleation of PA6 in PP/PPgMA$_H$/PA6/PHO 3.7 blend. a) DSC cooling scans from indicated T_s values and b) subsequent DSC heating scans (A color

code have been employed to indicate the self-nucleation domains: red for *Domain I*, blue for *Domain II* and green for *Domain III*)

At higher T_s values, the DSC cooling scans remained the same (without indication of PA6 crystallization (red curves)), but as the T_s temperature was decreased until 225 ºC, a small exothermal signal appeared at 183.6 ºC that indicated the transition from *Domain I* to *Domain II* (see Figure 4.15a). At 225 ºC, the self-nucleation domain started, which means that from these temperature and below some of the PA6 droplets have been injected with enough self-nuclei that enhanced its crystallization, and therefore, it takes place at the expected temperature for bulk PA6. As the T_s values were further reduced, an increase in the PA6 crystallization temperature as well as in its enthalpy were obtained as expected.

The self-nucleation technique demonstrated that the lack of active nuclei led to the fractioned crystallization behavior observed for the PA6 phase in the blends, as the droplet size decreased. The transition from *Domain II* to *Domain III* occurred at 221 ºC, a temperature in which a second melting peak appeared in the subsequent heating scan (see Figure 4.15b). This higher temperature endothermic peak corresponds to the melting of the annealed crystals at T_s.

From the figures shown above, a visual representation of the three domains of self-nucleation has been drawn in Figure 4.16 for the PP/PPgMA$_H$/PA6/PHO 3.7 blend. A standard DSC melting trace of this blend is plotted employing the same color code to indicate the determined self-nucleation domains: red for *Domain I*, blue for *Domain II* and green for *Domain III*. The domain transitions are marked by vertical lines. On top of the DSC heating trace, the variation of peak crystallization temperatures T_c as a function of T_s values is plotted.

As can be seen from Figure 4.16, the domain window of exclusive self-nucleation (*Domain II*) is very narrow (only 4 degrees) and the self-nuclei are most probably made of crystal fragments, since most of the domain covers the tail of the melting peak [86]. Regarding the T_c variation with Ts, the observed exponential increase in crystallization temperature upon crossing from *Domain I* to *Domain II* indicates the large increase in nucleation density that is provoked by self-nucleation [85, 87]. No crystallization exotherms were detected inside *Domain I*, as it was mentioned earlier (because of the fractionated crystallization). In the transition to *Domain III* the T_c values continue to increase until they started to decrease slightly. The self-nucleation protocol was also applied to some selected samples (see Table 4.10). Comparing with neat PA6, the transition temperatures from *Domain III* to *Domain II* were very close or identical, which means that the PA6 phase was able to produce self-nuclei without difficulties regardless of the droplet size.

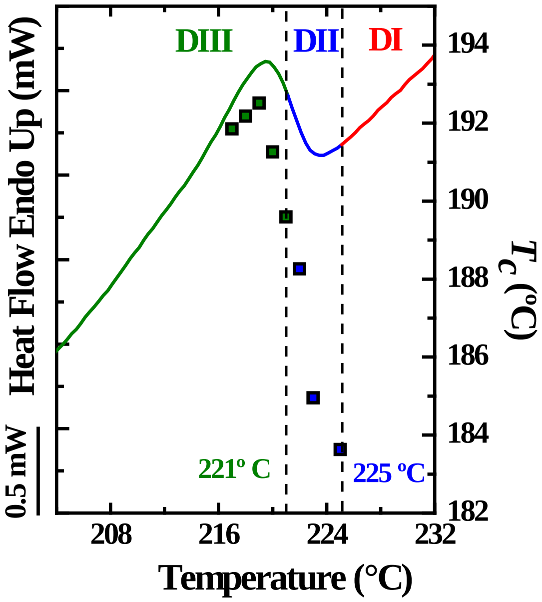

Figure 4.16 Representation of the self-nucleation domains for PA6 in nanocomposite PP/PPgAMH/PA6/PHO 3.7 on top of the standard DSC melting trace. The data points represent peak crystallization temperatures (plotted on the left-hand side y axis) as a function of T_s values.

Table 4.10 Transition temperatures of the self-nucleation domains in selected samples.

Sample	Transition temperatures (°C)	
	DI to *DII*	*DII* to *DIII*
PA6	225	221
PP/PA6	224	221
PP/PPgMA$_H$/PA6/PHO 3.7	225	221
PP/PPgMA$_H$/PA6/PHO 1.6	224	221

4.3.3 Mechanical properties of the PP/PA6 blends with and without nanosilica and compatibilizer agents

Tensile tests were performed to the neat polymers (PP and PA6) and to all blends with both compatibilizing agents and NS. The tensile properties obtained from averaging at least 5 valid tests are summarized in Table 4.11.

The immiscible nature of the PP/PA6 blend leads to a strong reduction on the elongation at break and this observation has been reported previously [20, 103]. This behavior is due to a delamination process that is a consequence of the poor interfacial adhesion [20]. The addition of the compatibilizing agents increased enormously the elongation at break of the 80/20 PP/PA6 binary blend, particularly when the high grafting level compatibilizing agent was employed (PPgMA$_H$). In this last case, the elongation at break increased from 11 % for the neat blend to 262% for the compatibilized blend (i.e., a value comparable to that of neat PP). The role of the compatibilizer is to reduce the interfacial tension. This result is expected, since PPgMA is a well-known compatibilizing agent for the PP/PA blends [20]. The PPgMA compatibilizer decreased the droplet size and enhanced the adhesion between the phases, which in turn favored the stress transfer from the PP matrix to the PA6 dispersed phase and prevented early crack initiation at the interface and its growth [24]. Besides the ductility, the Young modulus values were also improved while the other properties remained similar to neat PP.

In former publications [37, 51] was reported the effect of the addition of hydrophobic NS as a morphology modifier to an 80:20 PP/PA blend. Even though a fine-tuned morphology with a very small droplet size was obtained, no improvement was observed on the ductility of the blends. In this report, we examine the combined effect of adding both compatibilizing agents and silica nanoparticles in the mechanicalperformance of the blends.

Table 4.11 Tensile properties and impact resistance of neat PP, PA6 and blends.

Sample	Young modulus (MPa)	Stress at yield (MPa)	Elongation at yield (%)	Stress at break (Mpa)	Elongation at break (%)	Impact resistance (J/m)
PP	1622 ± 51	33 ± 1	6.7 ± 0,2	20 ± 1	259 ± 42	17.8 ± 0.1
PA6	2654 ± 39	62 ± 3	3.3 ± 0.1	68 ± 2	181 ± 4	59 ± 5
PP/PA6	1763 ± 78	31 ± 1	4.9 ± 0.2	17 ± 1	11 ± 1	15.3 ± 0.1
PP/PPgMA$_M$/PA6	1842 ± 69	35 ± 1	5.4 ± 0.1	21 ± 2	140 ± 20	17.9 ± 0.1
PP/PPgMA$_H$/PA6	1942 ± 34	38 ± 1	5.6 ± 0.1	28 ± 2	262 ± 20	38 ± 5
PP/PPgMA$_H$/PA6/PHI 3.8	1780 ± 36	35.1 ± 0.5	5.2 ± 0.1	33 ± 1	7.8 ± 0.5	7.61 ± 0.01
PP/PPgMA$_H$/PA6/PHO 3.7	1896 ± 34	36.1 ± 0.2	4.4 ± 0.1	18 ± 4	20 ± 1	17 ± 1
PP/PPgMA$_H$/PA6/PHO 1.6	1893 ± 72	35.0 ± 0.5	5.1 ± 0.1	22 ± 1	278 ± 25	22 ± 1
PP/PPgMA$_H$/PA6/PHO 0.9	2241 ± 87	38 ± 1	5.0 ± 0.2	23 ± 2	220 ± 58	25.4 ± 0.1

The addition of ~ 4 % NS led to a strong reduction of elongation at break in the compatibilized blends (PP/PPgMA$_H$/PA6/PHI 3.8 and PP/PPgMA$_H$/PA6/PHO 3.7). The loss of ductility was more remarkable when the hydrophilic NS was employed. The sample failure occurred right after yielding. When the hydrophobic NS was used, some neck stabilization was achieved but the final breaking strain was only 20 %. The addition of ~4 % NS deteriorated the improved ductility gained with addition of the PPgMA agent. Between both samples, the one with PHI exhibited a larger PA6 droplet size (0.51 μm), while the other with PHO had the smaller particle size of all the blends (0.20 μm, see Table 4.4). However, tuning the morphology is not the only factor to adjust in order to obtain new blends with well-balanced properties. The toughness in filled polymer blends is controlled by a good adhesion between all the components, since an effective stress transfer between the matrix and both the filler and the polymeric dispersed phase is required [103]. The TEM images presented in Figure 4.9 showed a PP-PA6 interface completely saturated by NS nanoparticles. Thus, the most likely explanation of the loss ductility is that, even though the compatibilizing agent did improve the adhesion between the PP and PA6 phases, the high concentration of rigid NS nanoparticles surrounding the PA6 droplets interfered with the interfacial adhesion achieved, making the stress transfer between the PP matrix and the PA6 droplets difficult. The deformation mechanism that could lead to loss of ductility in binary blends mixed with nanoparticles is very difficult to assess. A de-cohesion process may have been taken place [37].

The aforementioned mechanical performance was similar to that observed in a previous report for the same blend with 5 % hydrophobic NS without compatibilizing agent [37, 51]. This proved that the NS act only as droplet size modifier avoiding coalescence with no influence in the interfacial adhesion. Its use in combination with a compatibilizing agent further decreases the droplet diameter if we compared with the PA6 droplets size reported in the previous work [37] with the one presented here (0.20 μm). A refined droplet size is expected to contribute to a good mechanical performance. Nevertheless, adding 4 % or more saturates the interface and impoverishes the adhesion between the phases, and ultimately, the mechanical properties. The loss of ductility in blends with nanoparticles located at the interface has been reported for other polymeric systems [38, 39, 57, 58, 104].

In view of the negative outcome in the mechanical performance, reducing the PHO-NS content was the strategy followed to evaluate the effect of NS content. The hydrophobic NS and the $PPgMA_H$ were chosen since this filled compatibilized blend had the smallest particle size and higher elongation at break (0.20 μm and 20 %). Despite the fact that decreasing the PHO content increased the droplet size, the ductility of the blend was remarkably improved. The elongation at break increased from 20 % to 278 and 220 % (see $PP/PPgMA_H/PA6/PHO$ 1.6 and $PP/PPgMA_H/PA6/PHO$ 0.9 in Table 4.11. These blends exhibited a ductility that matches that of $PP/PPgMA_H/PA6$ blend. This observation is in agreement with the morphology of the blends. The TEM images of these two blends (see Fig. 3b. and c.) showed a PP-PA6 interface less saturated with NS nanoparticles. Thus, the NS did not interfere negatively with the action of the compatibilizing agent, and the good adhesion between the phases was preserved. The other mechanical properties, such as tensile strength and Young modulus remained similar or were slightly improved.

Regarding the impact resistance, the behavior observed was similar to the tensile properties. Table 4.11 resumes the Izod impact resistance of the neat polymers, the compatibilized $PP/PPgMA_H/PA6$ blend, and the compatibilized blends with a decreasing content of hydrophobic NS.

As mentioned earlier, a blend with well-balanced properties was obtained as PHO-NS content was decreased. However, it was not as good as the impact resistance of the compatibilized blend without NS. Again, the NS nanoparticles located at the interphase probably acted as stress concentrating particles. The plastic deformation of the PP matrix is the main mechanism responsible for toughening [19]. At high deformation rate (as in impact testing), interfacial debonding is crucial to allow the deformation of the polymer matrix. However, early decohesion at the interphase should be avoided, and a good compatibilizing agent contributes to such a purpose since it impoves interfacial adhesion. Since both PA6 and NS are more rigid particles than the PP matrix, a deficient adhesion between the matrix and the dispersed phase might lead to fast nucleation and growth of cracks without leaving time for the shear yield deformation of the PP matrix [19].

4.3.4 Barrier properties of the PP/PA6 blends with and without nanosilica and compatibilizer agents

Among the systems analyzed, the blend with a high grafting level compatibilizing agent and 1.6 % of hydrophobic silica nanoparticles (PP/PPgMA$_H$/PA6/PHO 1.6) exhibited the best balance between a refined morphology and mechanical performance. For these reasons, this blend was chosen to perform measurements of its carbon dioxide and oxygen permeability. In Fig. 11., CO_2 and oxygen permeability are depicted for pure PP, the PP/PA6 blend compatibilized with PPgMA$_H$ agent (identified in the figure as PPgMA$_H$), and the PP/PA6 blend compatibilized with PPgMA$_H$ agent and filled with 1.6 % hydrophobic NS (identified in the figure as PPgMA$_H$/PHO 1.6). Some reports have been published on permeability properties of blends [105] and multilayer films [106] composed of PP and PA compatibilized with PPgMA. However, to our knowledge, no reports have been published on barrier properties of compatibilized PP/PA6 blends mixed with silica nanoparticles.

Since, PA has excellent barrier properties; the addition of only 20 % improves the permeability resistance of the PP matrix. The reduction of the CO_2 permeability was remarkable while the oxygen permeability decrease was less significant (see the blend with only PPgMA$_H$ in Figure 4.17). The addition of hydrophobic NS further reduced the gas permeability of the blend although to a lesser extent (see PPgMA$_H$/PHO 1.6 in Figure 4.17). Compared to neat PP matrix, the reduction reached for this blend in the

CO_2 and oxygen permeability was 75 and 22 %, respectively. However, compared with the compatibilized blend, the improvement obtained was less noticeable (10 % for CO_2 and 8 % for oxygen permeability). The observed behavior agrees well with the morphology of these blends. The PP/PPgMA$_H$/PA6/PHO 1.6 blend had a PA6 droplet size slightly smaller than the PP/PPgMA$_H$/PA6 blend which translate into a slightly higher average droplet number per cm^3 (71 vs 47 x 10^{11}, see Table 2). The small differences observed might obey to the larger number of well dispersed PA6 droplets that created a more tortuous path for the diffusion of the gas molecules through the PP matrix.

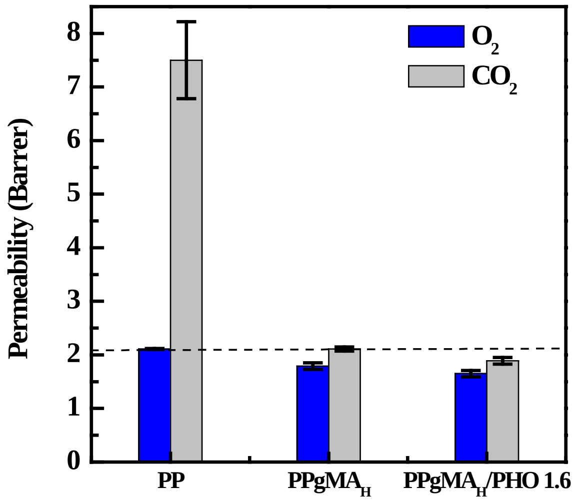

Figure 4.17 Carbon dioxide and oxygen permeability of pure PP, PP/ PPgMA$_H$/PA6 blend and PP/ PPgMA$_H$/PA6/PHO 1.6 nanocomposite. In this figure, PP corresponds to the neat polymer, PPgMA$_H$ to the PP/PA6 blend compatibilized with PPgMA$_H$ agent, and PPgMA$_H$/PHO 1.6, to the PP/PA6 blend compatibilized with PPgMA$_H$ agent and filled with 1.6 % hydrophobic NS.

In addition to the PA6 dispersed phase, the NS nanoparticles have also been proven to reduce the gas permeability in polymer films. Nanocomposites of PP and NS compatibilized with PPgMA exhibited a reduction of 30 % in the oxygen permeability [107]. Likewise, the addition of only 0.09 % of NS nanoparticles modified with an ethylene-vinyl acetate emulsion reduced by 28 % the oxygen permeability of a PP film [108].

Besides the morphology of the blend, the crystallinity of the PP matrix might have also play a role on the barrier properties improvement. Since the crystalline regions are considered impermeable, diffusion of the molecules occurs only through the amorphous region. Therefore, an increase in the crystallinity leads to a positive effect on the barrier properties [108]. Even though the crystallinity of the PP matrix in these two blends did not change significantly (see χ_c for PP, PP/PPgMA$_H$/PA6 and PP/PPgMA$_H$/PA6/PHO 1.6 in Table 4.7), the values agreed well with the results and a tendency towards a decrease in the gas permeability as the PP crystallinity degree increases was observed. This fact might contribute, although in a lesser extent, to the improved barrier properties of the PP/PPgMA$_H$/PA6/PHO 1.6 blend.

4.4 CONCLUSIONS

Further comprehension of the benefits and drawbacks of adding NS particles to PP/PA6 inmiscible blends was attained, and the following conclusions derived from this study:

- The strategy of combining PPgMA compatibilizing agents and NS to fine-tune the morphology of a PP/PA6 80:20 blend is successful.
- Hydrophobic NS is more efficient than hydrophilic NS in refining the size of PA6 droplets, and the addition of ~ 4 % produces the smallest droplet size.
- Comparing with the uncompatibilized and unfilled PP/PA6 blend, a remarkable reduction of 88 % in droplet size was achieved with addition of hydrophobic NS.
- The dramatic reduction in particle size is due to the preferred location of the nanoparticles at the polymer-polymer interphase, creating a physical barrier that avoids coalescence and stabilizes the dispersed phase.
- Interfacial tension estimations indicate that hydrophobic NS is more affine to the PP phase than to the PA6 phase, as it was shown by TEM observations.
- As the PA6 phase crystallizes first, the solid droplets cause a nucleating effect of the PP matrix.
- The small PA6 droplet size induces fractioned crystallization of the PA6 phase.
- Self-nucleation experiments demonstrated that the fractionated crystallization behavior is due to the lack of active heterogeneities in many droplets.
- The PA6 phase was able to produce self-nuclei without difficulties regardless of the droplet size, since the transition temperatures from *Domain III* to *Domain II* were very close or identical to that of the neat PA6.
- A reduced droplet size does not always lead to an improvement in overall performance of the blend. The filled compatibilized blend with the smallest particle size (i.e. PP/PPgMA$_H$/PA6/PHO 3.7) exhibited the worst mechanical performance (low elongation at break and impact resistance).

- As the hydrophobic nanosilica content was reduced, the PA6 droplet size slightly increased, but the ductility of the blend (i.e. PP/PPgMA$_H$/PA6/PHO 1.6) was remarkably improved. Also, the impact resistance was slightly increased.

- An enhanced ductility demonstrated a better interfacial adhesion between the phases. As the hydrophobic NS content is lower, the interface became less saturated. A saturated interphase with rigid silica nanoparticles works against the enhanced interfacial adhesion promoted by the PPgMA compatibilizing agent.

- NS cannot promote interfacial adhesion and the reduction of the droplet size obeys only to the nanoparticle action as interfacial modifier.

- The PP/PA6 blend compatibilized with PPgMA$_H$ and mixed with 1.6 % of hydrophobic NS yielded the best balance of properties: fine-tuned morphology, improved ductility, suitable impact resistance; and reduced oxygen and CO_2 permeability. This sample represents a successful attempt to obtain a PP/PA6 blend stabilized with NS nanoparticles that exhibits good mechanical and barrier performance.

4.5 REFERENCES

[1] *Market Study: Polypropylene*. Available: http://www.ceresana.com/en/market-studies/plastics/polypropylene

[2] J. A. Brydson, "11 - Aliphatic Polyolefins other than Polyethylene, and Diene Rubbers," in *Plastics Materials (Seventh Edition)*Oxford: Butterworth-Heinemann, 1999, pp. 247-310.

[3] R. Lieberman and C. Stewart, "Propylene Polymers," in *Encyclopedia of Polymer Science and Technology*: John Wiley & Sons, Inc., 2002.

[4] J. A. Brydson, "18 - Polyamides and Polyimides," in *Plastics Materials (Seventh Edition)*Oxford: Butterworth-Heinemann, 1999, pp. 478-530.

[5] R. J. Palmer, "Polyamides, Plastics," in *Encyclopedia of Polymer Science and Technology*: John Wiley & Sons, Inc., 2002.

[6] M. Kohan, *Nylon Plastics*. New York: John Wiley & Sons, 1973.

[7] C. Koning, M. V. Duin, C. Pagnoulle, and R. Jerome, "Strategies for compatibilization of polymer blends," *Progress in Polymer Science,* vol. 23, pp. 707-757, 1998.

[8] C. C. Sarath, R. A. Shanks, and S. Thomas, "Chapter 1 - Polymer Blends," in *Nanostructured Polymer Blends*Oxford: William Andrew Publishing, 2014, pp. 1-14.

[9] E. R. Sadiku and E. S. Ogunniran, "Chapter 4 - Compatibilization as a Tool for Nanostructure Formation," in *Nanostructured Polymer Blends*Oxford: William Andrew Publishing, 2014, pp. 101-131.

[10] G. Groeninckx, C. Harrats, M. Vanneste, and V. Everaert, "Crystallization, Micro- and Nano-structure, and Melting Behavior of Polymer Blends," in *Polymer Blends Handbook*, L. A. Utracki, Ed. Dordrecht: Springer Netherlands, 2014, pp. 291-446.

[11] A. Ajji, "Interphase and Compatibilization by Addition of a Compatibilizer," in *Polymer Blends Handbook*, L. A. Utracki and C. A. Wilkie, Eds. 2nd ed. Dordrecht: Springer, 2014, pp. 447-516.

[12] S. C. Agwuncha *et al.*, "Crystallization and Morphological Changes in Nanostructured Polymer Blends," in *Design and Applications of Nanostructured Polymer Blends and Nanocomposite Systems*, R. Shanks and S.

Chandrasekharakurup, Eds. Boston: William Andrew Publishing, 2016, pp. 287-312.

[13] N. G. McCrum, C. P. Buckley, and C. Bucknall, *Principles of polymer engineering*. New York: Oxford University Press, 1996.

[14] C. Bucknall and D. R. Paul, *Polymer blends, formulation and performance* New York John Wiley and Sons, 2000.

[15] L. M. Robeson, *Polymer Blends, a comprehensive review*. Cincinnati: Carl Hanser Publisher, 2007.

[16] A. Isayev, *Encyclopedia of polymer blends. Fundamentals*. Weinheim: Wiley-VCH, 2011.

[17] A. Taguet, P. Cassagnau, and J.-M. Lopez-Cuesta, "Structuration, selective dispersion and compatibilizing effectof (nano)fillers in polymer blends," *Progress in Polymer Science,* vol. 39, pp. 1526-1563, 2014.

[18] S. C. Agwuncha *et al.*, "Immiscible Polymer Blends Stabilized with Nanophase," in *Design and Applications of Nanostructured Polymer Blends and Nanocomposite Systems*, R. Shanks and S. Chandrasekharakurup, Eds. Boston: William Andrew Publishing, 2016, pp. 215-237.

[19] N. Zeng, S. L. Bai, C. G'Sell, J. M. Hiver, and Y. W. Mai, "Study on the microstructures and mechanical behaviour of compatibilized polypropylene/polyamide-6 blends," *Polymer International,* vol. 51, no. 12, pp. 1439-1447, 2002.

[20] A. González-Montiel, H. Keskkula, and D. R. Paul, "Impact-modified nylon 6/polypropylene blends: 2. Effect of reactive functionality on morphology and mechanical properties," *Polymer,* vol. 36, no. 24, pp. 4605-4620, 1995.

[21] L. A. Pinheiro, C. S. Bittencourt, and S. V. Canevarolo, "Real time assessment of the compatibilization of polypropylene/polyamide 6 blends during extrusion," *Polymer Engineering & Science,* vol. 50, no. 4, pp. 826-834, 2010.

[22] F. Ide and A. Hasegawa, "Studies on polymer blend of nylon 6 and polypropylene or nylon 6 and polystyrene using the reaction of polymer," *Journal of Applied Polymer Science,* vol. 18, no. 4, pp. 963-974, 1974.

[23] T. Inoue, "Morphology of Polymer Blends," in *Polymer Blends Handbook,* L. A. Utracki, Ed. Dordrecht: Springer Netherlands, 2003, pp. 547-576.

[24] H. Liu, T. Xie, Y. Zhang, Y. Ou, and G. Yang, "Phase morphology development in PP/PA6 blends induced by a maleated thermoplastic elastomer," *Journal of Polymer Science Part B: Polymer Physics,* vol. 44, no. 7, pp. 1050-1061, 2006.

[25] H.-S. Moon, B.-K. Ryoo, and J.-K. Park, "Concurrent crystallization in polypropylene/nylon-6 blends using maleic anhydride grafted polypropylene as a compatibilizing agent," *Journal of Polymer Science Part B: Polymer Physics,* vol. 32, no. 8, pp. 1427-1435, 1994.

[26] T. Tang and B. Huang, "Fractionated crystallization in polyolefins–nylon 6 blends," *Journal of Applied Polymer Science,* vol. 53, no. 3, pp. 355-360, 1994.

[27] O. T. Ikkala, R. M. Holsti-Miettinen, and J. Seppälä, "Effects of compatibilization on fractionated crystallization of PA6/PP blends," *Journal of Applied Polymer Science,* vol. 49, no. 7, pp. 1165-1174, 1993.

[28] R. Holsti-Miettinen, J. Seppälä, and O. T. Ikkala, "Effects of compatibilizers on the properties of polyamide/polypropylene blends," *Polymer Engineering & Science,* vol. 32, no. 13, pp. 868-877, 1992.

[29] A. Nuzzo, E. Bilotti, T. Peijs, D. Acierno, and G. Filippone, "Nanoparticle-induced co-continuity in immiscible polymer blends - A comparative study on bio-based PLA-PA11 blends filled with organoclay, sepiolite, and carbon nanotubes," *Polymer,* vol. 55 pp. 4908-4919, 2014.

[30] G. Filippone, A. Causa, M. S. d. Luna, L. Sanguigno, and D. Acierno, "Assembly of plate-like nanoparticles in immiscible polymer blends – effect of the presence of a preferred liquid–liquid interface," *Soft Matter,* vol. 10, pp. 3183–3191, 2014.

[31] S. Sinha Ray and M. Bousmina, "Effect of organic modification on the compatibilization efficiency of clay in an immiscible polymer blend," *Macromolecular Rapid Communications,* vol. 26, pp. 1639-1646, 2005.

[32] S. Sinha Ray, S. Pouliot, M. Bousmina, and L. A. Utracki, "Role of organically modified layered silicate as an active interfacial modifier in immiscible polystyrene/polypropylene blends," *Polymer,* vol. 45, no. 25, pp. 8403-8413, 2004.

[33] B. Chen and J. R. G. Evans, "Mechanical properties of polymer-blend nanocomposites with organoclays: Polystyrene/ABS and high impact polystyrene/ABS," *Journal of Polymer Science Part B: Polymer Physics,* vol. 49, no. 6, pp. 443-454, 2011.

[34] A. C. Baudouin, D. Auhl, F. Tao, J. Devaux, and C. Bailly, "Polymer blend emulsion stabilization using carbon nanotubes interfacial confinement," *Polymer,* vol. 52, no. 1, pp. 149-156, 2011.

[35] A. C. Baudouin, J. Devaux, and C. Bailly, "Localization of carbon nanotubes at the interface in blends of polyamide and ethylene-acrylate copolymer," *Polymer,* vol. 51, no. 6, pp. 1341-1354, 2010.

[36] A. C. Baudouin, C. Bailly, and J. Devaux, "Interface localization of carbon nanotubes in blends of two copolymers," *Polymer Degradation and Stability,* vol. 95, no. 3, pp. 389-398, 2010.

[37] F. Laoutid, E. Estrada, R. M. Michell, L. Bonnaud, A. J. Müller, and P. Dubois, "The influence of nanosilica on the nucleation, crystallization and tensile properties of PP-PC and PP-PA blends," *Polymer,* vol. 54, pp. 3982-3993, 2013.

[38] F. Laoutid, D. Francois, Y. Paint, L. Bonnaud, and P. Dubois, "Using nanosilica to fine-tune morphology and properties of polyamide 6/poly(propylene) blends," *Macromolecular Materials and Engineering,* vol. 298, pp. 328-338, 2013.

[39] F. Laoutid, D. Francois, Y. Paint, L. Bonnaud, and P. Dubois, "Morphology and properties of polyamide 6 / poly(propylene) blends fine-tuned with nanosilica," *Macromolecular Symposia,* vol. 321-322, pp. 90-84, 2012.

[40] L. Elias, F. Fenouillot, J.-C. Majeste, G. Martin, and P. Cassagnau, "Migration of nanosilica particles in polymer blends," *Journal of Polymer Science Part B: Polymer Physics,* vol. 46, pp. 1976-1983, 2008.

[41] L. Elias, F. Fenouillot, J. C. Majesté, P. Alcouffe, and P. Cassagnau, "Immiscible polymer blends stabilized with nano-silica particles: Rheology and effective interfacial tension," *Polymer,* vol. 49, no. 20, pp. 4378-4385, 2008.

[42] L. Elias, F. Fenouillot, J.-C. Majesté, and P. Cassagnau, "Morphology and rheology of immiscible polymer blends filled with silica nanoparticles," *Polymer,* vol. 48, pp. 6029-6040, 2007.

[43] J. Vermant, G. Cioccolo, K. Golapan Nair, and P. Moldenaers, "Coalescence suppression in model immiscible polymer blends by nano-sized colloidal particles," *Rheologica Acta,* vol. 43, no. 5, pp. 529-538, 2004.

[44] M. Salzano de Luna and G. Filippone, "Effects of nanoparticles on the morphology of immiscible polymer blends – Challenges and opportunities," *European Polymer Journal,* vol. 79, pp. 198-218, 2016.

[45] R. Scaffaro and L. Botta, "Nanofilled Thermoplastic-Thermoplastic Polymer Blends " in *Nanostructured Polymer Blends*, S. Thomas, R. Shanks, and S. Chandrasekharakurup, Eds. United Kingdom: Elsevier, 2014, pp. 133-160.

[46] S. Melle, M. Lask, and G. G. Fuller, "Pickering Emulsions with Controllable Stability," *Langmuir*, doi: 10.1021/la047691n vol. 21, no. 6, pp. 2158-2162, 2005/03/01 2005.

[47] F. Gubbels, R. Jerome, E. Vanlathem, R. Deltour, S. Blacher, and F. Brouers, "Kinetic and Thermodynamic Control of the Selective Localization of Carbon Black at the Interface of Immiscible Polymer Blends," *Chemistry of Materials*, vol. 10, no. 5, pp. 1227-1235, 1998/05/01 1998.

[48] F. Gubbels *et al.*, "Design of Electrical Composites: Determining the Role of the Morphology on the Electrical Properties of Carbon Black Filled Polymer Blends," *Macromolecules*, vol. 28, no. 5, pp. 1559-1566, 1995/02/01 1995.

[49] F. Fenouillot, P. Cassagnau, and J.-C. Majesté, "Uneven distribution of nanoparticles in immiscible fluids: Morphology development in polymer blends," *Polymer*, vol. 50, pp. 1333-1350, 2009.

[50] R. Foudazi and H. Nazockdast, "Rheology and morphology of nanosilica-containing polypropylene and polypropylene/liquid crystalline polymer blend," *Journal of Applied Polymer Science*, vol. 128, no. 6, pp. 3501-3511, 2013.

[51] L. Sangroniz *et al.*, "The outstanding ability of nanosilica to stabilize dispersions of Nylon 6 droplets in a polypropylene matrix," *Journal of Polymer Science Part B: Polymer Physics*, vol. 53, no. 22, pp. 1567-1579, 2015.

[52] R. Salehiyan, Y. Yoo, W. Jin-Choi, and K. Hyun, "Characterization of morphologies of compatibilized polypropylene/polystyrene blends with nannoparticles via nonlinear rheological properties from FT-Rheology," *Macromolecules*, vol. 47, no. 12, pp. 4066-4076, 2014.

[53] Y. Liu and M. Kontopoulou, "The structure and physical properties of polypropylene and thermoplastic olefin nanocomposites containing nanosilica," *Polymer*, vol. 47, no. 22, pp. 7731-7739, 2006.

[54] J. Ville, P. Médéric, J. Huitric, and T. Aubry, "Structural and rheological investigation of interphase in polyethylene/polyamide/nanoclay ternary blends," *Polymer*, vol. 53, no. 8, pp. 1733-1740, 2012.

[55] J. Huitric, J. Ville, P. Ḿd́ric, M. Moan, and T. Aubry, "Rheological, morphological and structural properties of PE/PA/nanoclay ternary blends:

Effect of clay weight fraction," *Journal of Rheology,* vol. 53, no. 5, pp. 1101-1119, 2009.

[56] W. Li, A. B. Spoelstra, and J. G. P. Goossens, "Morphology and rheological properties of silica-filled poly(carbonate)/poly(methyl methacrylate) blends," *Polymer Engineering & Science,* vol. 55, no. 9, pp. 1951-1959, 2015.

[57] Q. Zhang, H. Yang, and Q. Fu, "Kinetics-controlled compatibilization of immiscible polypropylene/ polystyrene blends using nano-SiO2 particles," *Polymer,* vol. 45, no. 6, pp. 1913-1922, 2004.

[58] R. Scaffaro, L. Botta, M. C. Mistretta, and F. P. La Mantia, "Preparation and characterization of polyamide 6/polyethylene blend-clay nanocomposites in the presence of compatibilisers and stabilizing system," *Polymer Degradation and Stability,* vol. 95, no. 12, pp. 2547-2554, 2010.

[59] S. H. Lee, M. Bailly, and M. Kontopoulou, "Morphology and Properties of Poly(propylene)/Ethylene-Octene Copolymer Blends Containing Nanosilica," *Macromolecular Materials and Engineering,* vol. 297, no. 1, pp. 95-103, 2012.

[60] J. S. Hong, Y. K. Kim, K. H. Ahn, S. J. Lee, and C. Kim, "Interfacial tension reduction in PBT/PE/clay nanocomposite," *Rheologica Acta,* vol. 46, no. 4, pp. 469-478, 2007// 2007.

[61] J. S. Hong, H. Namkung, K. H. Ahn, S. J. Lee, and C. Kim, "The role of organically modified layered silicate in the breakup and coalescence of droplets in PBT/PE blends," *Polymer,* vol. 47, no. 11, pp. 3967-3975, 5/17/ 2006.

[62] P. Li *et al.*, "Fractionated crystallization and morphology of PP/PS blends in the presence of silica nanoparticles with different surface chemistries," *Colloid and Polymer Science,* vol. 291, no. 7, pp. 1693-1704, 2013// 2013.

[63] G. Chen *et al.*, "Hybrid nanoparticles with different surface chemistries show higher efficiency in compatibilizing immiscible polymer blends," *Composites Science and Technology,* vol. 105, pp. 37-43, 2014.

[64] H. Frensch, P. Harnischfeger, and B. J. Jungnickel, "Fractionated Crystallization in Incompatible Polymer Blends," in *Multiphase Polymers: Blends and Ionomers,* vol. 395, L. A. Utracki and R. A. Weiss, Eds.: ASC Symp Series, 1989, p. 101.

[65] J. S. Borah, N. Karak, and T. K. Chaki, "Effect of organoclay platelets on morphology and properties of LLDPE/EMA blends," *Materials Science and Engineering: A,* vol. 528, no. 6, pp. 2820-2830, 3/15/ 2011.

[66] M. Entezam, H. A. Khonakdar, A. A. Yousefi, S. H. Jafari, U. Wagenknecht, and G. Heinrich, "On nanoclay localization in polypropylene/poly(ethylene terephthalate) blends: Correlation with thermal and mechanical properties," *Materials & Design,* vol. 45, pp. 110-117, 2013.

[67] F. Xiang *et al.*, "Largely enhanced ductility of immiscible high density polyethylene/polyamide 6 blends via nano-bridge effect of functionalized multiwalled carbon nanotubes," *Polymers for Advanced Technologies,* vol. 22, no. 12, pp. 2533-2542, 2011.

[68] L. Sangroniz, J. K. Palacios, M. Fernández, J. I. Eguiazabal, A. Santamaria, and A. J. Müller, "Linear and non-linear rheological behavior of polypropylene/polyamide blends modified with a compatibilizer agent and nanosilica and its relationship with the morphology," *European Polymer Journal,* Article vol. 83, pp. 10-21, 2016.

[69] F. Fenouillot, P. Cassagnau, and J.-C. Majesté, "Uneven distribution of nanoparticles in immiscible fluids: Morphology development in polymer blends," *Polymer,* vol. 50, no. 1333-1350, 2009.

[70] Y. Tang *et al.*, "Investigation on polypropylene and polyamide-6 alloys/montmorillonite nanocomposites," *Polymer,* vol. 45, no. 15, pp. 5317-5326, 2004.

[71] H. Yang *et al.*, "Largely improved toughness of PP/EPDM blends by adding nano-SiO2 particles," *Polymer,* vol. 48, no. 3, pp. 860-869, 2007.

[72] J. Chen *et al.*, "A simple strategy to achieve very low percolation threshold via the selective distribution of carbon nanotubes at the interface of polymer blends," *Journal of Materials Chemistry,* 10.1039/C2JM34295B vol. 22, no. 42, pp. 22398-22404, 2012.

[73] W. Li, J. Karger-Kocsis, and R. Thomann, "Compatibilization effect of TiO2 nanoparticles on the phase structure of PET/PP/TiO2 nanocomposites," *Journal of Polymer Science Part B: Polymer Physics,* vol. 47, no. 16, pp. 1616-1624, 2009.

[74] R. Scaffaro, M. C. Mistretta, and F. P. La Mantia, "Compatibilized polyamide 6/polyethylene blend-clay nanocomposites: Effect of the degradation and stabilization of the clay modifier," *Polymer Degradation and Stability,* vol. 93, no. 7, pp. 1267-1274, 2008.

[75] S. Bose, A. R. Bhattacharyya, P. V. Kodgire, and A. Misra, "Fractionated crystallization in PA6/ABS blends: Influence of a reactive compatibilizer and multiwall carbon nanotubes," *Polymer,* vol. 48, no. 1, pp. 356-362, 1/5/ 2007.

[76] O. M. Istrate, M. A. Gunning, C. L. Higginbotham, and B. Chen, "Structure–property relationships of polymer blend/clay nanocomposites: Compatibilized and noncompatibilized polystyrene/propylene/clay," *Journal of Polymer Science Part B: Polymer Physics,* vol. 50, no. 6, pp. 431-441, 2012.

[77] H. Yang, Q. Zhang, M. Guo, C. Wang, R. Du, and Q. Fu, "Study on the phase structures and toughening mechanism in PP/EPDM/SiO2 ternary composites," *Polymer,* vol. 47, no. 6, pp. 2106-2115, 3/8/ 2006.

[78] M. L. Arnal, M. E. Matos, R. A. Morales, O. O. Santana, and A. J. Müller, "Evaluation of the fractionated crystallization of dispersed polyolefins in a polystyrene matrix," *Macromolecular Chemistry and Physics,* vol. 199, no. 10, pp. 2275-2288, 1998.

[79] S. Chandrasekhar, "Stochastic problems in physics and astronomy," *Reviews of Modern Physics,* vol. 15, no. 1, pp. 1-89, 1943.

[80] S. Wu, *Polymer Interface and Adhesion*. New York: CRC Press, 1982.

[81] S. Wu, "Surface and Interfacial Tension of Polymers, Oligomers, Plasticizers, and Organic Pigment," in *Polymer Handbook*, J. Brandrup, E. Immergut, and E. Grulke, Eds. 4th ed. New York: John Wiley & Sons, 1999, pp. VI/522-VI/531.

[82] D. W. van Krevelen and K. te Nijenhuis, *Properties of polymers*, 4 ed. Amsterdam: Elsevier B.V., 2009.

[83] D. Cwikel, Q. Zhao, C. Liu, X. Su, and A. Marmur, "Comparing Contact Angle Measurements and Surface Tension Assessments of Solid Surfaces," *Langmuir,* doi: 10.1021/la1020252 vol. 26, no. 19, pp. 15289-15294, 2010/10/05 2010.

[84] B. Fillon, B. Lotz, A. Thierry, and J. C. Wittmann, "Self-nucleation and enhanced nucleation of polymers. Definition of a convenient calorimetric “efficiency scale” and evaluation of nucleating additives in isotactic polypropylene (α phase)," *Journal of Polymer Science Part B: Polymer Physics,* vol. 31, no. 10, pp. 1395-1405, 1993.

[85] B. Fillon, J. C. Wittmann, B. Lotz, and A. Thierry, "Self-nucleation and recrystallization of isotactic polypropylene (α phase) investigated by differential scanning calorimetry," *Journal of Polymer Science Part B: Polymer Physics,* vol. 31, no. 10, pp. 1383-1393, 1993.

[86] R. M. Michell, A. Mugica, M. Zubitur, and A. J. Müller, "Self-Nucleation of Crystalline Phases Within Homopolymers, Polymer Blends, Copolymers, and Nanocomposites," 2016.

[87] A. J. Müller and M. L. Arnal, "Thermal fractionation of polymers," *Progress in Polymer Science,* vol. 30, no. 5, pp. 559-603, 2005.

[88] Z. Huang, J.-F. Su, X.-Q. Su, Y.-H. Guo, L.-J. Teng, and C. Min Yang, "Preparation and permeation characterization of β-zeolite-incorporated composite membranes," *Journal of Applied Polymer Science,* vol. 112, no. 1, pp. 9-18, 2009.

[89] M.-F. Laguna, J. Guzmán, E. Riande, and E. Saiz, "Experimental and Simulation Studies on the Transport of Argon through Poly(pentaerythritoltribenzoate acrylate)," *Macromolecules,* doi: 10.1021/ma9805654 vol. 31, no. 21, pp. 7488-7494, 1998/10/01 1998.

[90] A. Chaos, J. M. García, M. Iriarte, J. Fernández, J. R. Sarasua, and A. Etxeberria, "Miscibility and Transport Properties of Poly(lactide)/Phenoxy System," *Macromolecular Symposia*, vol. 321-322, no. 1, pp. 20-24, 2012.

[91] F. P. La Mantia, "Blends of polypropylene and nylon 6. Influence of the compatibilizer, molecular weight, and processing conditions," *Advances in Polymer Technology,* vol. 12, no. 1, pp. 47-59, 1993.

[92] M. Gahleitner, B. Kretzschmar, D. Pospiech, E. Ingolic, N. Reichelt, and K. Bernreitner, "Morphology and mechanical properties of polypropylene/ polyamide 6 nanocomposites prepared by a two-step melt-compounding process," *Journal of Applied Polymer Science,* vol. 100, no. 1, pp. 283-291, 2006.

[93] J. Roeder, R. V. B. Oliveira, M. C. Gonçalves, V. Soldi, and A. T. N. Pires, "Polypropylene/polyamide-6 blends: influence of compatibilizing agent on interface domains," *Polymer Testing,* vol. 21, no. 7, pp. 815-821, 2002.

[94] R. M. Michell and A. J. Müller, "Confined Crystallization of Polymeric Materials," *Progress in Polymer Science,* vol. 54-55, pp. 183-216, 2016.

[95] Frensch H, P. Harnischfeger, and B. J. Jungnickel, "Fractionated Crystallization in Incompatible Polymer Blends," in *Multiphase Polymers: Blends and Ionomers,* vol. 395, L. A. Utracki and R. A. Weiss, Eds.: ASC Symp Series, 1989, p. 101.

[96] A. J. Müller, V. Balsamo, and M. L. Arnal, "Nucleation and crystallization in diblock and triblock copolymers," *Advances in Polymer Science,* vol. 190, pp. 1-63, 2005.

[97] R. M. Michell, I. Blaszczyk-Lezak, C. Mijangos, and A. J. Müller, "Confinement effects on polymer crystallization: From droplets to alumina nanopores," *Polymer,* vol. 54, pp. 4059-4077, 2013.

[98] G. Chen *et al.*, "Hybrid nanoparticles with different surface chemistries show higher efficiency in compatibilizing immiscible polymer blends," *Composites Science and Technology,* vol. 105 pp. 37-43, 2014.

[99] R. A. Morales, M. L. Arnal, and A. J. Müller, "The evaluation of the state of dispersion in immiscible blends where the minor phase exhibits fractionated crystallization," *Polymer Bulletin,* vol. 35, no. 3, pp. 379-386, 1995.

[100] A. J. Müller, M. L. Arnal, and V. Balsamo, "Crystallization in block copolymers with more than one crystallizable block," *Lecture Notes in Physics,* vol. 714, pp. 229-259, 2007.

[101] A. Sánchez, C. Rosales, E. Laredo, A. J. Müller, and M. Pracella, "Compatibility Studies in Binary Blends of PA6 and ULDPE-graft-DEM," *Macromolecular Chemistry and Physics,* vol. 202, no. 11, pp. 2461-2478, 2001.

[102] M. S. Sánchez, V. Mathot, G. V. Poel, G. Groeninckx, and W. Bruls, "Crystallization of polyamide confined in sub-micrometer droplets dispersed in a molten polyethylene matrix," *Journal of Polymer Science Part B: Polymer Physics,* vol. 44, no. 5, pp. 815-825, 2006.

[103] S. Y. Fu, X. Q. Feng, B. Lauke, and Y. W. Mai, "Effects of particle size, particle/matrix interface adhesion and particle loading on mechanical properties of particulate-polymer composites," *Composites, Part B: Engineering,* vol. 39, no. 6, pp. 933-961, 2008.

[104] B. Zhang, J. S.-P. Wong, D. Shi, R. C.-M. Yam, and R. K.-Y. Li, "Investigation on the mechanical performances of ternary nylon 6/SEBS elastomer/nano-SiO2 hybrid composites with controlled morphology," *Journal of Applied Polymer Science,* vol. 115, no. 1, pp. 469-479, 2010.

[105] D. Kim and S. W. Kim, "Barrier property and morphology of polypropylene/polyamide blend film," *Korean Journal of Chemical Engineering,* vol. 20, no. 4, pp. 776-782, 2003// 2003.

[106] D. Jarus, A. Hiltner, and E. Baer, "Barrier properties of polypropylene/polyamide blends produced by microlayer coextrusion," *Polymer*, vol. 43, no. 8, pp. 2401-2408, 2002.

[107] V. Vladimirov, C. Betchev, A. Vassiliou, G. Papageorgiou, and D. Bikiaris, "Dynamic mechanical and morphological studies of isotactic polypropylene/fumed silica nanocomposites with enhanced gas barrier properties," *Composites Science and Technology*, vol. 66, no. 15, pp. 2935-2944, 2006.

[108] D. Li, J. Zhang, W. Xu, and Y. Fu, "Effect of SiO2/EVA on the mechanical properties, permeability, and residual solvent of polypropylene packaging films," *Polymer Composites*, vol. 37, no. 1, pp. 101-107, 2016.

CHAPTER V

FINAL REMARKS AND PERSPECTIVES

The development of polymeric multiphasic materials will continue in the eye of research and industry for the next decades. The ongoing technological requirements demand more sophisticated materials, with easy and low-cost processing, and specific properties. Therefore, designing tuned-property materials requires a deep comprehension of the structure and properties of each phase, and of the influence of each component over the others.

The field of block copolymers has aroused a worldwide rising interest since the very beginning. The emerging advances in synthetic routes, physical and structural characterization, theory, and simulation, will push forward the transfer of research findings into novel technologies and products, during the coming decades. In multicrystalline block copolymers, microphase separation driven by crystallization forces self-assemby into well ordered lamellar nanostructures, depending on the crystallization conditions, composition and physical features of the blocks. These ordered nanostructures can be used in lithography, medical and optoelectronic devices. Additionally, multicrystalline block copolymers allow the study of the crystallization behavior at the nanoscale under confinement environment, and the crystallization analysis becomes more challenging as the number of potentially crystalline phases increases.

Particularly, the complexity of the crystallization behavior of PEO-*b*-PCL-*b*-PLLA triblock terpolymers with three crystallizable phases relies on different competitive effects that depend on the crystallization conditions and the particular physical properties of the blocks. In that sense, whether one of the phases is molten, amorphous or crystalline, it would affect the ability to crystallize of the others two, and as a result, complex opposite effects such as plasticizing, nucleation, anti-plasticizing and confinement might take place. A trilamellar morphology can be tailored to tune the biodegradability of the material at the nanoscale. For instance, PLA–PCL–PEO–PCL–PLA nanoparticles can have different drug delivery profiles depending on whether the core is semicrystalline or amorphous.

The addition of a third crystallizable block would definitely broaden the potential features of these terpolymers for particular applications as biodegradable materials. Further analyses of the nucleation, crystallization and melting behavior, with novel techniques such as FSC, are highly recommended. Surely, understanding the crystallization behavior of triple crystalline triblock terpolymers is expected to be in the focus of researchers for the next years.

The field of polymer blends will continue growing in the near future. The production of polymer blends represents an important part of the total production of plastic materials worldwide, since they have applications in a wide range of fields: packaging, sports, recreation equipments, medical devices, recycling, automotive.

Polymer blending is a direct approach to develop economic and enhanced materials that benefits from increasingly modern technologies. Additionally, the high demand of materials with high performance under specific conditions calls for a deep comprehension of polymer blend properties. The major challenge is to deliver synergistically improved blends. To address this, the strategies include the addition of compatibilizing agents and nanofillers.

During the last decade, the role of nanofillers in immiscible polymer blends has evolved from reinforcement agents to interfacial modifiers. Extensive research has been conducted in the migration of the nanoparticles, since their final location will affect the blend properties. In fact, the mechanical performance of immiscible blends can be compromised by the nanofiller presence at the interface. Thus, a comprehensive control of blend morphology and properties has not been completely attained so far. In the foreseeable future, refinement of the dispersed phase morphology and optimization of the blend performance will continue by changing mixing conditions, type and filler composition, compatibilizing agents and minority phase content, especially for systems other than the PP/PA6 blend. The next trends point to enhancing blends of recycled components, scaffold templating for tissue engineering applications, water purification membranes, biodegradable polymer blends, and polymeric systems with liquid-liquid interfaces.

CHAPTER VI

APPENDIX

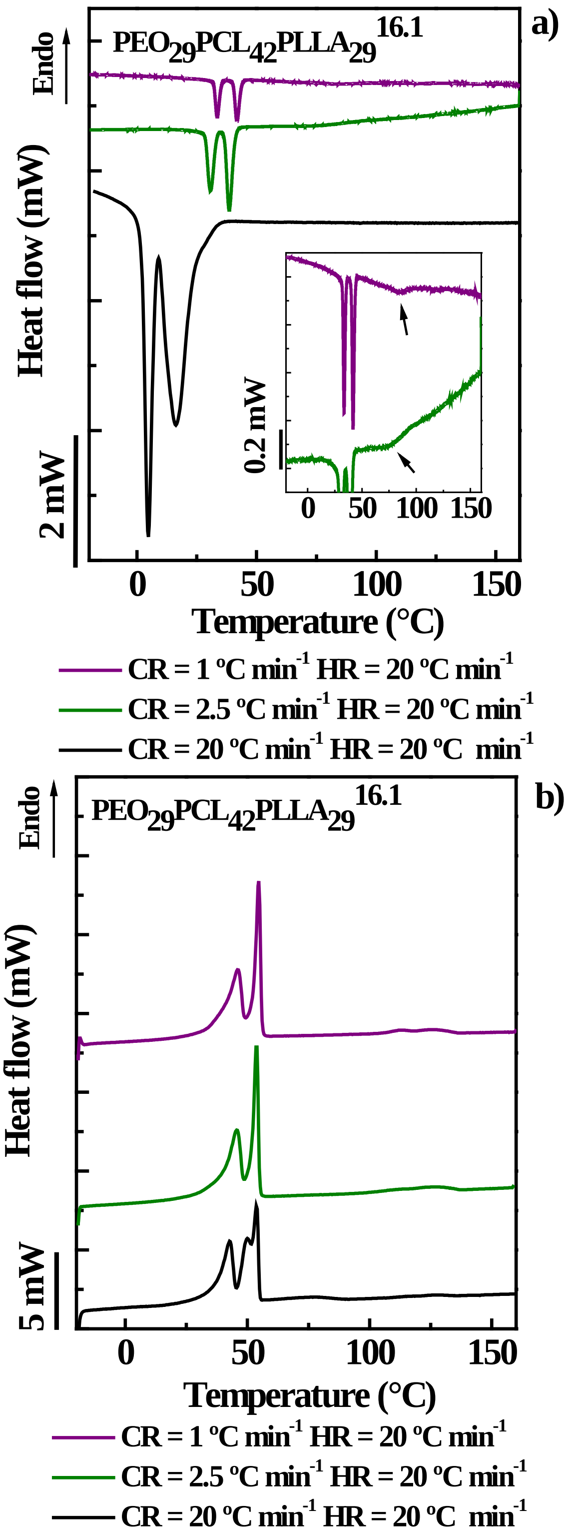

Figure 6.1a) DSC cooling scans at several cooling rates (CR) after melting at 160 ºC for 3 min and b) Subsequent DSC heating scans at 20 ºC min-1 for $PEO_{29}PCL_{42}PLLA_{29}^{16.1}$.

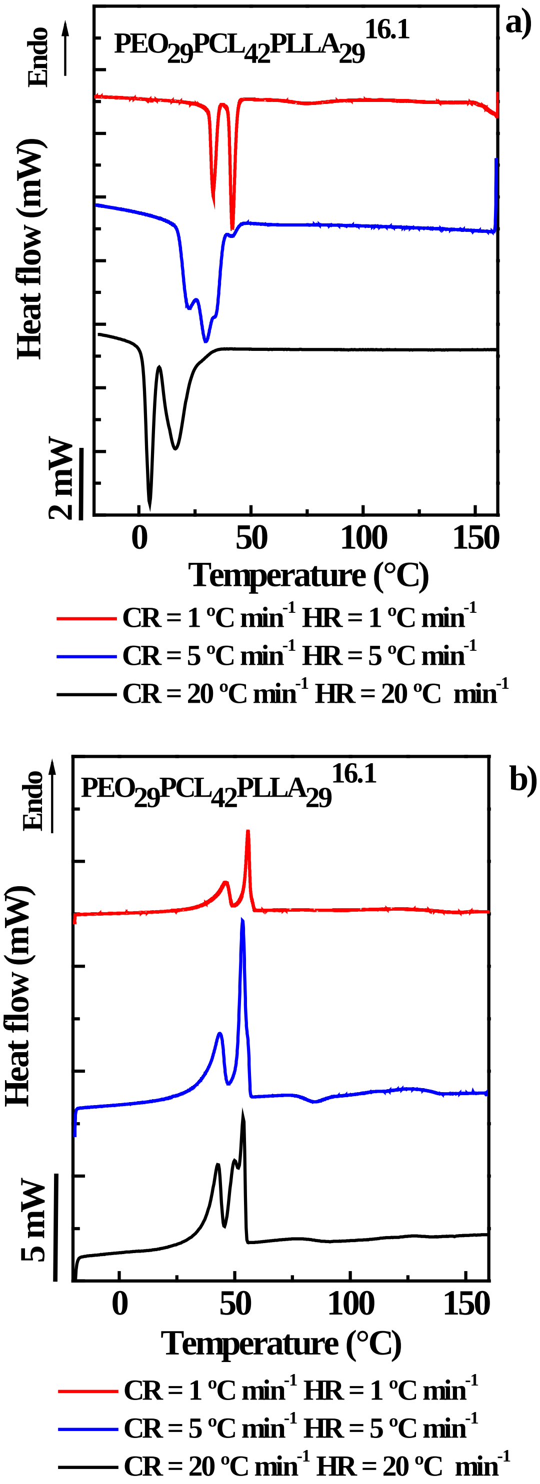

Figure 6.2 DSC cooling scans at several cooling rates (CR) after melting at 160 ºC for 3 min and b) Subsequent DSC heating scans at several heating rates (HR) for PEO$_{29}$PCL$_{42}$PLLA$_{29}^{16.1}$.

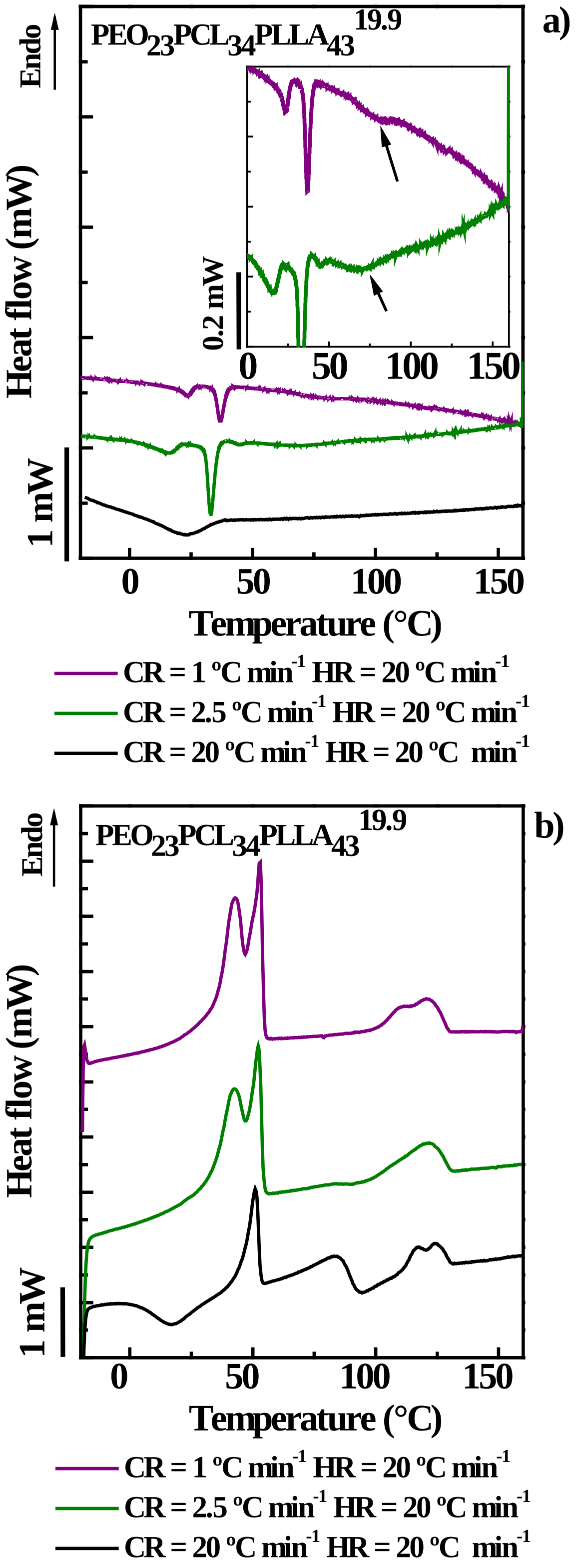

Figure 6.3a) DSC cooling scans at several cooling rates (CR) after melting at 160 ºC for 3 min and b) Subsequent DSC heating scans at 20 ºC min^{-1} for $PEO_{23}PCL_{34}PLLA_{43}^{19.9}$.

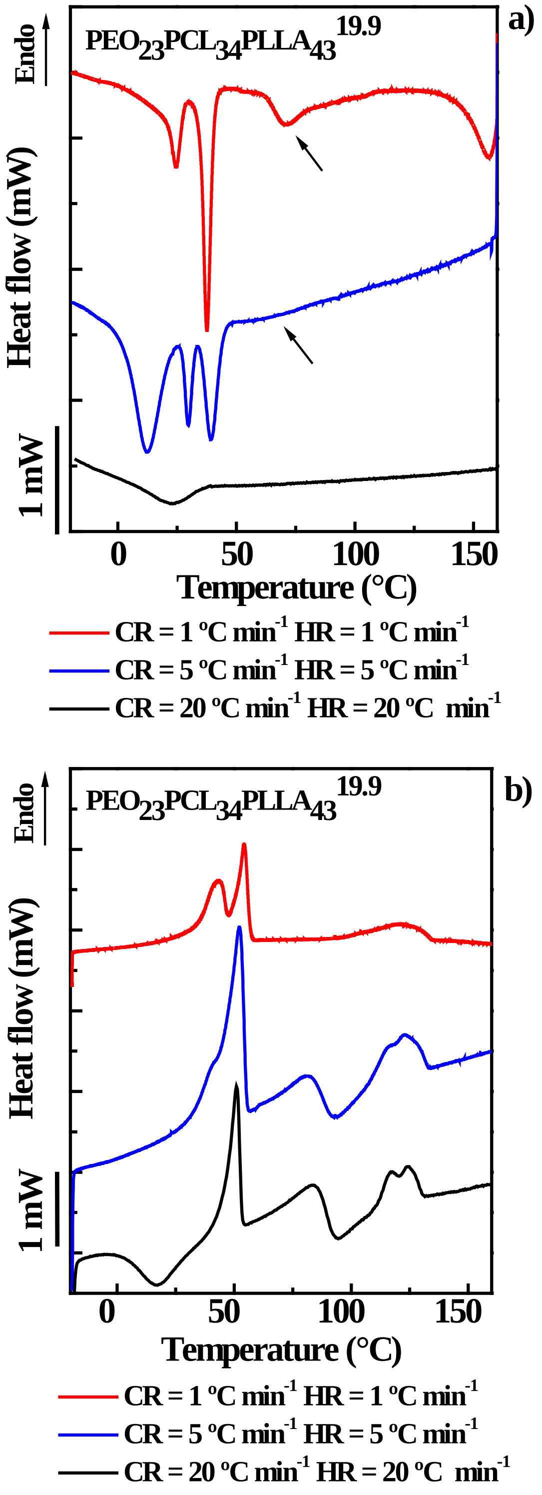

Figure 6.4a) DSC cooling scans at several cooling rates (CR) after melting at 160 ºC for 3 min and b) Subsequent DSC heating scans at several heating rates (HR) for $PEO_{23}PCL_{34}PLLA_{43}^{19.9}$.

Table 6.1 Crystallization and melting temperatures of PEO$_{29}$PCL$_{42}$PLLA$_{29}^{16.1}$and PEO$_{23}$PCL$_{34}$PLLA$_{43}^{19.9}$ triblocks terpolymers compared to r linear diblock copolymers reported in the literature.

	PLLA			PCL			PEO			
Sample code	Block M_w (kg mol^{-1})	T_c (ºC)	T_m (ºC)	Block M_w (kg mol^{-1})	T_c (ºC)	T_m (ºC)	Block M_w (kg mol^{-1})	T_c (ºC)	T_m (ºC)	Ref.
PEO$_{29}$PCL$_{42}$PLLA$_{29}^{16.1}$	**4.7**	**75.0**	**124.5**	**6.8**	**41.7**	**56.9**	**4.6**	**33.5**	**48.0**	**Samples reported here**
PEO$_{23}$PCL$_{34}$PLLA$_{43}^{19.9}$	**8.5**	**72.3**	**121.8**	**6.8**	**36.7**	**54.2**	**4.6**	**22.1**	**45.0**	
L$_{93}$C$_{7}^{18}$	15.7	102.6	171.7	1.7						Castillo, 2010[2]
L$_{81}$C$_{19}^{21}$	16.7	102.8	170.5	3.9						
L$_{60}$C$_{40}^{21}$	12.4	102.8	168.9	8.5	0.5-11.3	54.4				
L$_{55}$C$_{45}^{18}$	**9.5**	**98.3**	**166.9**	**8.1**	**20.8**	**55.0**				
L$_{44}$C$_{56}^{25}$	**11.1**	**91.8**	**166.5**	**14.2**	**23.2**	**56.5**				
L$_{32}$C$_{68}^{22}$	6.9	100.3	161.0	14.9	28.1	56.9				
L$_{10}$C$_{90}^{24}$	2.4	86.8	141.5	21.5	32.5	57.7				
PLLA2300*b*PEG5000	**2.3**	**93.0**	**140.1**				**5.0**	**34.1**	**54.7**	Sun, 2004[1]
PLLA6300*b*PEG5000	**6.3**	**105.2**	**153.8**				**5.0**	**34.6**	**42.2**	
PLLA12000*b*PEG5000	12.0	116.3	162.4				5.0	12.9	37.2	
PEO$_{5}$-*b*-PLLA$_{16}$	16.0	90.6	141.2				5.0		41.2	Huang,2008[3]
PEO$_{5}$-*b*-PLLA$_{30}$	30.0	100.0	142.1				5.0		39.7	
2LPCL$_{50}$-*b*-PLLA$_{43}$	12.45	102.4	151.7	11.33	12.6	51.2				Wang,2006[5]
PEOCL56				**6.24**	**30.4**	**55.4**	**5.0**	**30.4**	**55.4**	He, 2006[6]
PEOCL62				8.13	34.3	56.3	5.0	28.7	56.3	
PEG5000-PCL1000				1.0			5.0	34.7	59.8	Sun, 2011[7]
PEG5000-PCL2900				2.9			5.0	30.0	51.0/54.9	
PEG5000-PCL9200				9.2	34.6	56.7	5.0	29.3	44.6	
PCL$_{13}$-PEG$_{45}$-PCL$_{13}$				**3.0**	**16.5**	**51.7**	**2.0**	**12.2**	**41.2**	Wei, 2009[8]

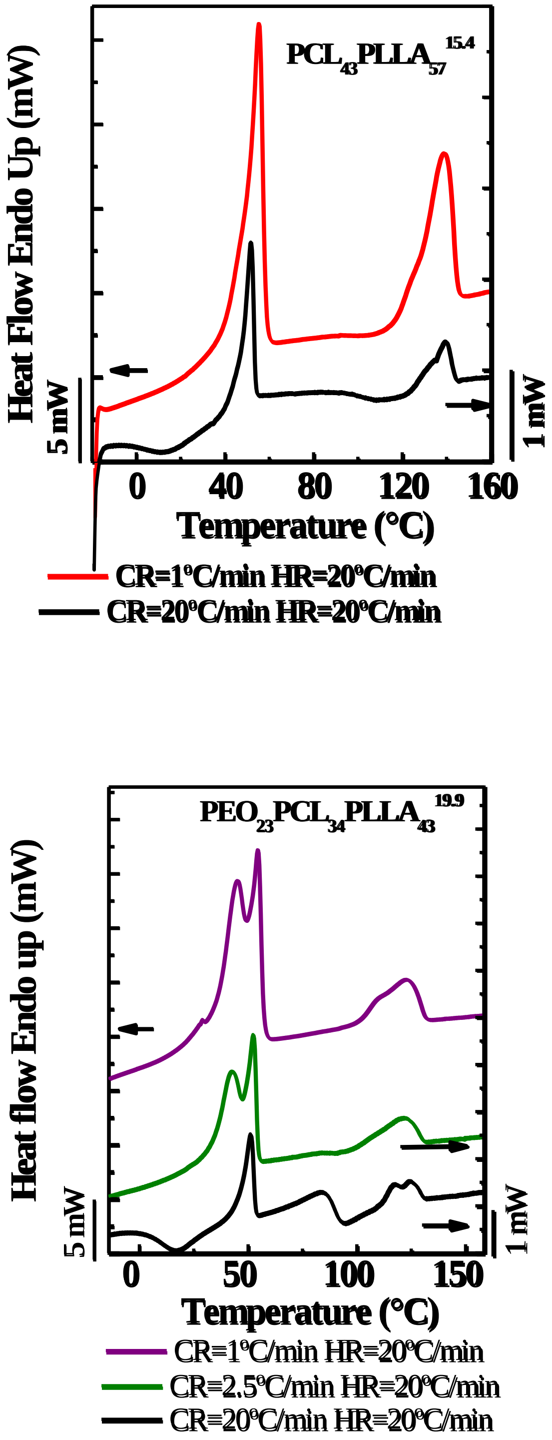

Figure 6.5 DSC heating scans at 20 ºC min^{-1} after cooling at different cooling rates (CR) for the indicated samples.

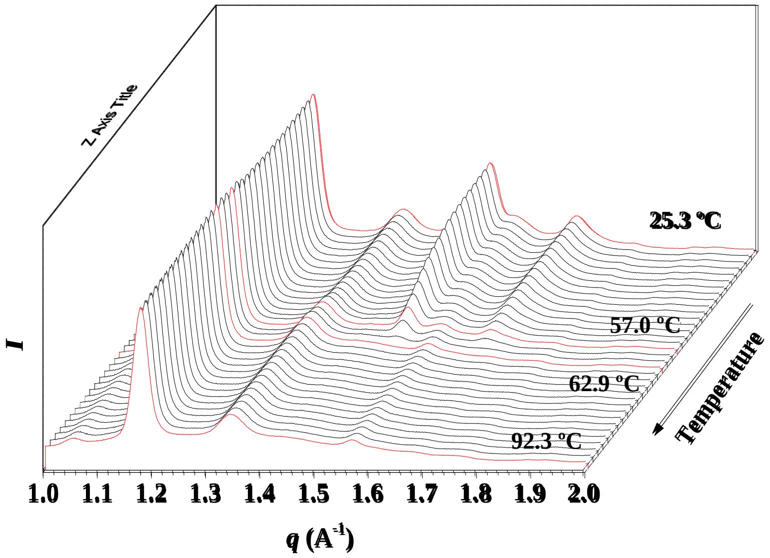

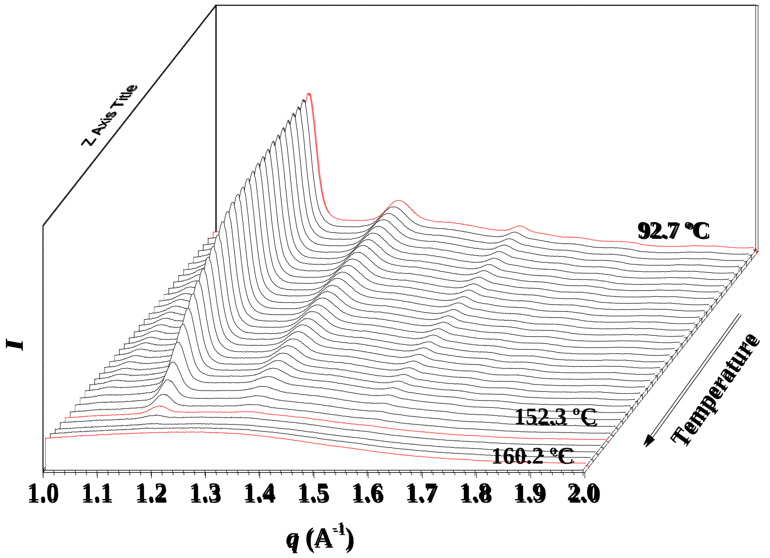

Figure 6.6 WAXS patterns taken during heating after isothermally crystallizing the $PCL_{43}PLLA_{57}^{15.4}$ sample in two step: first at 81 ºC and then at 49.5 ºC.

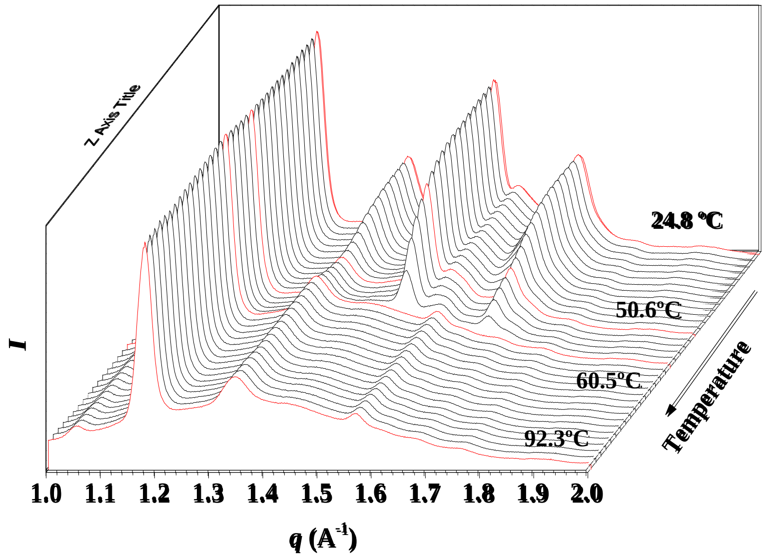

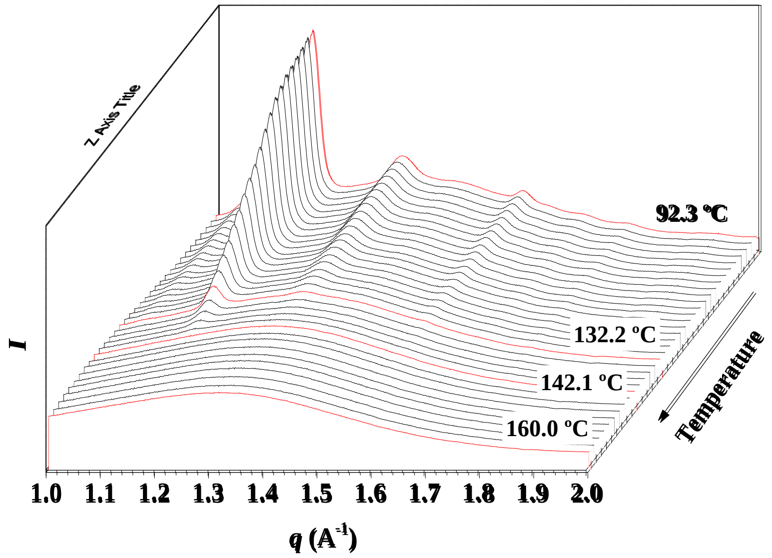

Figure 6.7 WAXS patterns taken during heating after isothermally crystallizing the $PEO_{23}PCL_{34}PLLA_{43}^{19.9}$ sample in two step: first at 81 ºC and then at 50 ºC.

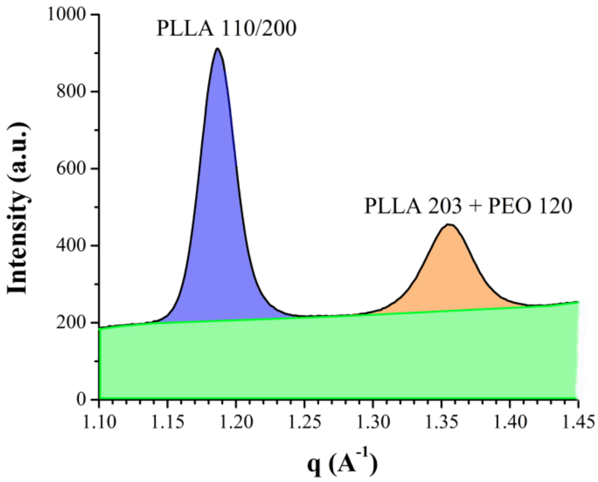

Figure 6.8 Intensity ratio between $PLLA_{113/203}$+PEO_{120} and $PLLA_{110/200}$ signals of the $PEO_{23}PCL_{34}PLLA_{43}^{19.9}$ terpolymer

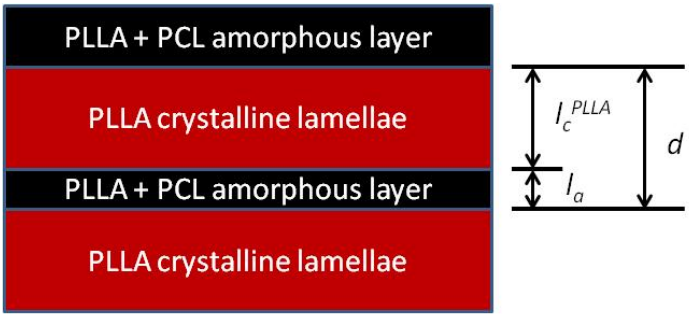

Figure 6.9 Scheme of the lamellar structure of PLLA.

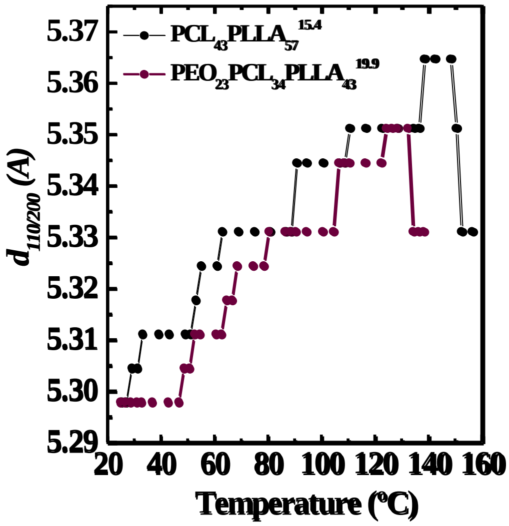

Figure 6.10 Evolution of $d_{110/200}$ interplanar distance during heating.

Table 6.2 Unit cell parameters of PLLA.

Temperature (ºC)	$d_{110/200}$ (Å)	d_{203} (Å)	*a* (Å)	*b* (Å)	*c* (Å)
25	5.2979	4.639	10,596	6.117	28.813
60	5.311	4.654	10.622	6.133	28.980
100	5.3311	4.674	10.662	6.156	29.156
120	5.3512	4.674	10.702	6.179	28.801

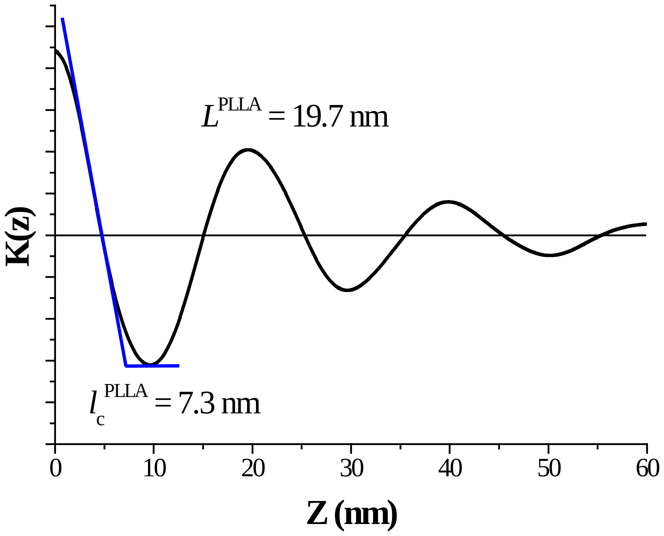

Figure 6.11 One dimensional electron density correlation function of the diblock copolymer at 92.3° C, showing the values for long period and crystalline lamellar thickness.

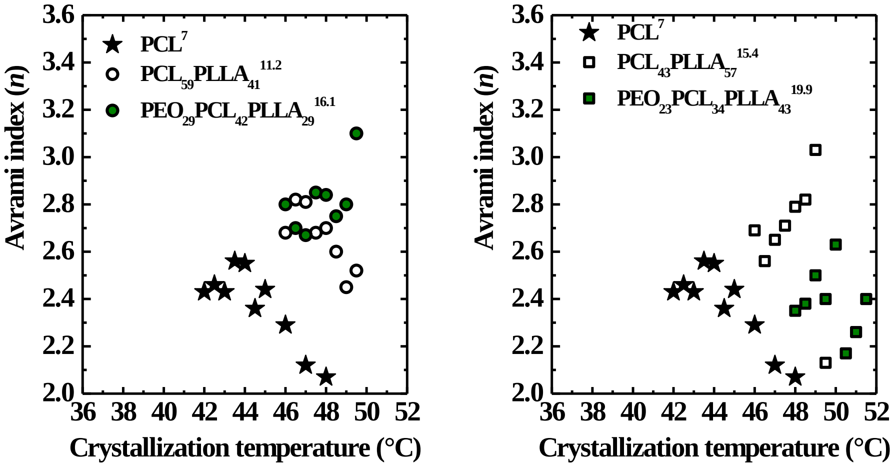

Figure 6.12 Avrami index values of the PCL homopolymer and PCL block within the diblock copolymers and terpolymers indicated, after first isothermally crystallizing the PLLA block until saturation.

References of Table 6.1

(1) Sun, J.; Hong, Z.; Yang, L.; Tang, Z.; Chen, X.; Jing, X. *Polymer* 2004, *45*, 5969-5977.

(2) Castillo, R. V.; Müller, A. J.; Raquez, J. M.; Dubois, P. *Macromolecules* 2010, *43*, 4149-4160.

(3) Huang, S.; Jiang, S.; An, L.; Chen, X. *J. Polym. Sci., Part B: Polym. Phys.* 2008, *46*, 1400-1411.

(4) Muller, A. J.; Avila, M.; Saenz, G.; Salazar, J. In *Poly(Lactic Acid) Science and Technology: Processing, Properties, Additives and Applications*, Jimenez, A.,Peltzer, M.,Ruseckaite, R., Eds.; The Royal Society of Chemistry: Cambridge, 2015; Chapter 3, p 66.

(5) Wang, J. L.; Dong, C. M. *Macromol. Chem. Phys.* 2006, *207*, 554-562.

(6) He, C.; Sun, J.; Ma, J.; Chen, X.; Jing, X. *Biomacromolecules* 2006, *7*, 3482-3489.

(7) Sun, J.; He, C.; Zhuang, X.; Jing, X.; Chen, X. *J. Polym. Res.* 2011, *18*, 2161-2168.

(8) Wei, Z.; Liu, L.; Yu, F.; Wang, P.; Qi, M. *J. Appl. Polym. Sci.* 2009, *111*, 429-436."